General Disclaimer

One or more of the Following Statements may affect this Document

- This document has been reproduced from the best copy furnished by the organizational source. It is being released in the interest of making available as much information as possible.

- This document may contain data, which exceeds the sheet parameters. It was furnished in this condition by the organizational source and is the best copy available.

- This document may contain tone-on-tone or color graphs, charts and/or pictures, which have been reproduced in black and white.

- This document is paginated as submitted by the original source.

- Portions of this document are not fully legible due to the historical nature of some of the material. However, it is the best reproduction available from the original submission.

Produced by the NASA Center for Aerospace Information (CASI)

FINAL REPORT 12411-6011-R000

JULY 1970

(4)

ADVANCED SPACECRAFT VALVE TECHNOLOGY



Prepared for

THE JET PROPULSION LABORATORY
PASADENA, CALIFORNIA 91103

under

NATIONAL AERONAUTICS AND SPACE ADMINISTRATION
Contract NAS 7-717

N70-39401 (ACCESSION NUMBER)
227 (PAGES)
CR-86435 (NASA CR OR TMX OR AD NUMBER)
FACILITY FORM 602

N70-39404 (THRU)
1 (CODE)
25 (CATEGORY)

IRW SYSTEMS GROUP

ONE SPACE PARK • REDONDO BEACH • CALIFORNIA

FINAL REPORT NO. 12411-6011-R000

JULY 1970

N70-39401

ADVANCED SPACECRAFT VALVE TECHNOLOGY

Prepared for

THE JET PROPULSION LABORATORY
PASADENA, CALIFORNIA 91103

under

NATIONAL AERONAUTICS AND SPACE ADMINISTRATION
CONTRACT NAS 7-717

R. J. Salvinski, Program Manager

H. L. Burge, Manager
Applied Technology Department

D. H. Lee, Manager
Technology Laboratory

TRW SYSTEMS GROUP
ONE SPACE PARK · REDONDO BEACH, CALIFORNIA

FOREWORD

This final report was prepared by TRW Systems Group, Redondo Beach, California, and contains the results of work undertaken for the purpose of advancing valve technology used on liquid propulsion spacecraft engines. The work was accomplished under Contract NAS 7-717 from October 1968 to May 1970. The program was originated and managed by the Jet Propulsion Laboratory under the technical direction of Mr. Louis R. Toth. The NASA Program Manager was Mr. Frank E. Compitello, Code RPL, Office of Advanced Research and Technology.

The work performed on the program was accomplished by TRW Systems Group, Science and Technology Division. The Program Manager was Mr. R. J. Salvinski of the Applied Technology Department. Technical efforts provided for this program by the several TRW Systems Group personnel are acknowledged:

Mr. C. Armstrong	Applied Technology Department
Mr. N. Doshi	Applied Technology Department
Mr. O. Fiet	Applied Technology Department
Mr. R. Hammel	Materials Science Department
Mr. M. Makowski	Applied Technology Department
Mr. C. Mangion	Applied Technology Department
Dr. H. Mann	Thin Film Department
Mr. R. Porter	Fluid and Electrical Systems Department
Mr. J. Reger	Materials Science Department

The results of efforts made on two subcontracts in support of this program are also acknowledged:

Professor R. W. Christy	Dartmouth College, Hanover, New Hampshire
Professor M. W. Roberts	University of Bradford, Bradford, England
Dr. J. R. H. Ross	University of Bradford, Bradford, England

CONTENTS

		Page
1.0	INTRODUCTION	1-1
2.0	MECHANICAL CONTROLS	2-1
2.1	Introduction	2-1
2.2	Seal Development Study	2-2
2.3	Valve Development Study	2-5
2.4	Test	2-6
2.5	Valve Disconnects	2-10
2.5.1	Requirements	2-12
2.5.2	Design Configurations	2-12
2.5.3	Problem Areas	2-13
2.5.4	Approach to the Design of Disconnects	2-14
2.5.5	Available Disconnects	2-18
2.6	Thermal Actuator Development	2-20
2.6.1	Thermal Actuated Valves	2-27
2.7	References	2-35
3.0	NONMECHANICAL CONTROLS	3-1
3.1	Introduction	3-1
3.2	Propulsion Application Studies	3-5
3.2.1	Propellant Flow Control	3-5
3.2.2	Hybrid Flow Regulator	3-12
3.2.3	Hybrid Flow Regulator Concept	3-17
3.3	Component Development	3-20
3.3.1	Proportional Amplifier Evaluation	3-20
3.3.2	Configuration of Cavitating Venturi Sump	3-21
3.3.3	Cavitating Venturi Sump Test Results	3-24
3.3.4	Preliminary Tests	3-24
3.4	Component Evaluation	3-26
3.4.1	Cavitating Flow Characteristic	3-26
3.4.2	Return Flow Capability	3-29
3.4.3	Water Return Throttling Capability	3-36
3.4.4	Gas Return Throttling Capability	3-36
3.4.5	Venturi Sump Applications	3-39
3.5	References	3-39

CONTENTS (CONT.)

	Page
4.0 TECHNOLOGY SUPPORT	4-1
4.1 Energized Seals	4-1
4.1.1 General	4-1
4.1.2 Teflon Evaluation	4-4
4.1.3 Nitrile Rubber Evaluation	4-9
4.1.4 Silicone Rubber Evaluation	4-9
4.2 Metal/Metal Interference Seals	4-16
4.2.1 Test Methods	4-16
4.2.2 Test Results	4-18
4.2.3 Conclusions	4-22
4.3 Thin Film University Program	4-23
4.4 References	4-23
APPENDIX A - THE FORMATION OF SURFACE FILMS BY ELECTRON BOMBARDMENT	A-1
APPENDIX B - PHYSICAL AND CHEMICAL PROPERTIES OF THIN POLYMER FILMS	B-1
5.0 NEW TECHNOLOGY	5-1
DISTRIBUTION LIST	

ILLUSTRATIONS

Figure No.		Page
1-1	Program Plan	1-3
2-1	Energized Seal	2-4
2-2	Valve and Seal Test Fixture	2-4
2-3	Schematic Diagrams of Five Functionally Different Disconnects	2-17
2-4	Disconnect for Hazardous Fluids	2-19
2-5	Actuator Pellet	2-21
2-6	Thermal Expansion Actuator	2-21
2-7	Test Setup	2-22
2-8	Deflection Vs. Load at Various Temperatures-3118 RTV	2-24
2-9	Deflection Vs. Load at Various Temperatures-RTV 615.	2-25
2-10	Stroke Vs. Temperature at Two Loads	2-26
2-11	Thermohermetic Isolator	2-28
2-12	High Pressure Micro Valve	2-32
2-13	Final Design - Vacuum Valve	2-34
3-1	Nonmechanical Controls Program Plan	3-3
3-2	Concept of Single Source Fluidic Throttling	3-12
3-3	Typical Monopropellant Feed System	3-12
3-4	Hybrid Fluid Flow Regulator	3-14
3-5	Simplified Hybrid Flow Regulator-Scheme I	3-14
3-6	Simplified Hybrid Flow Regulator-Scheme II	3-16
3-7	Simplified Hybrid Flow Regulator-Scheme III	3-16
3-8	Hybrid Fluidic Propellant Flow Regulator	3-19
3-9	Pressure Reference for Flow Regulator	3-19
3-10	Balanced Mechanical Stage Concept	3-19
3-11	Test Setup - Water Calibration of G.E. AM-12 Proportional Gain Block	3-22
3-12	Water Calibration of G.E. AM-12 Proportional Gain Block	3-22
3-13	Cavitating Venturi Sump Configuration	3-23
3-14	Venturi Sump Test Setup and Instrumentation	3-25
3-15	Fluidic Control Demonstration Test Setup	3-25
3-16	Venturi Sump Cavitation Characteristic	3-27
3-17	Venturi Sump Cavitation Characteristic	3-27

ILLUSTRATIONS (CONT.)

Figure No.		Page
3-18	Venturi Sump Cavitation Characteristic.....	3-27
3-19	Venturi Sump Cavitation Characteristic.....	3-27
3-20	Venturi Sump in Cavitation.....	3-28
3-21	Venturi Sump Return Orifice Calibration.....	3-30
3-22	Venturi Sump Return Orifice Calibration.....	3-30
3-23	Venturi Sump Return Flow Capability.....	3-31
3-24	Venturi Sump Return Flow Capability.....	3-31
3-25	Venturi Sump Return Flow Capability.....	3-31
3-26	Venturi Sump Return Flow Capability.....	3-31
3-27	Return Flow in Venturi Sump.....	3-32
3-28	Return Flow in Venturi Sump.....	3-33
3-29	Return Flow in Venturi Sump.....	3-34
3-30	Return Flow in Venturi Sump.....	3-35
3-31	Venturi Sump Throttling Characteristic.....	3-37
3-32	Venturi Sump Throttling Characteristic.....	3-37
3-33	Venturi Sump Throttling Characteristic.....	3-38
3-34	Venturi Sump Throttling Characteristic.....	3-38
3-35	Venturi Sump Throttling Characteristic.....	3-38
3-36	Venturi Sump Throttling Characteristic.....	3-38
3-37	Nitrogen-Water Interaction in Venturi Sump.....	3-40
3-38	Nitrogen-Water Interaction in Venturi Sump.....	3-41
4-1	Test Fixture for Cylindrical Sample.....	4-6
4-2	Pressure Vs. Deflection Curves for Teflon (TFE).....	4-7
4-3	Pressure Vs. Deflection Curves for Teflon (TFE).....	4-8
4-4	Pressure Vs. Deflection for Nitrile Rubber.....	4-11
4-5	Test Fixture for Molded Sample.....	4-12
4-6	Pressure Vs. Deflection for Silicone Rubber.....	4-14
4-7	Interference Fit Ball Seal Test Fixture.....	4-17

TABLES

Table No.		Page
2-1	Valve Leakage Test Data Using Energized Seal.....	2-7
2-2	Valve Contamination Test Leakage Data, Teflon Seat..	2-10
2-3	Estimated Disconnect Fitting Operating Parameters...	2-11
2-4	Functional Requirements and Design Approaches.....	2-15
2-5	Environmental Factors and Effects.....	2-16
3-1	Propulsion Applications of Fluidics.....	3-6
3-2	Relative Importance of Specific Application Areas...	3-7
3-3	Cavitating Venturi Sump Test Instrumentation.....	3-25
4-1	Computed β of Teflon and Rubber.....	4-2
4-2	Range of Poisson's Ratio for Crystalline and Rubbery Materials.....	4-3
4-3	Compressibility Data for Teflon TFE.....	4-5
4-4	Compressibility Data for Nitrile Rubber.....	4-10
4-5	Compressibility Data for Silicone Rubber.....	4-15
4-6	Sphere Diameter.....	4-17
4-7	Tube Diameter.....	4-17
4-8	Summary of Test Results for Stainless Steel Tubes...	4-19
4-9	Summary of Test Results for Aluminum Tubes.....	4-20

1.0 INTRODUCTION

N70-39402

This report describes the results of the Advanced Spacecraft Valve Technology Program under Contract NAS 7-717. The effort was performed by TRW Systems Group during the period October 1968 to May 1970. The program is designed to advance the art of valves and controls used on manned and unmanned spacecraft liquid chemical propulsion systems. In addition, an Advanced Valve Technology Compilation was prepared representing the valve technology associated with spacecraft propulsion requirements, problems, and a review of new valve concepts and new valve technology.

The controls studied are to be used with earth storable and space storable propellants at pressures to 1000 psia and operate reliably in the space environment for periods of up to ten years. The ten year requirement is considered in conjunction with longer missions, beyond Jupiter to the outer planets, Saturn, Uranus, Neptune and Pluto.

Consideration is given to actuating concepts for controlling low flow (micro valves) and flows representing up to 1000 lb_f thrust engines.

Functional parametric requirements for valves and actuators included zero leakage, service life (in the range of 1000 to 50,000 cycles), low weight, minimum size, minimum pressure drop, and minimum power consumption. Environmental parametric requirements included zero gravity, radiation, shock and vibration, sterilization (300°F temperature soak, and/or ethylene oxide sterilant), thermal cycling, thermal shock, vacuum and other effects anticipated by operating for periods of two, five, and ten years in the space and planetary environments within the solar system.

The classes of controls considered are: (1) mechanical controls represented by those valves designed using moving mechanical elements and elements such as diaphragms and flexures, and (2) nonmechanical controls represented by a group of controls that use no moving parts and include the class of components defined as fluidics.

The major emphasis of the work performed and reported was directed toward the use of the space storable propellants oxygen difluoride (OF_2) and diborane (B_2H_6). Leakage criteria used in this program is defined in the JPL Technical Report 32-926 (Basic Criteria and Definition of Zero Fluid Leakage). Thrust levels used for specific valve and control applications are 50 lb, 200 lb and 1000 lb.

The valve compilation is produced in two volumes; Volume I - Mechanical Controls and Volume II - Nonmechanical Controls. The compilation is divided into eight major sections which make up the two volumes.

Volume I - Mechanical Controls

1.0 Introduction
2.0 Operational, Functional and Environmental Considerations
3.0 Materials
4.0 Valves
5.0 Leakage and Seal Technology
6.0 Valve Actuators
7.0 Instrumentation and Measurement

Volume II - Nonmechanical Controls

8.0 Fluidics

This report presents the results of the major technology developed under contract NAS 7-717. A detailed presentation of much of the results during the period of performance is reported under the Advanced Valve Compilation, Volumes I and II. Reported herein is the technology evolved on valve sealing, actuators, valve development and fluidics.

A detailed breakdown of the specific tasks under the program plan are described in Figure 1-1.

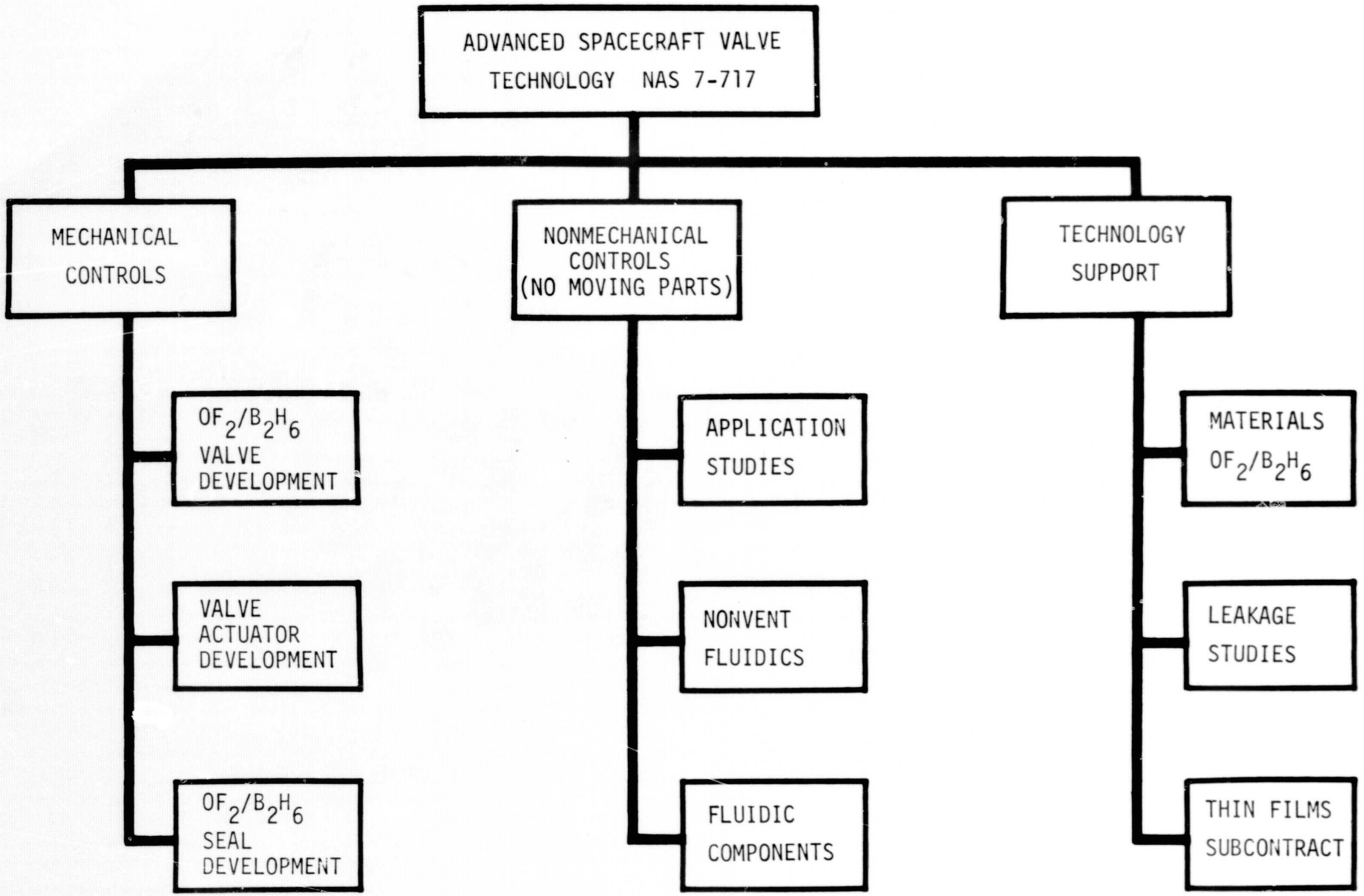


Figure 1-1. Program Plan Elements

2.0 MECHANICAL CONTROLS

2.1 INTRODUCTION

Mechanical controls represent the class of valve and fluid controls which are made up of elements designed to function as seals, moving parts, bearings, and hermetic enclosures. Seal technology is presently inadequate to meet the requirements of zero leakage in controlling highly reactive propellants. Therefore, the major developments under this program were focused on valve sealing.

Because of the use of highly reactive propellants (OF_2 and B_2H_6), only plastic, metal or ceramic seals are compatible. Only metal and ceramic materials may be suitable with OF_2 under dynamic flow conditions. It also appears possible to improve leakage by the use of larger actuation forces acting on a metal seat interface.

The major objective of this task was to improve leakage control for three types of valves: 1) shutoff, 2) pulse mode, and 3) disconnects. The specific tasks taken to meet these objectives were:

(1) The study and laboratory demonstration of sealing techniques. The effort was designed to include seal materials and seat geometry studies.

(2) The design and feasibility testing of a valve which could be used to function as a shutoff, pulse mode or disconnect, meeting the zero leakage criteria.

(3) The study and feasibility demonstration of high force thermal valve actuators for high and low temperature service.

An additional task was to review the functional and design requirements of valve disconnects. The results of this study are described in Section 2.5. Section 4.0 describes the results of an investigation of metal to metal interference seals.

2.2 SEAL DEVELOPMENT STUDY

Seal technology is presently inadequate to meet the requirements of zero leakage for valves controlling the flow of reactive rocket liquid propellants; specifically, oxygen difluoride, fluorine and diborane. Elastomers provide the answers to zero leakage but none have been found compatible with these propellants or suitable for use at cryogenic temperatures. Plastics such as Teflon may be compatible under static exposure to propellants and meet the low temperature requirements. However, Teflon is not sufficiently elastic to provide a zero leak seal using low actuation forces. Metal seals have been developed to meet zero leakage requirements using the flat interface design, although sufficient testing has not been accomplished to prove this approach under operational requirements of high cycle life, contamination insensitivity, wear and the long term exposure to reactive propellants.

It was the purpose of this study to develop seals to meet the zero leakage requirement, provide long term operation, exhibit contamination insensitivity, and be suitable for cryogenic service. The approach taken was to review the possibilities of using the elastic properties of polymers and the inherent advantages of metals. The criteria established included those possible designs which would be based on the use of state of the art materials. Dynamic flow of reactive propellants such as OF_2 over the valve seat interface dictated the use of metals. Zero leakage dictated the use of polymers. It was reasoned that a possible design would include the metal seat in series with a shielded polymer seal. A polymer such as Teflon would have to be considered since it was potentially compatible to static exposure to reactive oxidizers and capable of maintaining resilience at low temperatures. However, Teflon is not an elastomer. Therefore, attention was given to the design of a Teflon seal, while maintaining the benefits of the elastomer.

It was further reasoned that since elastomers sealed well due to the filling of the seal material into the micro asperities of the mating surface, sealing with Teflon might be accomplished by flowing Teflon in a similar manner. However, Teflon cold flows with time, bearing pressures are relieved, and sealing impaired. The major approach then was to design a seal fully containing the plastic, preventing cold flow. The plastic must be maintained at high compressive stress levels during its sealing life.

Another problem with sealing contained plastic was the need for high force actuators if high stresses were necessary, since the compressibility of Teflon was important to the success of this approach. This was overcome by taking advantage of the energy imparted by the actuator since the actuation force moves through a distance during valve operation. The energy approach was then decided a realistic means of compressing the contained materials whether elastomer, plastic or even metals, or the combinations of these. That is, the design of the seal was based on the amount of energy that could be imparted to the seal.

Three types of valves were considered: 1) shutoff, 2) pulse mode, and 3) disconnects. The common requirement for the three types, however, is zero leakage. One valve fixture was designed which could perform at least functionally within the operational characteristics of each valve type. It is recognized that design modifications or change in designs are possible for a particular application, however, the functions of sealing, actuation and the sequence of operation are common to design modifications. It is left to the interested designer to optimize these functions mechanically for suitable application since this program is not committed to an existing flight vehicle.

The design of the compressed seal is shown in Figure 2-1. The seal in this configuration was tested as part of the Valve Development Study described in Sections 2.3 and 2.4. The seal is enclosed in a groove such that no deformation of the seal geometry is possible within the seal groove. The actuation of the poppet along the seal surface compresses the seal and at the end of the valve stroke the seal is completely entrapped under a predetermined sealing stress. The seal is energized under compression and should maintain that state until the poppet load is removed. In order to minimize the actuation load the effective piston area of the poppet is small. The energy imparted to the seal is a function of the effective piston area, A, the effective piston stroke, x, and the seal stress, P. In integral form the energy is:

$$E = A \int_{x_1}^{x_2} p \, dx$$

The compressibility of polymer seal properties was investigated under Section 4.0.

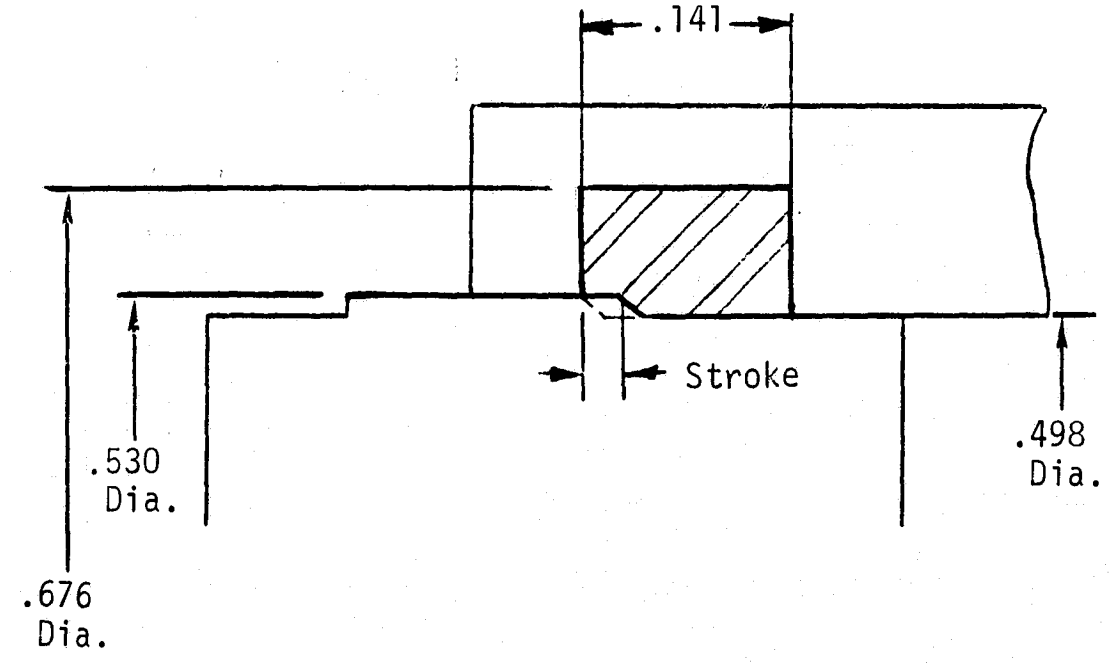


Figure 2-1. Energized Seal

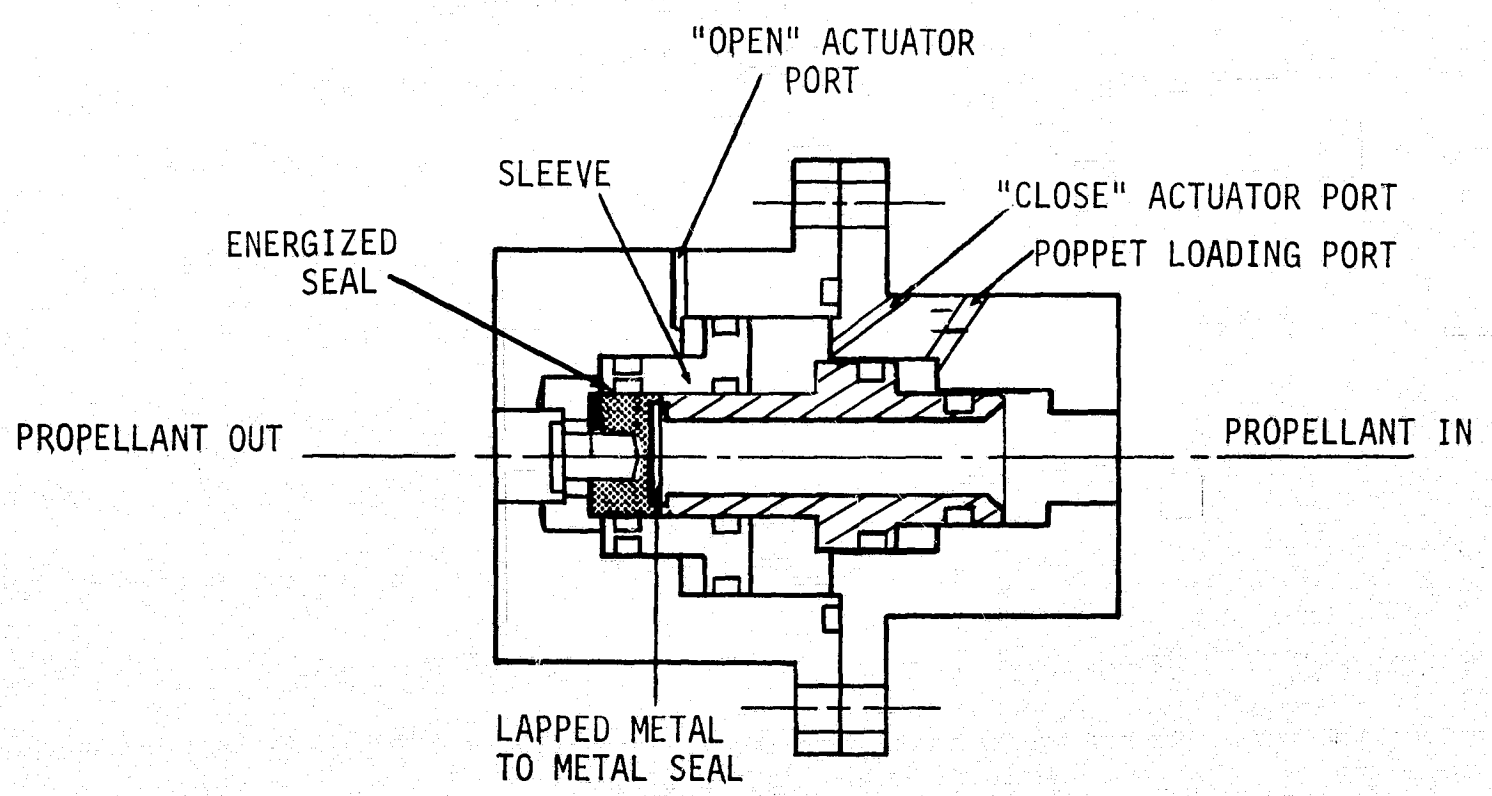


Figure 2-2. Valve and Seal Test Fixture

2.3 VALVE DEVELOPMENT STUDY

The major development focused around the seat or sealing configuration and one valve design was developed to meet the conditions of both the shutoff, pulse mode, and disconnect application. The valve was then fabricated to perform the feasibility testing of the seat configuration. The design incorporated the flexibility needed to investigate sealing techniques as well as operative functions such as its application as a disconnect or pulse mode valve.

The valve fixture design is shown in Figure 2-2. The design incorporates a flat metal seal and is the closed position in series with a polymer seal. For purposes of test economies, a pneumatic actuator was used, however, any suitable actuator can be coupled to the seat geometry. Where actuator "o" ring seals are shown, bellows may be substituted. The metal seal allows positive flow area and pulse mode operation and data is available on its leakage characteristics (Reference 1). The polymer seal is used for positive zero leak shutoff and is protected from dynamic flow of the propellants. Entrapment of propellants between the two seals is minimized by the cylindrical design and placement of the polymer seal.

The flat metal seat was a machined surface and a leakage check showed gross leakage. Therefore, the flat metal seat did not effect the energized seal leakage measurements. The energized seal ring used during the test program was machined from FEP Teflon to fit closely in the seal groove. It was necessary to cut the ring at one location to facilitate installation in the seal groove. The cut was performed diagonally with an exacto-knife to minimize chances of losing quantities of seal material and to allow a good close fit upon compression.

2.4 TEST

Initial checkout after seal installation indicated gas leakages readily discernable by bubbling in water at seal hydrostatic stresses to 4000 psi and inlet pressures of 15 psi. Following these initial tests with nitrogen the test fixture was set up to allow higher seal stresses and the working fluid was changed to helium to allow the use of a helium mass spectrometer for leak detection.

A test series was then performed at inlet pressures to 500 psi and seal stresses to approximately 12,000 psi. The results of this test series are presented in Table 2-1. Initially, the leakage increased from 3.4×10^{-9} at 100 psi and 12,000 psi seal stress to 4.4×10^{-9} at 100 psi and 1000 psi seal stress. Upon continued testing the indicated leak rate increased with time, inlet pressure and applied seal stress to a final value of 4.3×10^{-7} at 500 psi inlet and 12,000 psi seal stress. It is felt that the seal was probably saturated with helium and the increase in seal stress compressed the material reducing the quantity of helium which could be retained. This could have resulted in an increase in apparent leakage over the short term. The long term leakage trend was upward almost regardless of inlet pressure or seal stress indicating the possibility of a permeation or molecular leak.

Several additional tests were performed varying cycle life (Table 2-1). In all cases leakage was limited to the permeation level. Over 100 cycles were made on the valve and seal.

The important accomplishment was the achievement of zero leakage with Teflon seals using low actuation forces. The design principle appears sound and at cryogenic temperatures the seal should perform equally well. Long term missions of 10 to 15 years should not be detrimental to efficient sealing. However, additional testing should establish long term effects of propellant compatibility, environments such as space radiation or onboard nuclear radiation, and aging on the seal material properties.

Table 2-1. Valve Leakage Test Data Using Energized Seal

Run	Data Point	Cycles	Time Hrs.	Gas Differential Press. (Psid)	Seal Stress (Psi)	Leakage scc/sec He	Remarks
1	1	2	NA	30	4000	Gross	Seal preconditioned at 4000 psi by cycling twice
	2			50	2000		
	3			50	3000		
	4			50	4000	bubble/ 30 sec	
	5			50	6000	" "	
	6			50	8000	0	
	7			50	10000		
	8			50	12000		
	9			15	12000	3×10^{-9}	
	10			115	12000	3.4	
	11			141	12000	3.8	
	12			115	12000	3.6	
	13			115	10000	3.4	
	14			115	8000	3.4	
	15			115	6000	3.4	
	16			115	4000	3.8	
	17			115	2000	4.2	
	18			115	1000	4.4	
	19			30	2000	4.6	
	20			65	2000	1.0×10^{-8}	
	21			115	2000	1.1	
	22			165	2000	8.7	
	23			265	2000	1.3×10^{-7}	
	24			15	2000	2.0	
	25			420	2000	2.4	
	26			515	2000	2.6	
	27			515	4000	3.2	
	28			515	6000	3.4	
	29			515	8000	3.8	
	30			515	10000	4.0	
	31			515	12000	4.3	Test terminated and fixture disassembled for inspection
2	1		0		2000	-	
	2		1.5	15	12000	6.6×10^{-8}	
	3		1.8	15	12000	5.2	
	4		2.0	15	12000	5.0	
	5		2.3	115	12000	5.0	
	6		2.3	115	2000	4.8	
	7		2.4	115	2000	4.8	
	8		2.5	115	2000	5.2	
	9		2.5	15	10000	5.6	
	10		20.3	15	9000	8.8	

Table 2-1. Valve Leakage Test Data Using Energized Seal (Con't)

Run	Data Point	Cycles	Time Hrs.	Gas Differential Press. (Psid)	Seal Stress (Psi)	Leakage scc/sec He	Remarks
2	11	2	20.3	115	2000	8.2×10^{-8}	
	12		20.3	115	2000	8.2	
	13		20.4	115	4000	8.4	
	14		20.5	115	2000	8.2	
	15		20.6	115	6000	8.8	
	16		25.3	115	6000	9.4×10^{-7}	
	17		42.5	115	6000	1.22×10^{-6}	
	18		43.3	115	6000	1.14	
	19		43.3	115	2000	1.08	
	20		44.0	115	2000	1.16	
	21		44.0	115	8000	1.20	
	22		44.7	115	2000	1.12	
	23		44.8	115	2000	1.14	
	24		45.0	115	10000	1.28	
	25		46.6	115	10000	1.18	
	26		46.6	115	2000	1.08	
	27		46.8	115	2000	1.12	
	28		46.8	215	2000	1.12	
	29		46.9	315	2000	1.12	
3	1	1	0	115	2000	1.8×10^{-4}	
	2		.2	115	4000	1.8	
	3		.3	115	6000	3.0×10^{-5}	
	4		.4	115	8000	1.38	
	5		.6	115	8000	8.0×10^{-6}	
	6		.6	115	10000	8.0	
	7		1.6	115	10000	3.6	
	8		1.6	115	2000	2.6	
4	1	1	-	115	2000	5.2	Pressure relieved. Poppet closed with no pressure for 3 days
5	1	-	0	115	2000	6.0×10^{-9}	
	2		.2	115	2000	3.5×10^{-8}	
	3		.4	115	2000	8.8×10^{-8}	
	4		4.6	115	2000	1.18×10^{-6}	
6	1	1	0	115	2000	1.18	
	2		.1	115	8000	1.14	
	3		.15	115	8000	1.10	
	4		.2	115	8000	1.04	
7	1	1	-	115	8000	1.0	
8	1	1	-	115	8000	1.0	
9	1	1	-	115	8000	9.6×10^{-7}	
10	1	1	-	115	8000	8.8	
	2		20.6	115	8000	1.34×10^{-6}	
11	1	20	-	115	8000	9.6×10^{-7}	
12	1	20	-	115	8000	6.8	
13	1	50	-	115	8000	5.2	

The actuation force to close is 1/40 times the seal stress. The piston area to close the valve is 1.0 in^2 and the area of the piston to open is 0.7 in^2. It is important to note the actuation force to open was not consistent. Friction forces due the seal area and seal stress in some cases were high and did not follow the general relationship of friction force equals a constant times the normal load. The following table illustrates the changes in actuation force to open.

Force to Open, lb_f	Seal Stress, psi
32	12,000
35	2,000
37	2,000
31	2,000
28	8,000
28	8,000
28	8,000
28	8,000
28	8,000

The above forces are the breakaway forces due to friction or stiction. Probable reasons for the large variance may be due to the time the seal was allowed to remain at the stressed condition where cold flow allowed the Teflon to fill the asperities of the seal bearing area. If this is the case, smoother finishes are required. Also, the reduction of the seal material area exposed to the bearing should materially help in reducing the actuation force to open.

Another test performed showed the seal to be insensitive to particulate contaminants. The test data shown in Table 2-2 was taken during valve cyclic tests with the Teflon seal contaminated by blasting with silicon carbide grit (6μ particles) and dipped into 25μ to 60μ copper particles. No effect on leakage ratio was noted due to the particles. Examination of the seat after tests showed several particles solidly imbedded in the Teflon seal.

Table 2-2. Valve Contamination Test Leakage Data, Teflon Seat

Differential Pressure	Helium Leakage Scc/Sec	Remarks
115	2.5×10^{-8}	Pretest
115	1.2×10^{-7}	Pretest
115	6.0×10^{-8}	Seal contaminated with 25 and 60μ particles

2.5 VALVE DISCONNECTS

The valve fixture (Figure 2-2) described in Section 2.3 can function as a disconnect. The design allowed for zero leakage during storage using the energized seal. The metal seal would be lifted allowing flow to the system. The female part of the disconnect could also contain the energized seal and redundnant metal seat. However, a specific design configuration would depend on the required operating parameters and functional requirements. Therefore, a study of these parameters and functions which would dictate a specific disconnect design was indicated.

Disconnect fittings are used to connect and disconnect sections of fluid conduits to each other with the need for tools. These operations can be classified as manually versus remotely accomplished, and as valved (for spill-proof operation) versus non-valved. Liquid transfer and gas transfer circuits are the most common applications for disconnects in rocket systems; ordinarily the disconnect fittings are located at the interfaces between systems that must be separable (e.g., ground servicing to vehicle interface). Quick-connectors may be necessary where system components must be easily replaced during in-space maintenance on board vehicle and space stations.

The discussion herein will deal mainly with valved disconnects. Table 2-3 summarizes the probable ranges of the operating parameter values for OF_2, B_2H_6, N_2O_4, MMH, N_2H_4, helium, and nitrogen circuit disconnect fittings.

Table 2-3. Estimated Disconnect Fitting Operating Parameters

	Oxygen Difluoride (OF_2)	Diborane (B_2H_6)	Nitrogen Tetroxide (N_2O_4)	Monomethyl-hydrazine (MMH)	Hydrazine (N_2H_4)	Helium (He) for OF_2/ B_2H_6	Helium (He) for N_2O_4/ MMH	Nitrogen (N_2) for N_2O_4/ MMH	Helium (He) for N_2H_4	Nitrogen (N_2) for N_2H_4
Probable range of filling and storage temperature, °R	180/300	200/400	475/580	460/580	495/580	180/300	400/560	400/560	400/580	400/580
Probable range of filling and storage pressures, psia	14.7/150	14.7/150	14.7/150	14.7/150	14.7/150	14.7/4000	14.7/4000	14.7/4000	14.7/4000	14.7/4000
Probable range of fluid specific weight, lb/cu ft	79.9/104.3	23/32.5	87.3/94.2	53.1/56.9	61.4/63.9	0.0183/6.11	0.0098/ 3.19	0.0662/25	0.0098/ 3.19	0.0662/ 25
Probable range of filling rates, lb/sec	0.1/5	0.04/2	0.04/1.5	0.02/1.0	0.005/0.4	0.003/0.07	0.0007/ 0.02	0.005/0.2	0.00003/ 0.004	0.0002/ 0.03
Probable maximum acceptable pressure loss (ΔP) psid	20	20	30	30	30	100 @ lowest flow	100 @ lowest flow	100 @ lowest flow	100@ lowest flow	100@ lowest flow
Vapor pressure of fluids at maximum temperature, psia	137	90	48	3.2	1	(NA)	(NA)	(NA)	(NA)	(NA)

The values were estimated by calculating the likely system range sizes and then judging what the minimum and maximum filling times, allowable ΔP and temperature would be. Leakage rates were not estimated since those must be specific to an application; some estimates were given as illustrative examples in Reference 1, which contains an outline of how leak rate allowances might be calculated.

2.5.1 Requirements

Functional and design requirements of self-valving units are as follows. Before and after use the fitting must be protected from contamination by the local environment; this means that dirt, grease and moisture must be excluded. At least one-half of the fitting must be mobile so that the two halves can be brought into proper juxtaposition for joining them together; indexing, most desirably by guides, involves angle of incidence plus lateral (and in some designs, rotational) positioning. Once joined, the two halves must be locked together to sustain the pressure force, to oppose loads which would tend to separate them, and (in some designs) to apply bearing force to the seals. The fluid passages must be sealed to contain the fluid and, perhaps, any volume previously unfilled must be purged to remove air if it is undesirable and filled with the fluid to eliminate bubbles. In some operations, the fittings must be chilled. Valves must next be opened to permit flow. During flow, the pressure loss across the fitting should be at a minimum. Leakage must be limited and icing or other detrimental external occurrences should be minimized. Before the halves are separated, the valves must be closed and it may be necessary to purge or otherwise dispose of any trapped fluid that would be released (i.e., dribble volume is purged). The fitting halves are then unsealed and unlocked. Once separated, the dust covers should be replaced to prevent contamination.

2.5.2 Design Configurations

Disconnects for aerospace applications have been supplied in a limited range of design configurations. Generally, they are axially aligned with the conduits and of symmetrical construction around that longitudinal axis. Nearly always the pair of fittings consists of matching male and female halves; completely identical halves are rare if they exist at all.

Locking devices are usually a circular array of balls, dogs, or collets in one half which protrude into an opposing groove in the other half to lock them together. Longitudinally sliding sleeves move the balls, dogs, or collets radially from the locked to the unlocked locations and vice versa. Clamps, latches and threaded devices are rarely used for locking.

Face seals, cone seals, edge seals, and bore seals are commonly used on the valving units and to seal the halves together. Sliding seals are avoided if possible. Elastomeric materials are used wherever possible as it is difficult to secure very low leak rates with plastic or metallic seals.

Valving elements within disconnects are usually poppets but (butterfly) discs, gates and balls have been used where substantial dribble volumes are permissible and lower pressure losses are desired. A number of other types of elements could be used (e.g., sleeves, swinging discs and plugs) but these offer no generalized advantages over the designs in use unless special configurational requirements must be met.

2.5.3 Problem Areas

Disconnects designed with the features outlined above have suffered from a number of drawbacks which seriously limit their usefulness for OF_2 and B_2H_6 service. Leakage may be external before coupling (i.e., past the valving element) or external after coupling (i.e., past the joint seal or the internal static seals). (Spillage from the "dribble volume" after parting is another form of leakage but it is not controlled by seals.) Leakage is best controlled by elastomeric seals but these cannot be used, as yet, in OF_2 or B_2H_6 service. Leakage occurs because of contamination, damage to the sealing surfaces, or inadequate conformation of the sealing material to the sealing surface.

Jamming which prevents one or more of the mechanical operations to occur (joining, locking, valving, unlocking or parting) is caused by deformations, misalignments, friction or foreign material. In the latter category are dirt, ice, corrosion products, and salts formed by reaction of the propellants.

Table 2-4 summarizes the functional requirements and design approaches normally used to meet these requirements.

2.5.4 Approach to the Design of Disconnects

Disconnects can be engineered using straightforward design practice if unusual requirements do not exist but, in the present case, the propellant OF_2 is unusually reactive, the useful life is long (10 years), and very low leakage rate is demanded. These considerations may make it necessary to utilize unconventional approaches in order to secure acceptable performance. Table 2-5 summarizes the environmental factors and the resulting effects which must be accounted for in the design features of disconnects for spacecraft systems.

The functional sequence can be specified a number of ways but the ordering of the functions must be clearly shown. In some disconnects the functions are to be sequenced by means of mechanical interlocking (e.g., valves cannot be opened until the mated parts are locked together), therefore the design of the mechanism cannot be started until the sequence and desired interlocks are established. For example, the sequence may involve dribble volume purging before and after flow, preflow chilling, and prevention of liquification or icing on the surfaces of the disconnect. These unconventional functions may be added for safety reasons because of the propellant's properties (extreme toxicity and low temperature).

To illustrate some of the options available in terms of flow and valving, Figure 2-3 shows schematic diagrams of five different disconnects. The first (a) is a quick-connector application on the ports of a replaceable component. Next (b) is a simple valved disconnect of the conventional variety; the valves are more often check valves than not. To secure additional reliability in sealing, a series-redundant scheme might be used as shown in (c). Jacketed disconnects (d) might be used to provide for external chilling or to catch and purge any leakage from the propellant carrying center conduit. Finally, (e) depicts an arrangement which permits the dribble volume between the two halves to be purged.

Table 2-4. Functional Requirements and Design Approaches

Function	Requirement	Application	Design Approaches	
			Method	Usual Problems
Exclusion of contamination	Prevent contamination of fluid circuit	ABC	Dust cover Constant purge	Sealing, jamming Complexity, gas consumption
Containment of fluid	Prevent leakage from individual fittings to exterior	ABCD	Sealed sleeves Purged jacket	Sealing Complexity, gas consumption
Alignment	Guide mating parts	ABCD	Concentric cones Guide pins & grooves Flanges and slots	Large diameter Rotary alignment req'd Rotary alignment req'd
Sealing	Prevent leakage from joint between mated fittings	ABCD	Bore seals Edge seals Cone seals Face seals	Seal scrubbed, low sealing force Exposed to damage, precise loading req'd Precise loading req'd Seal retention, precise loading req'd
Locking	Secure mated fittings against separation or misalignment	ABCD	Dogs Balls Collets Latches Clamps Threaded sleeves	Subject to jamming Imprecise, galling High actuation force Rotary alignment req'd Increases diameter Subject to seizure
Clearing dribble volume	Remove air, moisture, or transferred fluid from between the mated fittings	ABD	Evacuation Purge Heaters and dump "Zero volume"	Complexity, perhaps slow Complexity Complexity, heats fitting True zero impossible to obtain
Chilling	Reduce fitting temperature so as to minimize vaporization of liquid	A	Cold gas purge Cold jacket Circulate liquid	Complexity Complexity, heavy Complexity
Valving	Start and stop flow through the fittings	ABC	Disc poppet Ball poppet Sliding sleeve Rotary plug Rotary ball Rotary sleeve Gate or blade	Cocking, high seating force necessary High seating force necessary Dual sliding seals Non-planer seals, subject to scrubbing Seals subject to scrubbing Non-planer seals, subject to scrubbing Seals subject to scrubbing
Surface	Prevent liquification of air or humidity, or formation of frost & ice on external surfaces	A	Heaters Hot jacket purge External gas flush Scraper Non-stick surface	Heat fitting Heats fitting, heavy Complexity Complexity Questionable effectiveness

A = OF_2/B_2H_6 systems

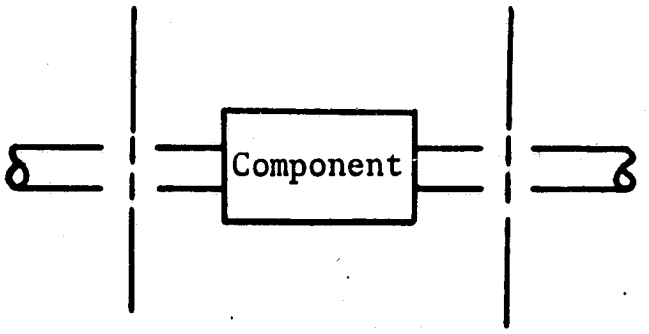
B = Earth storable systems

C = Inert gas systems

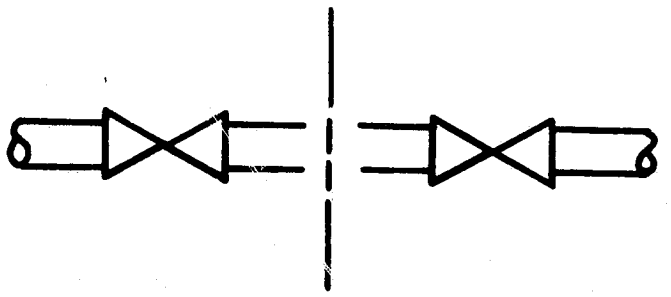
D = Space quick-connector

Table 2-5. Environmental Factors and Effects

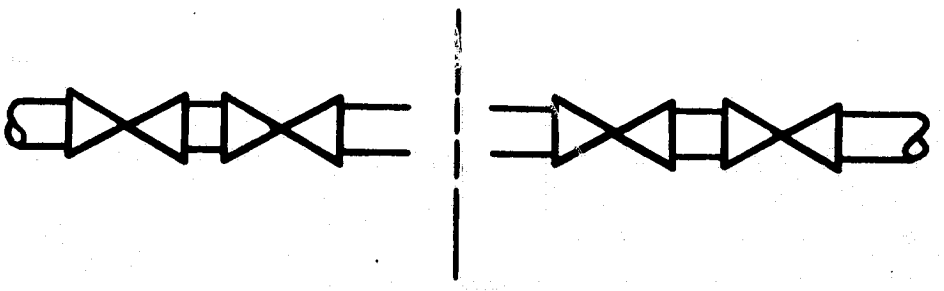
Fluid	Major Environmental Factors	Effects to be Considered
OF_2	Reactivity with metals	Forms fluoride coatings upon contact, may ignite and burn.
	Reactivity with polymers	May ignite and burn violently.
	Reactivity with water	May react violently.
	Low temperature	Makes some materials brittle, parts contract, cycling may cause thermal ratcheting.
B_2H_6	Reactivity with polymers	Reacts with some polymers.
	Reactivity with water	Forms solid crystals with water.
	Low temperature	Makes some materials brittle, parts contract, cycling may cause thermal ratcheting.
N_2O_4	Reactivity with polymers	Oxidizes essentially all polymers.
	Reactivity with water	Forms nitric acid, with water, which attacks many materials.
MMH	Reactivity with polymers	Reacts with many polymers.
N_2H_4	Reactivity with metals	Metals and oxides cause N_2H_4 to decompose.
	Reactivity with polymers	Reacts with many polymers.
	Auto decomposition	Decomposition to ammonia, nitrogen and hydrogen is function of temperature and surface catalysis.
Inert Gases	Permeability	Essentially all polymers are permeable to a greater or lesser degree
Atmosphere or space ambient	Humid salt-laden air at launch pad	Corrodes most common metals.
	High vacuum of space	Polymers and lubricants lose volatiles, clean surfaces may gall.
	High temperature in sunlight	Parts expand, cycling may cause thermal ratcheting, polymers may be degraded and flow plastically.
	Low temperature in shade	Parts contract, cycling may cause thermal ratcheting, polymers get rigid.



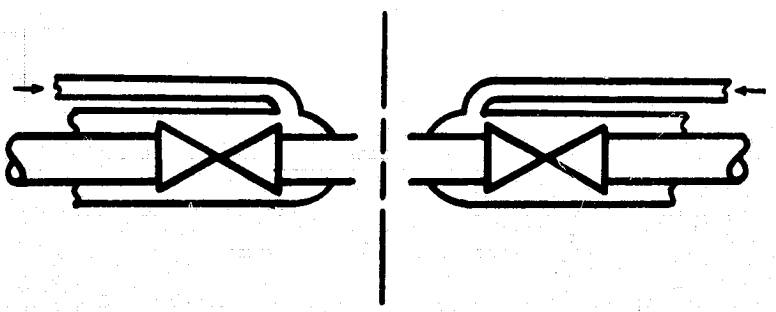
a. Quick-Connector



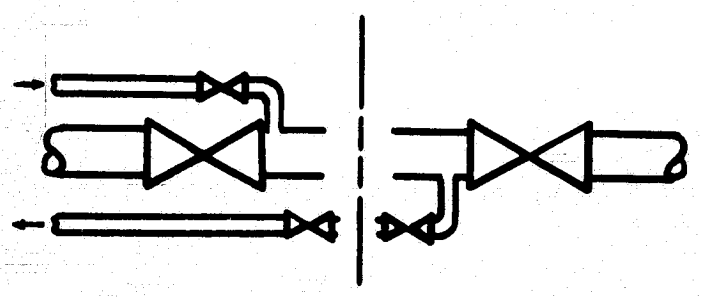
b. Simple Valved Disconnect



c. Series-Redundant Valved Disconnect



d. Jacketed Disconnects



e. Purged Dribble Volume Disconnect

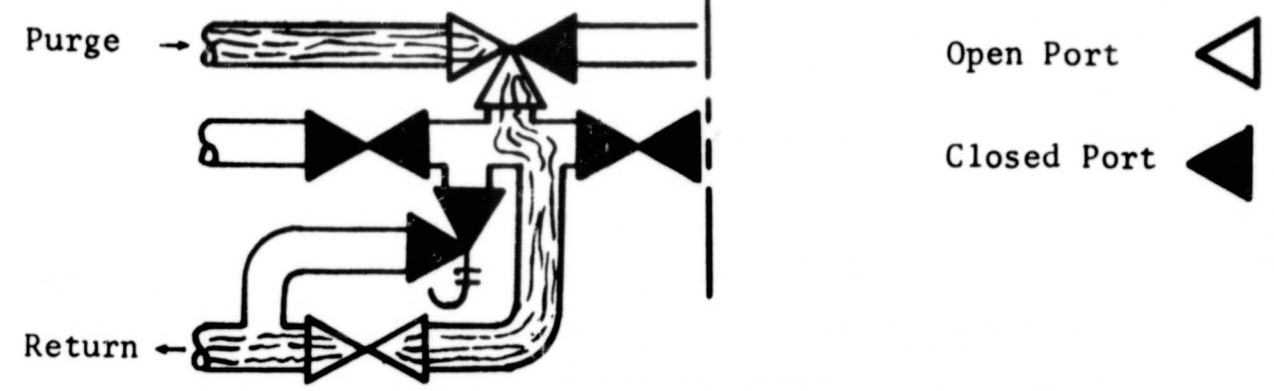
Figure 2-3. Schematic Diagrams of Five Functionally Different Disconnects

A still more complex disconnect is shown schematically in Figure 2-4. This arrangement has redundant valving, is capable of being purged or chilled before or after connection, and has provision for pressure relief of the fluid trapped between the shutoff valves. By suitable mechanical design the return circuit could be a concentric jacket to contain leakage.

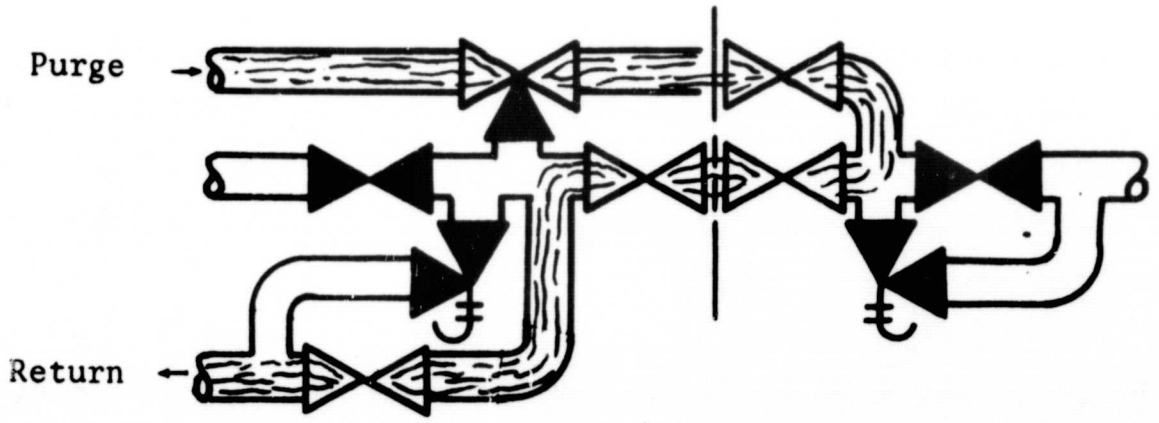
2.5.5 Available Disconnects

Several manufacturers and suppliers of disconnects were contacted to determine (1) if any disconnects had been designed for space storable propellant service, (2) if knowledgeable engineers in the field believed adequate technology was presently available upon which to base a design, and (3) if any designs representing substantial improvements over the state of the art developed in 1962 (date of previous survey under NAS 7-107, Reference 2) had been produced for either cryogenic or earth storable propellants. As far as could be determined from these sources, there have been no disconnects manufactured for, or tested with, space storable propellants. McDonnell Douglas is believed to be the only concern which has built a disconnect for a fluorinated oxidizer (F_2). (Reference 3).

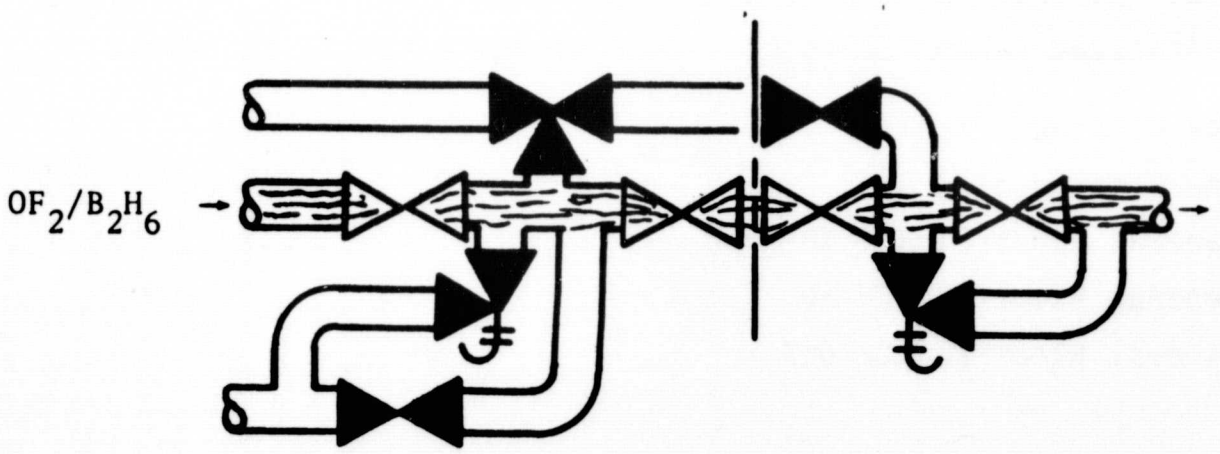
None of the engineers contacted who seemed aware of the nature of space storable propellants felt that conventional disconnects would be suitable for these fluids; several expressed opinions that new exploratory technology programs, considerable testing, and perhaps more precise definitions of the safety requirements would be necessary before reliable disconnects could be produced.



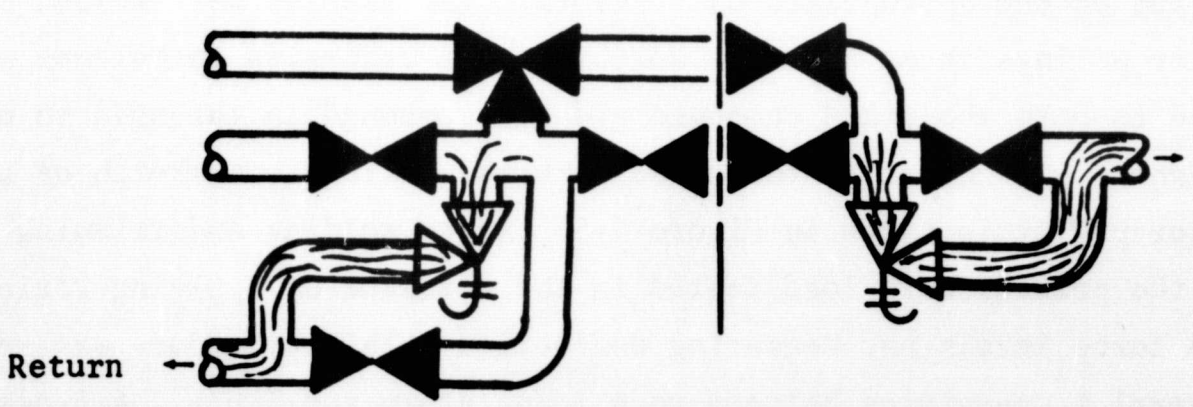
a. Purging (Ground Half Only)



b. Purging (Both Halves)



c. Flowing



d. Relief (Of Trapped Fluid)

Figure 2-4. Disconnect for Hazardous Fluids

2.6 THERMAL ACTUATOR DEVELOPMENT

Thermal actuators operate due to the change in volume in a material upon the application of thermal energy. The major advantages of thermal actuators is the production of high actuation forces, yet smaller in size, weight and power requirements than solenoid actuated valves. The major disadvantage of thermal actuation is the response time to actuate is longer, for example, than the solenoid actuator.

Initial work in thermal actuators for spacecraft rocket engine application was done under NASA Contract NAS 7-436, Reference 1. This testing was done at normal room temperature ambient. The work described here has been directed toward investigating the development of polymer heated actuators at service temperatures to 500°F.

During the course of this study, several room temperature vulcanizing (RTV) type silicone rubber compounds were evaluated. The selection of candidate materials was based on manufacturers' published data and manufacturers' representatives recommendations. The compounds tested included:

Dow Corning 501 RTV
Dow Corning 3118 RTV
General Electric RTV 30
General Electric RTV 60
General Electric RTV 615

In each case the catalyst recommended by the manufacturer was used. The recommended quantities of catalyst and rubber were blended and cured as indicated on the appropriate data sheets. The samples were molded into actuator pellets in an aluminum mold. Vacuum degassing techniques were applied to both the mixed compound and the compound in the mold to minimize the chances of bubbles in the cured actuator pellets. A sketch of an actuator pellet is shown in Figure 2-5. After molding and trimming to size, the pellets were load tested in the actuator by applying verious piston force levels and measuring deflection. This procedure was repeated at several temperatures between room temperature and 500°F. A cross-sectional sketch of the actuator is shown in Figure 2-6, while Figure 2-7 shows the test setup.

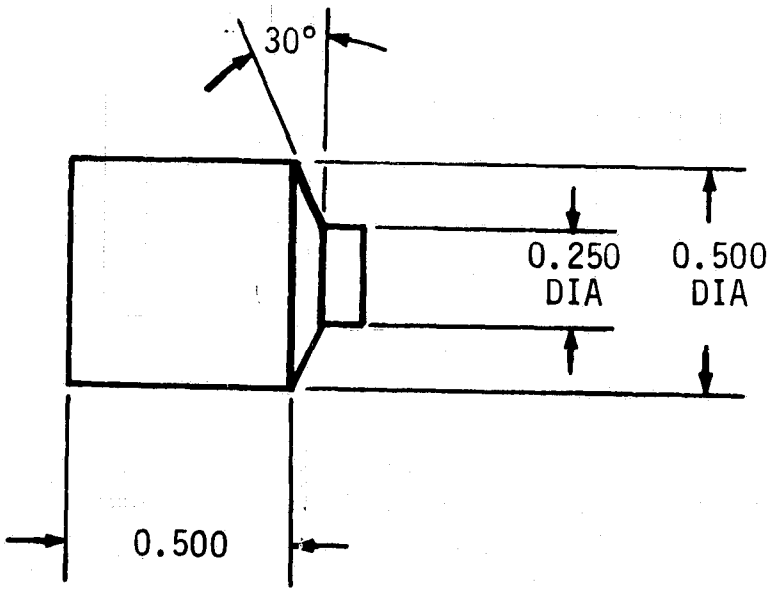


Figure 2-5. Actuator Pellet

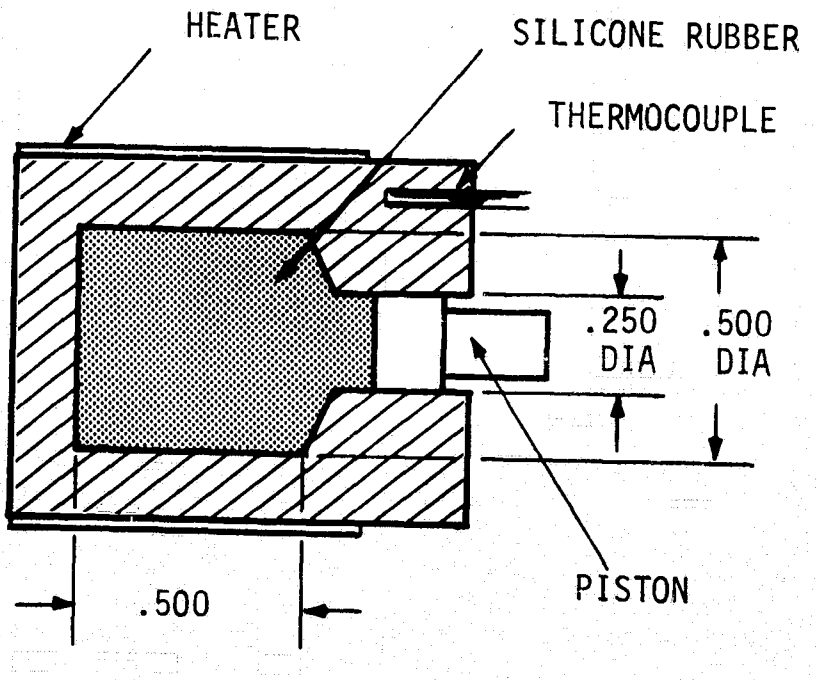


Figure 2-6. Thermal Expansion Actuator

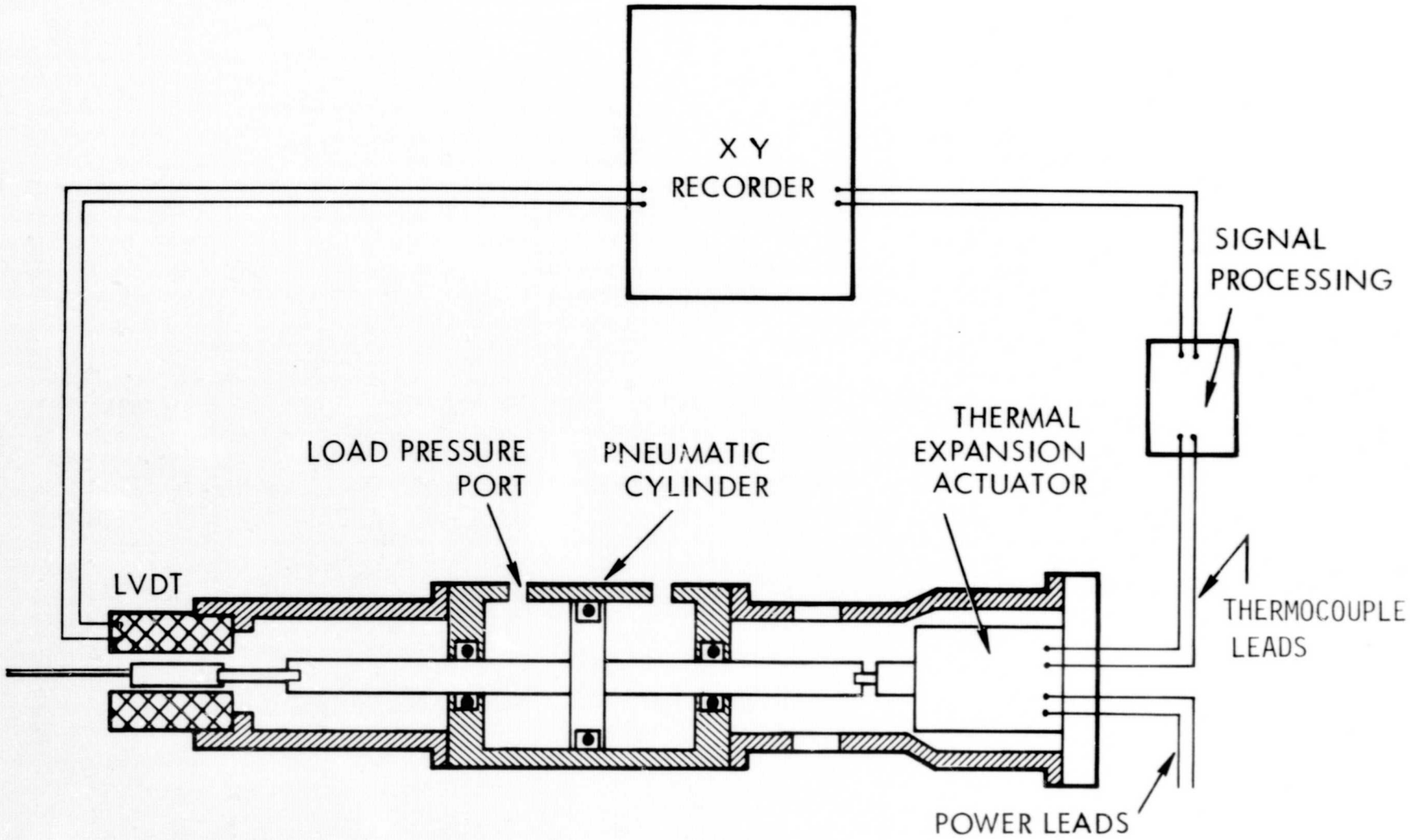


Figure 2-7. Test Setup

It was found that the RTV 30, 60 and 501 RTV depolymerized after being enclosed in the actuator for several hours at moderate temperatures (approximately 200°F). This resulted in the depolymerized liquid rubber extruding past the piston. Representatives of both rubber manufacturers were contacted in reference to this problem. Dow Corning recommended the use of an additive cured rubber, specifically their 3118 RTV rather than the condensation cured 501 RTV. General Electric recommended a thick cure catalyst for their RTV 30 and 60, however, this did not alleviate the problem. The subsequently recommended an additive cured system, RTV 615, to replace the condensation cured RTV 30 and 60.

The 3118 RTV and RTV 615 were tested for periods of several days at temperatures in excess of 500°F. Typical load-deflection curves at various temperatures are shown in Figure 2-8 for the 3118 RTV and Figure 2-9 for the RTV 615. Figure 2-10 shows approximate temperature-deflection curves for 3118 RTV and RTV 615, respectively.

The 3118 RTV showed very slight signs of extrusion upon test termination. The rubber matrix was found to be much softer than when originally installed and was slightly tacky. Some of the compound had adhered to the piston and remained attached upon piston removal. Other than as noted above, the actuator pellet was in satisfactory condition.

The 615 RTV showed signs of fine feathery extrusion around the piston. The rubber matrix was somewhat softened and had reduced tear and penetration resistance as compared to an unheated specimen. Some breakup of the compound into coarse grannules was noted in the central section just under the piston. This is not surprising since the piston stroke from ambient temperature to 525°F was in excess of 0.400 inch and the actuator pellet was forced down from its 0.500 inch diameter to the 0.250 inch piston bore diameter desired expansion. This particular condition should not cause a problem in extended use. It is recommended that any actuators using these compounds be fitted with metal piston ring seals to minimize the chances of matrix extrusion.

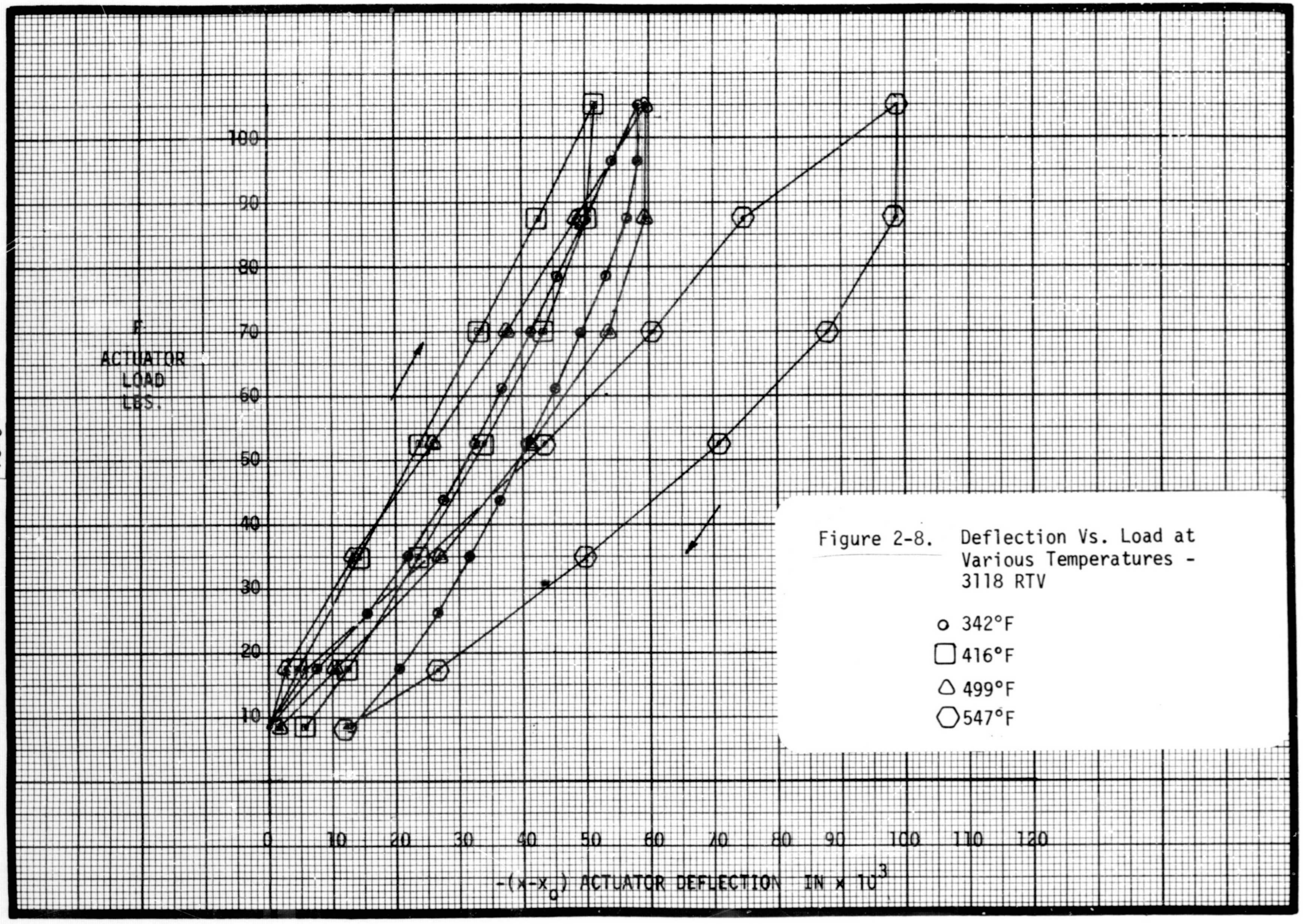


Figure 2-8. Deflection Vs. Load at Various Temperatures - 3118 RTV

- o 342°F
- □ 416°F
- △ 499°F
- ⬡ 547°F

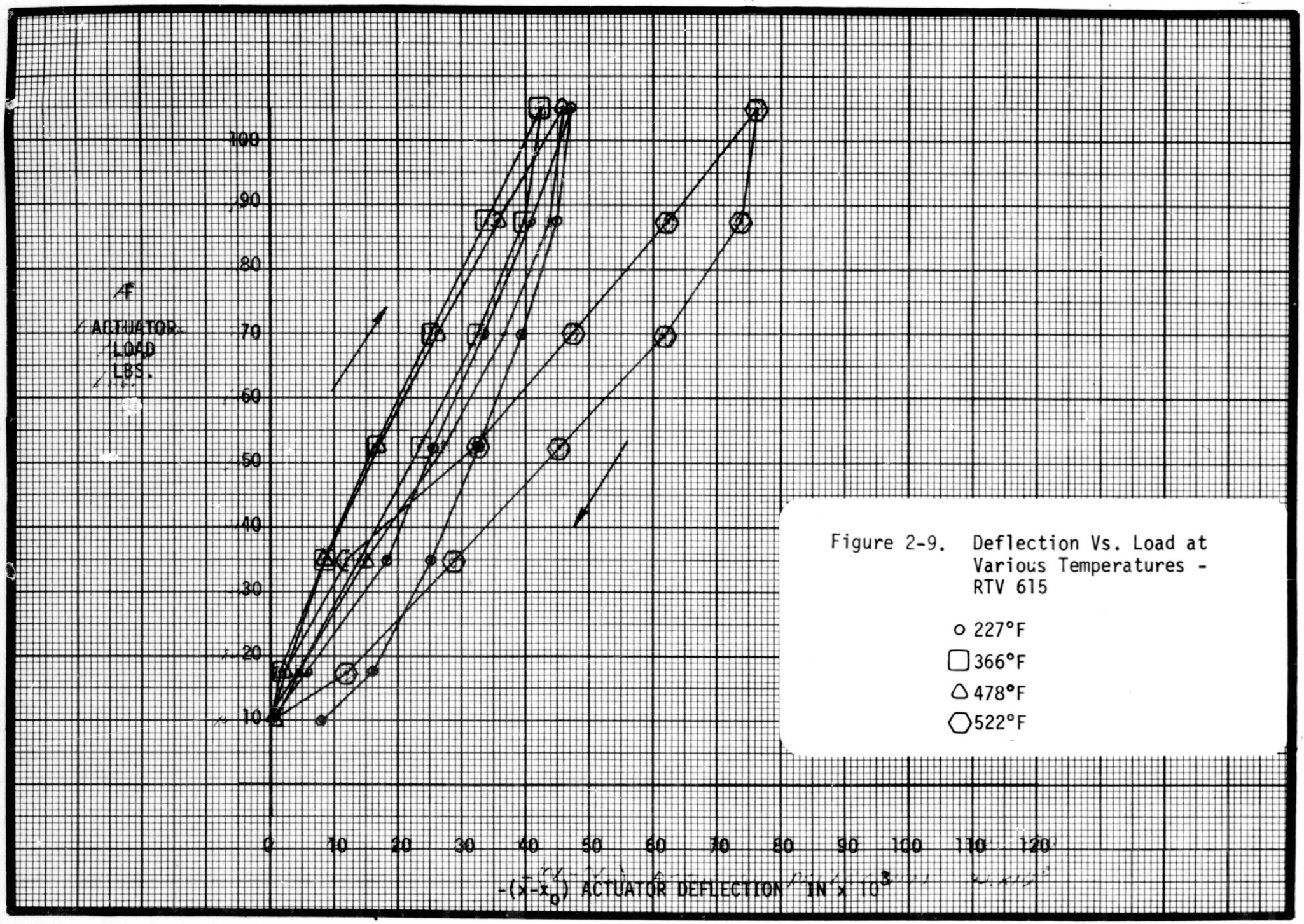


Figure 2-9. Deflection Vs. Load at Various Temperatures - RTV 615

○ 227°F
□ 366°F
△ 478°F
⬡ 522°F

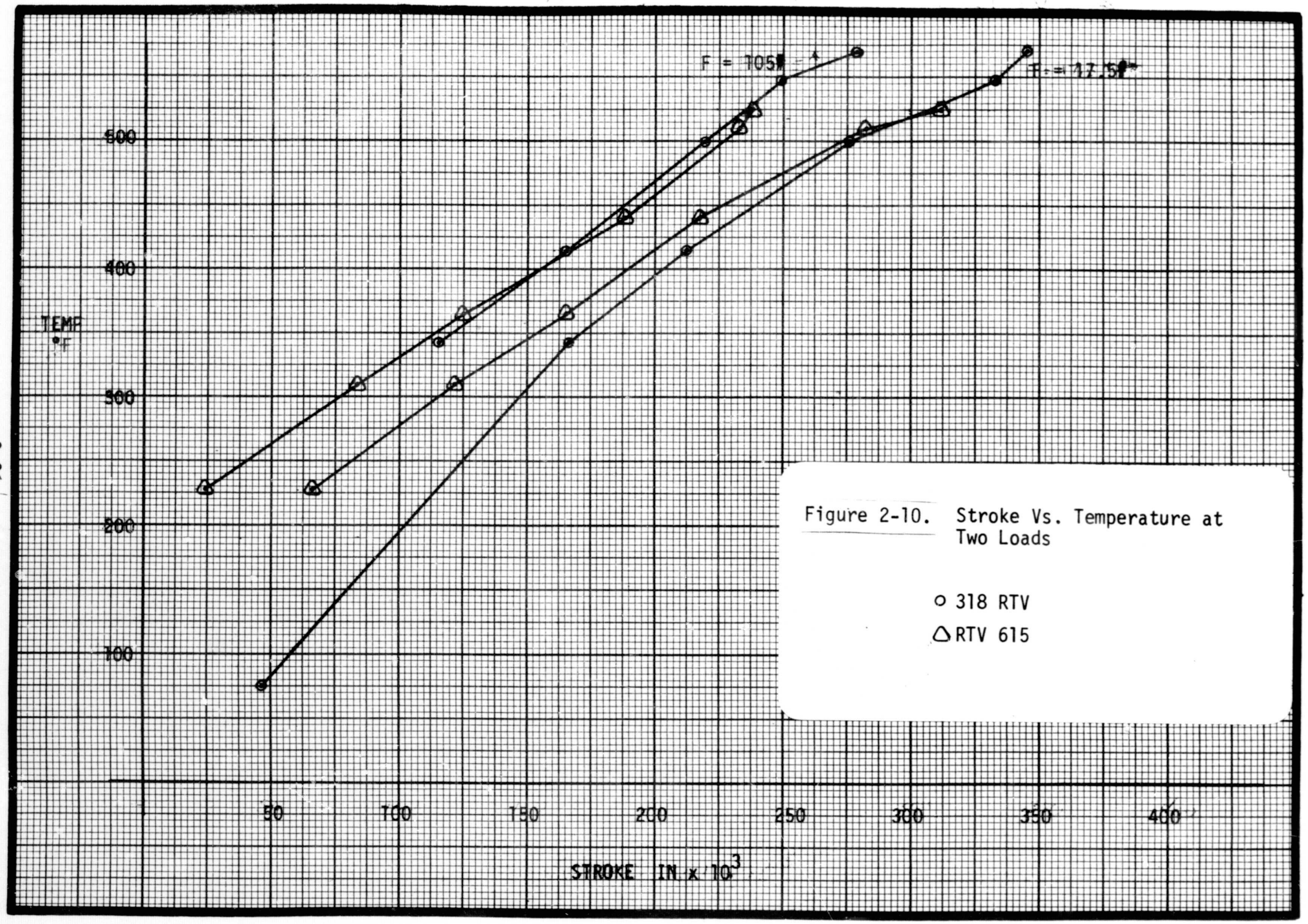


Figure 2-10. Stroke Vs. Temperature at Two Loads

○ 318 RTV

△ RTV 615

2.6.1 Thermal Actuated Valves

Thermal actuated valves can be used where major improvement is needed in actuation forces. Several valve design concepts were reported in Reference 1 under NASA Contract NAS 7-436. Most of the effort under NAS 7-436 was directed toward thermal expansion of metals to achieve high seat bearing stresses. This section deals with the use of expanding polymers for use as actuation techniques for valve applications.

2.6.1.1 Thermohermetic Isolation Valve Concept - Isolation valves actuated by squib type chemical actuators are used in spacecraft propellant and pressure systems where a gas or liquid must be contained for extended periods of time. The main advantage to this valve is that leakage is zero due to the hermetic seal. The qualification of squib valves for spacecraft systems is costly and time consuming since the actuators are one shot devices and several squibs must be fired to satisfactorily demonstrate the reliability of one or two flight actuators. The squib operated actuator can give extremely fast opening or closing response which may be necessary in some systems. In many systems, however, this high speed response is unnecessary and high stresses produced by the shock must be considered in the design.

The thermohermetic isolation valve concept shown in Figure 2-11 was conceived to provide a one actuation hermetically sealed valve. Where response time is not important the valve has the advantage of producing little or no hydraulic shock to the propulsion system. The valve opening can be programmed alleviating cavitation and extreme pressure forces. The actuator can be hermetically sealed, if necessary, isolating the material from the propellants used.

The hermetic isolator operates as follows (see Figure 2-11): Initially, the preformed diaphragm forms a hermetic welded seal between the inlet and outlet. The diaphragm is preformed to minimize deflections with upstream pressure variations. When flow is desired the heater is activated, thereby heating the valve housing and the heat sensitive material of the actuator. The heat sensitive material expands pushing the diaphragm cutter/poppet through the diaphragm. This cuts a pattern through the diaphragm allowing

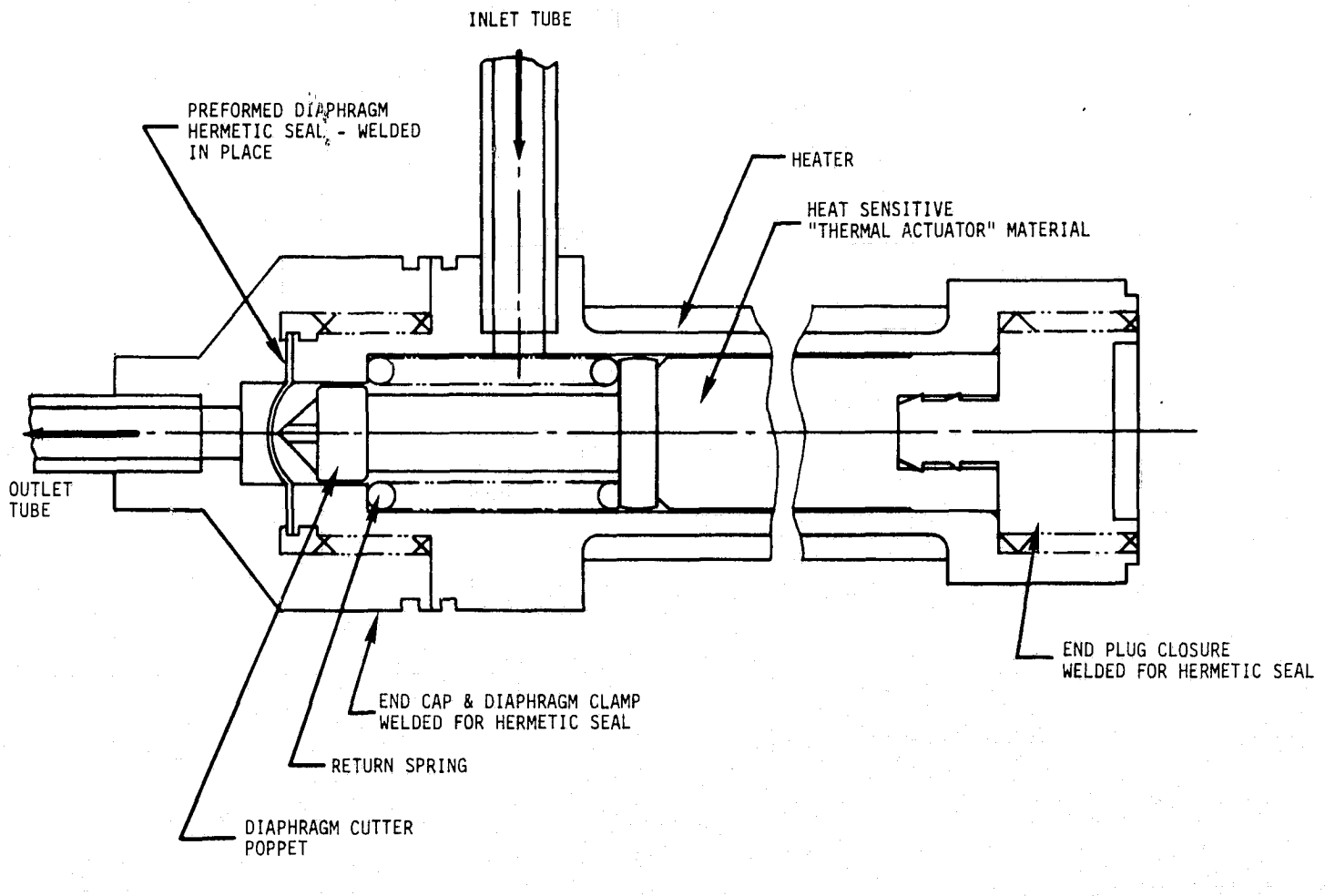


Figure 2-11. Thermohermetic Isolator

flow to commence without pieces of the diaphragm being torn loose. The inlet pressure assists in spreading the cut pattern in the diaphragm open. After the diaphragm is pierced the heater is de-energized, the housing and heat sensitive actuator material cooled, and the diaphragm cutter poppet is retracted by the return spring.

2.6.1.2 Micro Valve Applications - Valving for use in the control of fluidic or micro systems must be small, light and economical of power. Tight leakage requirements are more easily met if relatively large seat forces may be generated. High seat forces are difficult to obtain while maintaining small size and weight using conventional solenoid valve actuators. Thermal expansion actuators are capable of exerting very large forces in a relatively small sized package.

Silicone rubber thermal actuator performance was investigated as part of the Advanced Valve Technology Program (Reference 1). Based on this work,

two different valves utilizing two types of thermal actuators, were developed by TRW under contract to the Jet Propulsion Laboratory (JPL Contract 952762). The valving must be highly reliable, meet extremely stringent leakage requirements, and employ only materials which will not mask the analytic functions being performed. The valve was intended to control high pressure hydrogen gas and utilized a differential linear expansion polyimide rod actuator. Another valve developed for JPL was a vacuum valve and utilized a silicone rubber differential volume expansion actuator. Both valves incorporated magnetic latching to allow long "open" periods with no power drain.

Design Goals

The valve designs were intended to minimize size, weight and power input while maximizing reliability. A number of design goals were identified as target values for the program. These are as follows:

- Weight - less than 15 grams
- Volume - less than 1/2 cubic inch
- Peak Power - less than 15 watts
- Voltage - approximately 28 volts dc
- Total Electrical Energy - to be minimized
- Maximum Time to Actuator (open or closed) - 30 seconds
- Maximum Dead Time (time between actuations) - 2 minutes
- Valve Internal Size (bore):
  - High pressure valve - .010 to .030 inch
  - Vacuum valve - approximately .060 inch
- Valve Poppet Stroke:
  - High pressure valve - .010 to .020 inch
  - Vacuum valve - approximately .080 inch
- Poppet Seating Forces - approximately 3 lbs for both valves
- Seat Design - substantially per JPL sketch 11-6-69
- Leakage Goals:
  - Internal leakage - 10^{-8} sccs He at one atmosphere pressure differential
  - External leakage - 10^{-6} sccs He at one atmosphere pressure differential

- Valve Function - normally closed, i.e., closed for many months but in operating will be opened a total of about 25 times for a period of one (1) hour each cycle; valves shall require no power when closed. However, they are to be designed for a cyclic life of at least 1000 cycles.

- Environmental Conditions:

	High Pressure Valve	High Pressure Valve	Vacuum Valve	Vacuum Valve Actuator
Maximum Temperature	135°C[1]	135°C[1]	225°C[2]	135°C[1]
External Pressure	1,000 mb (earth)			
	520 mb (Mars)			
Maximum Shock	30 g 30 milliseconds			
Maximum Acceleration	25 g			

[1]Sterilization Temperature [2]Operating Temperature

High Pressure Valve Design

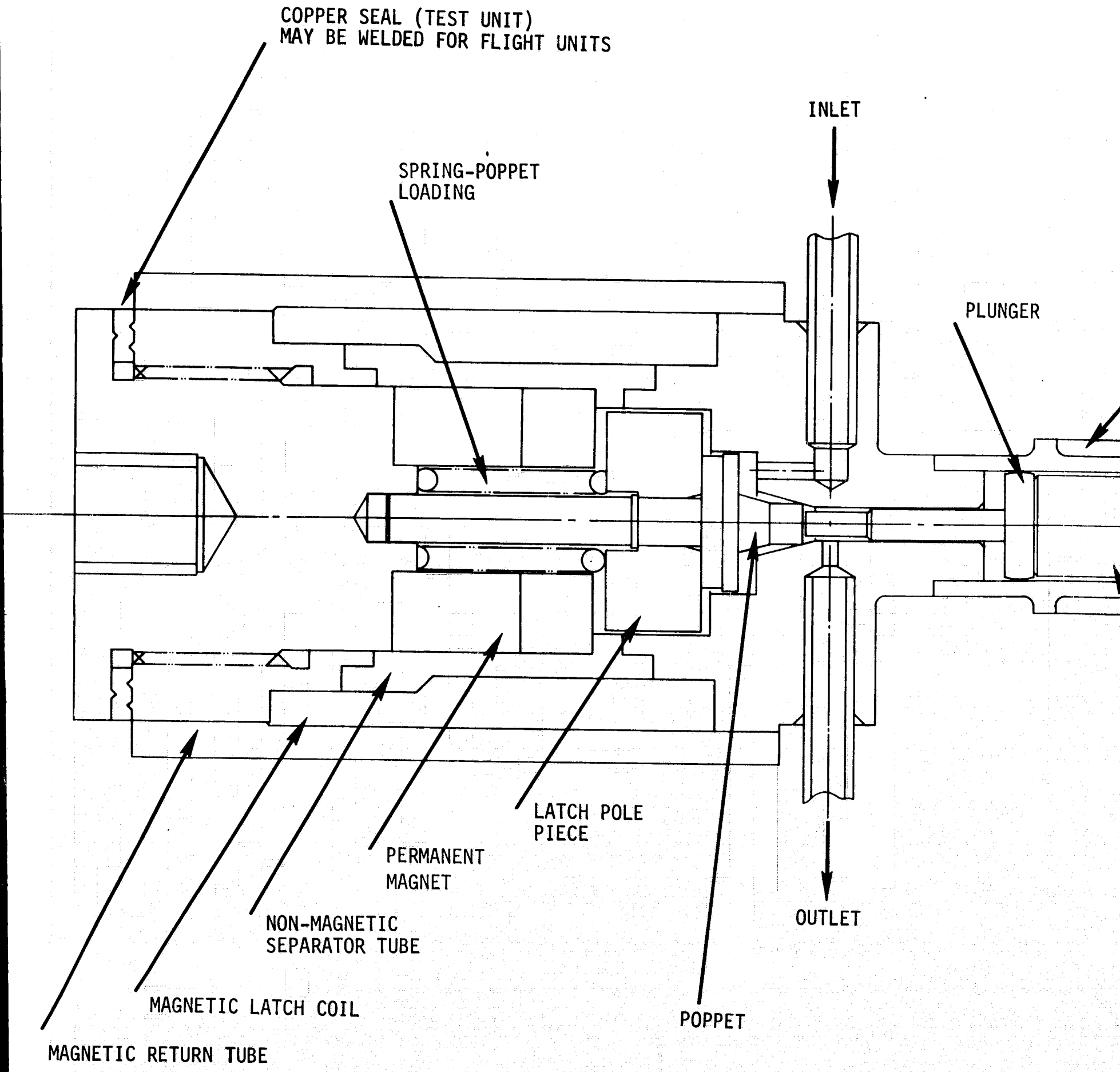
Two approaches were considered for the high pressure valve, the first utilizing a silicone rubber thermal actuator, the second a polyimide rod actuator. Calculations indicated that the silicone rubber actuator was capable of larger strokes per degree of actuator temperature rise, however, it requires a dynamic seal to isolate it from the hydrogen gas. The seal is required to prevent contamination of the hydrogen gas by the outgassing of the rubber which could cause errors in the planetary soil and atmospheric analysis. Since this is required to be a "zero leakage" valve, a bellows or diaphragm seal would be required.

The polyimide rod actuator has a lower thermal gain - or stroke per degree rise in actuator temperature, however, it does not outgas to a significant degree at the use temperature, therefore, it may be immersed in the hydrogen carrier gas. This capability of placing the actuator within the flow media completely eliminated the requirement for dynamic sealing in the high pressure valve. It was felt that this was a significant design simplification and an improvement in overall design reliability, therefore, the final design for the high pressure valve was based on the polyimide rod actuator.

In addition to the basic actuation requirements the valve was required to be capable of being latched in the open position without long term holding power requirements. Several latching approaches were considered including mechanical sears and detents. All of these required a second actuator to release the valve for closure and resulted in a significant increase in valve complexity. The final approach considered was a magnetic latch. Analysis indicated that magnetic latching could provide an effective, easily controlled latch with fast reaction time at a size and weight comparable to mechanical latches, and a considerable reduction in complexity. In addition, no added hermetic seals were required. Based on these factors, the magnetic latch was selected as the optimal approach and was incorporated into the final design.

The final high pressure valve design is shown in Figure 2-12 and operates as follows: When power is applied to the heater it heats the polyimide rod actuator which expands pushing the poppet off its seat and opening the valve. The magnetic latch coil is then momentarily energized and the valve is latched open due to the magnetic forces generated by the permanent magnet. The heater is de-energized and the valve remains open until it is commanded to close with no power being dissipated. To close the valve the latch coil is momentarily energized with reverse polarity and at about one-third the voltage relative to latching open. This releases the poppet and allows the valve to snap shut. This technique results in a valve with a relatively slow opening time - with high opening force capabilities - and a short closing time.

The seat design employed in this valve consists of a conical metal seat of 15 degrees including half angle and a polyimide poppet. The poppet sealing edge was initially left sharp and then coined into the seat to provide the sealing surface. The basic design for the seat was generated by the Jet Propulsion Laboratory. Leakages were found to be less than 5×10^{-8} sccs as measured with a helium mass spectrometer. The valves were to remain closed at 135°C to allow for system sterilization. When set to open at approximately 150°C the opening time was approximately 30 seconds at 28 volts. Power input was approximately 28 watts. Time between cycles (time to retract the thermal actuator) was approximately 60 seconds.



FOLDOUT FRAME

FOLDOUT FRAME

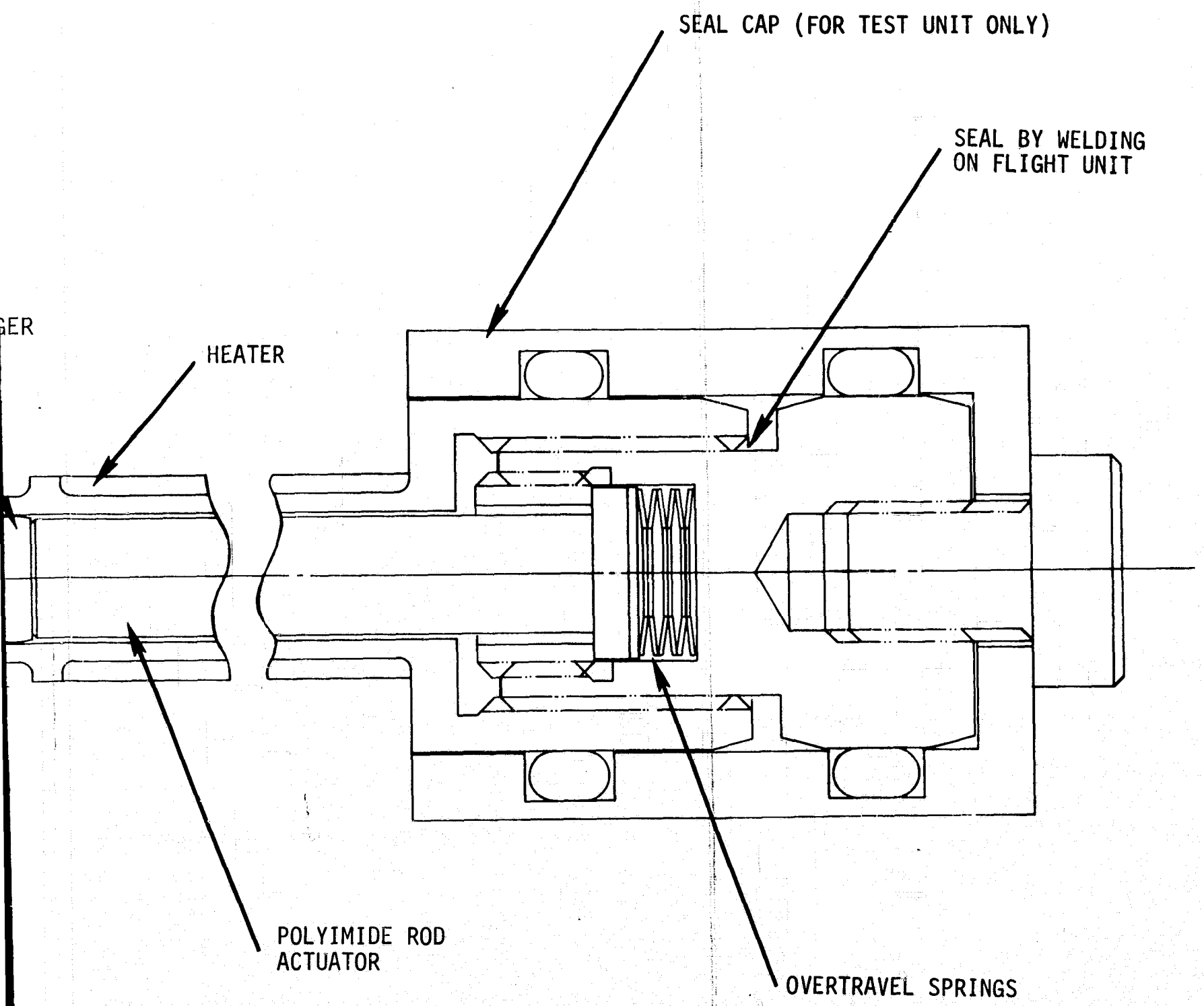


Figure 2-12. High Pressure Micro Valve
(Photo reduced from 10X t
approximately 6X size)

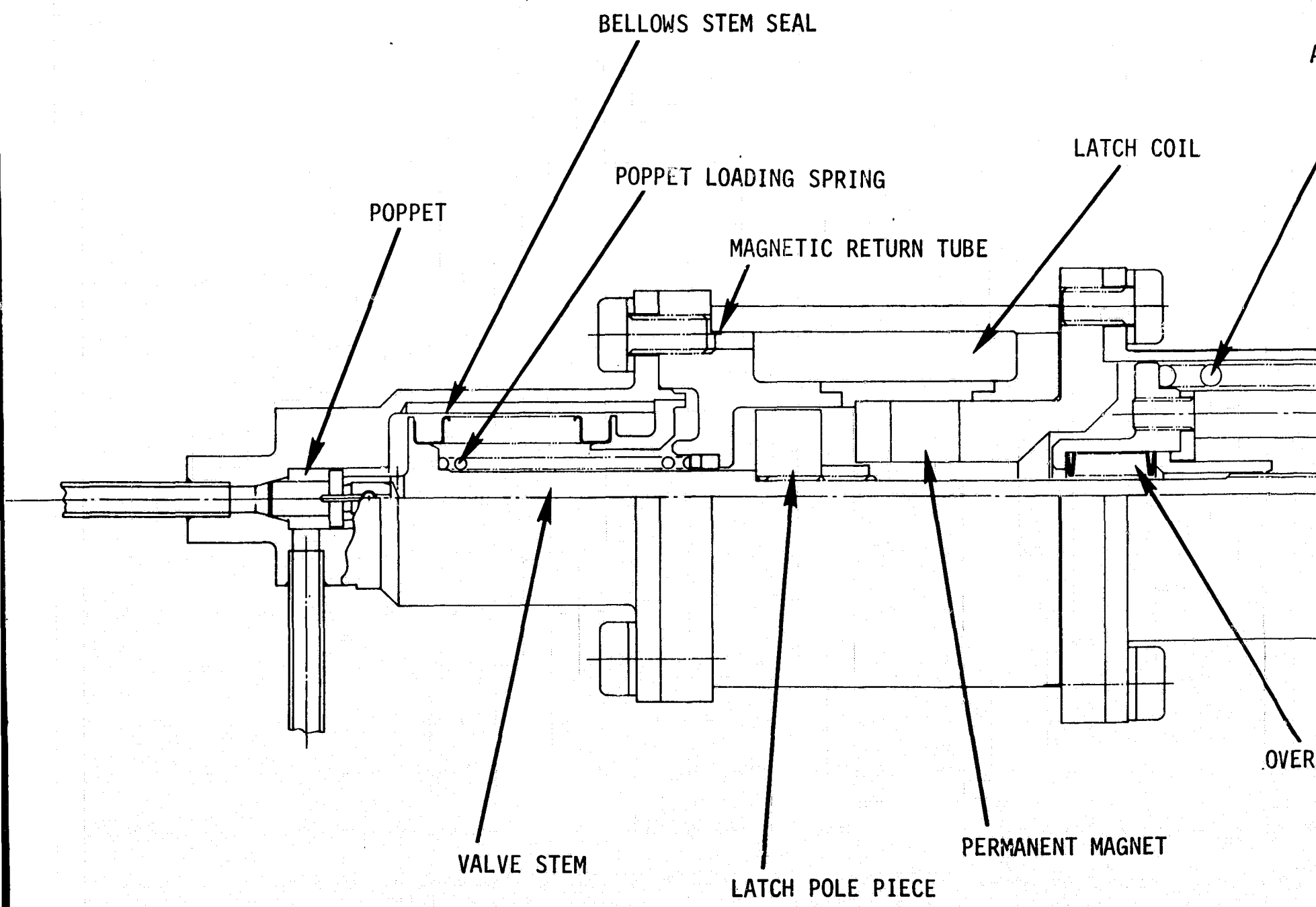
FOLDOUT FRAME 2

Considerable savings in power may be obtained at the expense of actuation time and/or time between cycles. This is accomplished by insulating the valve to eliminate heat losses. Power reductions of a factor of 10 compared to the 30 second actuation time power should be realizable. Valve latching and unlatching require very little power since only a very short pulse is required. Closing time is comparable to a solenoid valve once the time between cycles has elapsed and the thermal actuator has retracted.

Vacuum Valve Design

Two major approaches were considered for the vacuum valve. An approach incorporating the latch mechanism within the vacuum space and an approach wherein the latch is outside the vacuum space. In the former approach, the actuator piston may push directly on the poppet to open the valve with piston to valve housing sealing provided by a bellows. In the latter approach, however, a method of pulling the valve open must be devised or two bellows seals may be used; one to seal the actuator piston and one to seal the latch. Two approaches minimizing mechanical parts exposed to the vacuum were considered. One approach utilized a coaxial actuator concept where the silicone rubber expands against a differential piston. The other uses a direct acting piston and direction reversing mechanism. Evaluation testing indicated development problems existed in the application of the coaxial actuator, therefore, the final design was based on the direct acting approach.

The final vacuum valve design is shown in Figure 2-13 and operates as follows: When power is applied to the heater the silicone rubber actuator pellet is heated and expands pushing the piston against the housing. The actuator pulls the valve stem through the overtravel assembly opening the valve. When the valve is fully open a pulse of electrical energy is applied to the latch coil energizing the latch. The heater power is now turned off and the valve will remain open until commanded to close. Actuator retraction is assisted by the actuator return spring. Closure is commanded by applying a pulse of electrical energy of reverse polarity to the latch assembly, partially demagnetizing the magnet. The valve portion itself is bellows sealed and contains no organic materials other



FOLDOUT FRAME 1

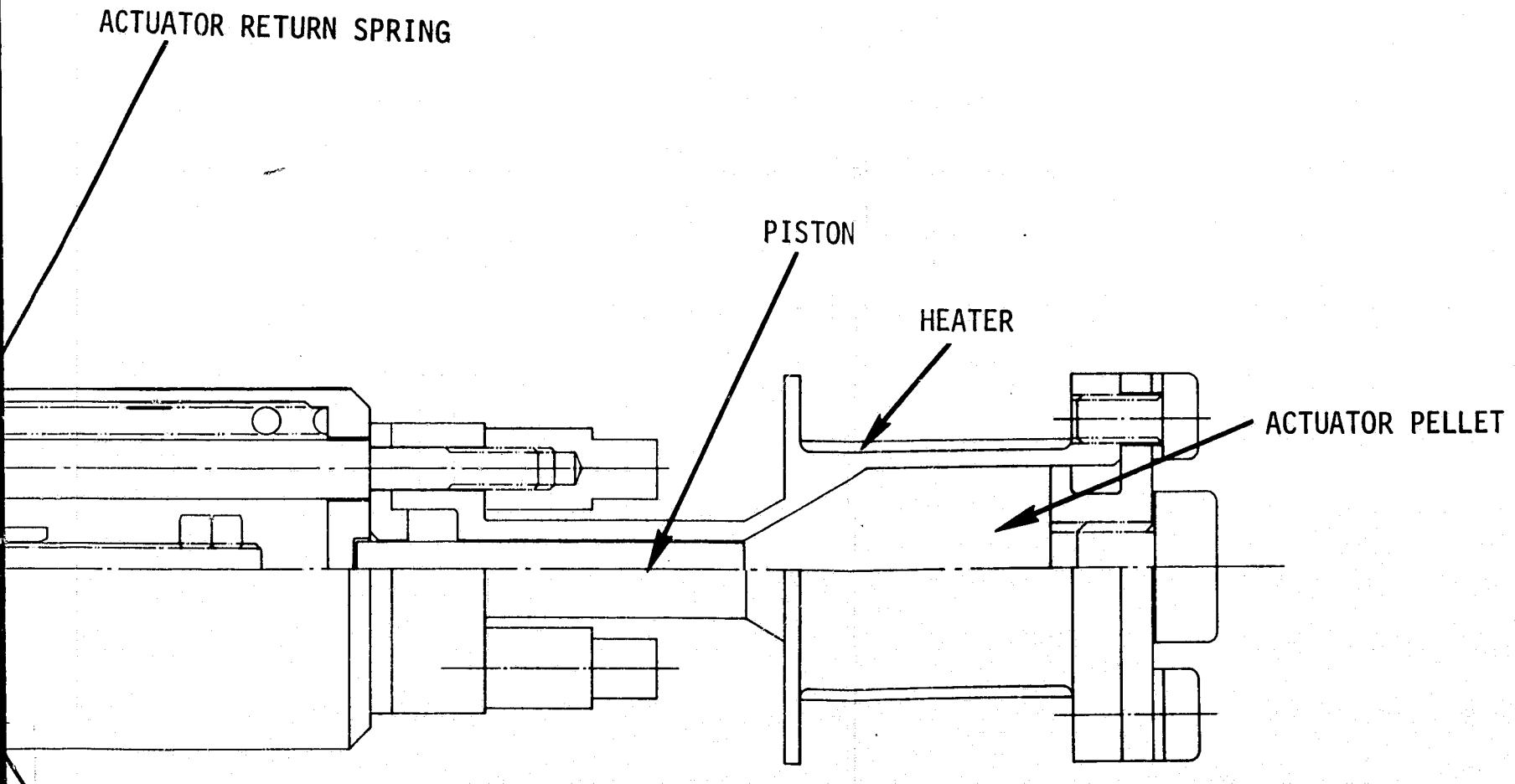


Figure 2-13. Final Design - Vacuum Valve (Photo reduced to approximately 3.5X size)

FOLDOUT FRAME 2

than the Vespel polyimide poppet. The housing has been grooved around the bellows to allow quick pumpout and eliminate trapped gas volumes.

The actuator has a separate return spring to assure that the poppet has the proper seating force upon valve closure. A certain time must be allowed between cycles for actuator retraction as with the high pressure valve. However, once valve closure is commanded it takes only a few milliseconds.

2.7 REFERENCES

1. "Advanced Valve Technology," TRW Final Report No. 06641-6023-R000, Contract NAS 7-436, January 1969.

2. "Advanced Valve Technology for Spacecraft Engines," TRW Final Report No. 8651-6016-RU000, Contract NAS 7-107, March 1963.

3. Van Horn, P. W. and G. F. Doel, "Disconnect Coupling Design Criteria for Fluorine Containing Oxidizers," Technical Report AFRPL-TR-67-149, by Missile and Space Systems Division of McDonnell Douglas Co., Report No. DAC-58548 to Air Force Rocket Propulsion Laboratory, Edwards, California, June 1967.

3.0 NONMECHANICAL CONTROLS

3.1 INTRODUCTION

Nonmechanical controls are here defined as those flow control elements which have no moving mechanical parts which are in sliding contact and include those controls known as fluidics. The purpose of the study performed and reported here was to define the applications of fluidics to liquid chemical propulsion for spacecraft. Primary emphasis was on the 50 to 1000 pound thrust engines using earth and space storable propellants.

Fluidic applications in liquid propulsion systems were considered in two phases: the hybrid applications and completely fluidic components and systems. The hybrid applications considered those components or systems using both the art associated with mechanical controls and the art associated with fluidic controls or elements. For example, a complete fluidic pulse mode or throttle engine may require a mechanical shutoff valve during the nonoperative phase.

A comprehensive study of the state of the art of fluidics and its application to liquid chemical propulsion systems has been accomplished under NASA contract NAS 7-436 (Reference 1). Interviews were made at several commercial companies and government agencies involved in fluidics, to establish the state of the art of components and systems and the problem areas relative to the aerospace applications of fluidics. Comprehensive literature and patent searches were completed. Terminology, nomenclature, drawing techniques, symbology, and definitions of circuit and performance parameters for aerospace applications were defined.

A complete review under NAS 7-436 was made of the theory of operation of the primary fluidic components, which were also assessed relative to liquid propulsion applications. Fluidic pressure regulation and specific propulsion subsystem application studies were also undertaken. Consideration was given to the effect of electrical forces on fluid behavior and electrical to fluid transducer concepts. A closed cycle capillary pumped fluidic power supply and radioisotope heat sources were also investigated under the referenced program.

Primary emphasis was directed toward solving three important problems which must be overcome before fluidic components would be competitive with mechanical controls for spacecraft applications. These problems were: 1) overboard venting of fluids was prohibited, 2) a pressure reference must be established inherent within the spacecraft, and 3) a shutoff function for fluidic systems must be found which, like fluidic elements, possesses no moving or sliding mechanical parts.

Solutions to the first two problems stated above were implemented and treated within the program effort. The third problem is essentially unsolved, however, several approaches to nonmechanical shutoff were investigated under NAS 7-436. The approaches taken in this investigation primarily involved the application of magnetic-liquid actuators and liquid-capillary shutoff concepts.

A more detailed and concise presentation of the work accomplished under this program and under Contract NAS 7-436 is given in the Advanced Valve Technology Compilation, Volume II Report. Figure 3-1 represents the program plan and scope of the study involving application studies, component development and component evaluation.

The results of previous studies has shown the current state of the art of fluidic technology is not adequate for the immediate development of practical applications of completely fluidic (no moving parts) controls to liquid propulsion systems. Fluidic applications in this area was then considered in two phases which are defined as hybrid and completely fluidic systems.

In both phases, the control functions considered include:

- Pressure and flow regulation of pressurants and propellants
- Instrumentation to sense system parameters
- Transducers to interface with other control disciplines
- Specific control functions - i.e., monopropellant and bipropellant feed systems, mixture ratio control, thrust vector control and attitude control.

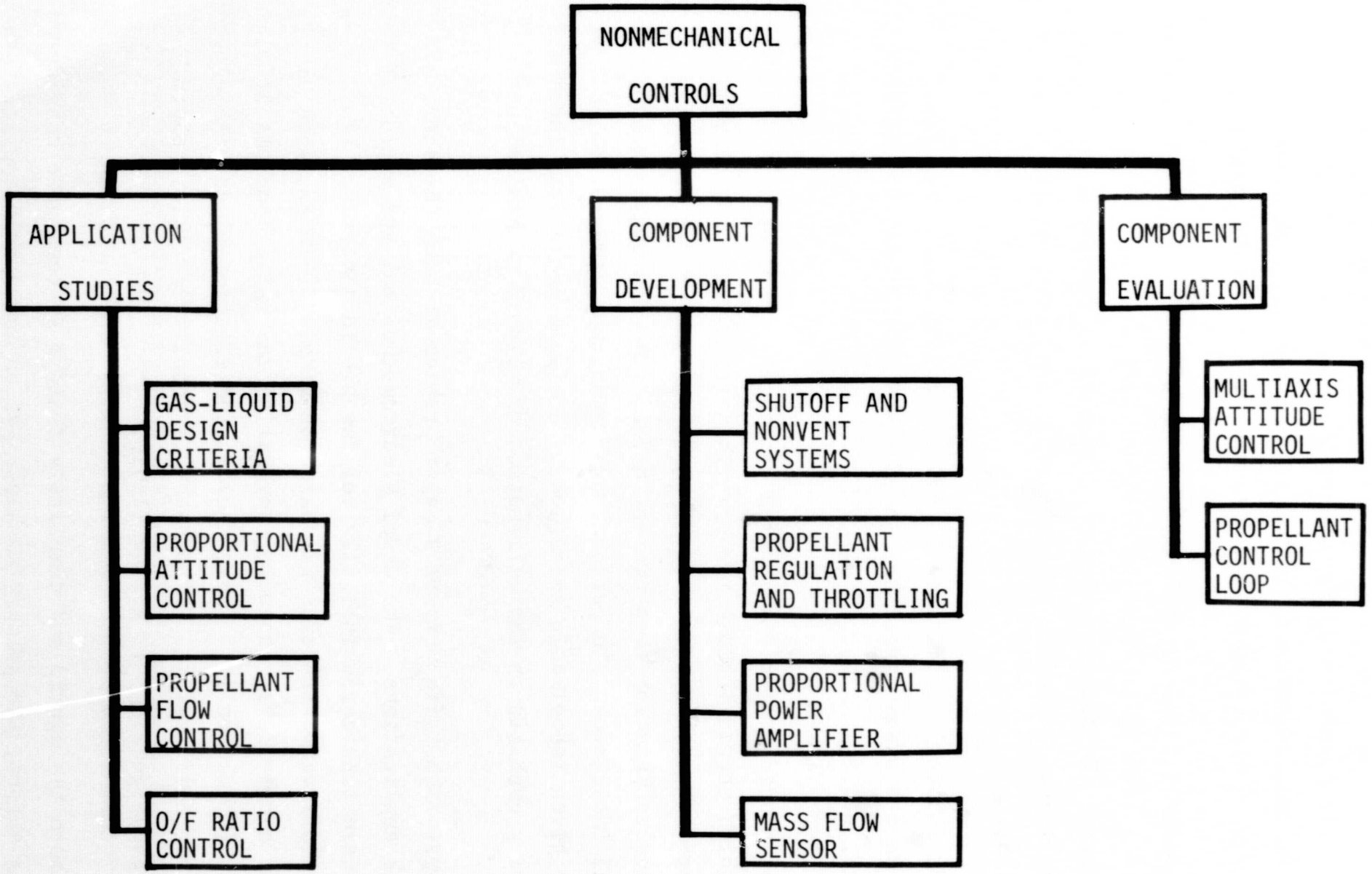

NONMECHANICAL CONTROLS
APPLICATION STUDIES
COMPONENT DEVELOPMENT
COMPONENT EVALUATION
GAS-LIQUID DESIGN CRITERIA
PROPORTIONAL ATTITUDE CONTROL
PROPELLANT FLOW CONTROL
O/F RATIO CONTROL
SHUTOFF AND NONVENT SYSTEMS
PROPELLANT REGULATION AND THROTTLING
PROPORTIONAL POWER AMPLIFIER
MASS FLOW SENSOR
MULTIAXIS ATTITUDE CONTROL
PROPELLANT CONTROL LOOP

Figure 3-1.

For the long term, the major technology improvements required to provide completely fluidic control functions are:

(1) High gain proportional amplifiers - both liquid and gas operated. Present amplifiers are limited to pressure gains of from 5 to 20, however, gains of 50 to 150 are required and appear feasible.

(2) Nonvented systems or methods of minimizing overboard vent requirements - venting or constant pressure dump sources are presently necessary to ensure predictable and optimum fluidic device performance. Absolute pressure references also require excessive venting.

(3) Power sources - recirculating power supplies need to be considered and on a systems basis the use of bleed gas, propellant boiloff gases, etc.

The use of hybrid controls was based on tradeoff studies with existing systems which should include size, weight, and reliability as well as performance. Electrical to fluid transducers are needed which have lower power consumption than present devices and preferably without mechanical interfaces. To perform power functions, consideration also has to be given to reliable specifically designed mechanical interfaces with primary emphasis on the elimination of sliding mechanical parts.

Control system shutoffs present a major problem in both the short and long range applications. The usual electromechanical and explosive type shutoffs were considered initially for the hybrid controls. The design of the shutoff valve function was based on simple flexures, such as diaphragms and bellows, including several of the valve concepts studied previously (Reference 1). These include the electroseal and the electromagnetic capillary valves. At present, a completely fluidic shutoff valve (without venting) is not available.

Although both the hybrid and completely fluidic systems were considered under this effort, the primary emphasis was on the hybrid applications.

To aid in the planning of the application studies, an effort was made to categorize the possible approaches fluidics can be used in propulsion controls. Six major categories were selected and defined (Table 3-1) and these were subsequently broken down into subcategories. The range of possible applications is quite broad and a complete comprehensive study was not within the scope of this task. Consequently, specific areas of detailed investigations were defined under each subcategory. These areas were then reviewed relative to the objectives of this task, and ratings were assigned in the order of importance with 1 being the most important (Table 3-2).

3.2 PROPULSION APPLICATION STUDIES

The primary application of fluidics to propulsion (Table 3-2) are pressure and flow regulation with no moving mechanical parts. Considerable effort has already been directed toward the pressure and flow control of air and gas pressurants, however, very little is known about the performance of fluidic devices using liquid propellants. Current studies consider propellant flow control and, more specifically, liquid propellant flow regulation.

A major consideration in the design of these systems is the need for a constant pressure sump without an overboard drain. The power loss represented by venting propellant will generally be a major consideration in systems analysis. It would appear that only a small amount of propellant venting would be tolerable from a practical standpoint.

3.2.1 Propellant Flow Control

Throttling devices are required to facilitate the regulation and flow control of pressurants and propellants. Simple, reliable mechanical throttles will be used in the hybrid controls to be considered in this program, with primary emphasis on the elimination of sliding mechanical parts. These devices can function without the overboard venting of propellants.

Table 3-1. Propulsion Applications of Fluidics

I. Fluidic Propellant and Pressurant Control Control components utilizing fluidic principles exclusively, i.e. no moving mechanical parts.	I-1 Pressure Control I-2 Flow Control I-3 Mixture Ratio Control I-4 SITVC
II. Instrumentation Fluidic control components required to sense system parameters and interface with other controls, including simple moving part concepts.	II-1 Sensors II-2 Electrical Interfaces II-3 Mechanical Interfaces II-4 Fluid Interfaces
III. Fluidic Techniques for Component and System Improvement The use of fluidic principles to improve the function of conventional components and systems.	III-1 Vortex Generation III-2 Jet Interaction III-3 Surface Interaction III-4 Combined Effects
IV. Fluidically Controlled Valves The use of fluidic controllers with specifically designed mechanical power stages.	IV-1 Shutoffs IV-2 Flow Control IV-3 Pressure Control
V. Fluidic Computation The use of fluidic computation techniques to perform propulsion related control functions.	V-1 Digital V-2 Analog V-3 Combined Techniques
VI. Major Applications Representative fluidic and hybrid applications wherein fluidic technology can make a significant contribution.	VI-1 Medium Thrust Propulsion VI-2 Attitude Control and Station Keeping VI-3 High Thrust Propulsion VI-4 Astronaut Mobility

Table 3-2. Relative Importance of Specific Application Areas

I. FLUIDIC PROPELLANT AND PRESSURANT CONTROL

I-1 Pressure Control

- Liquid Pressure Regulator (1)
- Liquid Pressure Relief (4)
- Gas Pressure Regulator (1)
- Gas Pressure Relief (3)
- Pressure Controllers (1)
- Mixed Media Pressure Regulator (1)

I-2 Flow Control

- Liquid Flow Regulator (1)
- Gas Flow Regulator (1)
- Mixed Media Flow Regulator (1)

I-3 Mixture Ratio Control

- Specific Application Without Moving Parts (2)

I-4 SITVC

- LITVC (2)
- Gas Injection (3)
- G.G. Controlled (3)
- Bleed System (4)

II. INSTRUMENTATION

II-1 Sensors

- Flow (4)
- Pressure (4)
- Temperature (4)
- Position (3)
- Speed (4)

Table 3-2. Relative Importance of Specific Application Areas (Continued)

II-2 Electrical Interfaces

- Electrical to Fluidic (4)
- Fluidic to Electrical (4)

II-3 Mechanical Interfaces (3)

II-4 Fluid Interfaces (2)

III. FLUIDIC TECHNIQUES FOR COMPONENT AND SYSTEM IMPROVEMENT

III-1 Vortex Generation

- Flow Limiting (2)
- Flow Separation (2)
- Signal Isolation (3)

III-2 Jet Interaction

- Flow Biasing (3)

III-3 Surface Interaction

- Geometric Biasing (3)
- Duct Shaping (3)
- Vane Control (2)

III-4 Combined Effects (3)

IV. FLUIDICALLY CONTROLLED VALVES

IV-1 Shutoffs

- Propellant Controlled - Actuated (1)
- Pressurant Controlled - Actuated (1)
- Pressurant Controlled - Propellant Actuated (1)

Table 3-2. **Relative Importance of Specific Application Areas (Continued)**

IV-2 Flow Control

- Propellant Controlled - Actuated (1)
- Pressurant Controlled - Actuated (1)
- Pressurant Controlled - Propellant Actuated (1)

IV-3 Pressure Control

- Propellant Controlled - Actuated (1)
- Pressurant Controlled - Actuated (1)
- Pressurant Controlled - Propellant Actuated (1)

V. FLUIDIC COMPUTATION

V-1 Digital

- Sequencing Functions (3)
- Timers (3)
- Digital Controllers (4)

V-2 Analog

- Analog Controllers (3)
- A.C. Techniques (4)

V-3 Combined Techniques

- Specific Examples (4)

VI. MAJOR APPLICATIONS

VI-1 Medium Thrust Propulsion (50 to 1000 pound thrust range)

- Monopropellant Feed Systems (1)
- Bipropellant Feed Systems (1)
- Propellant Management (3)
- Ground Support Equipment (4)
- Monopropellant Gas Generation Systems (3)

Table 3-2. Relative Importance of Specific Application Areas (Continued)

VI-2 Attitude Control and Station Keeping

- Single Source Attitude Control (3)
- Single Source Station Keeping (4)
- Proportional Attitude Control (2)
- Combined Attitude Control Station Keeping (4)

VI-3 High Thrust Propulsion

- Liquid Chemical Rockets (1)
- Nuclear Rockets (4)
- Solid Rockets (4)
- Hybrid Rockets (3)

VI-4 Astronaut Mobility

- Individual Space Propulsion Units (3)
- Space Transfer Vehicles (3)
- Ground Effect Machines (3)

Fluidic throttling devices with wide flow control ranges require overboard venting. The use of a nonvented device, such as the vortex amplifier, is impractical because the control pressure has to be significantly higher than the supply pressure to effect throttling. This means that a separate source of supply fluid is required or the supply flow has to be dropped in pressure to make the controls effective. In the latter case, the throttling range is drastically reduced.

In the ideal sense, an efficient method of throttling in a single source fluidic system is depicted in Figure 3-2. Control flow is bypassed from the supply stream to power a fluidic controller which adjusts the throttling device on the basis of an internal reference signal or an external command signal from an electrical to fluid transducer. Vent flow from the controller is returned and combined with the output flow. The controller functions on the differential pressure across the throttling device, which presents difficulties in that the supply and output pressures can vary independently and the fluidic circuitry must be designed to function on a variable differential pressure. In addition, the throttling device is operated with a control pressure lower than the supply pressure, and without an overboard vent there is no way of establishing an absolute pressure reference for the fluidic controller.

With these criteria, a study was made, in particular, with regard to the fluid mechanics of internal flow. To date, three conceptual devices have been defined which show considerable promise and should be investigated further.

(1) Bypass Venturi Throttle - This involves the injection of fluid in the low pressure throat section of a venturi, to throttle by an effective throat area change or induced cavitation.

(2) Vortexing Conical Diffuser - The mechanism of swirling flow through a convergent-divergent nozzle can cause reverse axial flow and in the ideal case a pronounced reduction of mass flow and, in some cases, flow stoppage. This mechanism coupled with control flow at the minimum nozzle area, to modulate the degree of swirl, has excellent potential as a fluid throttle.

(3) Cavitating Venturi Pressure Reference - A venturi section operated in cavitation has a relatively large cavitation bubble downstream of the throat which is essentially at the vapor pressure of the flowing liquid. In concept, the cavitation bubble would make a suitable nonventing absolute pressure reference for a fluidic controller if it can accept the reference signal flow without collapsing.

3.2.2 Hybrid Flow Regulator

This study is concerned with defining the methods of fluidically controlling the flow of a liquid monopropellant in a typical feed system in conjunction with a simple mechanical throttle. A typical system is defined in Figure 3-3. The flow range of interest is 0.25 to 5 lb/sec which corresponds to a thrust range of 50 to 1000 pounds. Initial consideration will be given to a flowrate of 1 lb/sec (200 pounds thrust), however, the study data should apply equally well to the control of bipropellants such as diborane and oxygen difluoride.

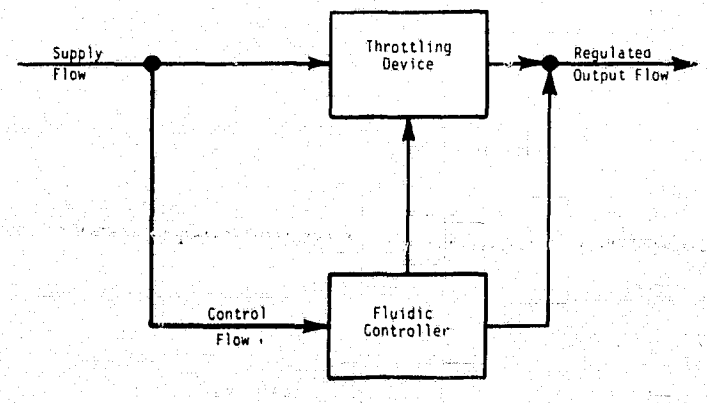


Figure 3-2. Concept of Single Source Fluidic Throttling

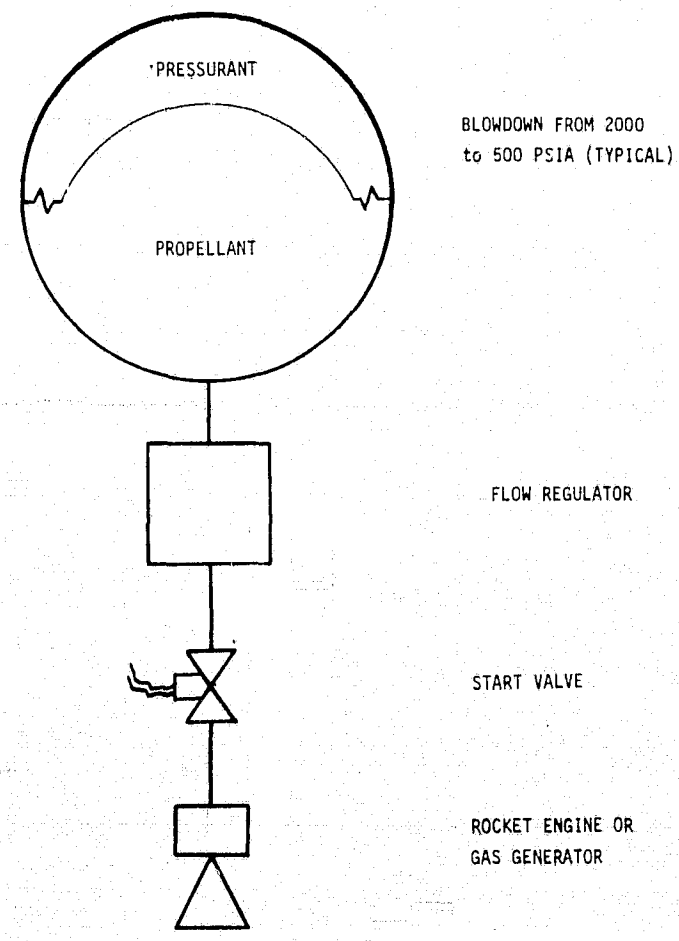


Figure 3-3. Typical Monopropellant Feed System

A direct-acting mechanical flow regulator maintains a constant flow rate by keeping the pressure drop across a fixed orifice constant regardless of variations in either the supply or discharge pressures. This is accomplished by the use of a pressure balanced control valve which acts as a variable orifice downstream of the fixed orifice. The pressure drop across the fixed orifice is impressed across a sensing diaphragm which is mechanically coupled to the control valve. Any variation of the pressure drop across the fixed orifice will cause the control valve to change the variable orifice setting so as to restore the original pressure drop.

A fluidic mechanization of the basic direct-acting mechanical flow regulator is shown in Figure 3-4. The difference in the characteristics of a nonlinear and a linear resistor is detected by the reference amplifier which vents directly into the cavitating venturi. The error signal is summed with a positive feedback signal in the summer-integrator, which controls the power amplifier to position the mechanical stage. The regulator performs a flow regulation function, in that the fluidic circuit adjusts the mechanical stage to maintain the downstream pressure at a constant absolute level. It is presumed that the vent flow to the cavitating venturi is a constant.

A simplified concept of the flow regulator was conceived in an effort to reduce the number of active elements, as shown in Figure 3-5. Essentially this circuit involves the consolidation of the integrator and power amplifier functions in one amplifier, which presumes an amplifier with a high open loop pressure gain (>50) would be available. A preliminary sizing of this simplified concept was accomplished utilizing the catalog performance of a General Electric AW32 proportional amplifier to determine relative flow rates.

Presuming initially, for maximum reliability, that the minimum constriction in all circuit elements would be 0.015 inch diameter and that the differential pressure across nonlinear resistor A_{01} is 60 psi

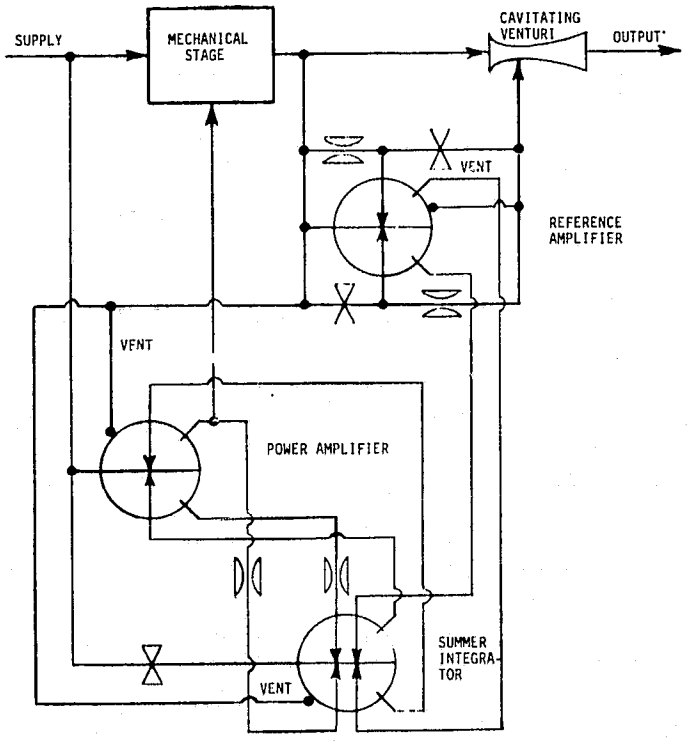


Figure 3-4. Hybrid Fluidic Flow Regulator

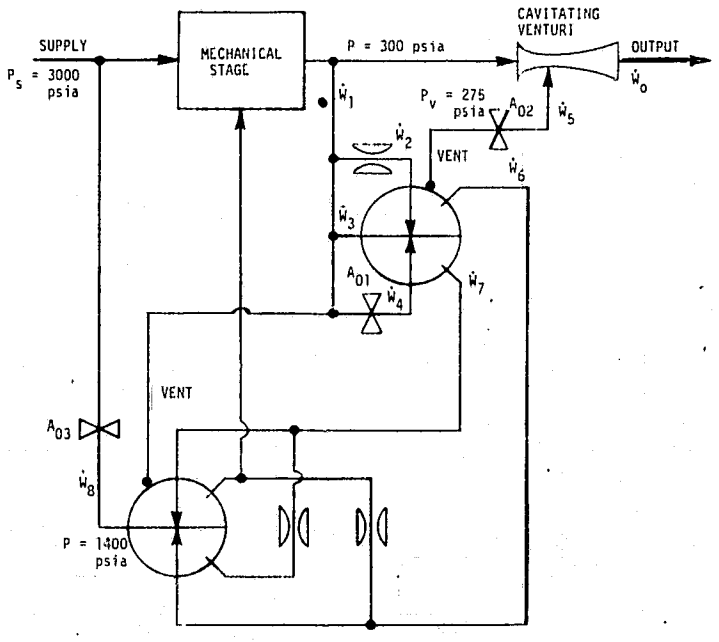


Figure 3-5. Simplified Hybrid Flow Regulator - Scheme I

$$\dot{W}_4 = 21.9\ C_f\ d_{01}^2\ (\Delta P)^{1/2}$$

$$= 21.9 \times .6 \times (1.5)^2 \times 10^{-4} \times \sqrt{60}$$

$$= 0.0228 \text{ lb/sec}$$

$\dot{W}_2 = \dot{W}_4$ when the set pressure is reached and $\dot{W}_3 = 10\ \dot{W}_2$ based on the AW32 amplifier characteristics.

$$\therefore \dot{W}_1 = \dot{W}_2 + \dot{W}_3 + \dot{W}_4$$

$$= 0.0228 + 0.228 + 0.0228$$

$$= 0.2736 \text{ lb/sec}$$

Since $\dot{W}_1$ is already 27 percent of the output flow, the differential pressure across A_{01} was reduced to 25 psi. Recalculating, $\dot{W}_1$ was reduced to 0.1776 lb/sec.

Continuing further, under quiescent conditions $\dot{W}_6 = \dot{W}_7 = .022$ lb/sec based on the AW32 amplifier performance, so that the vent flow

$$\dot{W}_5 = \dot{W}_1 - (\dot{W}_6 + \dot{W}_7) = 0.1336 \text{ lb/sec}$$

With this flowrate, the size of nonlinear orifice A_{02} becomes 0.0248 inch diameter. Further calculation at the maximum supply pressure of 3000 psia made it possible to determine system operating pressures as shown in Figure 3-5. The other important circuit parameters are $d_{03} = .0167$ inch and $\dot{W}_8 = 0.146$ lb/sec.

A review of the results of this preliminary sizing of the simplified flow regulator (Figure 3-5) indicated no particular problem with the size of circuit elements. Since the reference circuit vents ($\dot{W}_5$) only 0.1336 lb/sec it is possible that pressure regulation could be accomplished with a flow range of something <7.5. Flow range will improve at thrust levels greater than 2000 pounds. There is some concern as to whether the cavitating venturi can handle the reference circuit vent flow which is about 15.5 percent of the main flow through the cavitating venturi. No data is presently available to determine the feasibility of this vent scheme. An important point concerning this regulator is that the control inputs to the integrator-power amplifier would have to function in an interaction region at a slightly higher pressure. This mode of operation does not appear feasible at present.

Based on the above, a second simplified hybrid flow regulator was conceived as shown in Figure 3-6. The primary difference in Scheme II, is that the integrator-power amplifier also was made to vent directly into the cavitating venturi. Therefore, the circuit elements were carefully sized to minimize vent flow. Circuit parameters were calculated as for Scheme I and included in Figure 3-6.

A total vent flow for Scheme II was found to be 0.1248 lb/sec which is only about 12.5 percent of the flow required for a 2000 pound thrust monopropellant engine. The minimum nonlinear orifice size used was 0.012 inch in diameter, which would certainly be the smallest considered. The linear resistor in the reference circuit was estimated to be composed of 12 tubes, 20 inches

long with an I.D. of 0.010 inch. As shown in Figure 3-6, all of the other circuit elements are of practical size, so that this scheme appears feasible for both flow and pressure regulation. For pressure regulation, an electrical to fluid transducer would be installed around the nonlinear resistor A_{02} in the reference circuit, so that the reference pressure can be varied on command.

To reduce the number of active elements even further, it would be better to introduce the reference resistors directly into the integrator-power amplifier as shown in Figure 3-7. However, this could not be done unless the amplifier has an open loop pressure gain >100.

The results of this study thus far have pointed up two basic requirements regarding circuit elements for the flow regulator.

1. A cavitating venturi capable of handling a vent flow of about 10 percent of the mainstream flow at a constant absolute pressure level.

2. A fluidic proportional amplifier with a pressure gain >50 and preferably >100.

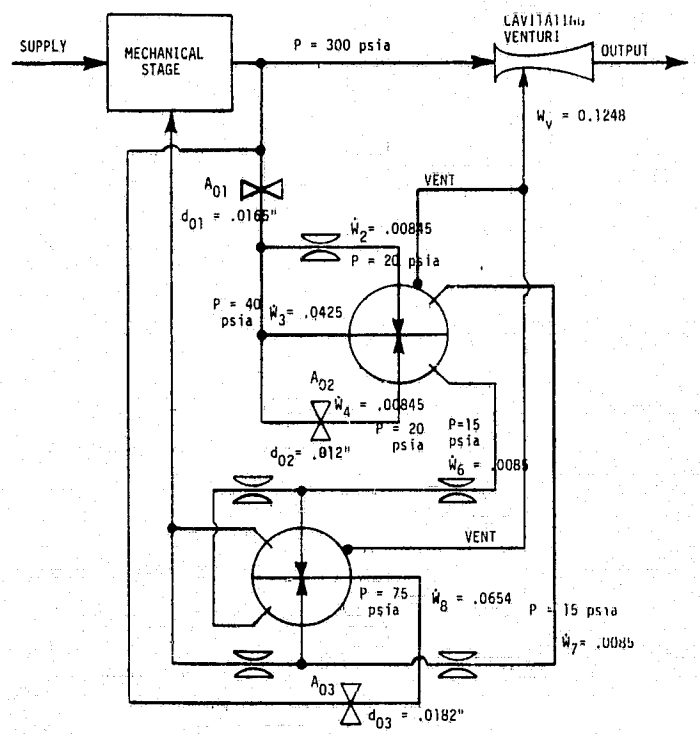


Figure 3-6. Simplified Hybrid Flow Regulator - Scheme II

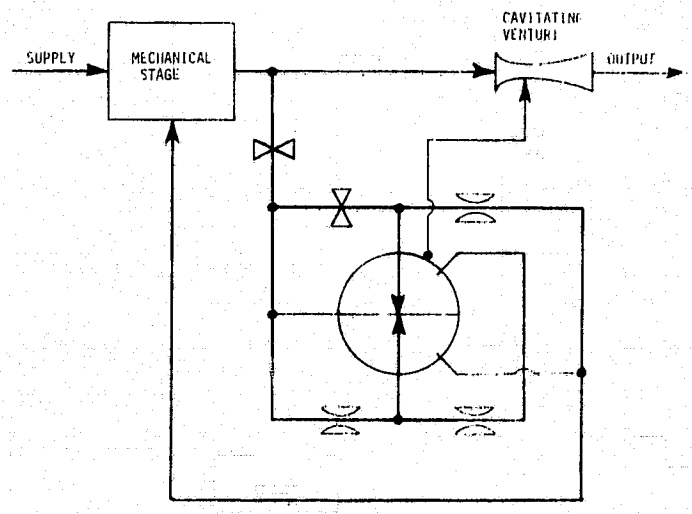


Figure 3-7. Simplified Hybrid Flow Regulator - Scheme III

3.2.3 Hybrid Flow Regulator Concept

A hybrid fluidic mechanization of the propellant flow regulator is shown in Figure 3-8. This regulator concept utilizes a mechanical stage to throttle the decaying pressure-flow source. The fluidic circuit provides the reference pressure signal and generates the error signal to control the mechanical stage. Bypass propellant is used to operate the fluidic circuit and is returned to the mainstream at the throat of a venturi section. Analysis and sizing of circuit parameters is presently underway.

The high gain proportional reference amplifier in the fluidic circuit detects the difference in the pressure-flow characteristics of a linear and nonlinear resistor (Figure 3-9) and generates a high or low differential error signal. The reference pressure point or regulator set point occurs when the differential pressures and flows in both resistors are equal. The error signal is received at the integrator-power amplifier which integrates the error by the use of positive feedback and generates a differential output signal to control the mechanical stage directly. To change the regulated flow rate on command, an electrical to fluidic transducer could be installed in parallel with the fixed nonlinear resistor in the reference circuit. Fluidic proportional amplifiers used in this regulator should have open loop pressure gains 50. This minimizes the number of active fluidic elements required so that the vent or bypass flow to the venturi is held to a minimum. Pressure gains of about 100 have been demonstrated experimentally at the Harry Diamond Laboratories.

The venturi throat provides a constant pressure sump for the fluidic control circuit. Since the pressure and flow are kept constant, the static pressure at the venturi throat should also be constant. Another possibility is to operate the venturi section in deep cavitation, so that the bypass control flow is injected into the cavitation bubble which is essentially at the vapor pressure of the flowing propellant. This provides the further advantage of isolating the regulator from downstream conditions.

The mechanical stage is conceived as a simple poppet valve which is positioned by a pressure balanced diaphragm actuator (Figure 3-10). Pressure balancing is required to minimize the control power requirement and further reduce the control bypass or vent flow. High reliability is maintained by eliminating all sliding parts in the mechanical stage. This is achieved by suspending the poppet on flexures, i.e., a diaphragm and two bellows.

Advantages of the Hybrid Regulator

(1) High reliability and long term storage capability in the space environment due to the elimination of all sliding parts.

(2) The capability of adjusting the flow rate on command over a 5 to 1 flow range in a 200 pound thrust engine system, and over a broader flow range at higher thrust levels.

(3) Can be operated on and stored wet with any liquid propellant.

(4) Proportional control with positive feedback provides near constant control loop gain over entire supply blowdown range.

(5) The cavitating venturi provides complete isolation from downstream conditions.

Applications of the Hybrid Regulator

(1) Flow regulation of all liquid propellants.

(2) Open and closed loop bipropellant oxidizer-fuel ratio controller.

(3) Wide range flow regulation on command or programmed.

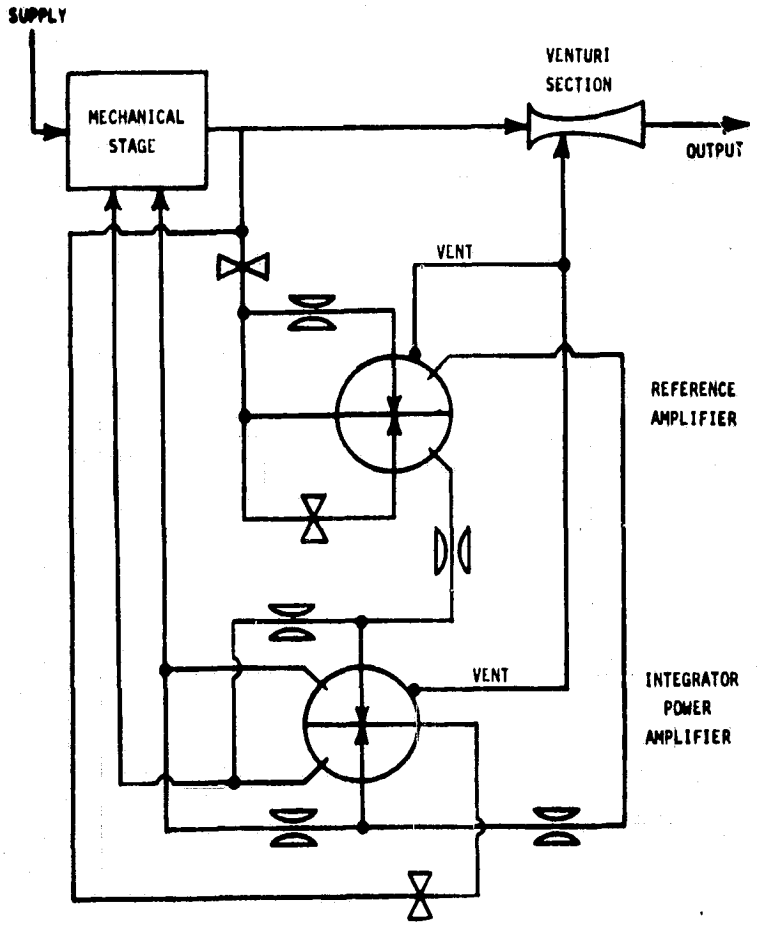


Figure 3-8. Hybrid Fluidic Propellant Flow Regulator

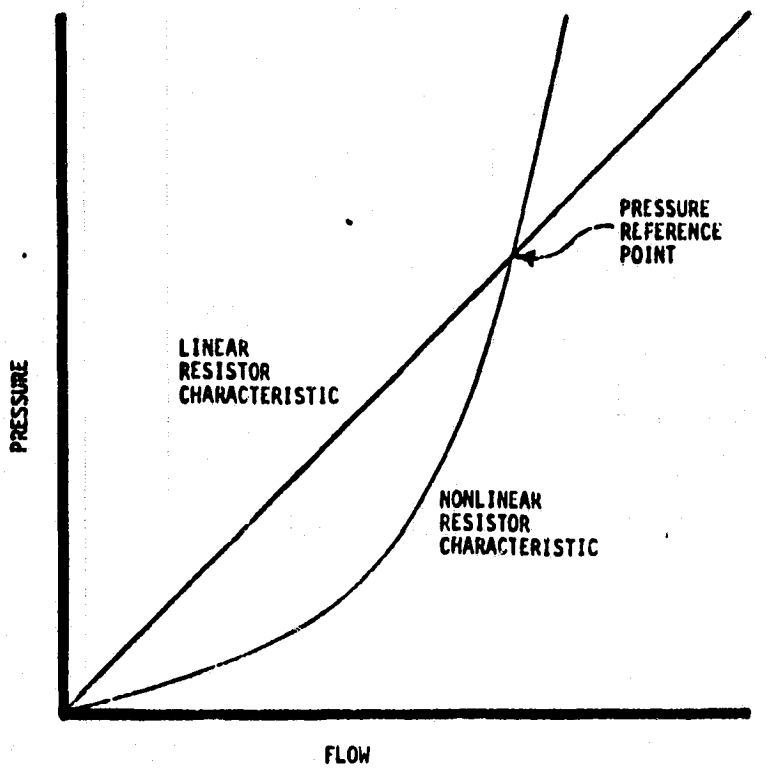


Figure 3-9. Pressure Reference for Flow Regulator

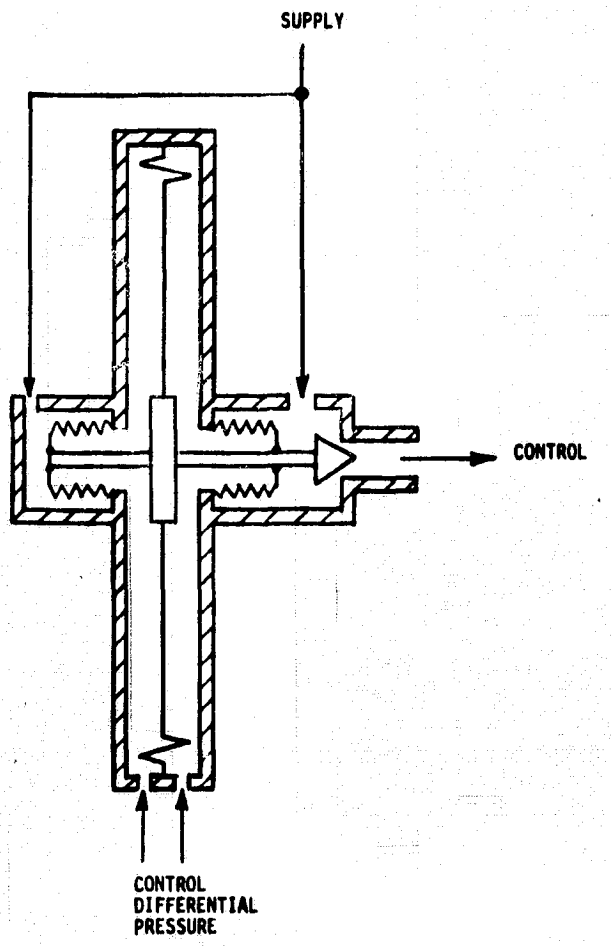


Figure 3-10. Balanced Mechanical Stage Concept

3.3 COMPONENT DEVELOPMENT

3.3.1 Proportional Amplifier Evaluation

Data supplied by General Electric for a water calibration of the AW 32 proportional amplifier indicates pressure gains in the range of 8.5 to 9.5 are possible with this amplifier in the supply pressure range of 4 to 12 psig under blocked load conditions. This compares to a maximum pressure gain of 6.5 which operated with air at 60°F. Although this was encouraging, no data was available on the operation of staged high gain blocks on water.

A test setup was made, so as to determine the steady state operational performance, on water, of the G.E. AM-12 proportional gain block.

This analog jet interaction fluidic device consists of five staged proportional amplifiers. The supply ports of the individual stages are internally manifolded to provide optimum pressure ratios between the stages.

The AM-12 gain block was operated submerged in a tank of water as shown in Figure 3-11. The supply and controls were supplied with separate water sources, such as a bladder type accumulator. Ten micron filtration was used for both the supply and controls. The test gages used for visual observation are shown in circles, and the pressure transducers (Pace-Wiancko) are shown in rectangles. The input control circuit is set up in a bridge or pressure divider circuit to allow the balancing of the input control bias and adjustment of the low differential input pressures needed to operate the AM-12 gain block.

The two submerged orifices are 0.012 inch diameter orifices and the two needle valves are Nupro S-series 0.031 inch equivalent orifice diameter.

Instrumentation List

Parameter	Range	Type
P_{01}	25 psid	Ashcroft-Heise
P_{02}	10 psig	Pace-Wiancko
ΔP_o	±10 psid	Pace-Wiancko
P_{c1}	5 psig	Ashcroft-Heise
P_{c2}	5 psig	Pace-Wiancko
ΔP_c	±0.01 and ±0.1 psid	Pace-Wiancko

X-Y Plotter - 8-1/2 x 11 inch size is adequate.

The test setup was completed and checked out and a preliminary calibration performed (Figure 3-12). A wide variation in the pressure gain of the AM-12 was noted at the two supply pressures used. Preliminary results indicate that the water performance of the AM-12, pressure gain, is much less than the performance on air, i.e., ~1500 on air versus ~200 on water. This variation in performance can be attributed to the sizes and supply ports for each stage in the AM-12 which need to be resized to provide optimum pressure ratios between the stages.

3.3.2 Configuration of Cavitating Venturi Sump

The test item, as shown in Figure 3-13, was originally made with an integral piston actuator to axially adjust the pintle position. For these tests, the pintle was modified, as shown, to allow the injection of return fluid into the cavitation region. The modification included drilling a return path from the outside of the piston to the center, cutting off and boring out the center of the pintle, and the addition of a constant diameter pintle extension with eight equally spaced return orifices. The valve body section was refabricated in Lucite utilizing the best available design parameters for the accelerating and diffusing sections.

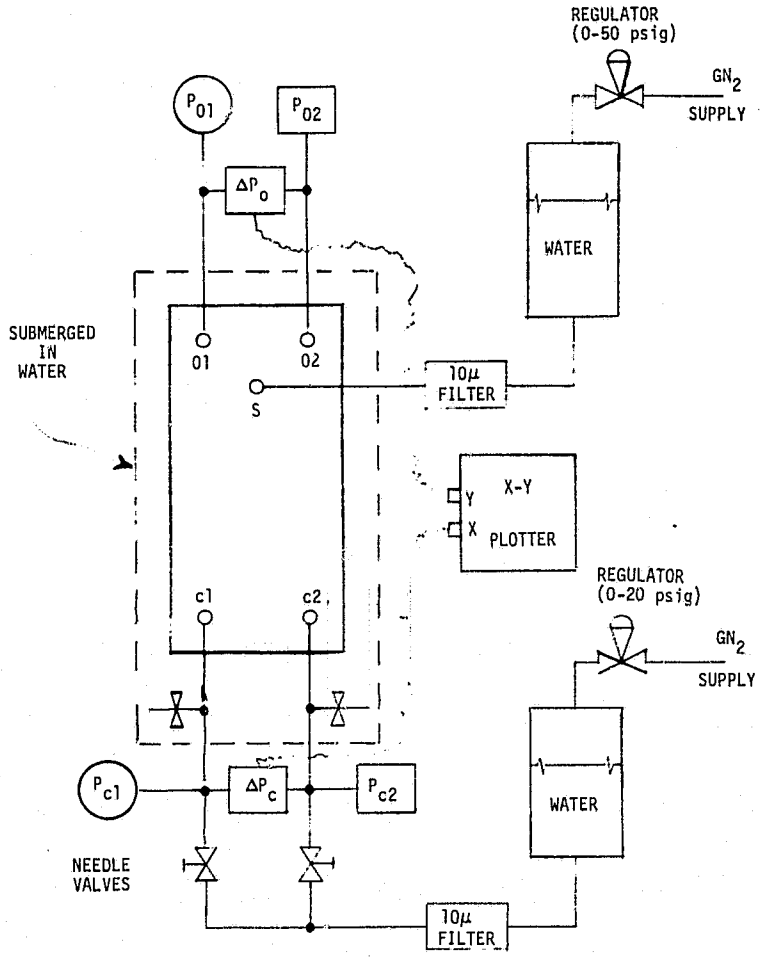


Figure 3-11. Test Setup - Water Calibration of G.E. AM-12 Proportional Gain Block

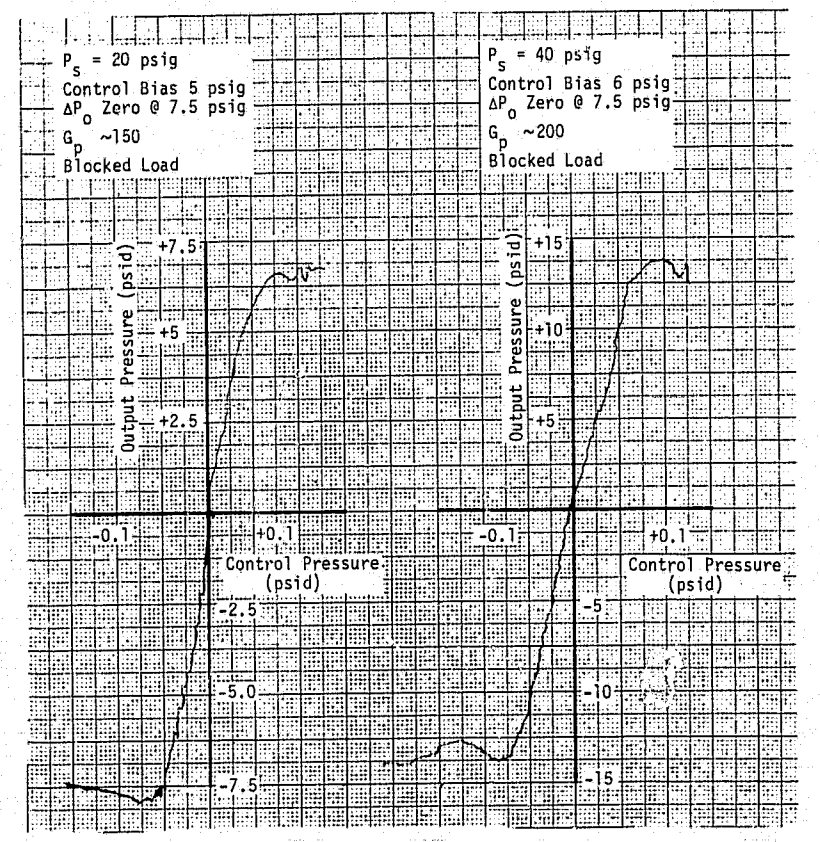


Figure 3-12. Water Calibration of G.E. AM-12 Proportional Gain Block

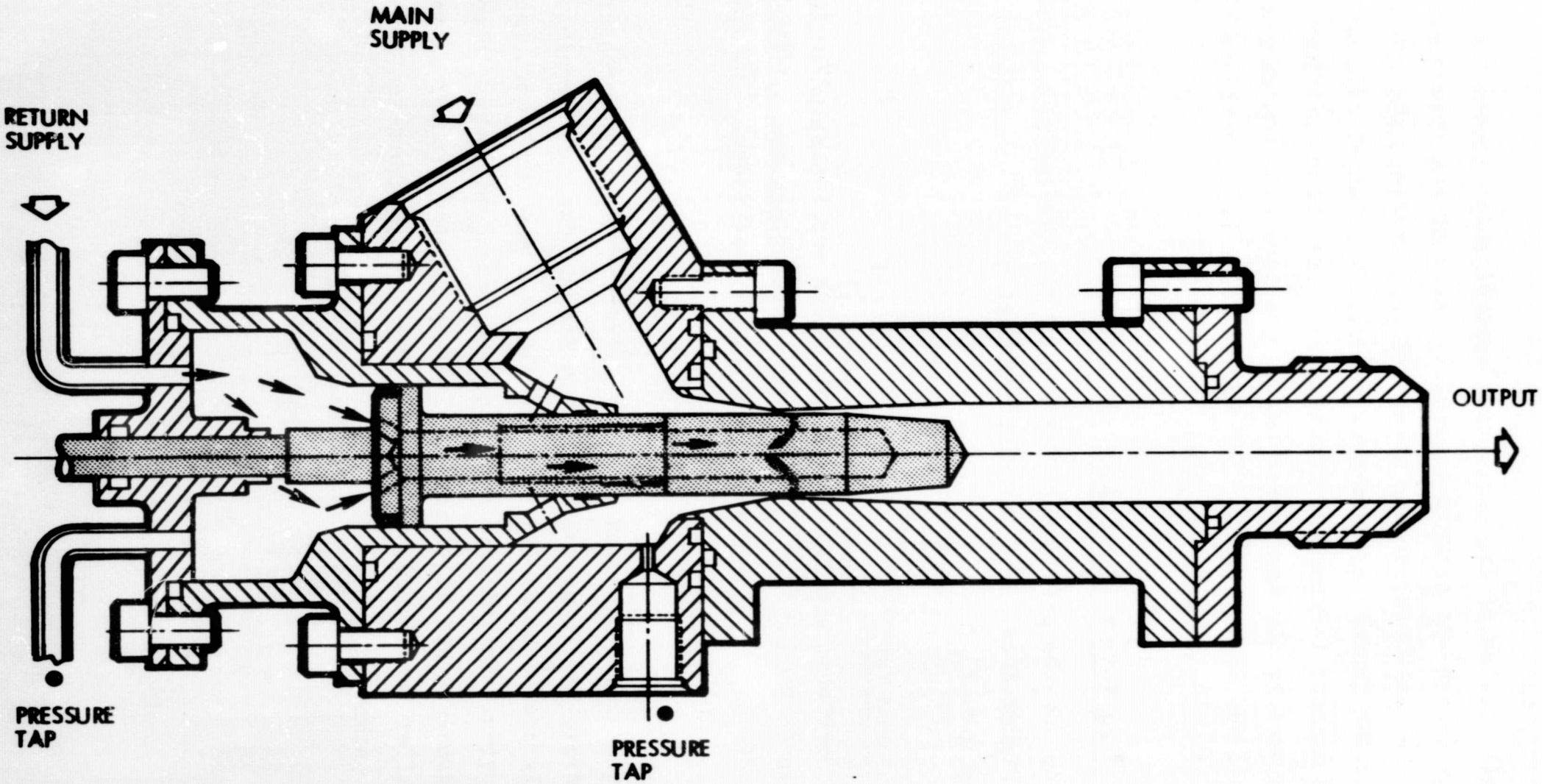


Figure 3-13. Cavitating Venturi Sump Configuration

The test configuration of the cavitating venturi sump allowed the adjustment of the pintle (which was clamped externally) so that the return orifices could be located anywhere between about 1/8 inch upstream and 3/8 inch downstream of the throat (minimum area point). This axial adjustment was accomplished without varying the throat area. The return orifices were also used to measure the cavitation bubble pressure when the cavitation characteristic was investigated. The Lucite valve body permitted visual observation of the cavitation region.

3.3.3 Cavitating Venturi Sump Test Results

The test setup for the preliminary testing of the cavitating venturi sump is shown in Figure 3-14. The test instrumentation and nomenclature is defined in Table 3-3.

3.3.4 Preliminary Tests

A fluidic proportional amplifier high gain block was installed in the test setup as shown in Figure 3-15. Preliminary testing was accomplished operating the fluidic amplifier with the return supply exhausting the return of the cavitating venturi sump.

The initial test results showed that the differential output pressure, ΔP_o, of the fluid amplifier and the return flow to the sump remained constant at main supply pressures of 135, 215 and 415 psia and throughout the entire cavitation regime. The fluidic amplifier was exercised several times at each supply pressure and at various cavitating levels. In all cases, the fluidic amplifier functioned properly and the output saturation level, ΔP_o maximum, was unchanged.

Table 3-3. Cavitating Venturi Sump Test Instrumentation

Parameter	Nomenclature	Range	Full Scale Accuracy (%)
Main Supply Flow	F.M. #1	4.5 to .5 gpm	± 1
Return Supply Flow	F.M. #2	0.3 to .03 gpm	± 1
Main Supply Pressure	P_s (high)	400 psig	± .25
Main Supply Pressure	P_s (low)	60 psig	± .1
Output Pressure	P_o	400 psig	± .25
Supply-Output Differential Pressure	ΔP_1 (high)	50 psid	± .5
Supply-Output Differential Pressure	ΔP_1 (low)	10 psid	± .5
Return Pressure	P_R (high)	100 psig	± .1
Return Pressure	P_R (low)	30 psig	± .1
Return Pressure	P_R (vacuum)	14.7 to 0.3 psia	± .25
Fluidic Amplifier Output Differential Pressure	ΔP_o	15 psid	± 1
Fluidic Amplifier Vent Pressure	P_V	100 psig	± 1
Fluidic Amplifier Supply Pressure	P_F	100 psig	± 1

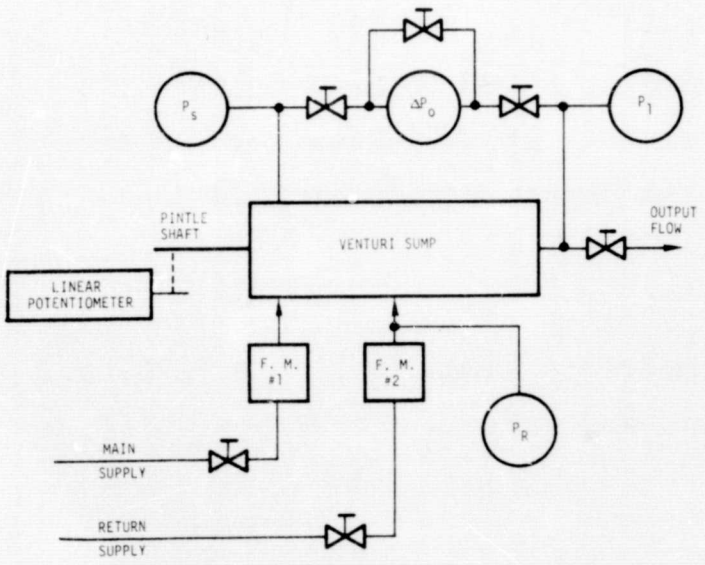


Figure 3-14. Venturi Sump Test Set-up and Instrumentation

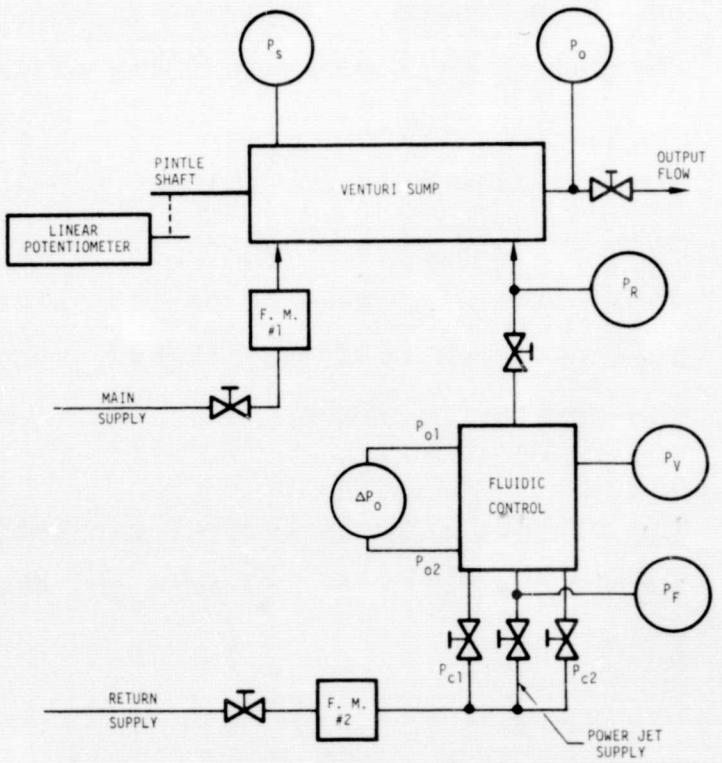


Figure 3-15. Fluidic Control Demonstration Test Setup

3.4 COMPONENT EVALUATION

3.4.1 Cavitating Flow Characteristic

Tests were performed with water to establish the cavitation performance of the venturi sump. A one-half inch axial adjustment of the pintle was possible, so that the return orifices in the sump could be located anywhere between about 1/8 inch upstream and 3/8 inch downstream of the throat without varying the throat area. Cavitation characteristic was investigated at each of five positions and at supply pressures of 100, 200 and 400 psia, so as to determine the effect of pintle and body centerline variations on performance. The test points were:

(1) Full in - 1/8 inch upstream of throat
(2) 25% in - at the throat (minimum area point)
(3) 50% in - 1/8 inch downstream of throat
(4) 75% in - 1/4 inch downstream of throat
(5) 100% in - 3/8 inch downstream of throat

The cavitation performance of the venturi sump is depicted in Figures 3-16 through 3-19. Although not optimum, the cavitation limits are more than adequate for the test model of the venturi. The limits vary from about 62 percent at 100 psia supply pressure to about 81 percent at 400 psia supply pressure. The limit is defined as maximum output pressure at which cavitation will occur in terms of the supply pressure (i.e., P_o/P_s x 100).

These limits hold for all the pintle positions except when the return orifices are at the throat (25 percent in) as shown in Figure 3-17. In this case, the presence of the return orifices at the throat causes turbulence which tends to slightly reduce the pressure recovery and hence the cavitation limit.

The venturi sump in several cavitation modes is shown in Figure 3-20 for supply pressures of 100 psia and 400 psia and various output pressures.

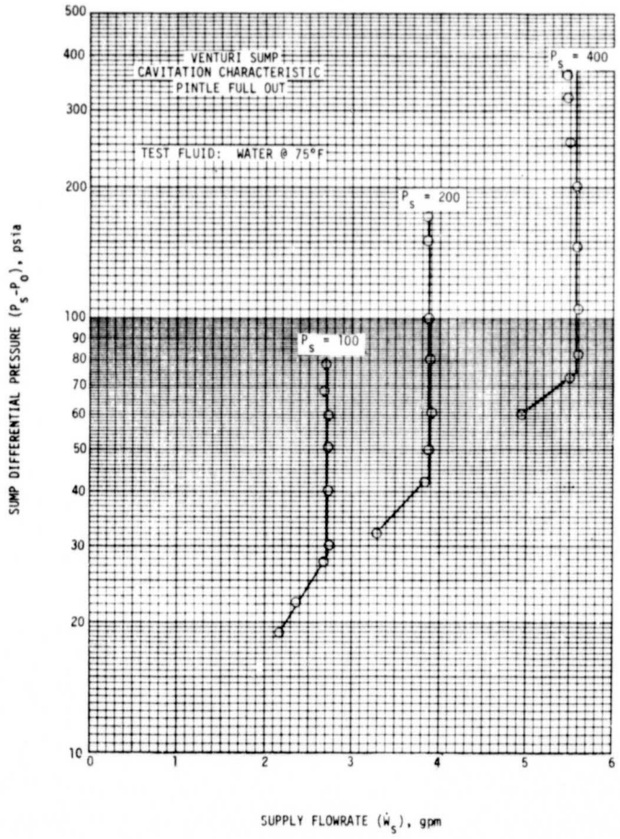


Figure 3-16

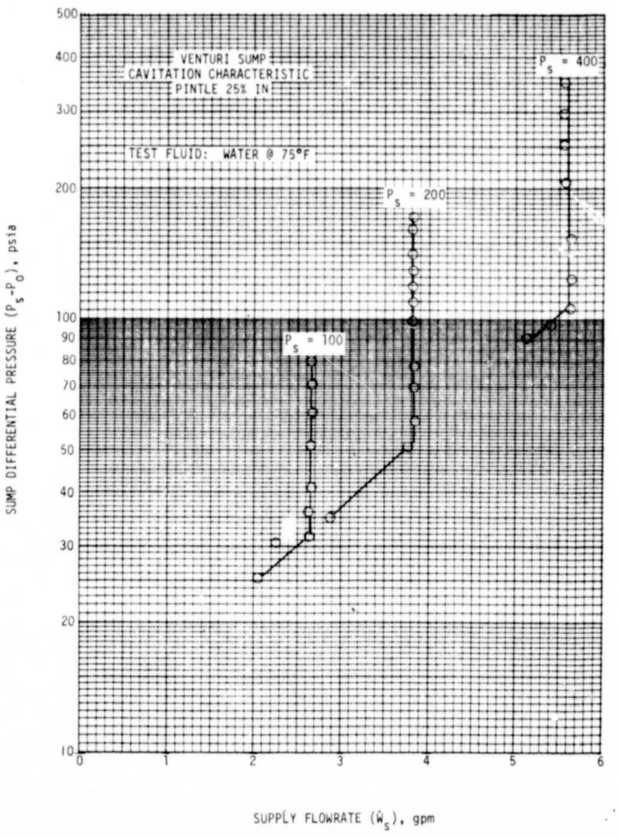


Figure 3-17

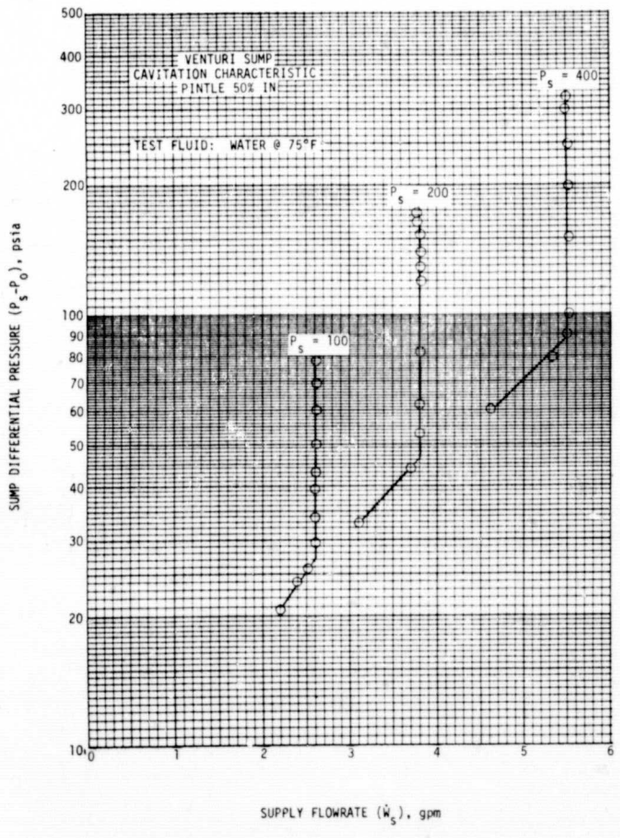


Figure 3-18

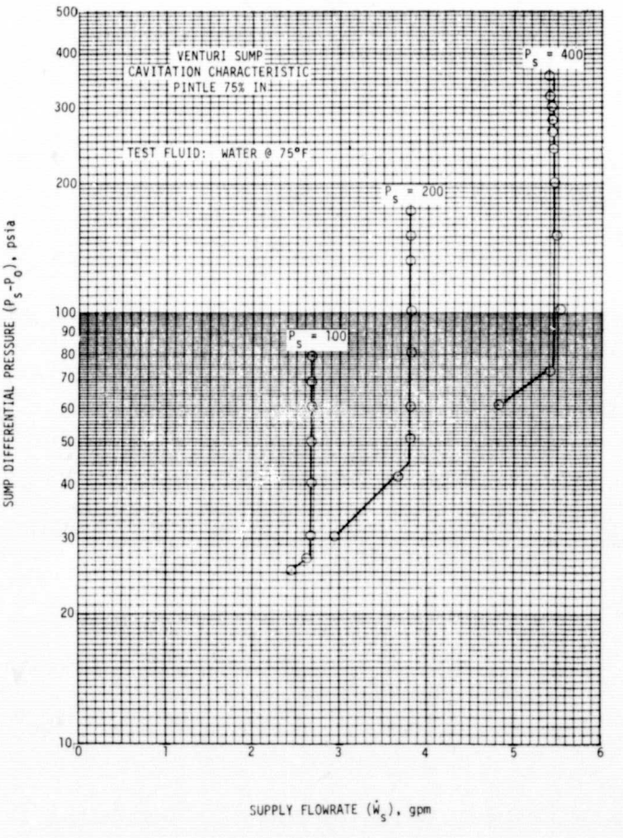


Figure 3-19

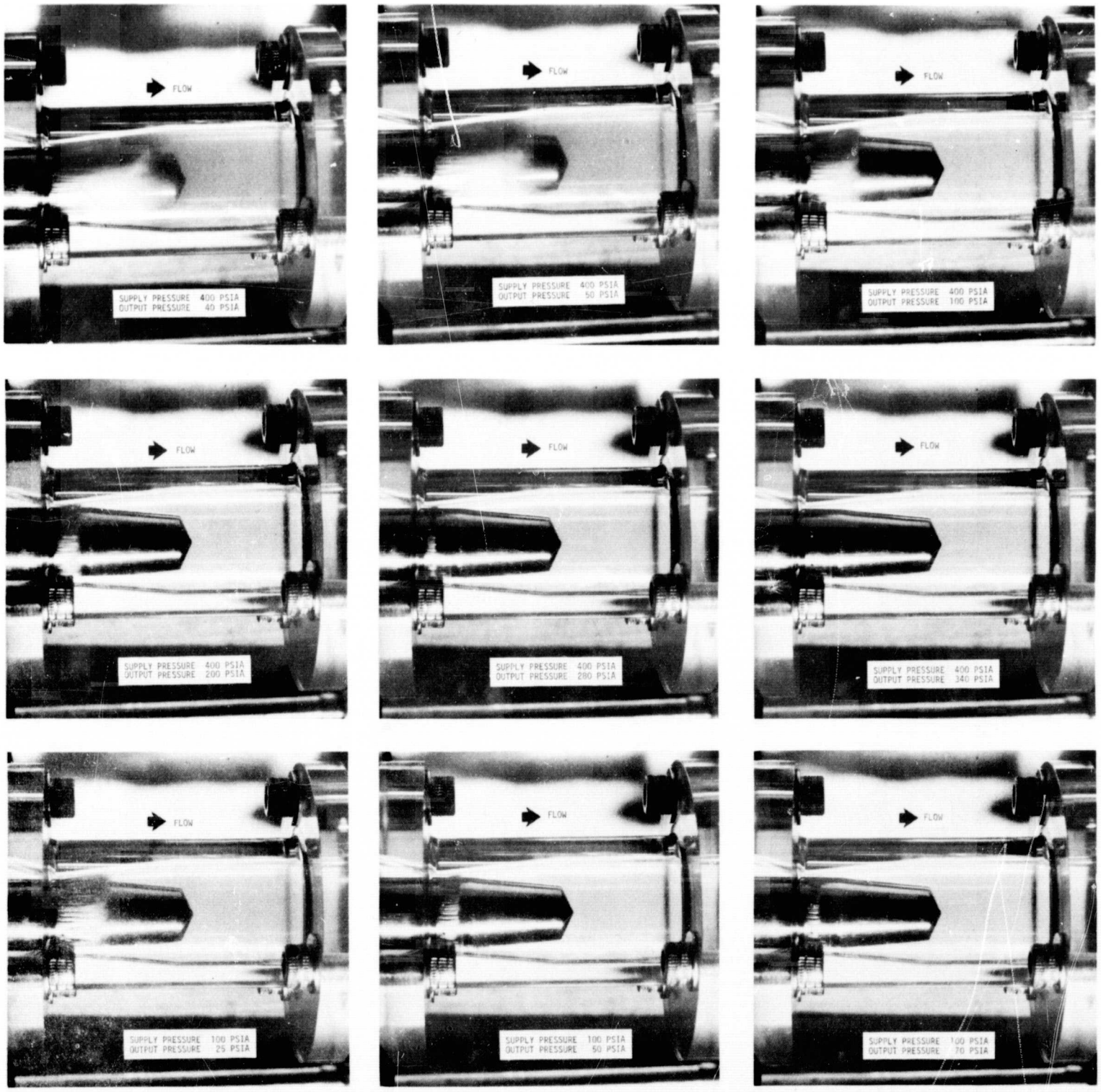


Figure 3-20. Venturi Sump in Cavitation (with Water @ 75°F)

Measurements were also made of the cavitation bubble pressure, by utilizing the return orifices as a pressure tap. It was noted that the measured cavitation bubble pressure was constant over a wide range of back pressures as long as the return orifices were covered by the cavitation bubble.

3.4.2 Return Flow Capability

Prior to determining the return flow capability of the venturi sump, the return orifices were calibrated with both water and gaseous nitrogen (Figures 3-21 and 3-22). Since it wasn't possible to measure the cavitation bubble pressure while the return supply was flowing, the return flow capability of the venturi sump with water supply and return flows was judged on the basis of how well the return flow in cavitation compared to the return orifice flow calibration. That is, if the test points fell on the return orifice flow calibration line, the return flow did not change the cavitation bubble pressure (presuming the bubble pressure was near zero psia).

The return flow capability of the venturi sump when in cavitation is shown in Figures 3-23 through 3-26. It can be seen that the best fits relative to the return orifice flow calibration occur with the pintle 37-1/2 percent in and 50 percent in. Excellent return flow capability at constant pressure was exhibited at the 37-1/2 percent in pintle position (15 percent with a 100 psia supply) and the 50 percent in pintle position (13.5 percent with a 100 psia supply and 9.5 percent with a 200 psia supply). These results also occurred over a wide range of back pressure. With the pintle 25 percent in (minimum area point), the return flow sees a higher pressure because the cavitation bubble forms further downstream. With the pintle 75 percent in and particularly 100 percent in, the return orifices are too far downstream so that the cavitation bubble only covers the orifices when the sump is in deep cavitation. The venturi sump in cavitation with the pintle 37-1/2 percent in and for various percentages of return flow and at several supply pressures and output pressure levels is shown in Figures 3-27 through 3-30.

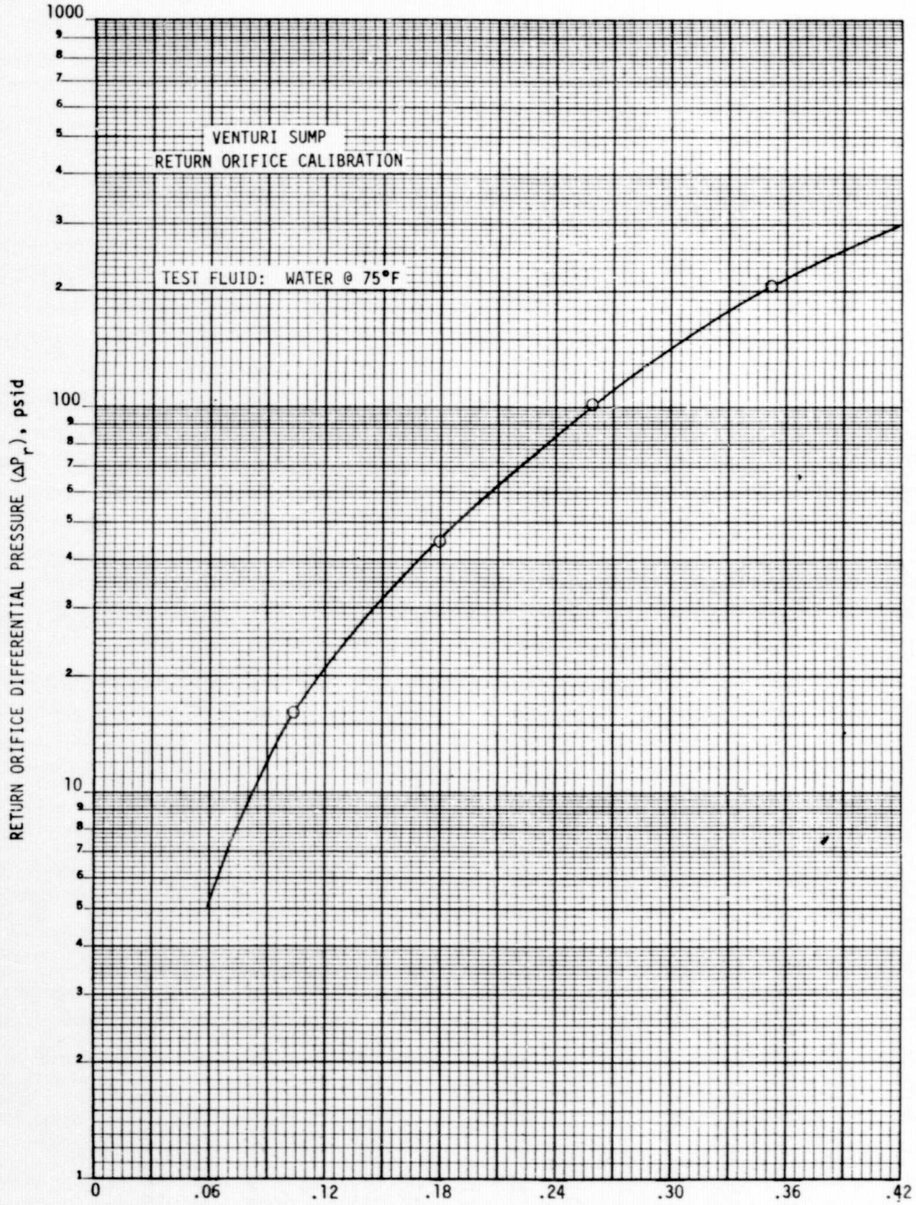


Figure 3-21

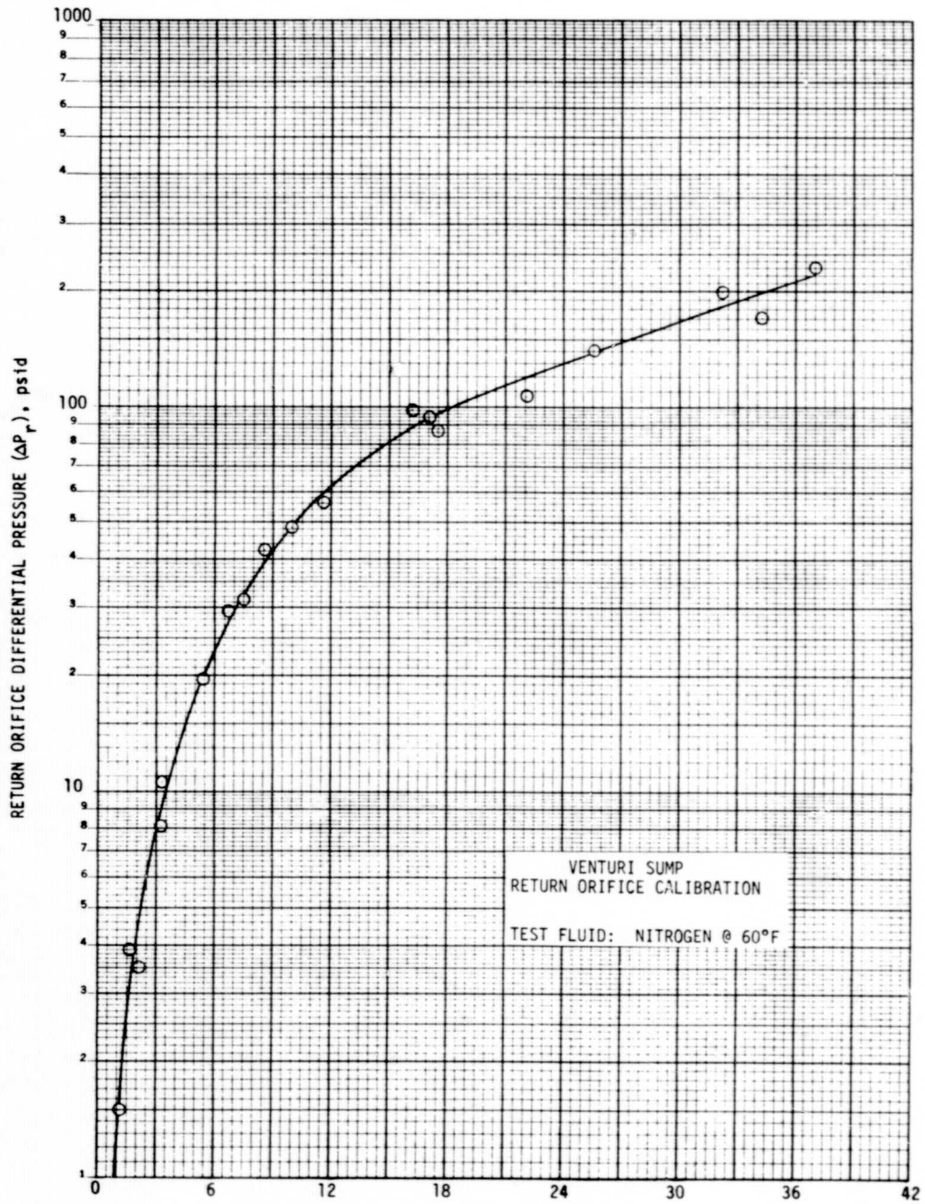


Figure 3-22

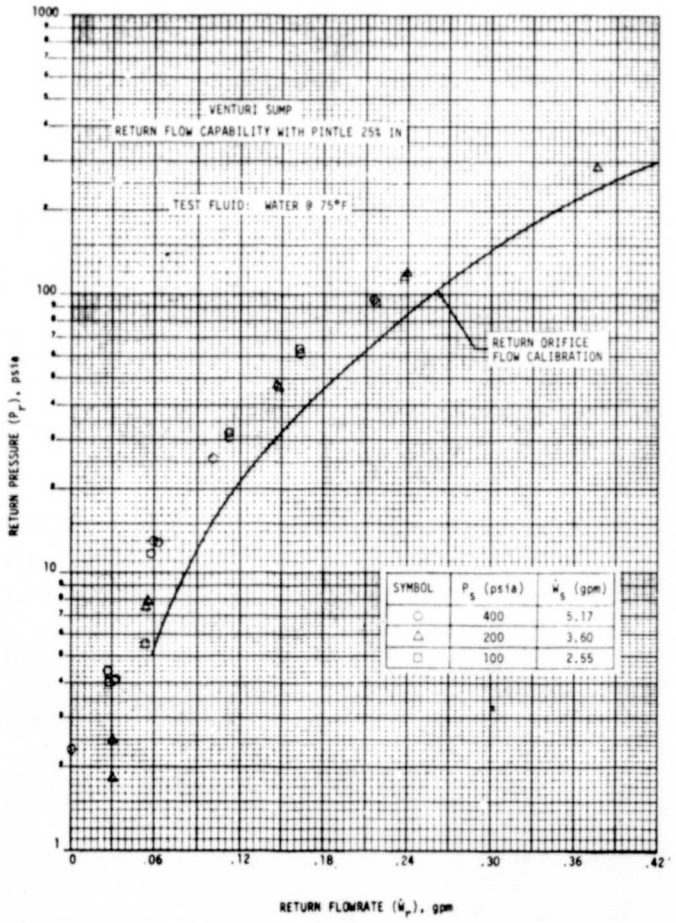


Figure 3-23

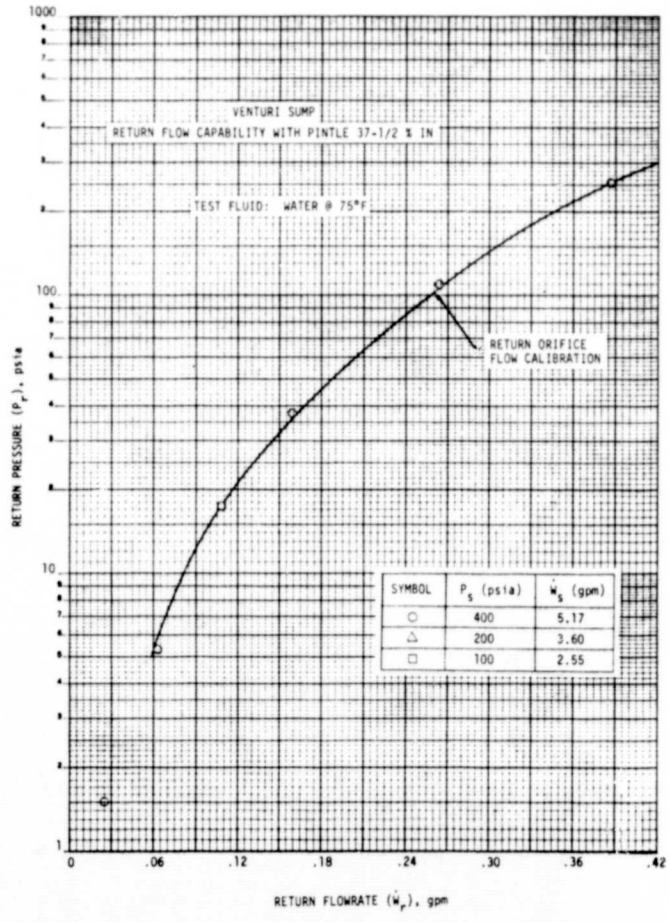


Figure 3-24

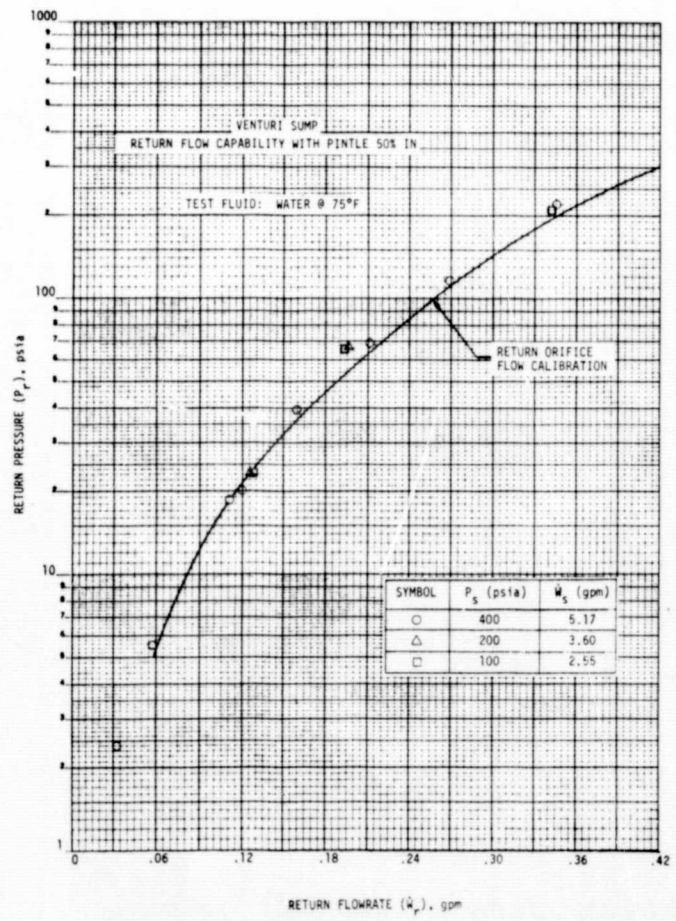


Figure 3-25

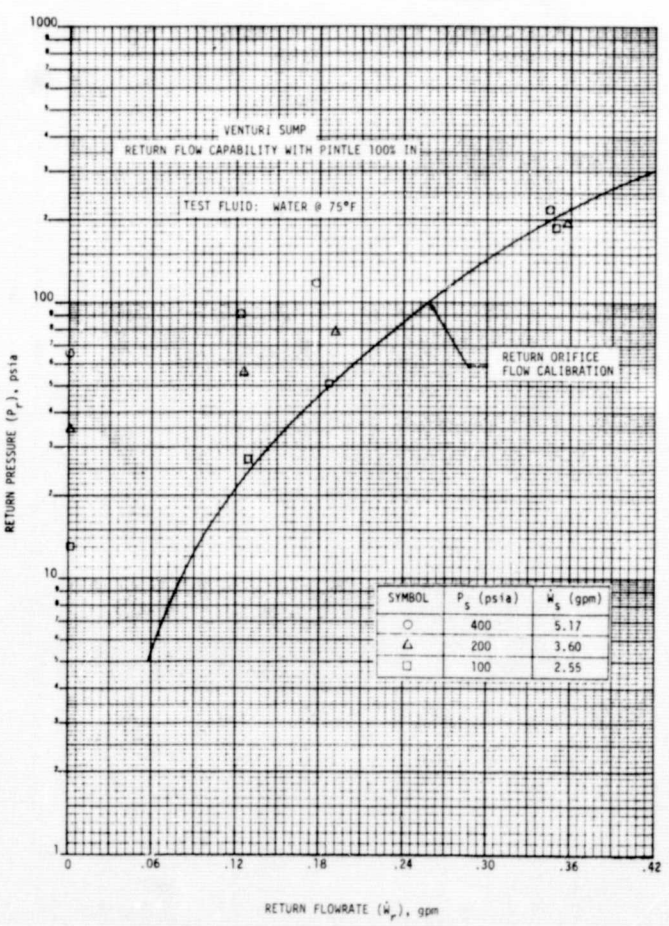
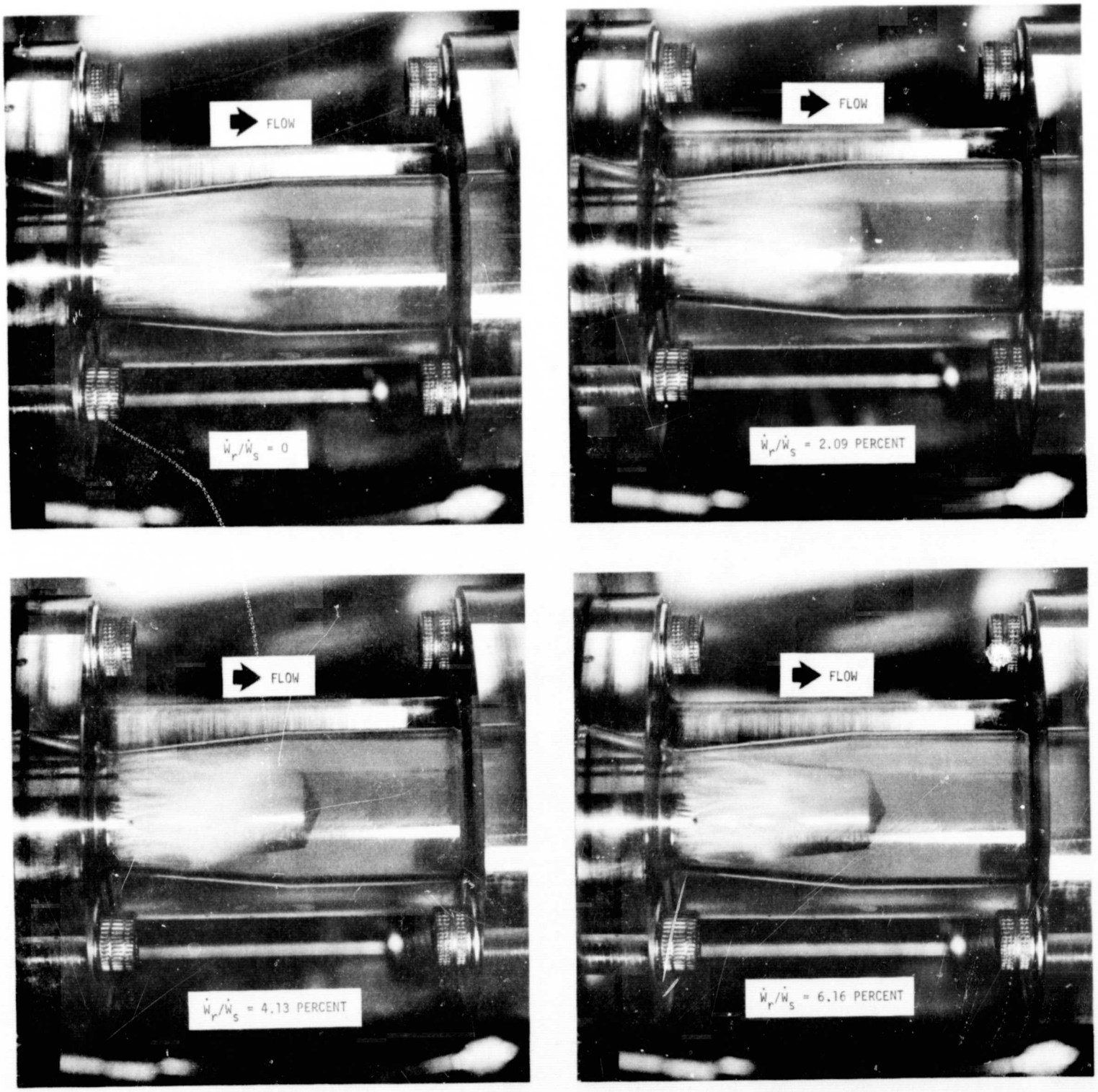
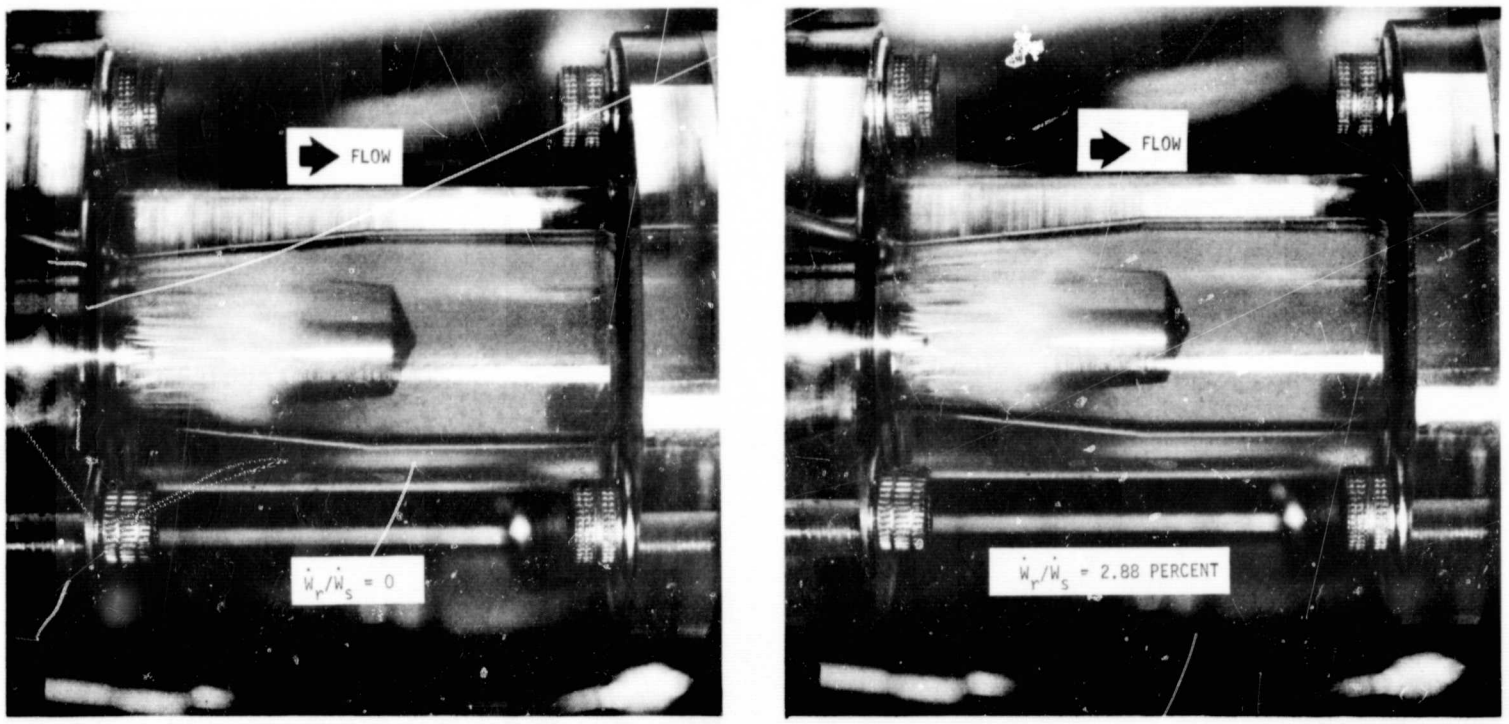


Figure 3-26



SUPPLY AND RETURN FLUID WATER @ 75°F

Figure 3-27. Return Flow in Venturi Sump (Pintle 37-1/2% In, Supply 400 psia 5 gpm, P_o/P_s = 0.2)



SUPPLY AND RETURN FLUID WATER @ 75°F

Figure 3-28. Return Flow in Venturi Sump (Pintle 37-1/2% in, Supply 200 psia 3.47 gpm, P_o/P_s = 0.132)

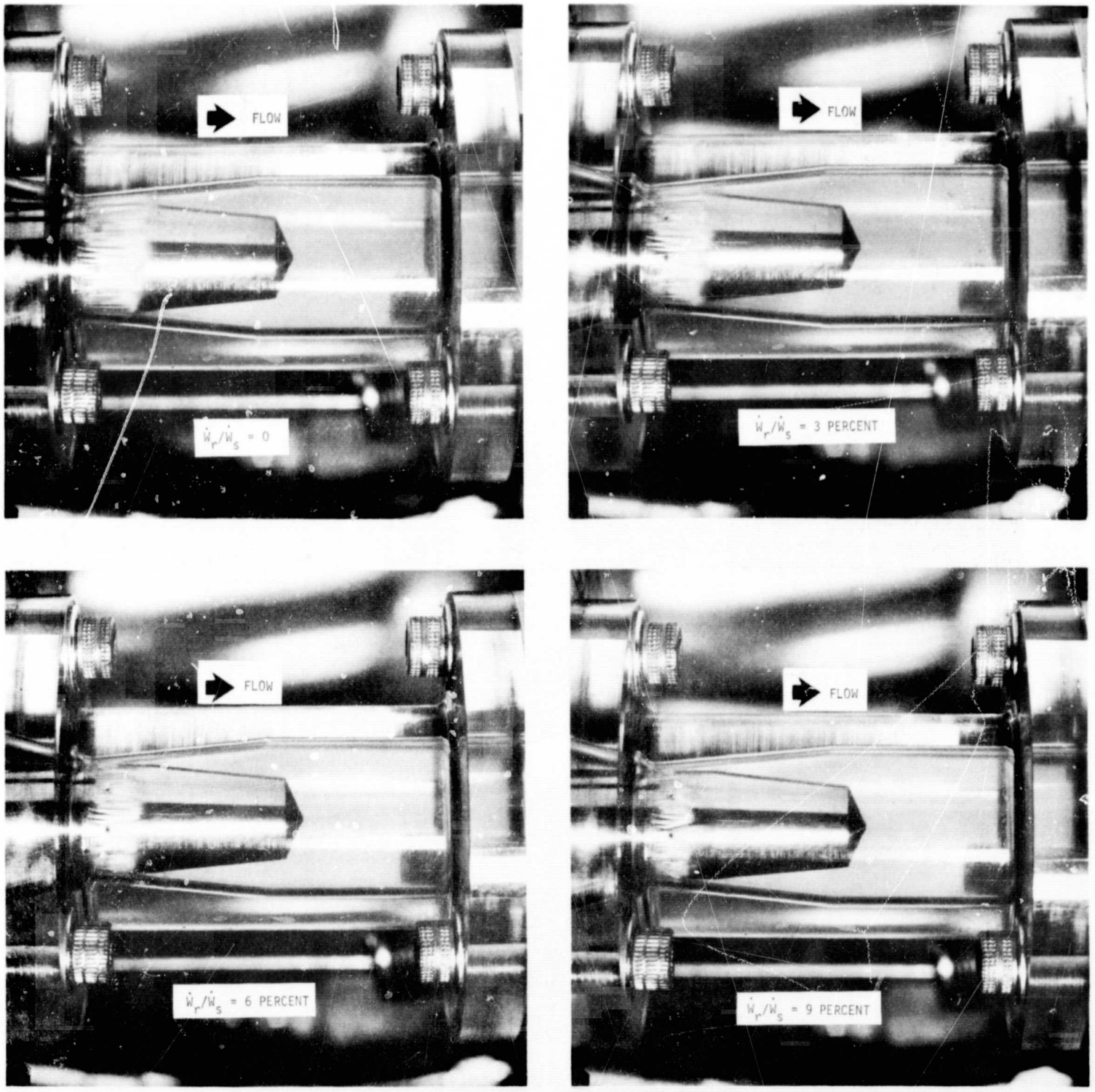
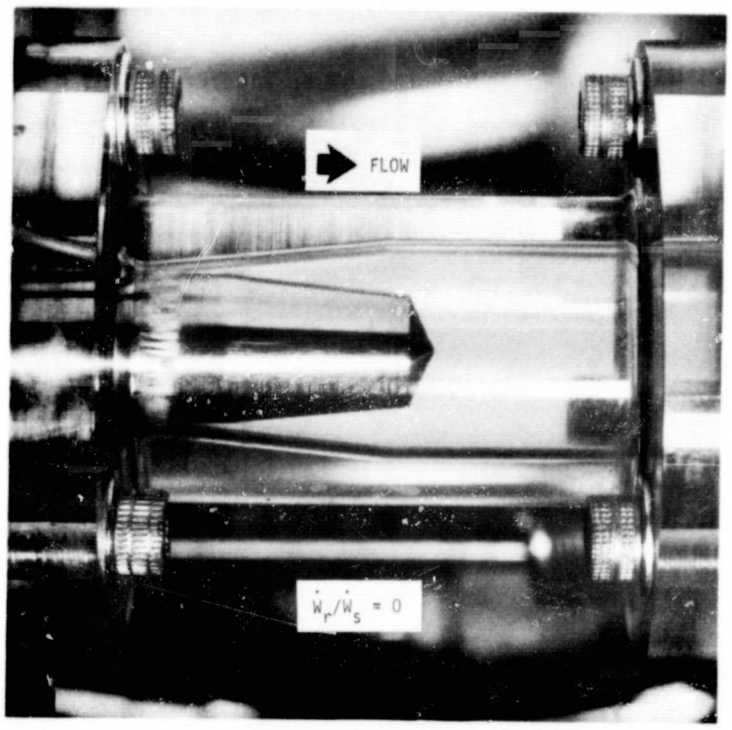
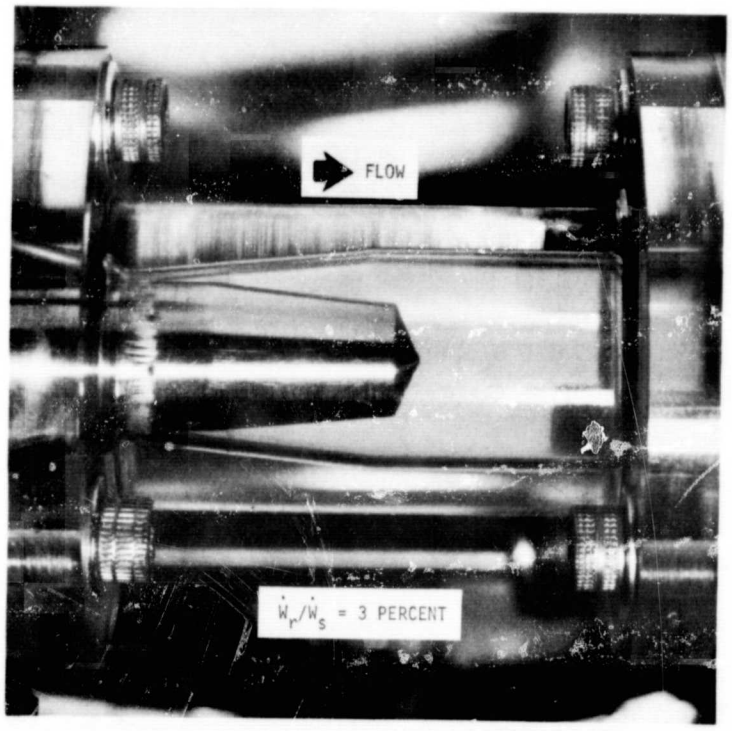
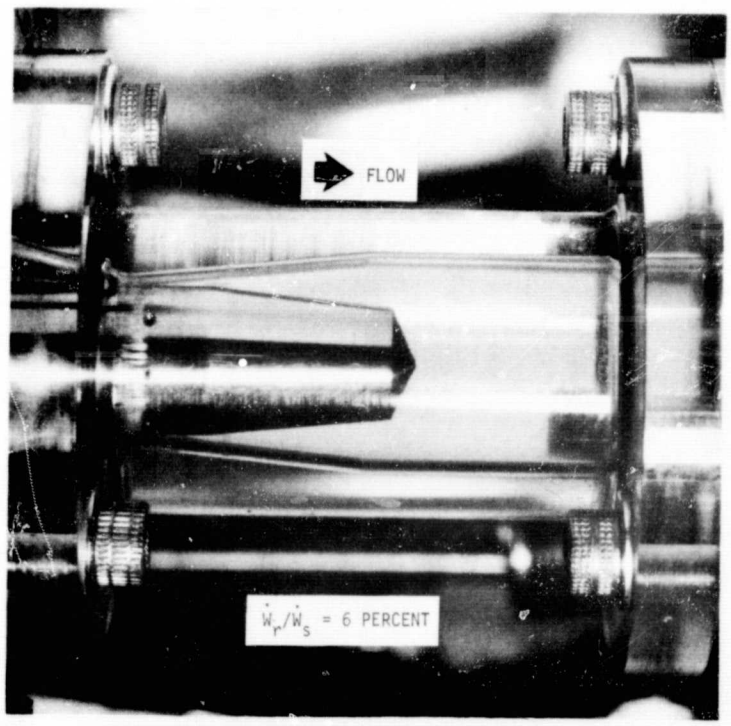
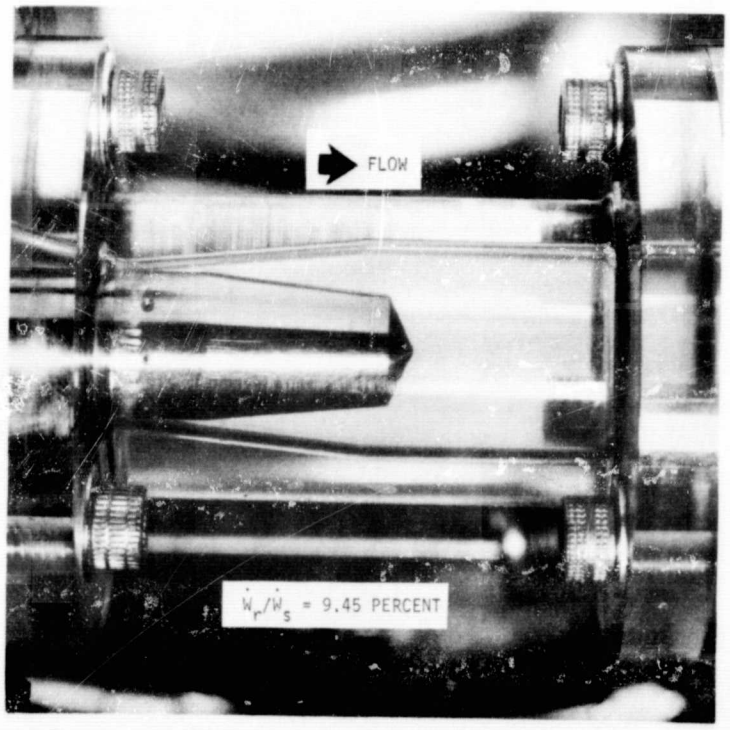


Figure 3-29. Return Flow in Venturi Sump (Pintle 37-1/2% in, Supply 200 psia 3.47 gpm, P_o/P_s = 0.25)









SUPPLY AND RETURN FLUID WATER @ 75°F

Figure 3-30. Return Flow in Venturi Sump (Pintle 37-1/2% in, Supply 200 psia 3.47 gpm, P_o/P_s = 0.5)

The current data does not reflect the ultimate return flow capability of the venturi sump, since the test return flows were limited by the available facility pressures. However, the initial testing did serve to prove out the venturi sump, which performed much better than anticipated. The optimum axial position for the return flow orifices was also located. In addition, visual observations of the cavitation region has indicated a possible improvement of the sump by returning fluid flow through an annular slit rather than the eight equally spaced orifices.

3.4.3 Water Return Throttling Capability

The throttling characteristic of the venturi sump was also investigated utilizing a water supply of 100 psia and water to throttle through the return supply at several pintle positions and back pressures. The data taken at pintle positions of 12-1/2 percent in and 25 percent in are representative (Figures 3-31 and 3-32) in that throttling gain was considerably less than 1 and excessive fluid power is required to perform liquid-liquid throttling in the present configuration.

3.4.4 Gas Return Throttling Capability

Additional testing was also performed to determine the throttling capability of the venturi sump utilizing a water supply and nitrogen to throttle through the return supply. The throttling characteristic was investigated with a 100 psia supply at three pintle positions (full out, 12-1/2 percent in, and 25 percent in - minimum area) and at three back pressures, i.e., P_o/P_s = 0.2, 0.5 and 0.8 (see Figures 3-33, 3-34 and 3-35).

Maximum throttling occurred with the pintle in the full out position (i.e., with the return orifices 1/8 inch upstream of the throat) and throttling improved as the back was increased. An important characteristic noted was that throttling of the initial 25 percent of the supply flow was accomplished with a gain of about 8, i.e., the water flow was throttled 8 times more than would be expected by the gas expansion alone. Initially, the supply flow at 100 psia was throttled 25 percent by a gas flowrate of 0.1 percent by weight, and 75 percent by a gas flowrate of 1 percent by weight. A comparison of the throttling characteristic at supply pressures

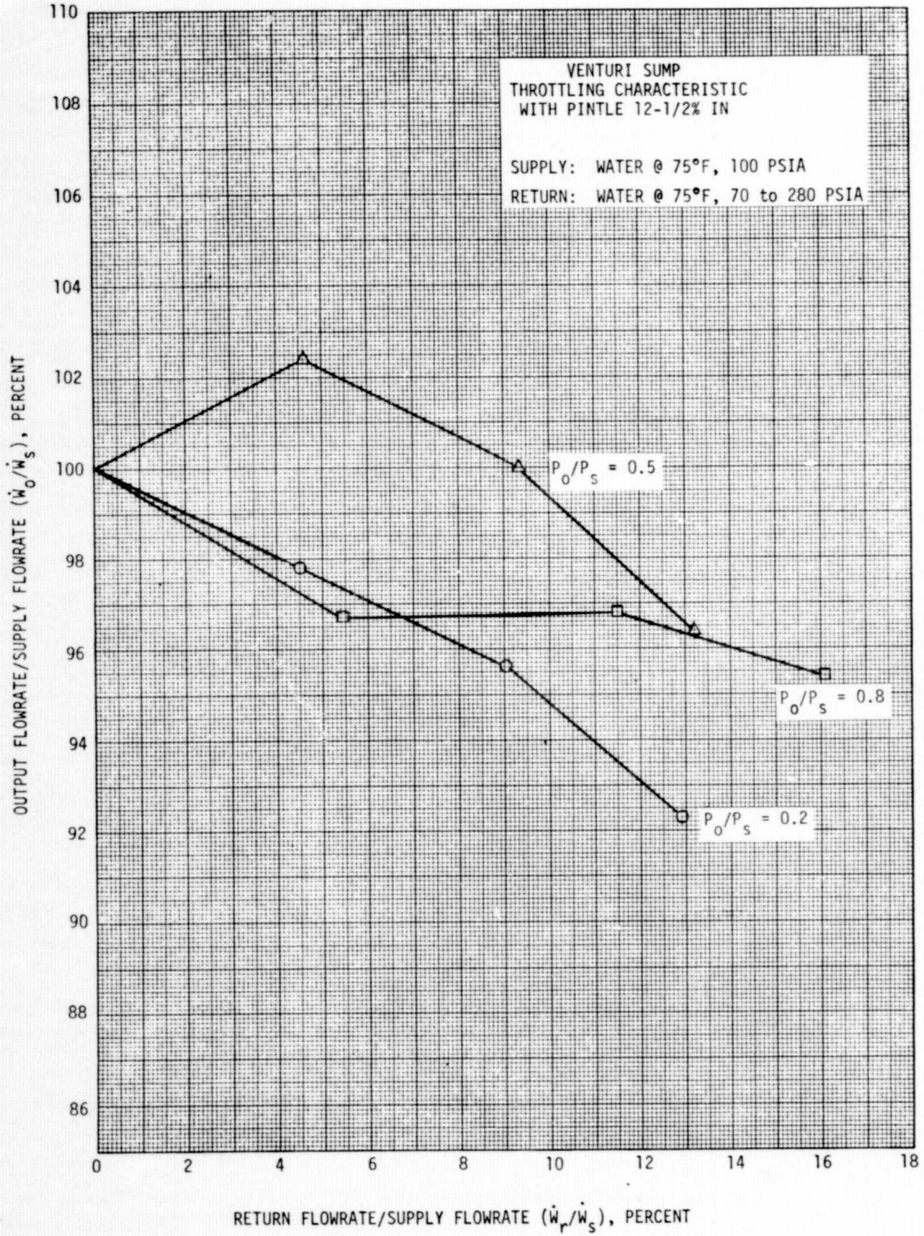


Figure 3-31

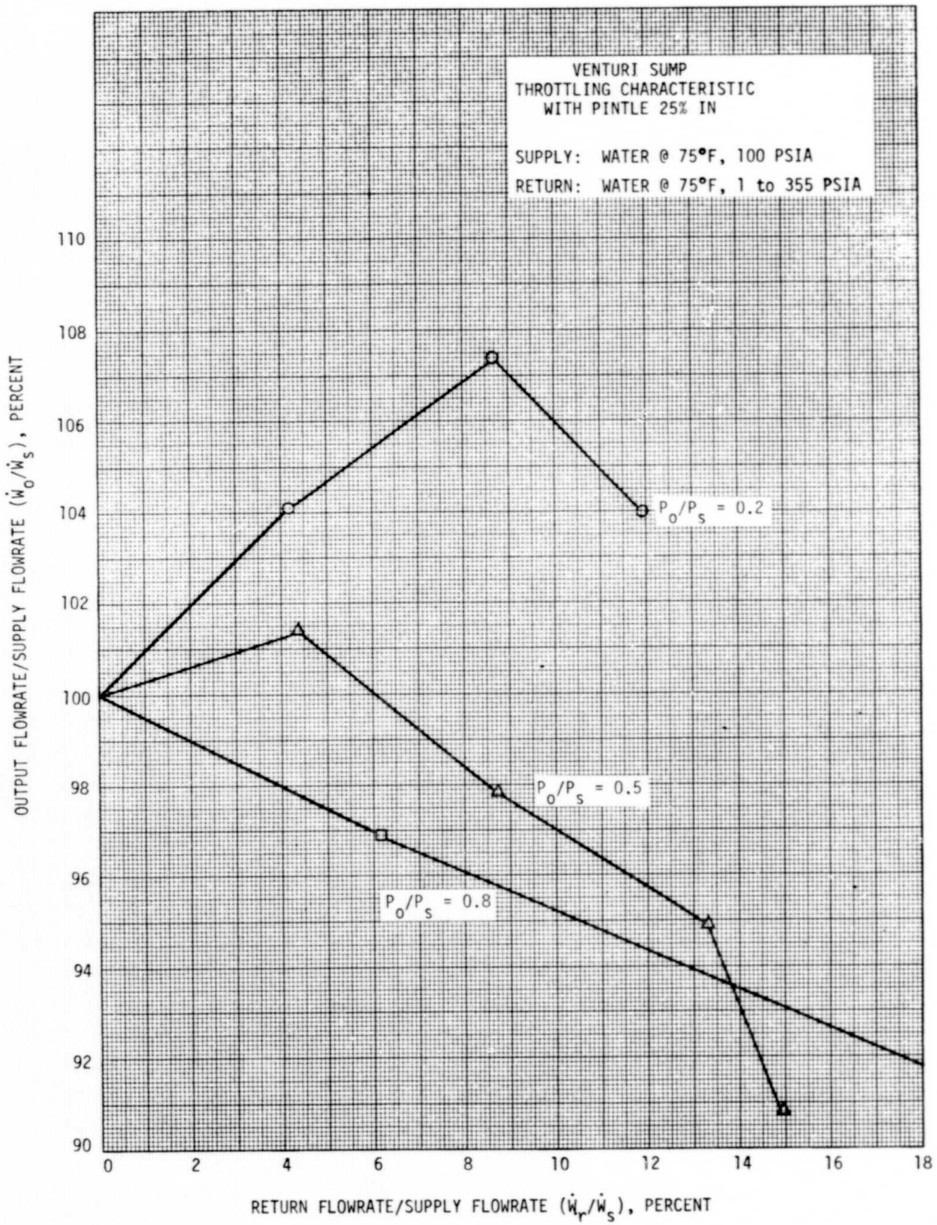


Figure 3-32

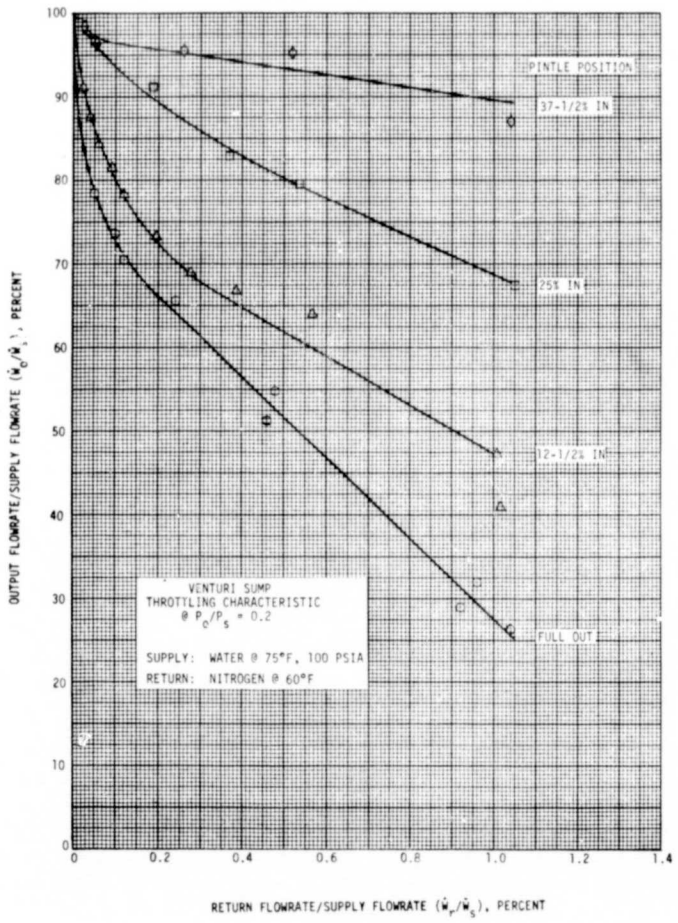


Figure 3-33

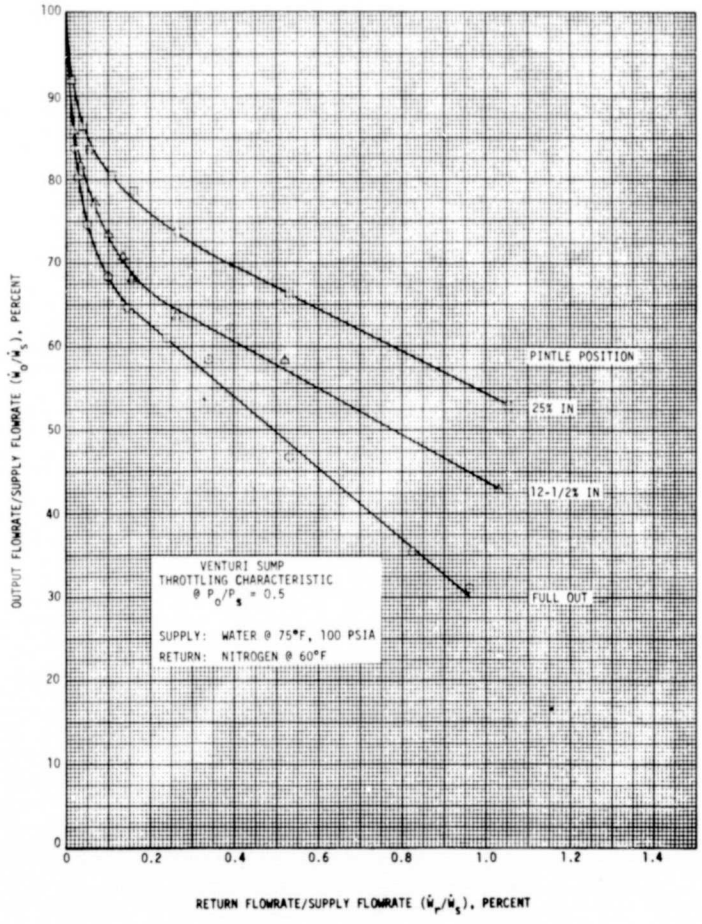


Figure 3-34

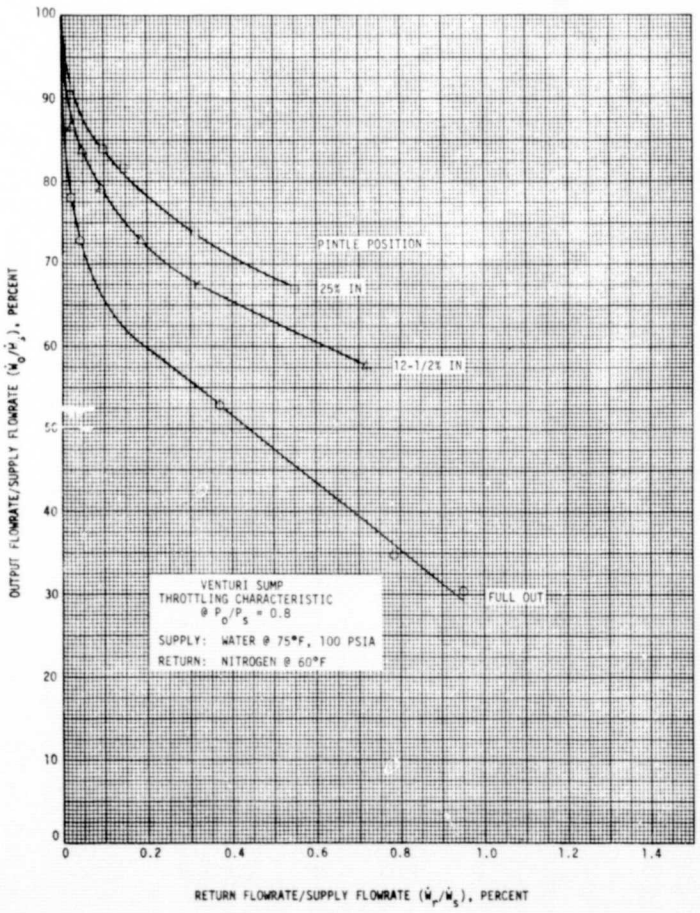


Figure 3-35

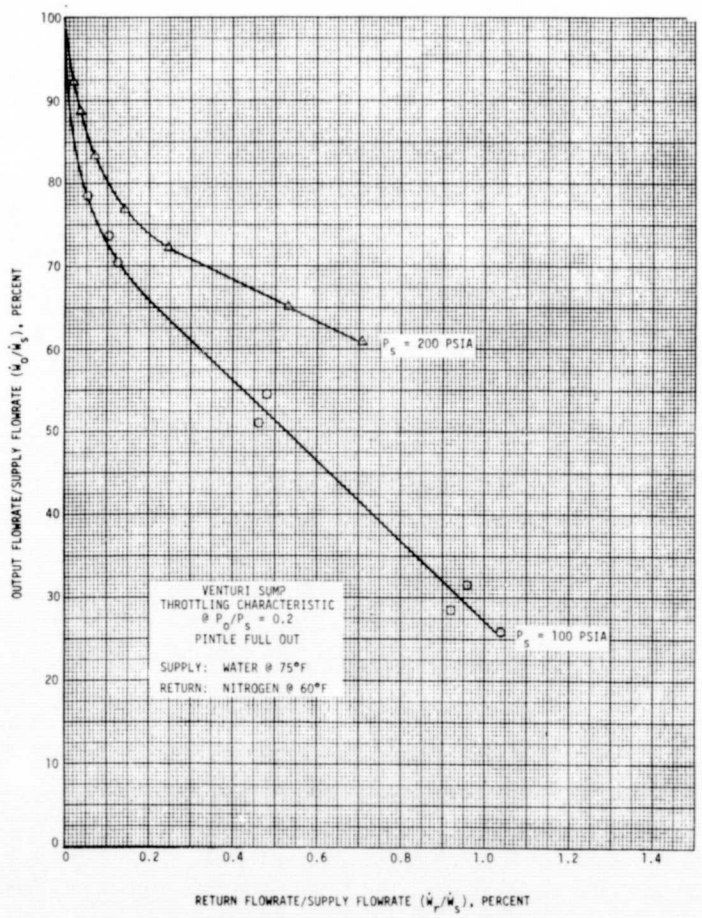


Figure 3-36

of 100 and 200 psia are given in Figure 3-36. It should be noted that the throttling gains at 200 psia are roughly half of those at 100 psia.

The turbulence introduced by the addition through the return of varying flow rates of nitrogen into the water supply of the venturi sump is shown in Figures 3-37 and 3-38. These photographs were taken with the water supply at 100 psia and a back pressure of 20 psia with the pintle at the full out and 12-1/2 percent in positions. Gas to water ratios of 0.016 percent by weight produced a high degree of turbulence and thorough mixing of the main stream. An annular return orifice should also provide a vast improvement in the performance of the venturi sump as a gas-liquid throttle.

3.4.5 Venturi Sump Applications

Important possible applications of the venturi sump include:

1. Constant pressure reference for space systems
2. Nonoverboard vent for fluidic systems
3. Fluidic propulsion controls - regulators, throttles, mixture ratio, SITVC
4. The combination and metering of reacting and nonreacting fluids in the chemical and food processing industries.

3.5 REFERENCES

1. "Advanced Valve Technology," Interim Report No. 06641-6014-R000, Contract NAS 7-436, November 1967.
2. "Advanced Valve Technology," Final Report No. 06641-6023-R000, Volume II, Nonmechanical Controls, Contract NAS 7-436, January 1969.

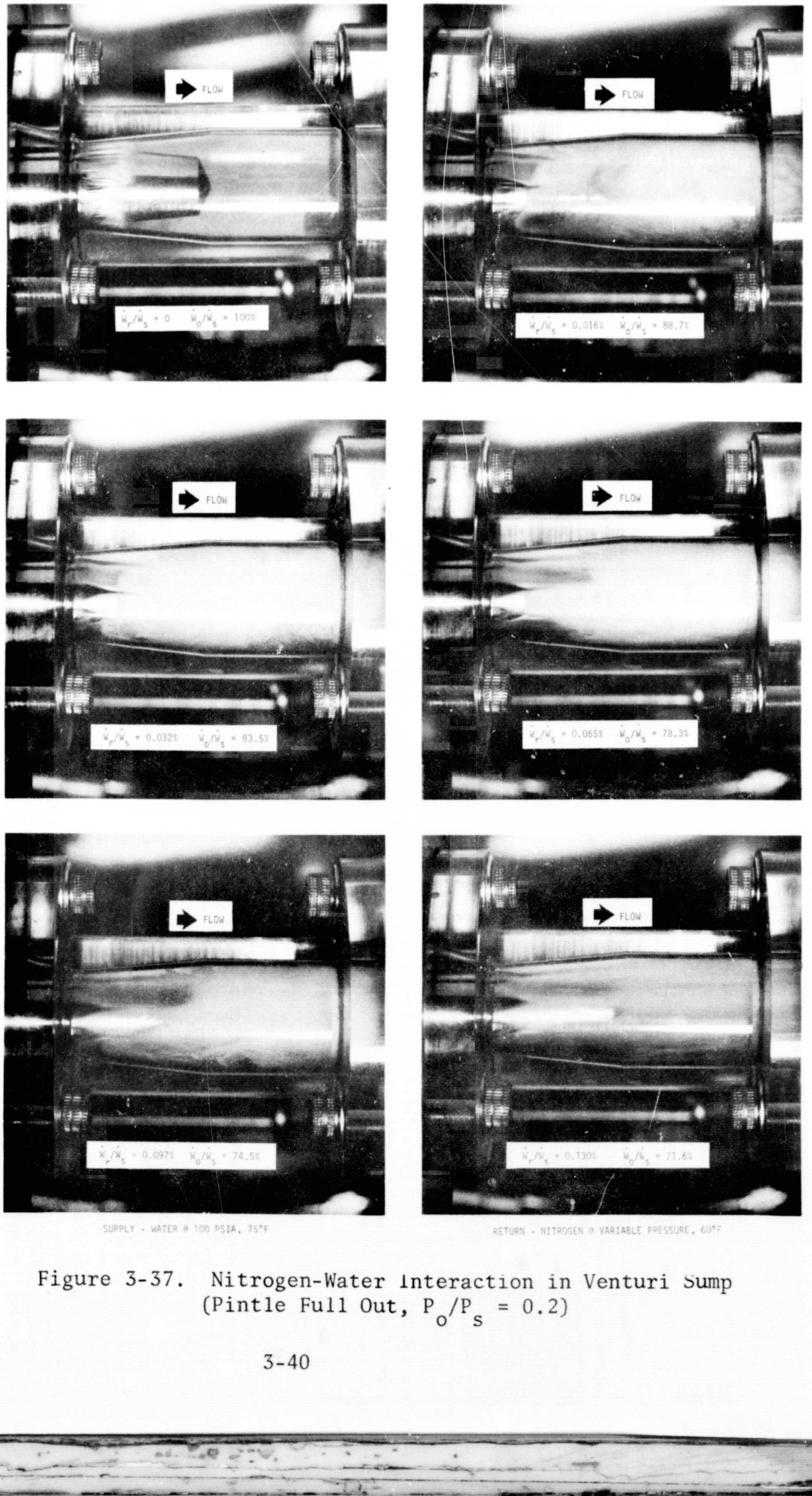


Figure 3-37. Nitrogen-Water Interaction in Venturi Sump (Pintle Full Out, P_o/P_s = 0.2)

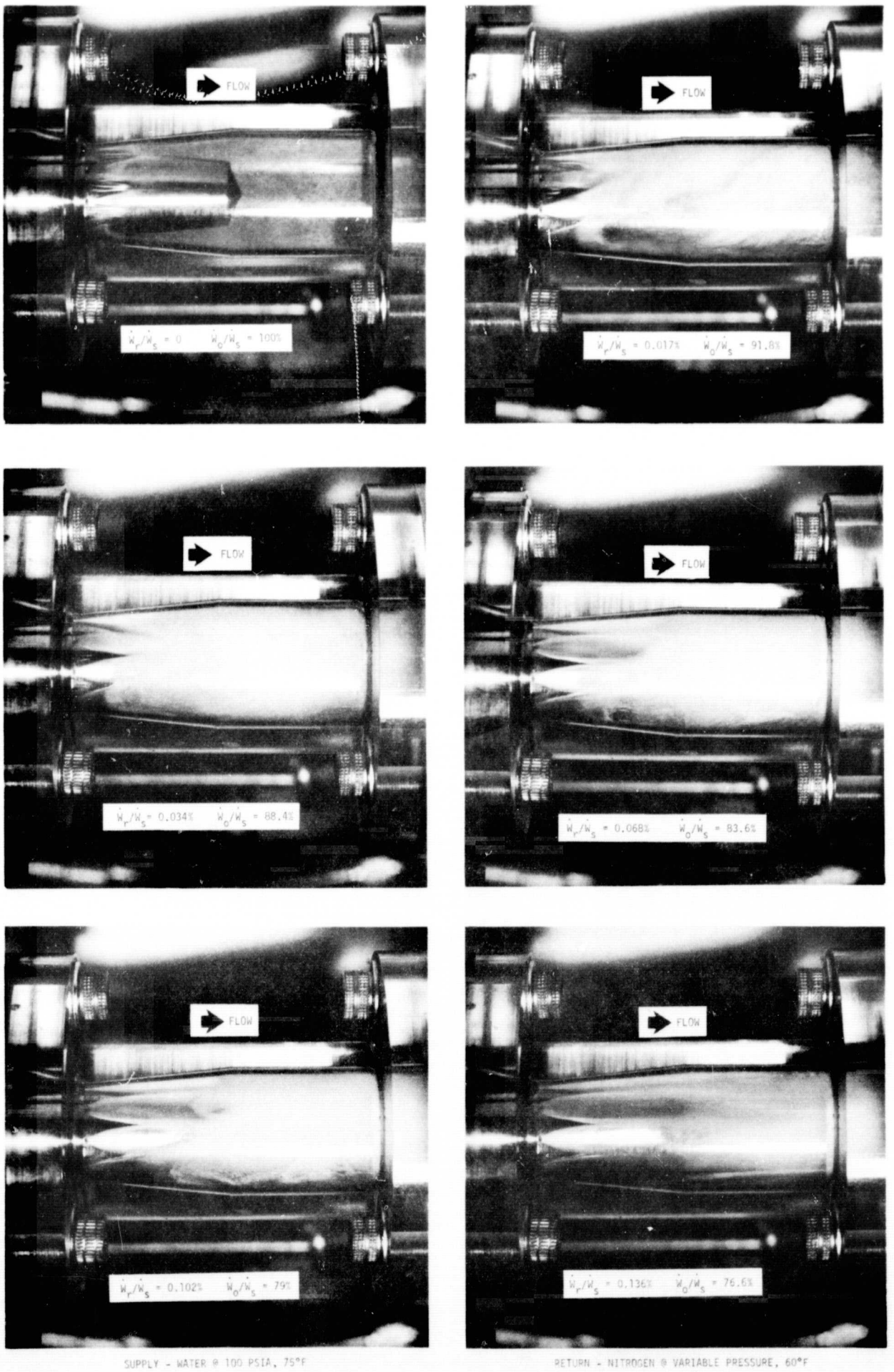


Figure 3-38. Nitrogen-Water Interaction in Venturi Sump (Pintle 12-1/2% in, P_o/P_s = 0.2)

4.0 TECHNOLOGY SUPPORT

The objective of this task was to provide technology necessary to support the development of mechanical and nonmechanical controls. The specific areas of technology support included propellant compatibility, seal, and leakage technology. The propellant compatibility efforts are reported under Volume I of the Valve Compilation Report.

4.1 ENERGIZED SEALS

The objective of this work was to determine the bulk modulus of the polymers and determine their effects under high compressive forces. It is believed that zero leakage can be effected with Teflon utilizing high compressive forces with the use of high force actuators. In addition, this method takes advantage of the energy output of the actuator, that is, the stroke times force, as in most cases only the end force of the actuator is used in sealing. Section 2.0 describes a seal concept using this approach.

The materials investigated were:

- TFE Teflon
- Nitro Rubber, Parker Spec. No. N219-7

4.1.1 General

Those materials which have the highest structural symmetry are those which have the lowest structural order. When the distances and directions from one atom to another are randomly distributed on a microscopic scale, then on a macroscopic scale the material will seem to possess spherical symmetry (isotopic) and its properties will not vary with direction. Amorphous materials such as rubber, wood, plastics (polymers), have varying degrees of structural order, but the degree of disorder arises from the fact that molecules in polymeric systems have very high molecular weight and are composed of basic units which are repeated at more or less regular intervals. These basic units may assume wide varieties of different shapes. Because different molecules may become entangled with one another (spagetti-like structure), they will not be able to crystallize completely from the solution. All polymers have varying amounts of elasticity and plasticity

which is a function of the factors such as molecular structure and density. When a high hydrostatic pressure is applied, in time the material deforms primarily due to the fact that the molecular distances are shortened.

The elastic behavior of an isotopic material is completely defined by two independent elastic constants. The rubbers and Teflon are generally isotopic in the unstretched state and can be considered to have two independent elastic constants. All four elastic constants of isotopic material are related by the following equation:

$$E = 3\beta(1-2\mu) = 2(1+\mu)\,G$$

where: E = Modulus of elasticity
G = Shear modulus
β = Bulk modulus
μ = Poisson's ratio

The computed values of bulk modulus for Teflon and rubber are listed in Table 4-1.

Table 4-1. Computed β of Teflon and Rubber (Ref. 1 and 2)

	E	μ	β
Rubber, Soft	150 psi	0.5	High
Rubber, Hard	500 psi	0.4999	5×10^5
Teflon, TFE	50,000 psi	0.46	2.07×10^5 psi
Teflon, FEP	50,000 psi	0.48	4.14×10^5 psi

In regards to Table 4-1, note the following:

- As μ approaches 0.5, β approaches infinity.
- The values of β computed are at very low hydrostatic pressure. At high stress levels, both E and β increase (Ref. 3).
- For Teflon, β reduces with time since E reduces with time (cold flow effect).

and E as a function of time are listed below:

Time	E	βTFE at 73°F
0	66,700	275,000 psi
200 hours	50,000	207,000 psi
1 year	40,000	156,000 psi

The range of Poisson's Ratio for crystalline and rubbery materials is given in Table 4-2.

Table 4-2. Range of Poisson's Ratio for Crystalline and Rubbery Materials

μ	E/β	G/β	E/G	Remarks
0.20	1.8	0.75	2.4	Range for crystalline
0.25	1.5	0.60	2.5	materials and glasses
0.30	1.2	0.463	2.6	
0.33	1.0	0.375	2.666	
0.4	0.6	0.214	2.8	
0.4996	0.0024	0.008	2.9992	Range for rubbery materials
0.4997	0.0018	0.0006	2.9994	
0.4998	0.0012	0.0004	2.9996	
0.49995	0.0006	0.0002	2.9998	
0.49995	0.0003	0.0001	2.9999	
0.50	0.000	0.000	3.00	

Stress Distribution in Rubbery Materials

Consider a cylinder of constant volume containing such a material and a piston compressing it. The strain in x, y and z directions are:

$$\varepsilon_x = \frac{1}{E} \left[\sigma_x - \mu\sigma_y - \mu\sigma_z\right] \quad (1)$$

$$0 = \frac{1}{E} \left[\sigma_y - \mu\sigma_x - \mu\sigma_z\right] \quad (2)$$

$$0 = \frac{1}{E} \left[\sigma_z - \mu\sigma_x - \mu\sigma_y\right] \quad (3)$$

Subtract (2) from (3)

$$\sigma_y - \sigma_z - \mu\sigma_z + \mu\sigma_y = 0$$

$$\therefore \boxed{\sigma_y = \sigma_z} \tag{4}$$

Rearrange (2) $$\sigma_z = \frac{\sigma_y}{\mu} - \sigma_x \tag{5}$$

From (3) and (5)

$$\frac{\sigma_y}{\mu} - \sigma_x = \mu\sigma_x + \mu\sigma_y$$

$$\sigma_y - \mu\sigma_x = \mu^2\sigma_x + \mu^2\sigma_y$$

$$\sigma_y = \frac{\mu(1+\mu)\sigma_x}{1 - \mu^2}$$

$$\sigma_y = \sigma_x \frac{\mu}{(1-\mu)} \tag{6}$$

For rubbery materials (Table 4-1):

$\mu \cong 0.5$ which gives

$$\boxed{\sigma_y = \sigma_x = \sigma_z}$$

4.1.2 Teflon Evaluation

The results of several tests to determine the compressibility of Teflon TFE are reported in Table 4-3. Bulk modulus values ranged from 16×10^6 psi to 23×10^4 psi at hydrostatic pressures of 8.750 psi to 1,460 psi.

The test was performed using a piston and cylinder (filled with Teflon) configuration as shown in Figure 4-1. Deflection curves as a function of hydrostatic pressure are given in Figure 4-2 and 4-3 for Teflon. The

Table 4-3. Compressibility Data for Teflon TFE

Steps	Cycles	Cylinder Press P_c psi	Hydrostatic Press. psi PH = 73 P_c	Total Deflection X Mils	Differential Deflection ΔX Mils	$\frac{\Delta P}{\Delta X}$	$\beta = 36.5 \frac{\Delta P}{\Delta X}$
1	1	120	8750	9.31	9.30		
2		100	7300	9.27	0.045	440×10^3	160×10^5
3		80	5850	8.91	0.36	56.0	20.5
4		60	4380	8.09	0.82	24.5	9.0
5		40	2920	6.36	1.73	11.6	4.2
6		20	1460	4.12	2.24	9.0	3.3
7		0	0	1.16	2.96	6.8	2.5
8	2	20	1460	1.34	0.18		
9		40	2920	2.51	1.17	17.0	6.2
10		60	4380	4.04	1.53	13.0	4.75
11		80	5850	5.71	1.67	12.0	4.4
12		100	7300	7.61	1.9	10.5	3.85
13		120	8750	9.37	1.76	11.3	4.14
14		100	7300	9.28	0.09	220.0	81.0
15		80	5850	8.88	0.40	50.0	18.3
16		60	4300	7.98	0.90	22.0	8.1
17		40	2920	6.45	1.53	13.0	4.75
18		20	1460	4.30	2.15	9.3	3.4
19	3	0	0	1.4	2.89	6.9	2.55
20		20	1460	1.62	0.22	91.0	33.0
21		40	2920	2.79	1.17	17.0	6.2
22		80	5850	5.99	3.2	12.5	4.6
23		100	7300	7.88	1.89	11.4	4.16
24		120	8750	9.77	1.89	10.5	3.65
25		140	10,200	11.75	1.98	10.0	3.65
26		120	8750	11.64	0.09	220.0	81.0
27		100	7300	11.21	0.45	44.5	16.3
28		80	5850	10.58	0.63	31.5	11.5
29		60	4300	9.54	1.04	19.2	7.0
30		40	2920	7.74	1.80	11.1	4.05
31		20	1460	5.24	2.15	9.7	3.55
32		0	0	2.09	3.15	6.4	2.35

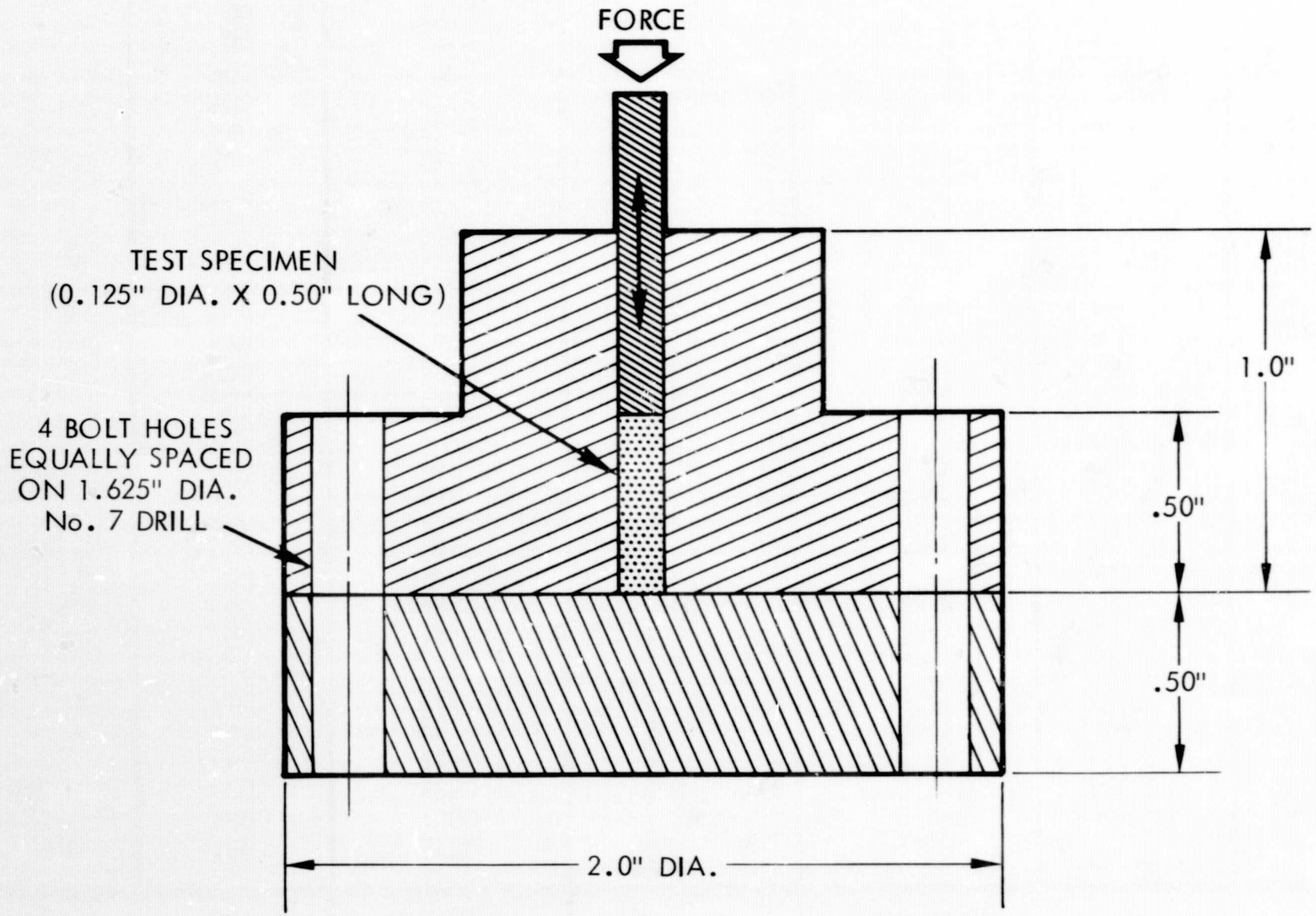


Figure 4-1. Test Fixture for Cylindrical Sample

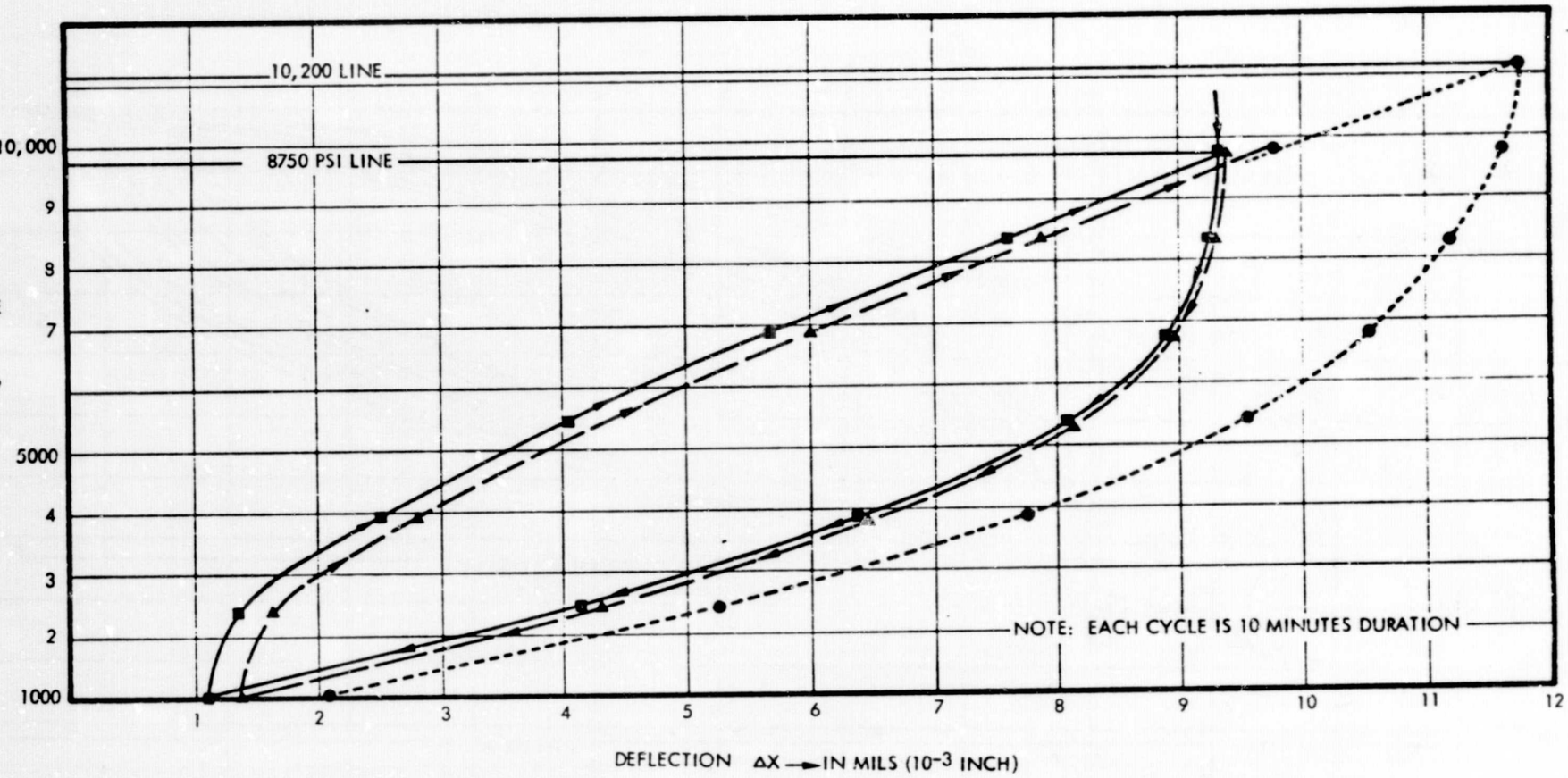


Figure 4-2. Pressure Vs. Deflection Curves for Teflon (TFE)

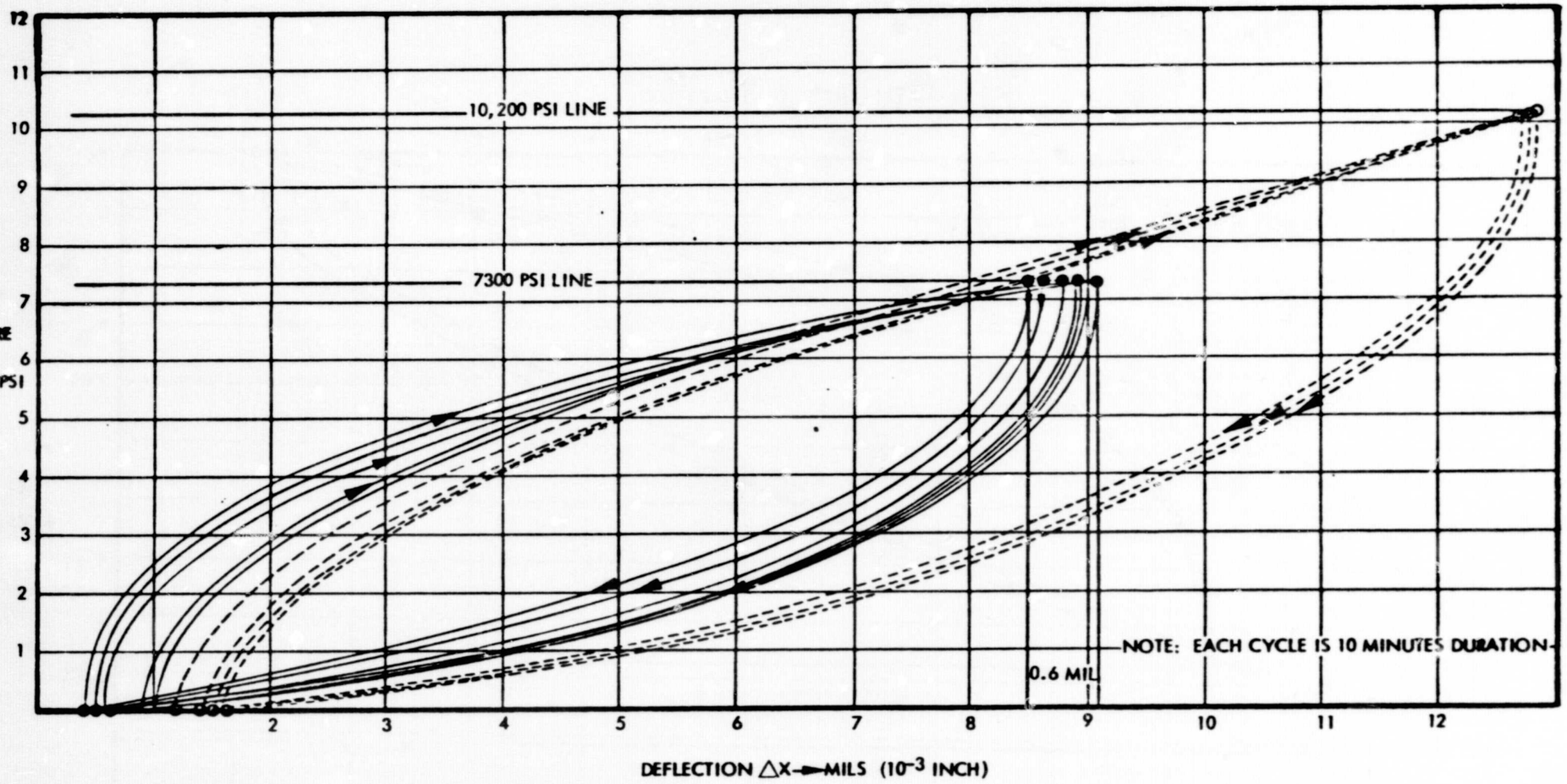


Figure 4-3. Pressure Vs. Deflection Curves for Teflon (TFE)

curves generated in Figure 4-3 show the effect of cycles on the repeatability of the stress deflection (stroke).

Permanent deformation was large for the first stroke, however, for a given stress level, the deformation was minimized during successive cycles. Examination of the Teflon material showed no evidence of breakdown in structural integrity.

4.1.3 Nitrile Rubber Evaluation

A test specimen of Nitrile rubber (Parker Compound N219-7) was evaluated in the test fixture shown in Figure 4-1. The specimen (0.125 inch diameter by 0.5 inch long) was initially subjected to several cycles of compression to minimize the initial deformation due to settling of the specimen in the mold. Three cycles of compression were then completed at the loadings shown in Table 4-4. Figure 4-4 illustrates the repeatability of the stress deflection curves of the Nitrile rubber sample over the three cycles. The bulk modulus of the sample ranged between 2.43×10^5 and 12.2×10^5 for the three cycles, which brackets the calculated value of 5×10^5 psi for hard rubber. It should also be noted from Figure 4-4 that the permanent deformation of the Nitrile rubber sample was negligible.

4.1.4 Silicone Rubber Evaluation

Silicone rubber (Dow Corning RTV 501) was evaluated in the test fixture shown in Figure 4-5. Prior to test the specimen cavity was filled with liquid RTV 501 and allowed to set overnight in an evacuated container to minimize voids or pockets in the mold. The specimen was first subjected to several cycles of compression prior to test.

Two cycles of compression were then completed on the sample at the test pressures shown in Table 4-5. Figure 4-6 illustrates the repeatability of the stress deflection curve for the silicone rubber sample and the initially low slope of the pressure versus deflection ($\Delta P/\Delta X$) curve. The bulk modulus of the sample ranged from 4.2×10^5 to 1.7×10^9 during the range of test loads. Although the bulk modulus of soft rubber is relatively high, the

Table 4-4. Compressibility Data for Nitrile Rubber
(Parker Compound N219-7)

Step	Hydrostatic Pressure, P (psi)	ΔP (psi)	Total Deflection, X (mils)	ΔX (mils)	$\frac{\Delta P}{\Delta X}$ (psi/mil)	Bulk Modulus, ($psi \times 10^{-5}$)
1	0	0	0	0	0	0
2	2920	2920	6.0	6.0	486.6	2.43
3	5840	2920	9.2	3.2	912.5	4.56
4	8760	2920	12.5	3.3	884.8	4.42
5	13140	4380	15.5	3.0	1460.0	7.30
6	14600	1460	18.3	2.8	521.0	2.60
7	0	0	0.6	17.7	0	0
8	2920	2920	6.0	5.4	547.0	2.73
9	5840	2920	9.2	3.2	918.75	4.60
10	8760	2920	12.5	3.3	884.8	4.42
11	13140	4380	15.5	3.0	1460.0	7.30
12	14600	1460	18.3	2.8	521.4	2.61
13	10220	4380	16.5	1.8	2433.3	12.16
14	8760	1460	14.0	2.5	584.0	2.92
15	5840	2920	10.5	3.5	834.28	4.17
16	2920	2920	7.0	6.4	834.28	4.17
17	0	0	0.6	5.0	0	0
18	2920	2920	5.6	3.4	584.0	2.92
19	5840	2920	9.0	3.2	858.8	4.30
20	8760	2920	12.2	2.9	912.5	4.56
21	11680	2920	15.1	2.9	1006.89	5.03
22	14600	2920	18.0	1.5	1006.8	5.03
23	11680	2920	16.5	2.7	1946.6	9.73
24	8760	2920	13.8	3.3	1080.0	5.40
25	5840	2920	10.5	4.8	884.8	4.42
26	3139	2701	5.7	5.1	562.7	2.81
27	0	3139	0.6		616.0	3.08

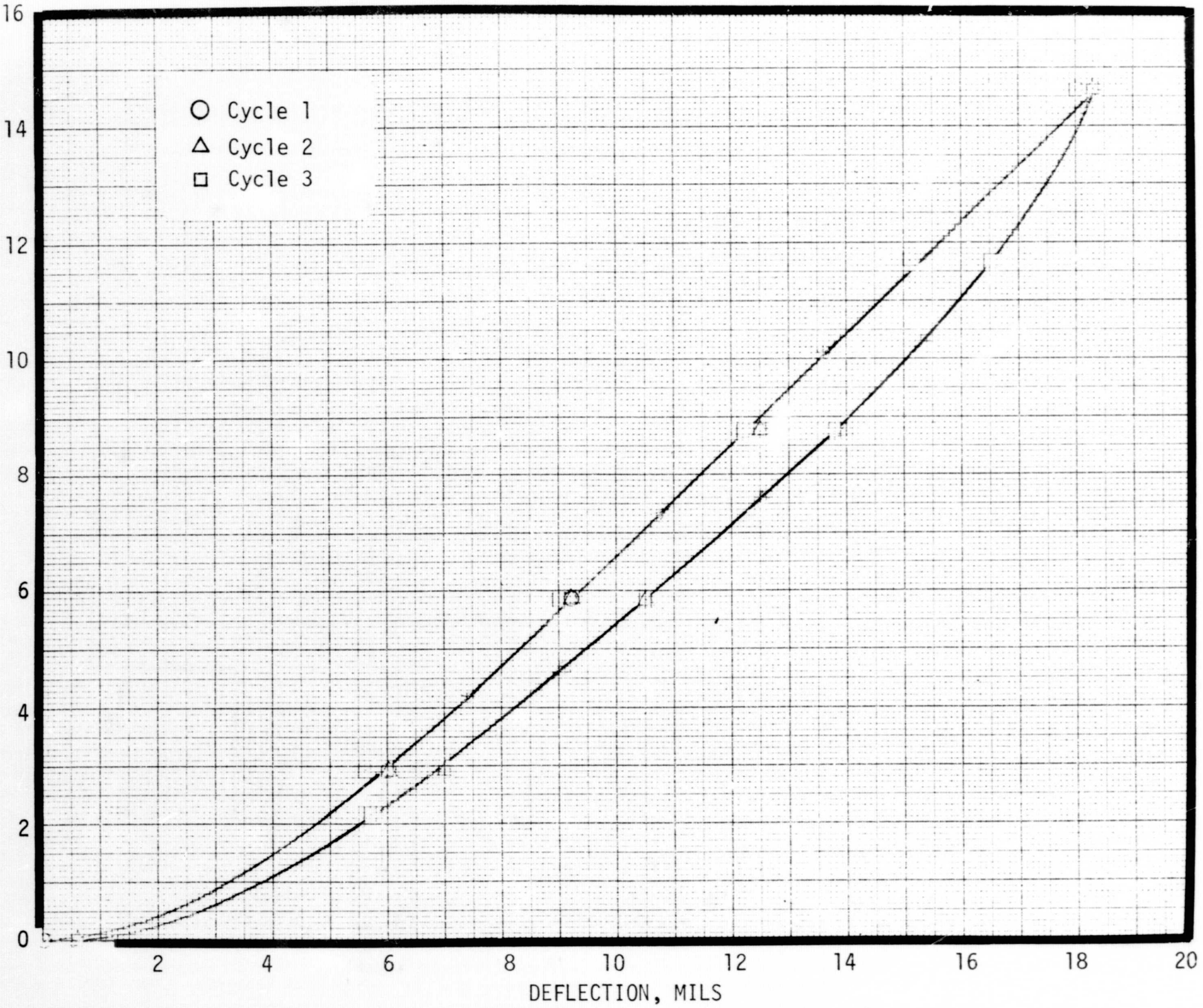


Figure 4-4. Pressure Vs. Deflection For Nitrile Rubber (Parker Compound N219-7)

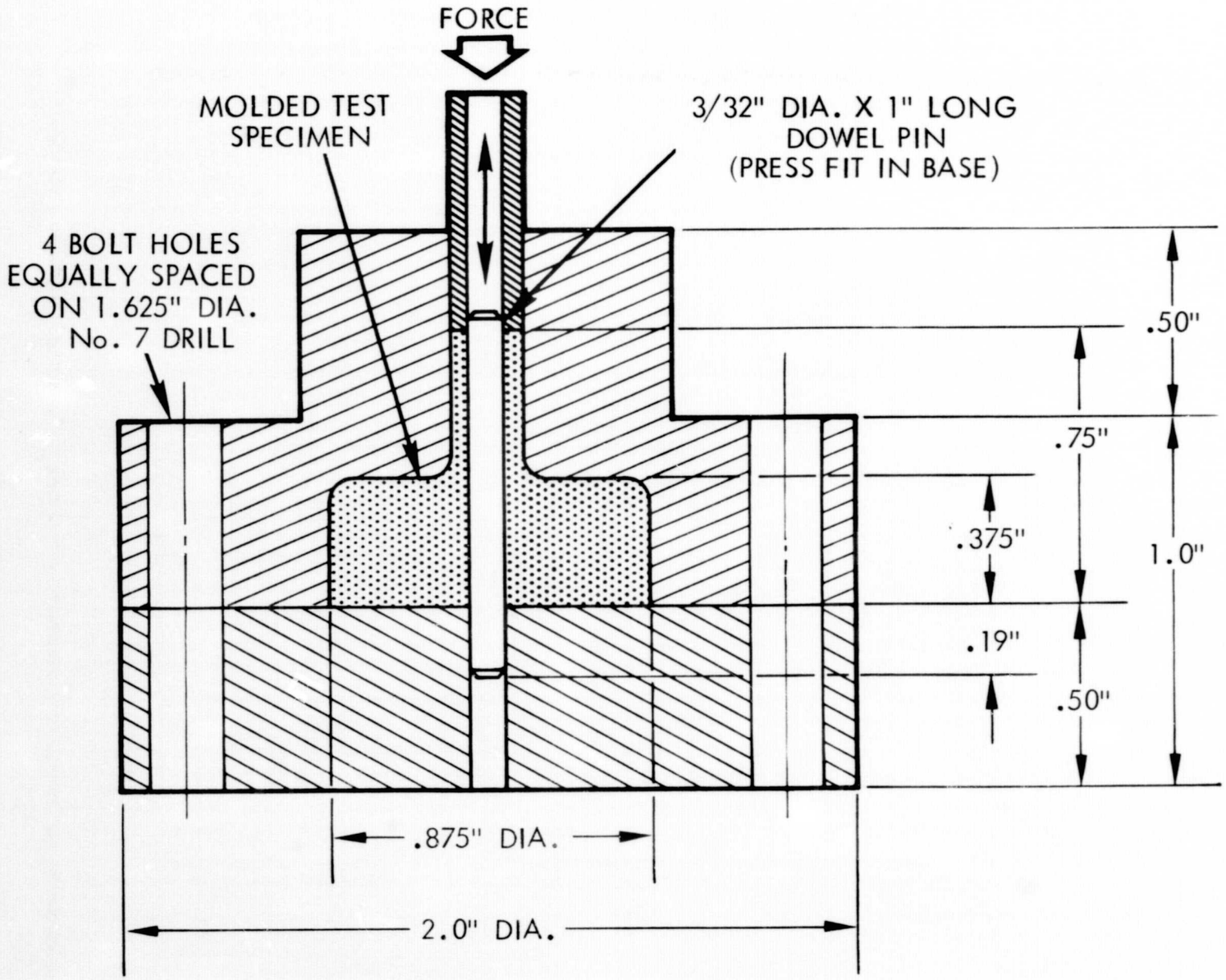


Figure 4-5. Test Fixture for Molded Sample

Table 4-5. Compressibility Data for Silicone Rubber
(Dow Corning RTV 501)

Step	Hydrostatic Pressure, P (psi)	ΔP (psi)	Total Deflection, X (mils)	ΔX (mils)	Bulk Modulus, β_{-6} (psi x 10^{-6})
1	0	0	0	0	0
2	915	915	9.0	9.0	4.69
3	1830	915	13.6	4.6	9.19
4	3752	1922	16.4	2.8	31.8
5	5490	1738	17.5	1.1	73.0
6	7320	1830	18.5	1.0	84.7
7	9150	1830	18.8	0.3	282.0
8	10980	1830	19.8	1.0	84.7
9	9150	1830	19.8	0	0
10	7320	1830	19.75	0.05	1694.0
11	5490	1830	19.3	0.45	188.0
12	3660	1830	18.6	0.7	120.0
13	1830	1830	17.2	1.4	60.4
14	0	1830	0.8	16.4	5.15
15	915	915	10.0	9.2	4.60
16	1830	915	14.0	4.0	10.6
17	3843	2013	16.5	2.5	37.1
18	5490	1647	17.5	1.0	76.3
19	7320	1830	19.0	1.5	56.3
20	9150	1830	19.8	0.8	106.0
21	10980	1830	20.0	0.2	423.0
22	5124	5856	19.4	0.6	450.0
23	3660	1464	18.7	0.7	96.3
24	1830	1830	17.1	1.6	52.9
25	1464	366	16.8	0.3	56.4
26	1098	366	16.1	0.7	24.1
27	732	366	14.7	1.4	12.1
28	366	366	12.9	1.8	9.38
29	146	220	11.9	1.0	10.2
30	110	36	7.9	4.0	0.42
31	0	110	0.5	7.4	0.687

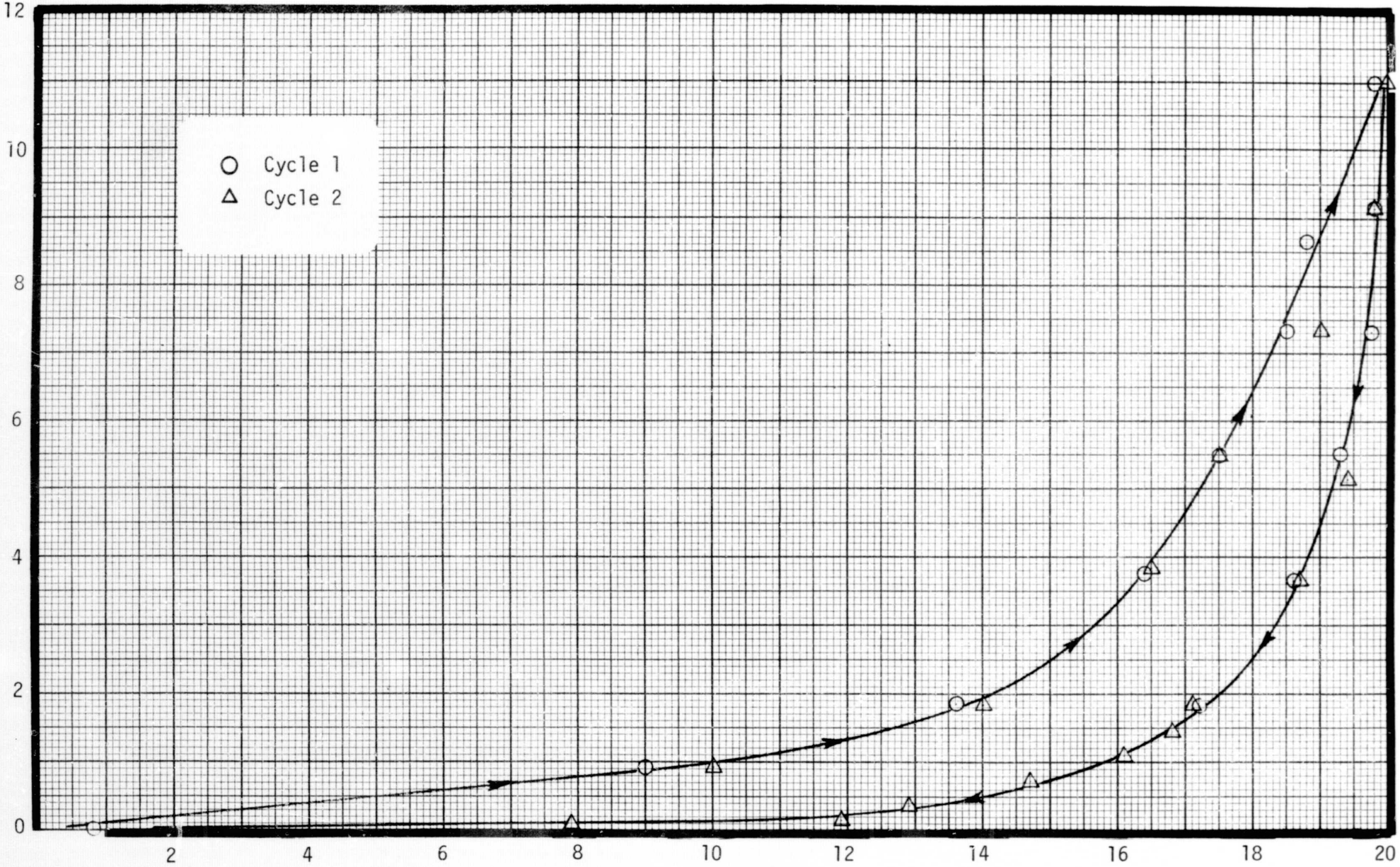


Figure 4-6. Pressure Vs. Deflection for Silicone Rubber (Dow Corning RTV 501)

wide range of modulus in the test sample is not normal and is probably due to:

1. Voids or cavities in the molded sample, and
2. Improper transfer of the hydraulic pressure from the upper tubular part of the sample (Figure 4-5) to the bulk of the sample in the lower cavity.

The test with the silicone rubber sample was inconclusive, although the measured bulk modulus of about 30×10^6 psi at the higher deflections appeared normal for a soft rubber. Both of the test samples exhibited repeatable stress deflection curves with negligible permanent deformation, so that it can be concluded that each of these materials can be utilized successfully in a zero leak seal using the energized seal concept.

4.2 METAL/METAL INTERFERENCE SEALS

The purpose of this investigation was to investigate (1) the gas leakage around a precision sphere forced into a tube with a smaller precision internal diameter and (2) the forces required for insertion and extraction of the sphere.

4.2.1 Test Methods

The test was performed with selected spheres and three tubes constructed from 17-4 PH stainless steel and two tubes constructed from 6061-T6 aluminum. Spheres of three different materials; tungsten carbide, synthetic ruby, and pure aluminum oxide were used. The nominal size of the spheres and tube inside diameter were 0.2500 inch. The configuration of the interference fit ball seal test fixture is shown in Figure 4-7.

Prior to testing, the internal diameter of the tubes were measured with a Federal Inc., Model 1368-2RI Precision Master Comparator and the diameter of each ball was measured with a Pratt and Whitney Measuring Machine. The diameter of the spheres and tubes are shown in Tables 4-6 and 4-7. The roundness and surface finish of each tube and a representative sampling of spheres were measured on a Bendix Proficorder Pilotor, Model No. 1. The parts were ultrasonically cleaned in Freon TF and individually bagged in clean polyethylene bags. The ruby spheres were examined under polarized light and the C axis of the sphere (which is perpendicular to the slip plane) was lightly marked with a felt pen. Precautions in handling were taken during testing to insure cleanliness of the spheres and tubes.

The O.D. of the tube was first measured and then the tube was placed in the holder (Figure 4-7). A sphere was placed on the hole entrance, and the top of the sphere was lightly marked with a felt pen to insure repeatability of reinsertion position. The test fixture was assembled and placed in a Baldwin Universal testing machine, which was used to apply the load and obtain a force readout. A Collins LVDT indicator was used to measure the displacement. The load-displacement curves were plotted on an X-Y plotter, and the ball was initially inserted to a depth of 0.200 inch.

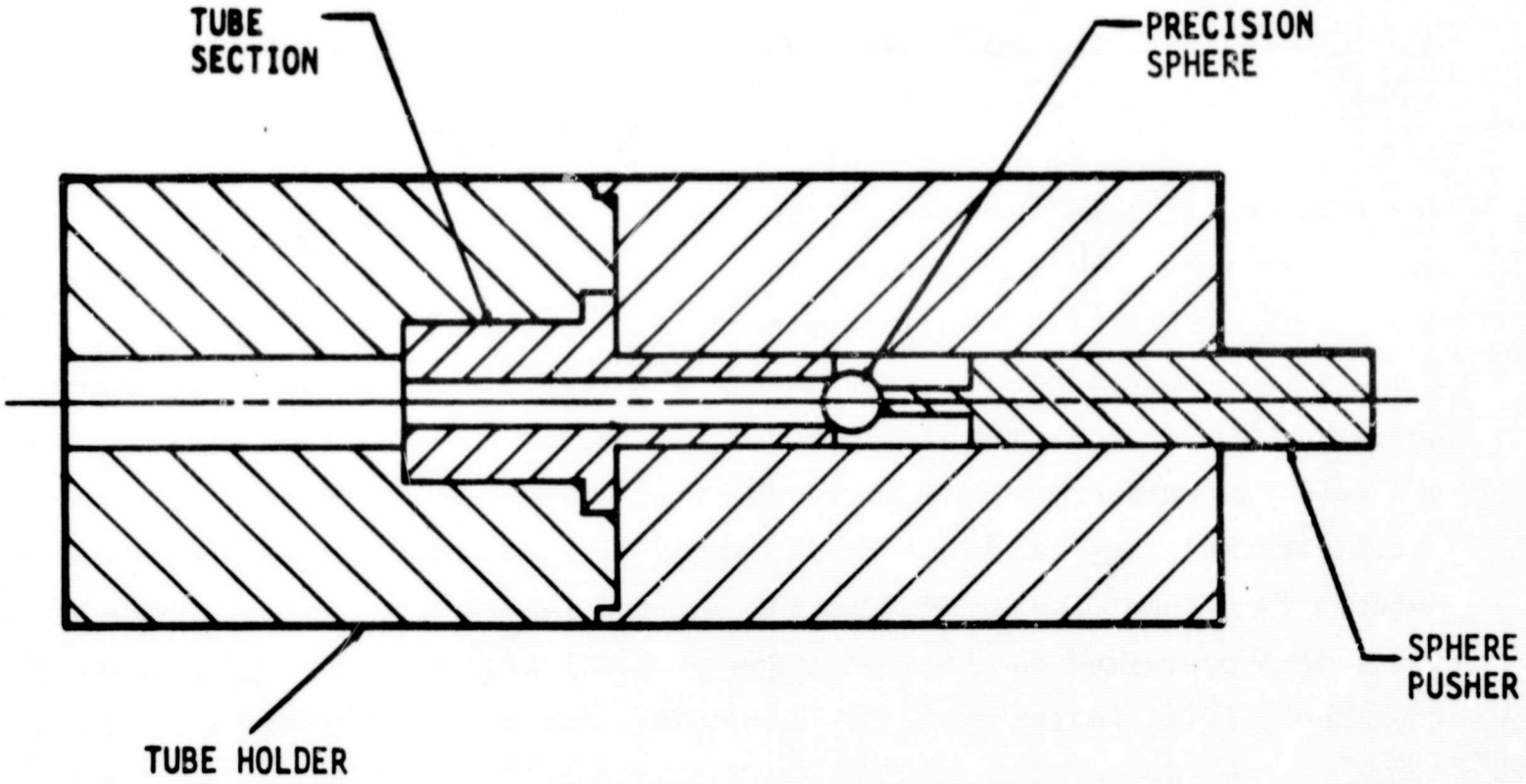


Figure 4-7. Interference Fit Ball Seal Test Fixture

Table 4-6. Sphere Diameter

Ball	Material	Diameter
2	Tungsten Carbide	0.24997
3	" "	0.24998
7	" "	0.24996
9	" "	0.24996
14	Ruby	0.24985
21	Alumina	0.24999
23	"	0.24997
24	"	0.24996

Table 4-7. Tube Diameter

Tube No.	Material		Internal Diameter
	17-4PH	Aluminum	
1	X		0.24987
2	X		0.24955
3	X		0.24993
4		X	0.24975
5		X	0.24988

The tube with the ball inserted was then helium leak-checked with a Veeco Model MS-9 leak detector. After the leak check, the O.D. of the tube was remeasured and the tube was reassembled into the test fixture.

The fixture was then inverted in the tensile tester and the ball was forced out of the tube. This procedure was repeated at least three times with the exception that the ball reinsertion depth was 0.150 inch. In all cases, a low (30-50 pounds per minute) loading rate was used to minimize friction heating. The initial tests on new tubes utilized the tungsten carbide spheres. These spheres were utilized first because the roughness traces indicated that they had the best finish of all the spheres. Each tube was matched to a sphere so as to give the desired interference fit. Subsequent tests were performed on the used tubes with the alumina and ruby spheres, thus the initial interference fit is unknown for these experiments.

4.2.2 Test Results

The test results are summarized in Tables 4-8 and 4-9. A description of each test series is discussed below.

(1) Tungsten Carbide Sphere, 17-4 PH Tube

The shape of the load-displacement curve in all cases was the same: a relatively slow rise to maximum force value upon insertion, and a sharp rise to maximum force value when the sphere was pushed out, then a relatively rapid falling off. Except for test No. 4, each traversement took a progressively larger force to move the sphere. Examination of the spheres showed that tungsten carbide sphere No. 7 had two "wear marks" on it; one at the equator and one approximately 0.005 inch down from the equator in the insertion direction. Microscopic examination showed that the "wear" marks were smeared metal. The metal was smeared in both directions on the equatorial mark, but away from the insertion direction on the lower mark, indicating that it was made during the insertion cycle. Examination of the tubes did not reveal any wear marks or signs of plastic deformation in the holes. Although the O.D. of the tube increased when the ball was inserted, the O.D. reverted to normal upon removal of the ball, which indicates that if plastic deformation occurred it did not extend to the outside of the tube.

Table 4-8. Summary of Test Results for Stainless Steel Tubes

Test No.	Materials		Initial Diametral Interference (μinches)	Penetration Depth (inches)	Maximum Force (pounds)		Leak Rate (scc/sec)
	Tube	Sphere			Insertion	Extraction	
1	17-4PH (Tube #3)	Tungsten Carbide (Sphere #3)	50	0.200	33	44	$>2.5\times10^{-5}$**
2				0.150	46	49.5	$>2.5\times10^{-5}$**
3				0.150	47	51	1.1×10^{-3}
4				0.150	36	40.5	2.9×10^{-4}
5	17-4PH (Tube #3)	Alumina (Sphere #21)	60*	0.150	59.5	66	2.9×10^{-3}
6				0.150	70	68	4.6×10^{-3}
7				0.150	80	83	5.5×10^{-3}
8	17-4PH (Tube #1)	Tungsten Carbide (Sphere #2)	100	0.200	47	61	1.2×10^{-4}
9				0.150	70	80	3.6×10^{-5}
10				0.150	82	91	6.7×10^{-5}
11				0.150	93.5	108	4.1×10^{-5}
12	17-4PH (Tube #2)	Tungsten Carbide (Sphere #7)	410	0.200	87	107	1.1×10^{-4}
13				0.150	110	123	7.2×10^{-5}
14				0.150	136	140	6.3×10^{-5}
15	17-4PH (Tube #2)	Ruby (Sphere #14)	300*	0.200	50	-	3.9×10^{-4}
16				0.050	72	-	4.3×10^{-4}
17				0.200	88	-	1.4×10^{-4}
18				0.050	105	-	5.0×10^{-4}
19				0.200	52	76	9.4×10^{-5}

*Estimated

**Readings were greater than leak detector maximum range - the range was increased for subsequent tests.

Table 4-9. Summary of Test Results for Aluminum Tubes

Test No.	Materials		Initial Diametral Interference (μinches)	Penetration Depth (inches)	Maximum Force (pounds)		Leak Rate (scc/sec)
	Tube	Sphere			Insertion	Extraction	
1	6061-T6 (Tube #4)	Tungsten Carbide (Sphere #9)	210	0.200	22		1.1×10^{-2}
2				0.050		23	**
3				0.200	24		1.2×10^{-2}
4				0.100		23	1.4×10^{-2}
5				0.370	24		4.3×10^{-3}
6				0.190		25	9.9×10^{-3}
7				0.370	24		5.2×10^{-3}
8						27	-
1	6061-T6 (Tube #4)	Alumina (Sphere #24)	210*	0.300	30		1.4×10^{-3}
2				0.200		30	3.7×10^{-3}
3				0.300	24		1.0×10^{-3}
4				0.200		23	2.6×10^{-3}
5				0.300	19		1.2×10^{-3}
6				0		22	-
1	6061-T6 (Tube #5)	Alumina (Sphere #23)	170	0.300	18		2.0×10^{-2}
2				0.200		15	**
3				0.300	14		1.2×10^{-2}
4				0.200		15	**
5				0		18	-

*Estimated

**Leak rate was too great to allow pumpdown to leak detector.

(2) Alumina Sphere, 17-4 PH Tube

Examination of the roughness traces of the aluminum oxide spheres showed that they had the roughest finish of the three types of spheres (approximately 32 microinch rms). Consequently, the alumina test was performed after the tube had been used with tungsten carbide. After three cycles, the tube was visably scored, and a relatively high leak rate was measured. A wear mark was observed on the sphere after one cycle, and after completion of the alumina tests, microscopic examination showed metal embedded on the surface of the sphere. The load cycle curves were similar in shape to tungsten carbide.

(3) Ruby Sphere, 17-4 PH Tube

The tests using the ruby sphere were performed in a slightly different manner than the others. Since the tube had been used, it was decided to examine the effect of traversing the tube without removal. This was performed by inserting the sphere to a depth of 0.200 inch, leak testing, inverting the fixture and pushing the sphere back 0.150 inch, and leak testing again.

The load cycle curves were different than those of the other two types of spheres. The first cycle resulted in a relatively slow rise in load to the maximum value, but the remainder of the cycles gave curves which initially had a rapid rise and then a slow taper, except for test No. 17 which had a rapid rise, then slowly increased until the end of the traversement, when it again rose rapidly.

Examination of the tube after the tests did not indicate that scoring or any wear had occurred, but the sphere had a discontinuous wear mark at the equator. Microscopic examination showed that metal was embedded in small pits on the surface of the sphere. These pits were evidently present before testing, since examination of the sphere showed random pitting over the entire surface, corroborated by the roughness trace. The ruby sphere was inserted with the force parallel to the C axis.

(4) Tungsten Carbide Sphere, Aluminum Tube

The shape of the load-displacement curves for the aluminum tubes differed from stainless tubes in that there was a sharp increase in force until movement of the ball and then the force remained constant until the force was removed. The leak rate was at least 10 times greater than with the stainless tubes, but remained constant for a given depth. In some cases, the leak rate was so large that a leak measurement detector could not be performed. This was probably due to scratches and/or tool marks in the aluminum tube.

(5) Alumina Sphere, Aluminum Tube

The test with alumina spheres resulted in load-displacement curves similar to the tungsten carbide sphere. The alumina spheres did indicate a lower leak rate, $1x10^{-3}$ scc/sec, than the tungsten carbide sphere with the same insertion forces. Examination of the alumina sphere after the test showed a heavy layer of aluminum on the sphere surface. The metal layer probably resulted in the lower leak rate and provided a "tight" metal to metal seal.

4.2.3 Conclusions

Minimum leak rate was observed when the interference fit was 0.0001 inch or greater. No significant difference was noted between 0.0001 and 0.0004 inch interference fit with tungsten carbide spheres.

Surface smoothness is extremely important for low leak rates, at least for hard materials. Although the data is limited, it appears that more than one cycle is beneficial for decreasing the leak rate.

The increase in force with cycle life is probably primarily due to work hardening of the tube, and secondarily, to increased friction from metal adhering to the sphere and causing metal-metal "sticktion." Variation of the force after the first cycle did not appreciably affect the leak rate.

4.3 THIN FILM UNIVERSITY PROGRAM

A technology has been developed for the formation of continuous films in vacuum by electron bombardment of a condensing siloxane monomer. The studies for determining these thin film properties were continued under this program to support possible benefits to advanced valve technology which might accrue by having surfaces coated with a highly stable film of this type.

In accomplishing the work consideration was given to those aspects that would support the overall program objectives, i.e., to advance component technologies for spacecraft propulsion applications. The areas where end use application of thin films may be advantageous to spacecraft components can be summarized as follows: anticold welding; lubrication; seal/leakage technology including valve seats; and propellant compatibility. The efforts related to propellant compatibility were limited to earth storables (hydrazine and nitrogen tetroxide), and space storables (oxygen difluoride and diborane).

The work effort performed by the University of Bradford and Dartmouth College has been completed. The results of the Bradford work are reported in the University Final Report under Subcontract No. AE868. The report has been reproduced and included in Appendix A. The results of the work performed by Dartmouth College under Subcontract No. AE866 are presented in Appendix B.

4.4 REFERENCES

1. MIL Standard Handbook - MIL-HDBK-149A, June 1965.
2. Teflon Mechanical Design Handbook, E. I. duPont deNemours and Company.
3. "Effects of Hydrostatic Pressure on the Mechanical Behavior of Polyethylene and Polypropylene," by Mears, Pae and Sauer; Journal of Applied Physics, Vol. 40, No. 11, October 1969.

APPENDIX A

THE FORMATION OF SURFACE FILMS BY ELECTRON BOMBARDMENT

Final report of work carried out during the period
October 1968 - September 1969
at the School of Chemistry
The University of Bradford

by

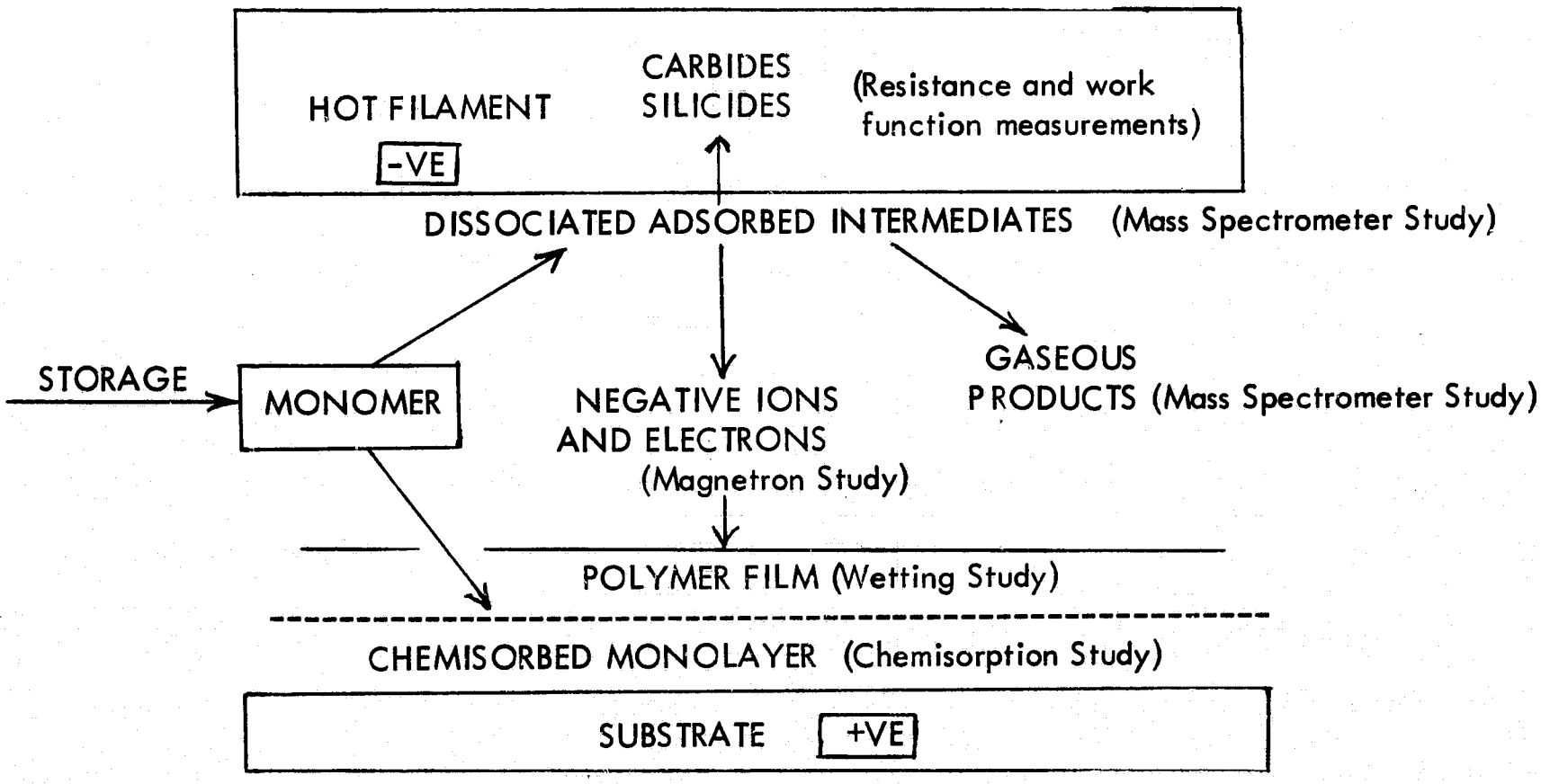
Professor M. W. Roberts
Dr. J. R. H. Ross
Mr. J. H. Wood
Mr. W. J. Murphy

N70-39403

SUMMARY AND CONCLUSIONS

The work to date has been directed at the determination of the mechanism of the formation of thin polymeric films from organic molecules by the electron beam technique, together with an examination of the properties of the polymers, mainly from the view of their wetting characteristics.

The following scheme shows the breakdown of the work and indicates the proposed mechanism for the polymerization process:



Initially, a study of the chemisorption of a possible monomer, tetramethylsilane (TMS), was made on tungsten and iron substrates. The bonding of the adsorbed layer will be related to the adhesion of the polymer. Preliminary experiments on the mechanism of the polymerization reaction indicated that it probably involved the formation of negative ions at the hot filament which then polymerize on striking the substrate. Negative ion formation from a variety of monomers has been confirmed using a magnetron cell, and the relative proportions of negative ions and electrons as a function of filament temperature and monomer pressure have been examined in detail. Carbiding of the emitting filament was also observed and this has

received some attention. A study of the stoichiometry of the polymerization reaction showed that the reaction depended on the applied voltage. Detailed examination of the voltage dependence has allowed a mechanism for the formation of the negative ions at the hot filament to be postulated.

In an effort to characterize the nature of the polymer surfaces prepared under a variety of conditions, a study using measurement of contact angles of drops of liquid of known surface tension γ has been initiated. The value of the surface tension γ_c of the liquid which just spreads on the surface is known to be characteristic of the surface. Using a series of solutions of butanol of known surface tension, it has been shown that butanol is adsorbed on the surface; when the concentration of butanol is such that spreading occurs, the value of the surface tension γ_c' is characteristic not of the original surface but of a surface covered with adsorbed butanol molecules. An examination of the adsorption allows a comparison of the properties of polymers prepared under a variety of conditions.

Further work should involve experiments designed to confirm the mechanism postulated for the formation of negative ions using several different monomers; rhenium filaments should be used for this work since it does not carbide very readily. Mass spectrometric experiments should also be carried out to identify the ions produced at the filament, and the reactions occurring when these ions strike a substrate should be examined in detail. These results will enable a greater understanding of the polymerization process to be achieved, and it will be possible to attempt a greater correlation between the properties of the completed polymer and the structure of the monomer. The wetting studies should be extended to other monomers and other substrates. It is probable that the mechanism postulated for the electron beam polymerization process will also hold at higher pressures in glow discharges involving either hot or cold cathodes. It might therefore be of considerable interest to initiate a program which would compare the properties of polymers made by different experimental methods (e.g. glow discharge) with particular reference to the wetting measurements mentioned above. Also the work offers the possibility of preparing composite materials by field accelerated reactions.

INTRODUCTION

In the second annual report[1], results were presented from which it was concluded that the process of polymer film formation from tetramethylsilane (TMS) by the so-called electron bombardment process involves the formation of negative ions at the cathode from which they are accelerated towards the substrate (or anode) where they polymerize. A method of measuring the separate contributions of negative ions and electrons using a magnetron cell was described.

This report presents further results on the kinetics of the reaction of tetramethylsilane obtained using the mass-spectrometric technique. A mechanism for the production of negative ions at the filament is proposed. The formation of negative ions from tetramethylsilane as well as from butadiene and neopentane has been examined by the magnetron technique. Using resistance measurement techniques, it was shown that the tungsten cathode gradually became carbided during the polymerization process, and these changes are described.

In order to examine the nature of the polymer formed, a study of the wetting characteristic has been undertaken. By measuring the angle of contact between drops of a series of liquids or of dilute aqueous solutions of alcohols, it has been shown possible to characterize the nature of the surface of the polymer. These wetting characteristics are reported for thin films formed from perfluorobutene-2 on tungsten substrates as a function of the potentials applied to the anode and the grid of the electron gun, and conclusions are drawn regarding the nature of the surface of the polymer.

The report is divided into three parts:

1. The mass spectrometer study of the kinetics of the reaction of tetramethylsilane with a tungsten filament, without and with a field.
2. An investigation of the production of negative ions from tetramethylsilane, butadiene, and neopentane.
3. A study of the wetting characteristics of thin polymeric films formed from perfluorobutene-2 on tungsten substrates.

1. MASS SPECTROMETER STUDY

The apparatus incorporating the mass spectrometer was described in the last annual report[1]. In several experiments, it was required to vary the distance between the cathode and the anode during the experiment, and this was achieved by means of a set of stainless steel bellows which allowed the anode ribbon to be moved through ~5 cm. In these experiments, the cathode was a straight wire parallel to the plane of the anode.

GENERAL FEATURES AND STOICHIOMETRY OF REACTION

The kinetics of the reaction of tetramethylsilane with a tungsten filament were found to depend on the applied field. The reactions will first be described qualitatively and then the kinetics will be described in more detail.

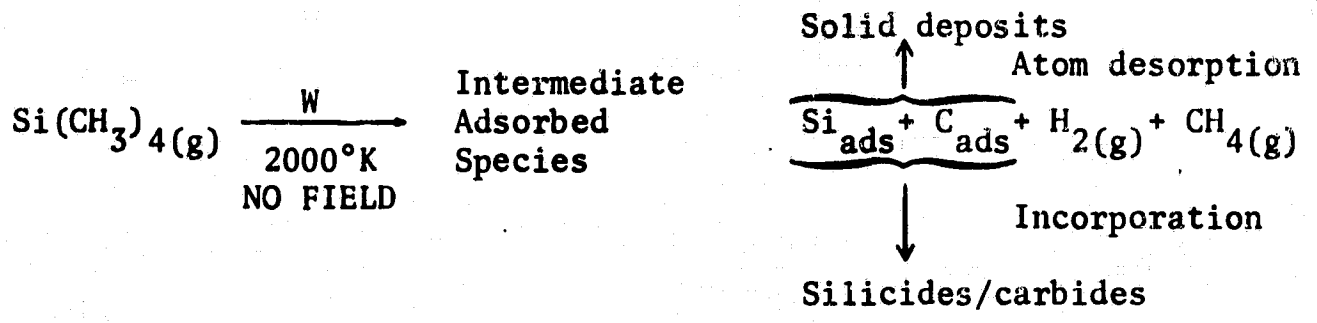
Typical primary data for the reaction of TMS with a tungsten filament without an applied field at a variety of filament temperatures are shown in Figure 1-1. The rate of disappearance of TMS is given by the decrease in the TMS ion current and the pressure at which the reaction occurs is given by the ion current as long as the leak to the mass spectrometer is close to the reaction vessel. With the filament at ~2000°K, rates of reaction of about 10^{14} molecules $cm^{-2}sec^{-1}$ were obtained at $p \simeq 10^{-4}$ torr. The stoichiometry of the reaction is given by equation (1), although initially some hydrogen was lost from the gas phase.

$$n\ Si(CH_3)_4\ (g) \xrightarrow[2000°K]{W} (SiC_{3.8}H\ O)_{n_{ads}} + 0.2nCH_4(g) + 5.6nH_2(g) \qquad (1)$$

The amount lost was consistent with that which can be taken up by pyrex glass at 20°C.[2] During reaction, a slight film was found to appear on the tungsten anode, which was at 298°K, but this was found to disappear on heating it to ~1000°K. A slight discoloration also appeared on the glass of the reaction vessel and this continued to build up with time. Shown in Figure 1-2 are Richardson plots (log I_e/T^2 vs. 1/T) of vacuum thermionic emission data ($p < 10^{-7}$ torr) obtained with a new, well outgassed tungsten filament (line 1) and with the same filament after

reaction without a field (line 2). A work function of 4.5 eV is calculated for the former and one of 6.0 eV for the latter. These results are consistent with carbiding/siliciding of the surface. Since the tungsten carbides are known to decompose completely in vacuum at ~2800°K by desorption of atomic carbon, small quantities of elemental carbon and silicon probably desorb even at ~2000°K and will account for the visible deposits on the ribbon and the glass envelope. The film on the ribbon either incorporates or decomposes on heating. The stoichiometry of the reaction shows that when a molecule reacts, complete breakdown of the skeleton occurs and this is in agreement with other studies (see Ref. 3).

The above observations are summarized by the following scheme:



(2)

The intermediate species will be discussed below when the mechanism is considered.

When a slowly increasing voltage was applied between the filament (cathode) and the ribbon (anode), an increase in the rate of reaction was found to occur at a voltage designated as V_c (see Figure 1-3); in most experiments, the interelectrode spacing was ~1 cm and V_c was between 20 and 30V. Figure 1-3 shows the rate, R, of disappearance of TMS, and the rate of appearance of hydrogen and methane plotted as a function of applied voltage V. Small quantities of ethylene were also produced. Figure 1-3 shows that the emission current also increases rapidly at V_c. Above V_c, the rate of reaction and the emission current change slowly with change in applied voltage. At voltages well above V_c (~100V), the rate of production of hydrogen increases once more, as shown in Figure 1-4. For comparison, the vacuum electron emission 1_e, obtained with the new filament is also shown. During the increase in R and 1 at V_c, a linear

relationship is found to exist between R and 1 (Figure 1-4). Expressing 1 in charge carriers/sec., the gradient of the line in Figure 1-4 corresponds to about one molecule of TMS reacting for each 5 charge carriers produced. The ratio depends on filament temperature and tends toward unity at lower temperatures. It is proposed that the increase in the rate of reaction and the simultaneous rise in emission is caused by the production of negative ions at the hot filament; the magnetron work has confirmed this. There is a simultaneous rapid increase in the emission of electrons. This must be caused by a change in the work function of the surface induced by the application of the voltage V_c.

Above the voltage V_c (20 to 30V) the stoichiometry of the reaction was found to have changed. At 50V, it was found to be given by equation (3), and at 200V, equation (4) applied. There is a marked difference in reaction with and without a field (c.p. equation (1)). It is not possible to separate from these

$$nSi(CH_3)_{4(g)} \longrightarrow (SiC_{3.3}H_{7.2})_{n_{ads}} + 1.4nH_{2(g)} + 0.3nCH_{4(g)} + 0.2nC_2H_{4(g)} \quad (3)$$

$$nSi(CH_3)_{4(g)} \longrightarrow (SiC_{3.3}H_{3.4})_{n_{ads}} + 3.1nH_{2(g)} + 0.5nCH_{4(g)} + 0.1nC_2H_{4(g)} \quad (4)$$

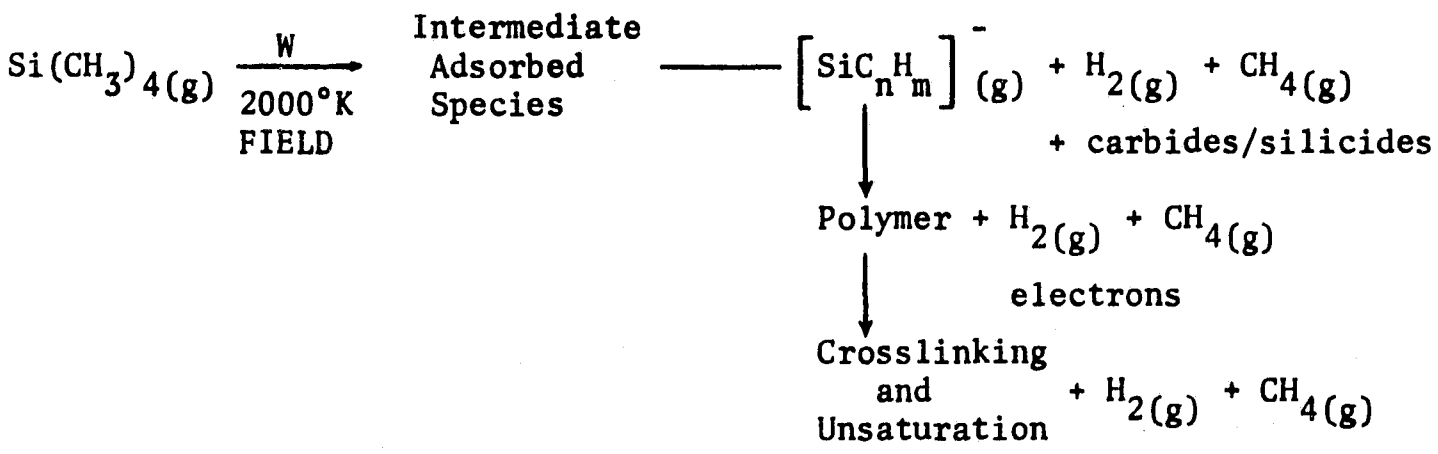
equations the contribution from the concurrent carbiding/siliciding reaction, as this reaction will be changed by the change in the work function of the surface. The desorbed negative ions must however contain some hydrogen, as a large proportion of the hydrogen is removed from the gas phase. This must occur by the formation of a thin polymer film on the ribbon surface. Thermal decomposition of this film caused hydrogen and methane to appear in the gas phase. The difference in stoichiometries observed at the two voltages occurs because the electrons emitted concurrently with the negative ions probably causes desorption of hydrogen and methane from the polymer already formed on the anode; this effect increases with increasing voltage. Further hydrogen and methane may be desorbed during the process occurring when the negative ions strike the anode, and as this process may depend on the energy of the negative ions,

3

it may also contribute to the observed change in stoichiometry. The ethylene observed may be formed at the filament, during the polymerization process, or by electron bombardment of the polymer.

As the products of the reaction may not all be formed at the filament, it is not possible to use their rate of formation to monitor the kinetics of the reaction. In order to use the rate of disappearance of TMS to study the kinetics, it must be assumed that each molecule of TMS which reacts forms a negative ion and that each ion is incorporated into the polymer. If this were not the case, new species containing silicon would be observed, which is not the case. Further support for this approach comes from the magnetron results, as the negative ion currents measured are of the same order as the rates of reaction measured mass spectrometrically.

The reactions thought to occur with an applied electric field are summarized by the following scheme:



(5)

Carbides and silicides may be formed from adsorbed intermediates not involved in the formation of the negative ions.

KINETICS OF THE REACTION WITHOUT A FIELD

The pressure dependence of the reaction at constant temperature is given by an expression of the type

$$R_T = k_T P^n_{TMS} \tag{6}$$

where k_T is a constant dependent on temperature. From a plot of log (R) vs. log (P_{TMS}) for data obtained at a filament temperature of 2000°K (see Figure 1-5), the value of n, the pressure dependence of the reaction, was found to be ~0.5. If the full rate expression is now given by equation (7), values of E and k can be obtained by

$$R = kP^{0.5} \exp - {}^{E}/_{RT} \tag{7}$$

correcting data obtained at various temperatures to one pressure and plotting log R_p vs 1/T. Figure 1-6 shows such plots corresponding to a constant pressure of 10^{-4}mm. Curve A corresponds to reaction with a new filament which had attained a constant activity, fully reversible with temperature cycling; curve B corresponds to the reaction after reaction had been carried out with a field for some time, and was also fully reversible. The values of E obtained from the gradients of the curves vary from ~60 kcal/mole at 1700°K to ~40kcal/mole at 2200°K for curve A, with correspondingly slightly lower values for curve B. The curvature of these lines may be due to a variation of either k or E with temperature (equation 7); the possible errors inherent in the measurement of T are not sufficient to cause the curvature which is found. Increasing temperature will give a decrease in the coverage of the surface by reactive intermediates, and this in turn may cause a change in the activation energy of the process. However, the coverage also varies with pressure and no change in k_T equation (6) and Figure 1-5 was found with variation of pressure. Therefore, E must remain essentially constant with variation of coverage, and so the curvature of the plots in Figure 1-8 must be explained solely by a variation of the coverage and hence k, with temperature. The decrease of k with increasing temperature gives a decrease in the gradient of the log R vs 1/T plots and hence an apparent decrease in

the activation energy. The vacuum work function corresponding to curve B was found to be ~3 eV (Figure 1-2, line 3) as opposed to a value of ~6 eV for curve A (Figure 1-2, line 2).

The following scheme is proposed to explain the observed results:

$$Si(CH_3)_{4(g)} \underset{\longleftarrow}{\xrightarrow{(I)}} R_{1_{ads}} + R_{2_{ads}} \xrightarrow{(II)} R_{3_{ads}} + R_{4_{ads}} + \ldots\ldots \xrightarrow{(III)} \text{carbides} + \text{silicides} \qquad (8)$$

Step I involves the formation of two adsorbed species R_1 and R_2, on the surface with the cleavage of either a C - H bond or a C - Si bond. It is postulated that further breakdown of one or other of these two species, to form other adsorbed radicals R_3, R_4, etc. is rate determining (step II). The silicon and the carbon of these radicals subsequently either becomes incorporated in the bulk or desorbs as atoms, or, as in the case for some of the carbon, desorbs as methane; the latter may also originate from R_1 or R_2, if C - Si bond cleavage occurred in step I. Each of the species R_1 and R_2 is in equilibrium with the gas phase once a steady state is set up, and so

$$R_{1_{ads}} = R_{2_{ads}} \alpha P^{1/2}_{TMS}$$

Hence, equation (9)

$$\Theta_{p,T} = k_T^1 \; p^{1/2}_{TMS} \qquad (9)$$

follows, where $\Theta_{p,T}$ is the extent to which the surface is covered by reactive species at temperature T and pressure p, and k_T^1 is a constant

which depends on T. Thus, an expression of the form of equation (7) may be set up. Further evidence for this rate determining step is obtained from the study of the carbiding reaction using resistance measurements.

DEPENDENCE OF V_c ON PRESSURE, ELECTRODE SPACING, AND FILAMENT TEMPERATURE

Figure 1-7 shows the effect of varying the pressure and the separation of the electrodes, d (see inset), on the critical voltage V_c. Various symbols are shown for d = 0.35 cm, corresponding to various filament temperatures. Although very different emission currents and rates of reaction are found at each temperature, V_c does not change with temperature. From the data of Figure 1-7, V_c is found to vary almost linearly with electrode separation d. Figure 1-8 shows plots of V_c versus d for various values of pressure. The dependence of V_c on d proves conclusively that the appearance of negative ions is not due to electron-molecule interaction in the gas phase. The plots of V_c versus d extrapolated to $V_c = 0$ do not intercept the d axis at d = 0 because of the non-ideal geometry of the electrodes; instead, they intersect at a negative value of d implying that the emission appears to originate behind the emitting surface. The relationship is sufficiently accurately described by equation (10) where ε_c is

$$\varepsilon_c = \frac{V_c}{d + 1.3} \tag{10}$$

the critical field at the surface of the filament. Hence, the experimental results of Figure 1-7 may be replotted as ε_c versus P, and are found to lie satisfactorily on one curve (Figure 1-9).

If the desorption of negative ions from the surface is rate determining, the rate R is given by an expression of the form of equation (11).

$$R = A \exp \left\{ -e \frac{(S - \phi)}{kT} \right\} \tag{11}$$

where A is a constant, e is the charge on an electron, ϕ is the work function of the surface, k is the Boltsmann constant, and T is the absolute temperature, and S includes terms such as the electron affinity of the radical giving the negative ion, the heat of adsorption of this radical on the surface, etc.

Equation (11) is related to the Saha-Langmuir expression for N.S.I. (see reference 4). The equation is modified, when a field is applied, by the inclusion of the Schottky terms $e\sqrt{e\varepsilon}$ in the exponential term[4, 5]. This arises due to the forace acting on the negatively charged species as it leaves the surface. As long as the constant A is not altered by the field, then

$$\log \frac{R_{(\varepsilon)}}{R_{(\varepsilon=0)}} = 1.906 \frac{\sqrt{\varepsilon}}{T} \qquad (12)$$

where $R_{(\varepsilon)}$ is the negative ion current with a field, $R_{(\varepsilon=0)}$ is that without, and ε is the field expressed in volt/cm. At a temperature of 2000°K, a 1% increase in the rate of negative ion formation would occur with a field of ~20 v/cm. In the experiments described above, the rate increased rapidly to a relatively large value at this voltage, and this could not be explained by the schottky term. The simultaneous large rise in emission current indicates quite clearly a change in the work function of the surface. If this occurs by a change in coverage according to an expression such as equation (13),

$$\phi_\theta = \phi_0 = C\theta \qquad (13)$$

where ϕ_θ is the work function at coverage θ. ϕ_0 that at $\theta = 0$, and C is a constant, which will depend on the dipole moment of the adsorbed species, then the change in coverage must be induced by the field. Thus A in equation (11) is also dependent on the field. A compensation between the Schottky term and the field dependence of the coverage is likely; i.e., the coverage θ_ε which can exist at any field ε is given by equation (14), where C_2 and C_3 are constants.

$$\theta_\varepsilon = C_2 \exp\left(-C_3 \varepsilon^{1/2}\right) \qquad (14)$$

when $\varepsilon = 0$, $\theta_{(\varepsilon=0)} = C_2$. If $C_2 > \theta_{p,\,T}$ (equation 9), then only when ε is such that $\theta_\varepsilon < \theta_{p,\,T}$ will the work function commence to drop and the rate of NSI will increase. Once ε controls the coverage, further increase in ε

causes a considerable increase in the rate. ε_c will therefore be given by that value of ε when $\theta_\varepsilon = \theta_{p,\,T}$, i.e.

$$C_2 \exp\,(-C_3\,\varepsilon_c^{1/2}) = k_T^1\,p_{TMS}^{1/2} \qquad (15)$$

Equation (15) suggests a plot of log p_{TMS} versus $\varepsilon_c^{1/2}$ for the critical conditions. Figure 1-10 shows such a plot for the data for d = 1.5 cm shown in Figure 1-7. Similar results were obtained for the other spacings. The curves drawn through the points in Figures 1-7 and 1-9 correspond to the best fits of lines such as these in Figure 1-10. The above theory is therefore shown to explain satisfactorily the experimental data. It should be noted that as the pre-exponential term is most affected by the applied field, ε_c should not depend on the filament temperature. This was observed experimentally (Figure 1-7).

It should be pointed out that the theory does not preclude the formation of negative ions below ε_c; ions could be produced at zero field, but the current would be reduced by space charge effects and the rate of reaction would be swamped by the carbiding/siliciding reaction.

REACTION ABOVE ε_c

Above ε_c, the rate will be independent of the pressure (i.e., θ is given by equation 14) as long as the rate determining step remains the desorption of negative ions. Assuming that the rate of the carbiding/siliciding reaction can be neglected, equation (1) can be modified to give equation (16), where A^1 is a new constant, using equation (14).

$$R = A^1 \exp\,(-C_3\,\sqrt{\varepsilon})\,\exp -e\,(S - \phi_\theta + \sqrt{e\varepsilon}) \qquad (16)$$

In order to test this theory for the rise of R above V_c, equation (13) must be included to allow for the variation of ϕ with voltage. Expansion of equation (14) gives

$$\theta = C_2\,(1 - C_3\varepsilon^{1/2} + \frac{C_3^{\,2}\varepsilon}{2!} - \frac{C_3^{\,3}\varepsilon^{3/2}}{3!} + \ldots\ldots) \qquad (17)$$

If $C_3 << \varepsilon$, then all terms after the second may be omitted. Combining this with equation (13) gives

$$\phi_\theta = \phi_0 + CC_2 \ (1 - C_3\varepsilon^{1/2}) \tag{18}$$

Hence, equation (16) becomes

$$R = A^1 \exp \ (-C_3 \sqrt{\varepsilon}) \exp \frac{(K - K^1 \ \varepsilon^{1/2})}{kT} \tag{19}$$

where K and K^1 are constants. Thus, at constant temperature, a plot of log (R) versus $\varepsilon^{1/2}$ should give a straight line.

However, the increase in the rate of reaction just above ε_c is so rapid that the data obtained is not sufficiently accurate to confirm this theory. Figure 1-11 shows a plot of log (R) versus $\varepsilon^{1/2}$ at a filament temperature of 1980°K. The data just above ε_c lie on a straight line, but other plots could equally well be used. However, Figure 1-11 does show that the mechanism of the reaction appears to change above this region of field and a pressure dependent process again takes over, the rate being dependent approximately on $P_{TMS}^{1.0}$. Figure 1-12 (a) shows data obtained at a variety of temperatures using one flow rate, plotted as log σ versus $\varepsilon^{1/2}$, where σ is the probability that a molecule striking the surface will form a negative ion. The number of molecules striking the walls α P_{TMS} and is given by the Hertz-Knudsen equation. The distinct breaks between the three rate determining processes can be clearly seen. Figure 1-12 (b) shows Arrhenius plots for data obtained at several fields above the second point of inflexion. The process at high fields is found to have an activation energy which remains constant at ~110 kcal/mole, with a pre-exponential term which increases steadily with increasing field. The data is not sufficiently sensitive to distinguish between a dependence of rate on ε or $\varepsilon^{1/2}$. As the rate of formation of negative ions is no longer dependent on the desorption process, but is dependent on the pressure, it is likely that the rate determining step must be step (1) of the scheme given in equation (8), i.e., the breakdown of the TMS molecule to form the two adsorbed radicals R_1 and R_2. subsequently, either R_1 or R_2 desorbs as a negative ion. The variation with

applied field of the pre-exponential term of the kinetic expression governing step (1) must be explained by a variation of the mobility of the surface complex with decrease of the work function of the surface. The activation energy for the process does not vary, and therefore must be close to the energy of the bond broken in forming R_1 and R_2, as otherwise a change in work function would affect the energetics. From the stoichiometry given in equation (3), assuming the carbiding/siliciding reaction to be negligible at 50V, it might be assumed that the negative ions formed are $Si(CH_3)_3^-$, and so R_1 would be the corresponding radical and R_2 would be CH_3. The energy of the C - Si bond in TMS is 71 kcal/mole which is relatively close to the activation energy for step (1).

Some of the radicals R_3, R_4, etc., may involve multiply bonded species which will be strongly bonded to the surface and will remain on the surface even when heated at ~2000°K in vacuum, only desorbing or incorporating at ~3000°K. Thus, the vacuum work function after reaction without a field will be affected by such species and will be higher than that for the clean surface. However, reaction with a field cuts down or excludes the formation of R_3, etc., and so the vacuum work function after reaction with a field will be much lower, as is the case (Figure 1-2). This surface probably corresponds to a mixed carbide/silicide.

In conclusion, the essential features of the work reported here are:

1. Negative surface ionisation begins to occur abruptly when the field at the emitting surface is increased.

2. The applied field causes a decrease in the coverage by reacting species, as well as a decrease in the energy of the desorption step (the Schottky effect).

3. A decrease of the coverage causes a decrease in the work function of the surface, and this favors the formation of negative ions.

4. The negative ions polymerise at the anode.

5. In the absence of a field, carbiding/siliciding of the tungsten filament predominates.

Future work on this topic will involve a study using rhenium as a filament material. This has the advantage that it does not carbide, and it will therefore be possible to confirm the above mechanism without the difficulties encountered in the present work due to changes in activity during carbiding and siliciding.

LEGENDS FOR FIGURES - PART 1

Figure 1-1 — Typical experimental data: ○, tetramethy Isilane; ▽, Hydrogen; □, methane.

Figure 1-2 — Richardson plots of vacuum thermionic emission data: line 1, clean filament; line 2, after reaction without a field; line 3, after reaction with a field.

Figure 1-3 — Effect of voltage V on rate of reaction R and emission current I: ○, rate of disappearance of TMS; rate of appearance of H_2, △; CH_4, □; C_2H_4, ▽; total emission current, ○; vacuum emission current, □.

Figure 1-4 — Plot of rate of reaction R versus total emission current I: ○, at V_c; □, below V_c; △, above V_c.

Figure 1-5 — Plot of log R versus log P for reaction without a field at 2000°K.

Figure 1-6 — Plot of log R versus 10^4 T°K for reaction without a field; ○, new surface; △, same surface after reaction with a field.

Figure 1-7 — Plot of V_c versus pressure P at a variety of inter-electrode separations; ○, ▽, +, 0.35 cm; □, 0.9 cm; △, 1.5 cm; ○, 2.05 cm. Filament temperatures: solid symbols, 1980°K; ○, 1820°K; +, 2140°K. The curves drawn represent the best fit to equation (12). The inset shows the electrode geometry.

Figure 1-8 — Plots ov V_c versus d. Symbsols as in Figure 1-7.

Figure 1-9 — Plot of $\varepsilon_c = \frac{V_c}{d + 1.3}$ versus p. Symbols as in Figure 1-7. The curve drawn is the best fit to equation (12).

Figure 1-10 Plot of $\varepsilon_c^{1/2}$ versus log p for separation d = 1.5 cm.

Figure 1-11 Plot of log R versus $\varepsilon^{1/2}$ at a filament temperature of 1980°K.

Figure 1-12 (a) Plots of log σ versus $\varepsilon^{1/2}$ for various filament temperatures; ○, 1870°K; □, 1914°K; △, 1960°K; data at 1850°, 1892° and 1938°K omitted for clarity.

(b) Plots of log σ versus 1/T°K for the data of Figure 1-12 (a) for various fields: line 1, 35V cm; line 2, 100V cm; line 3, 200V cm.

Figure 1-1. Typical Primary Data (Reaction Without Field)

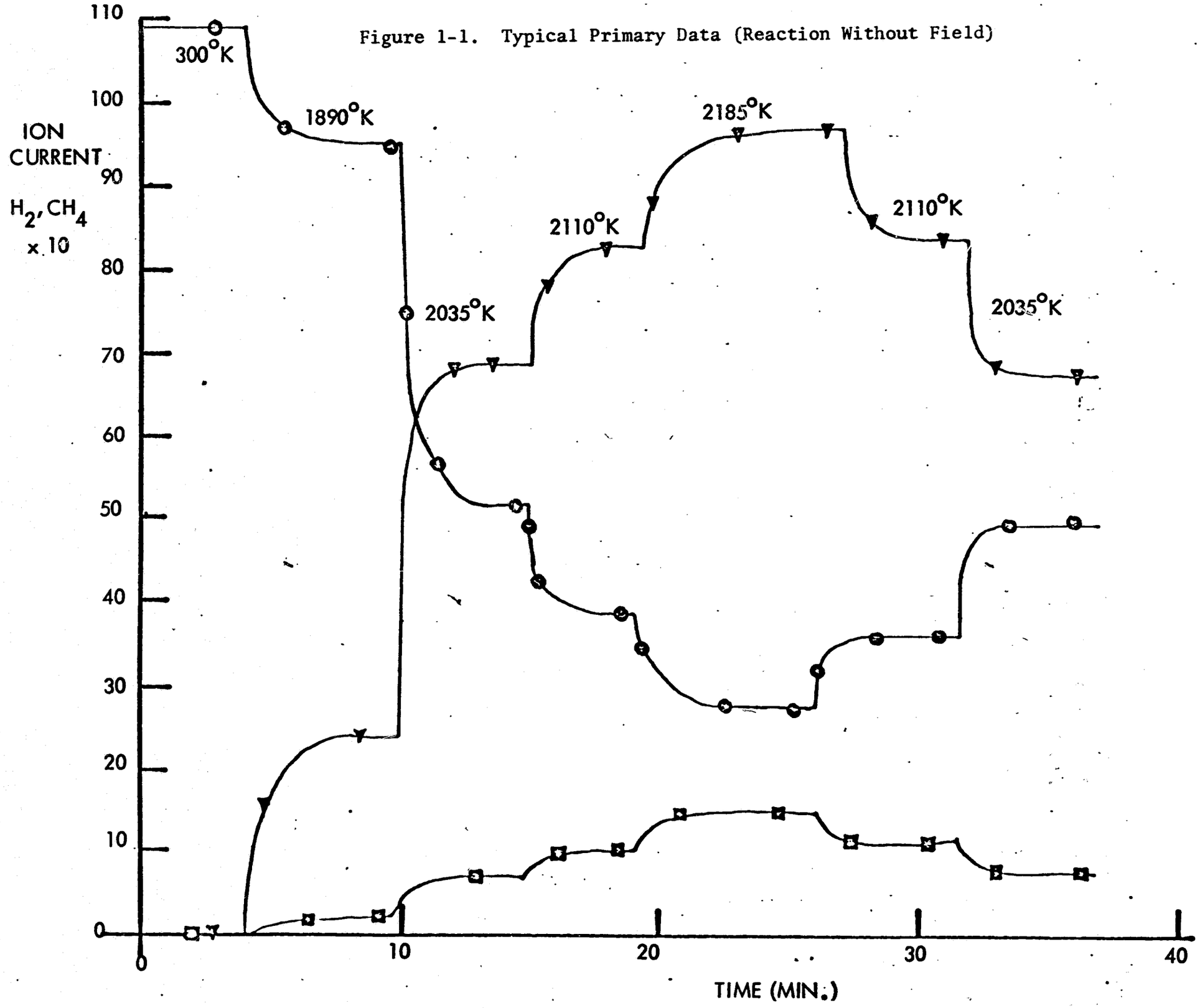


Figure 1-2

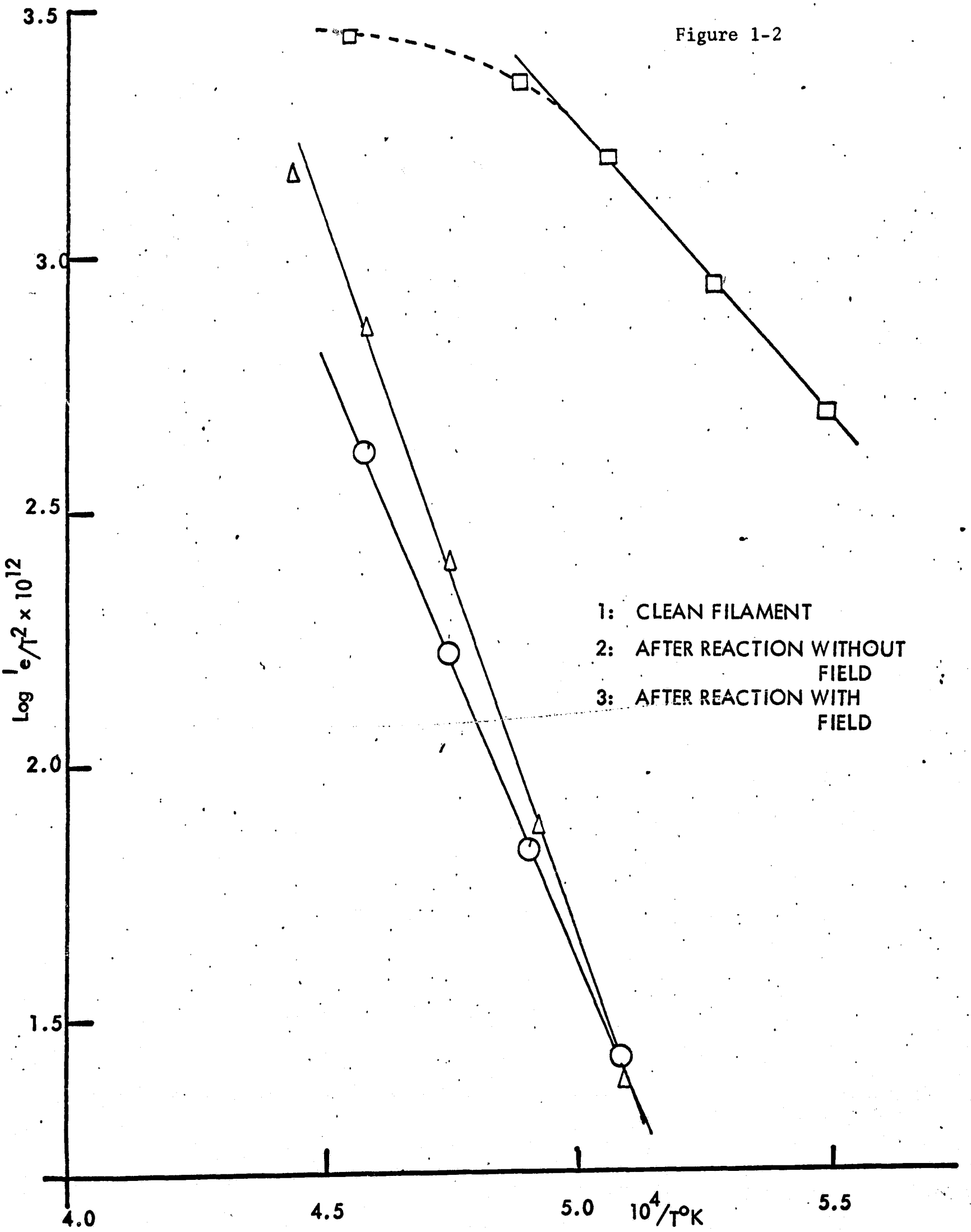
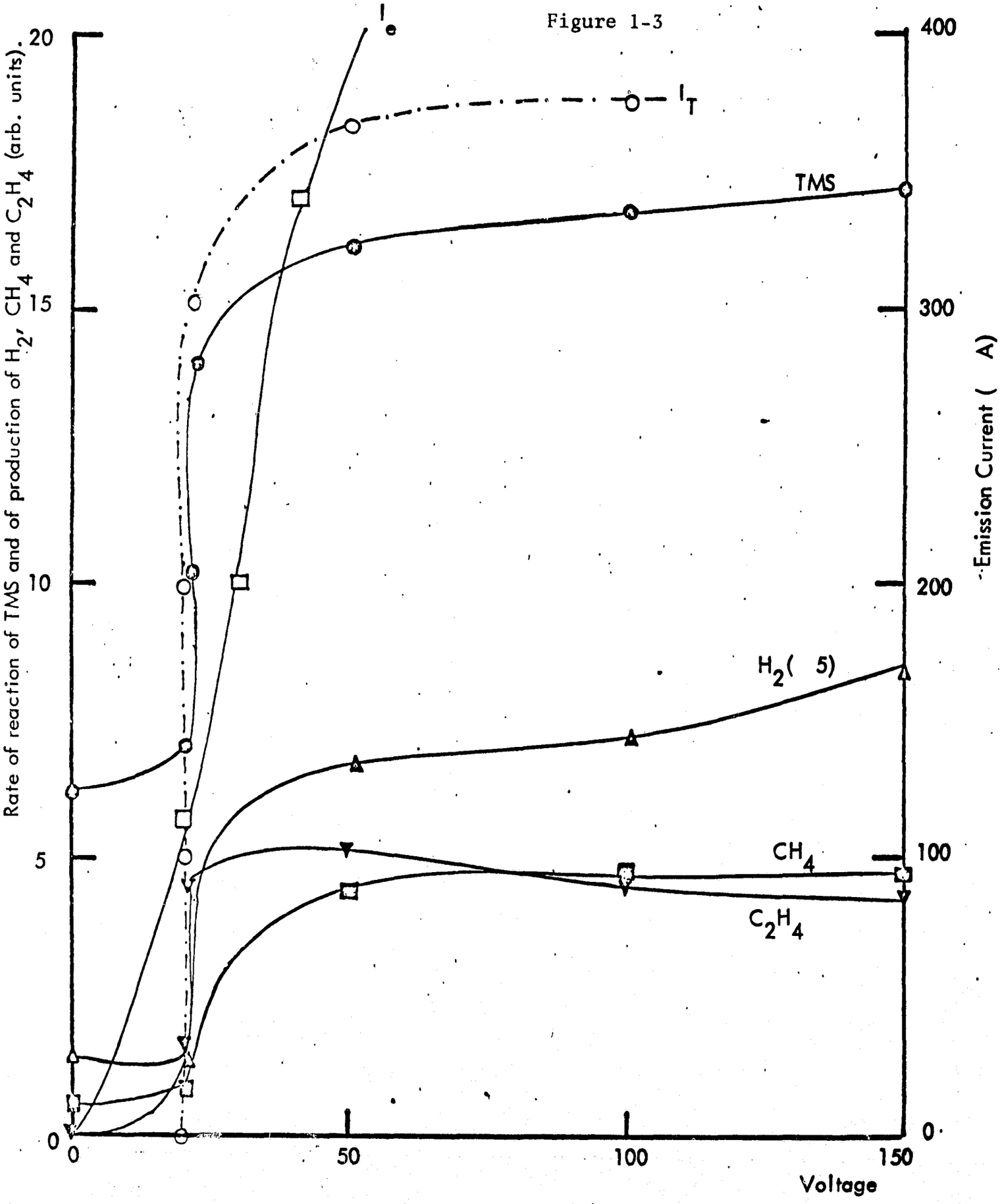

3.5
3.0
2.5
2.0
1.5
Log $I_e/T^2 \times 10^{12}$
4.0
4.5
5.0
5.5
$10^4/T°K$
1: CLEAN FILAMENT
2: AFTER REACTION WITHOUT FIELD
3: AFTER REACTION WITH FIELD

Figure 1-3


Rate of reaction of TMS and of production of H_2, CH_4 and C_2H_4 (arb. units).
Emission Current (A)
Voltage
I_e
I_T
TMS
H_2(5)
CH_4
C_2H_4
0
5
10
15
20
0
50
100
150
200
300
400
100

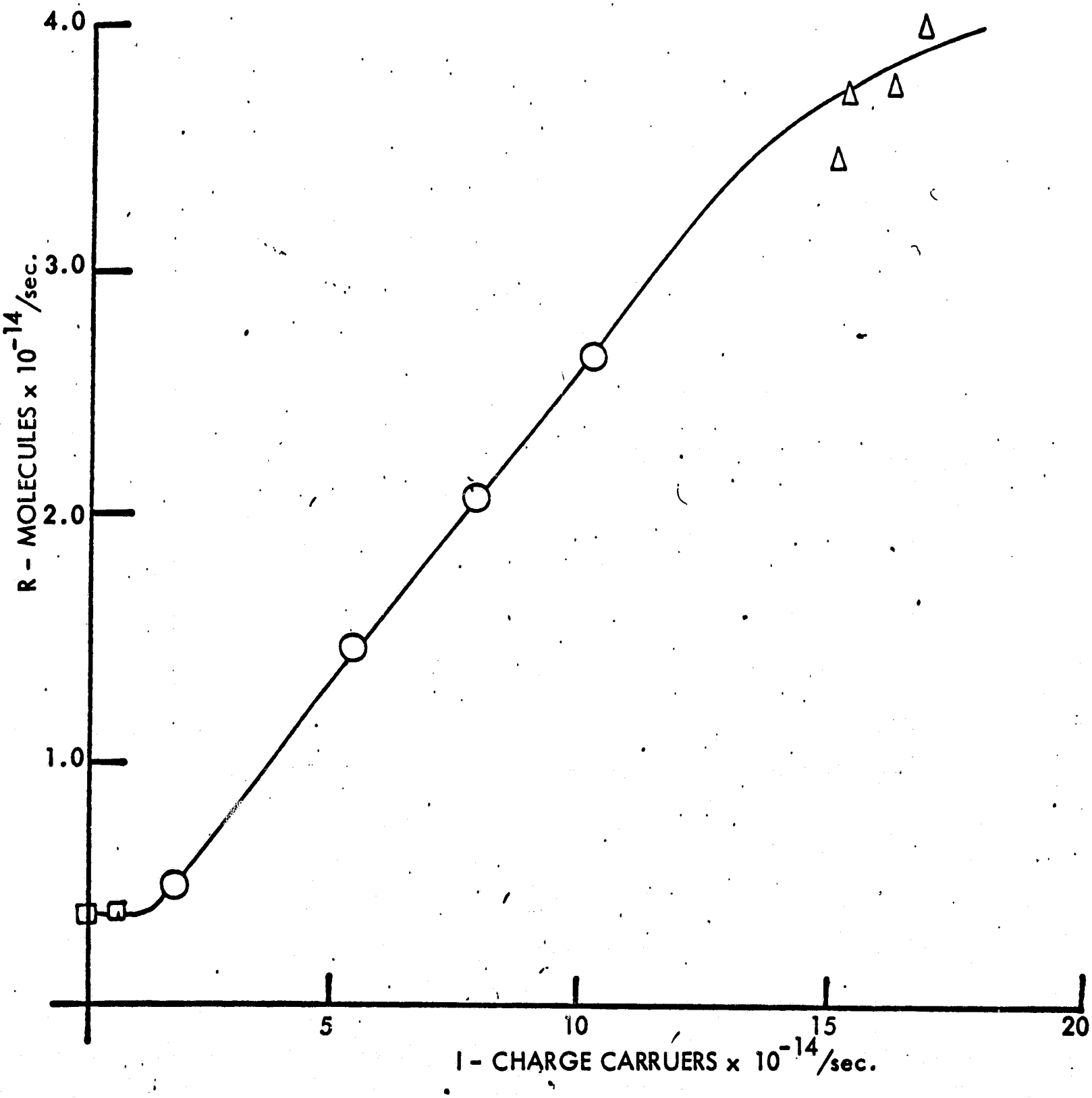

4.0
3.0
2.0
1.0
R - MOLECULES x 10^{-14}/sec.
5
10
15
20
I - CHARGE CARRUERS x 10^{-14}/sec.

Figure 1-4

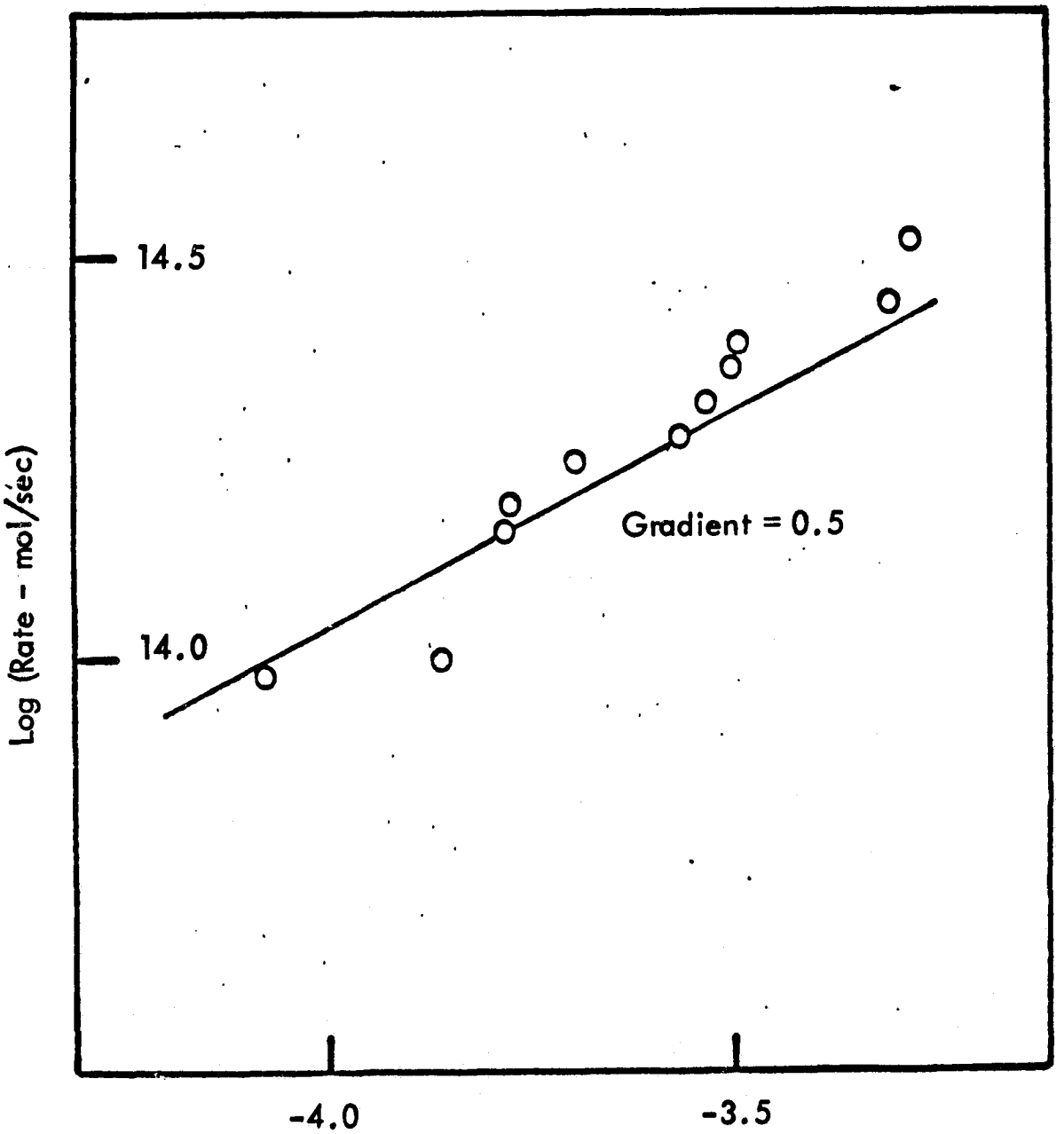


Figure 1-5

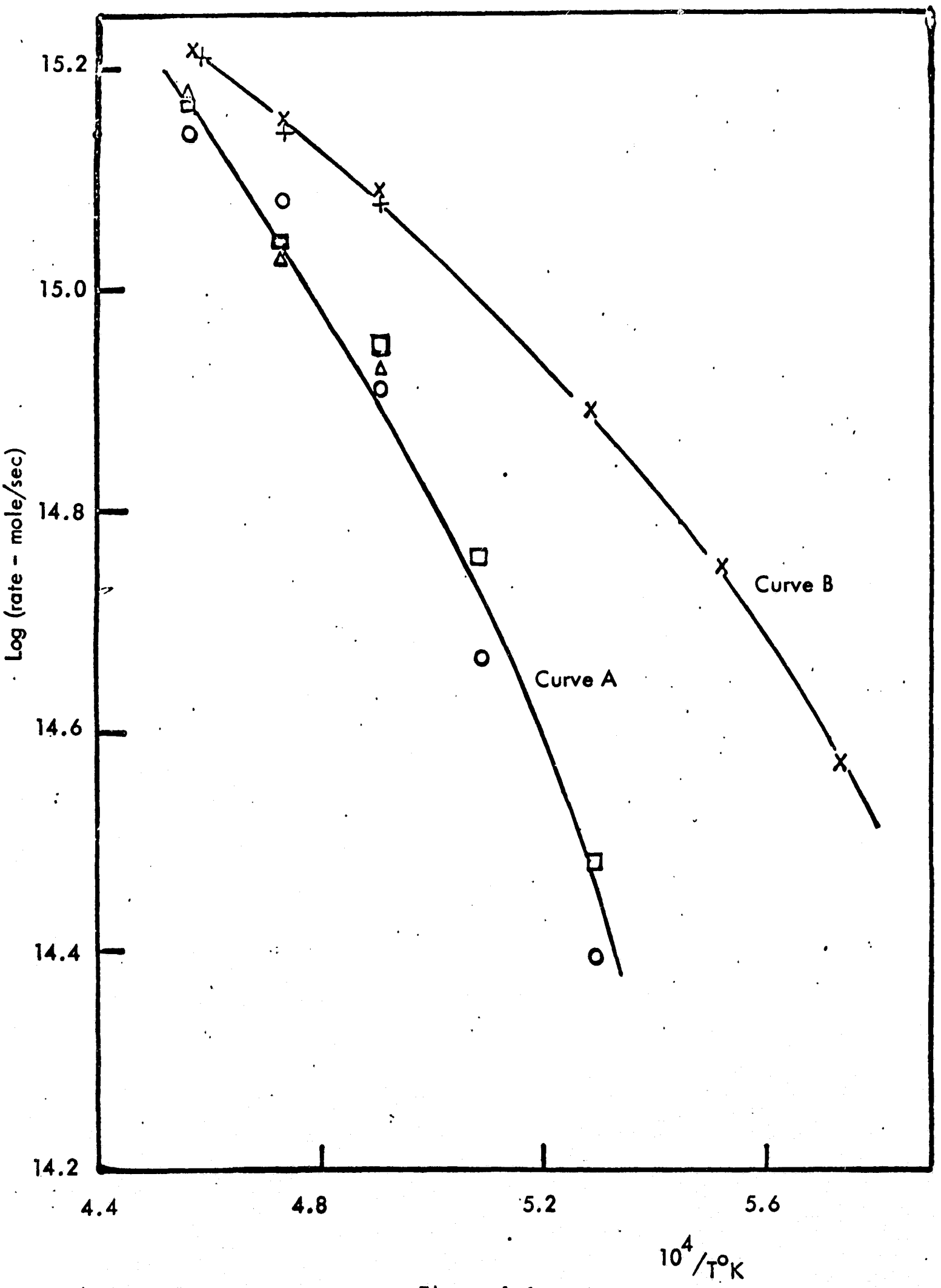

15.2
15.0
14.8
14.6
14.4
14.2
Log (rate - mole/sec)
4.4
4.8
5.2
5.6
$10^4/T^oK$
Curve A
Curve B

Figure 1-6

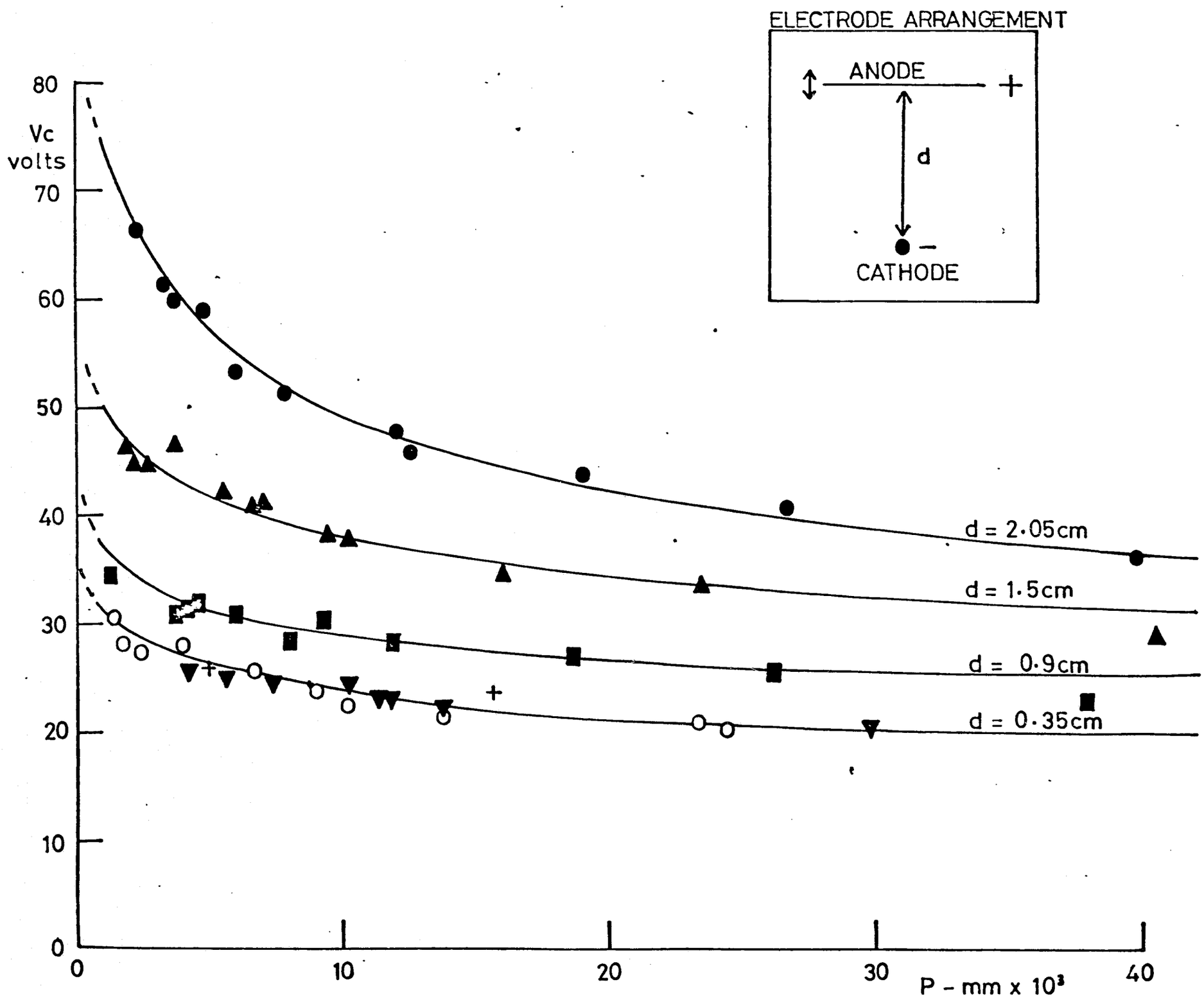

ELECTRODE ARRANGEMENT
ANODE
+
d
–
CATHODE
80
Vc
volts
70
60
50
40
30
20
10
0
0
10
20
30
40
P - mm x 10³
d = 2·05cm
d = 1·5cm
d = 0·9cm
d = 0·35cm

Figure 1-7

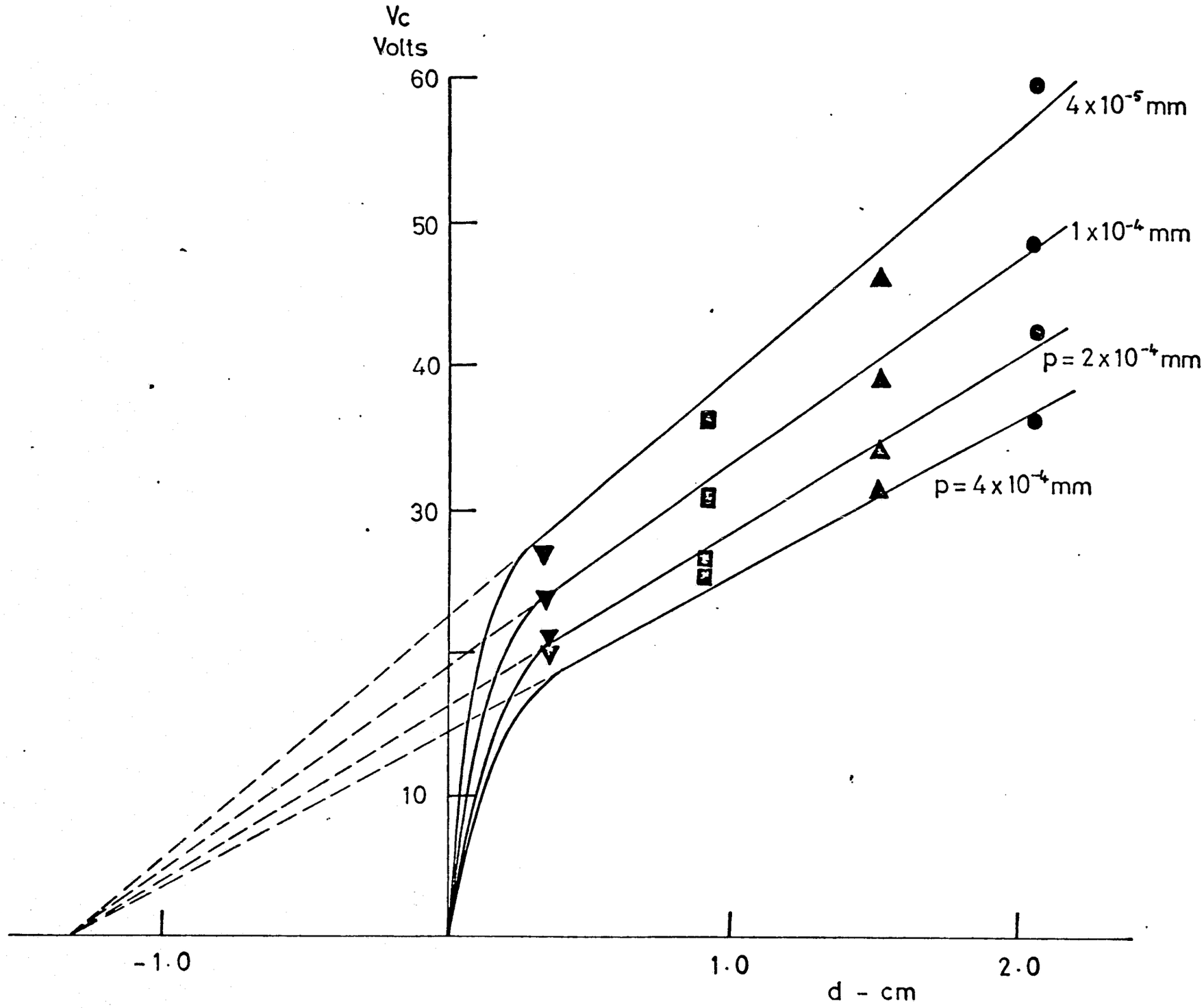

Vc
Volts
60
50
40
30
10
4 x 10⁻⁵ mm
1 x 10⁻⁴ mm
p = 2 x 10⁻⁴ mm
p = 4 x 10⁻⁴ mm
-1.0
1.0
2.0
d - cm

Figure 1-8

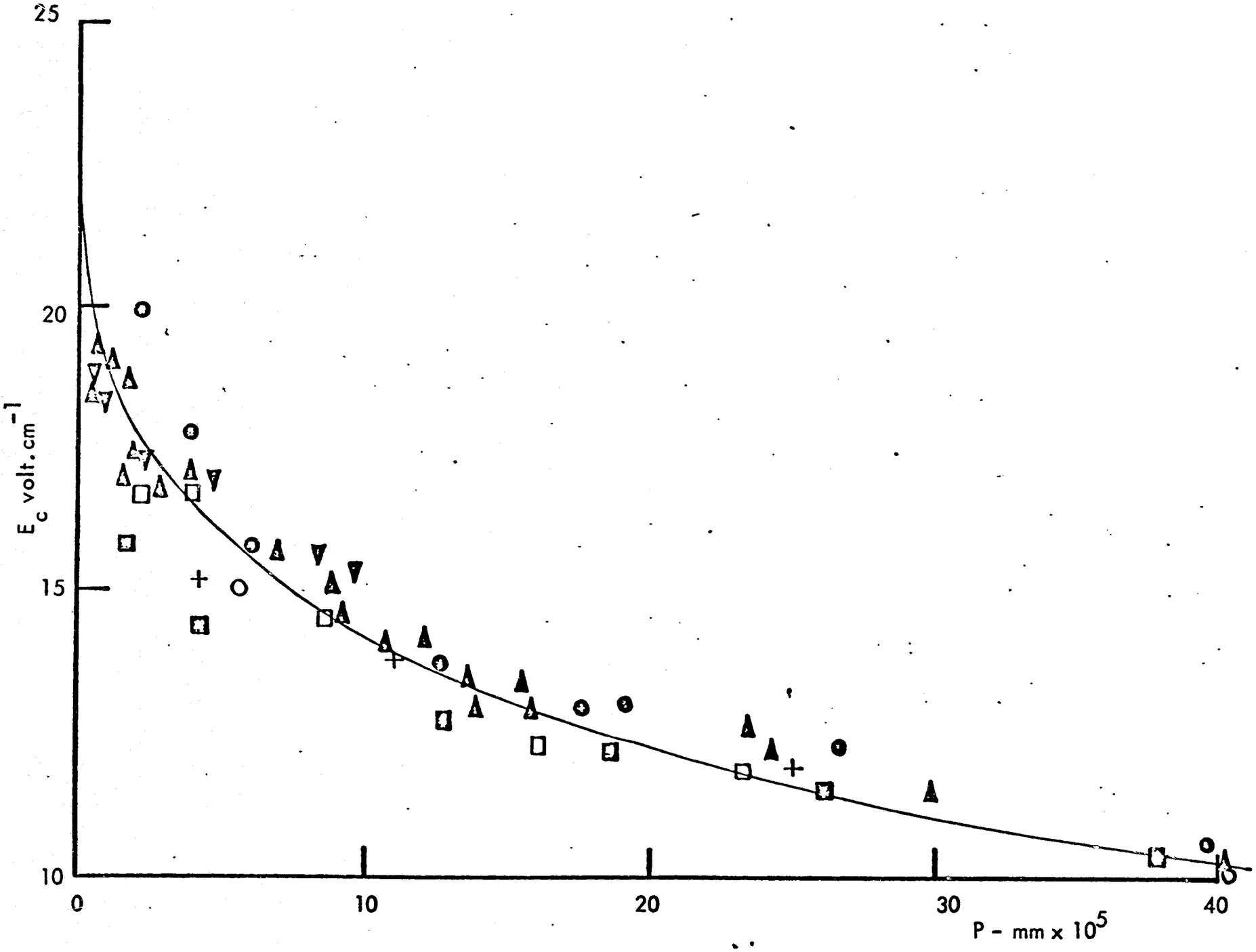


Figure 1-9

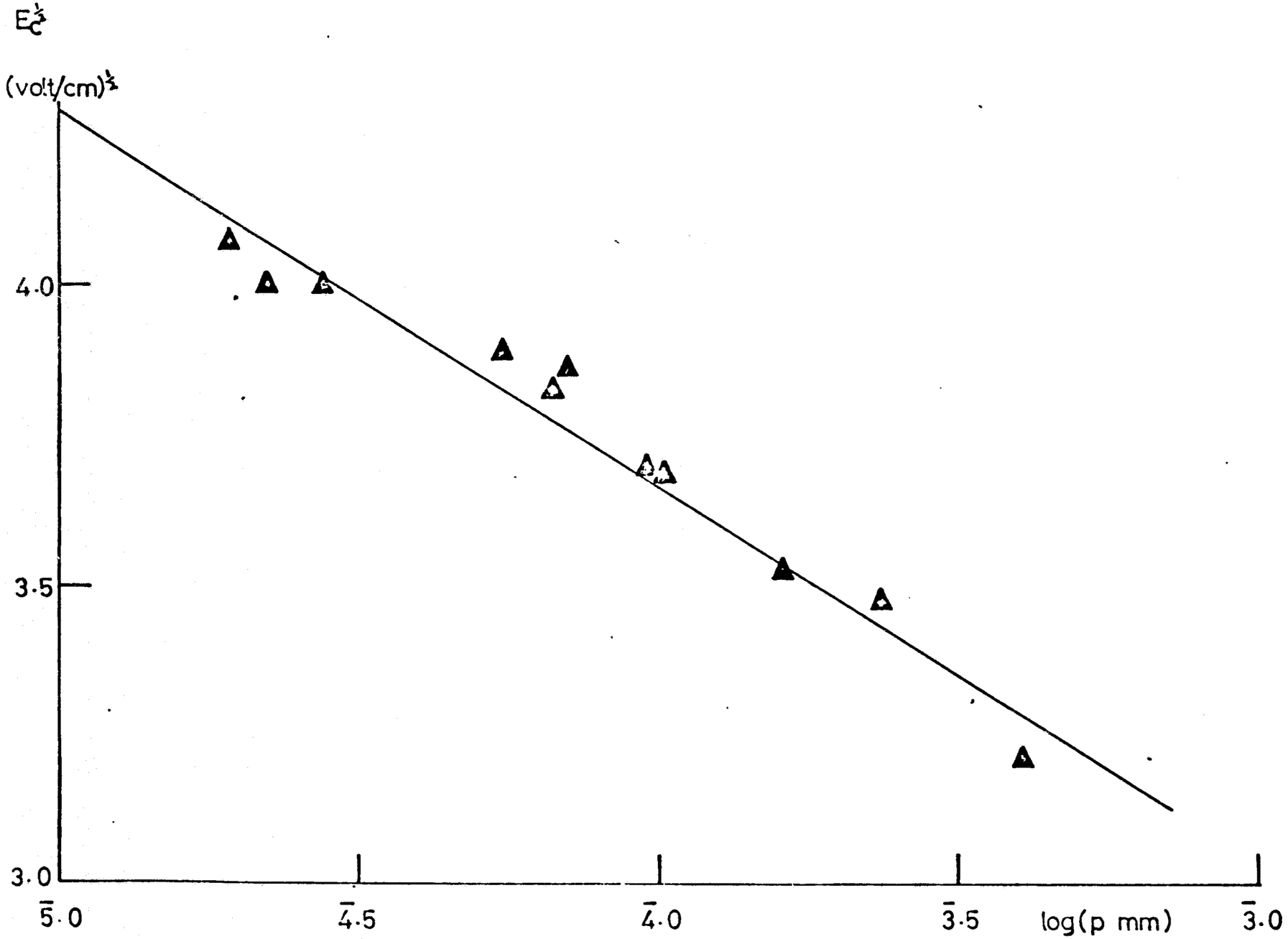

$E_c^{\frac{1}{2}}$
(volt/cm)$^{\frac{1}{2}}$
4.0
3.5
3.0
$\bar{5}.0$
$\bar{4}.5$
$\bar{4}.0$
$\bar{3}.5$
log(p mm)
$\bar{3}.0$

Figure 1-10

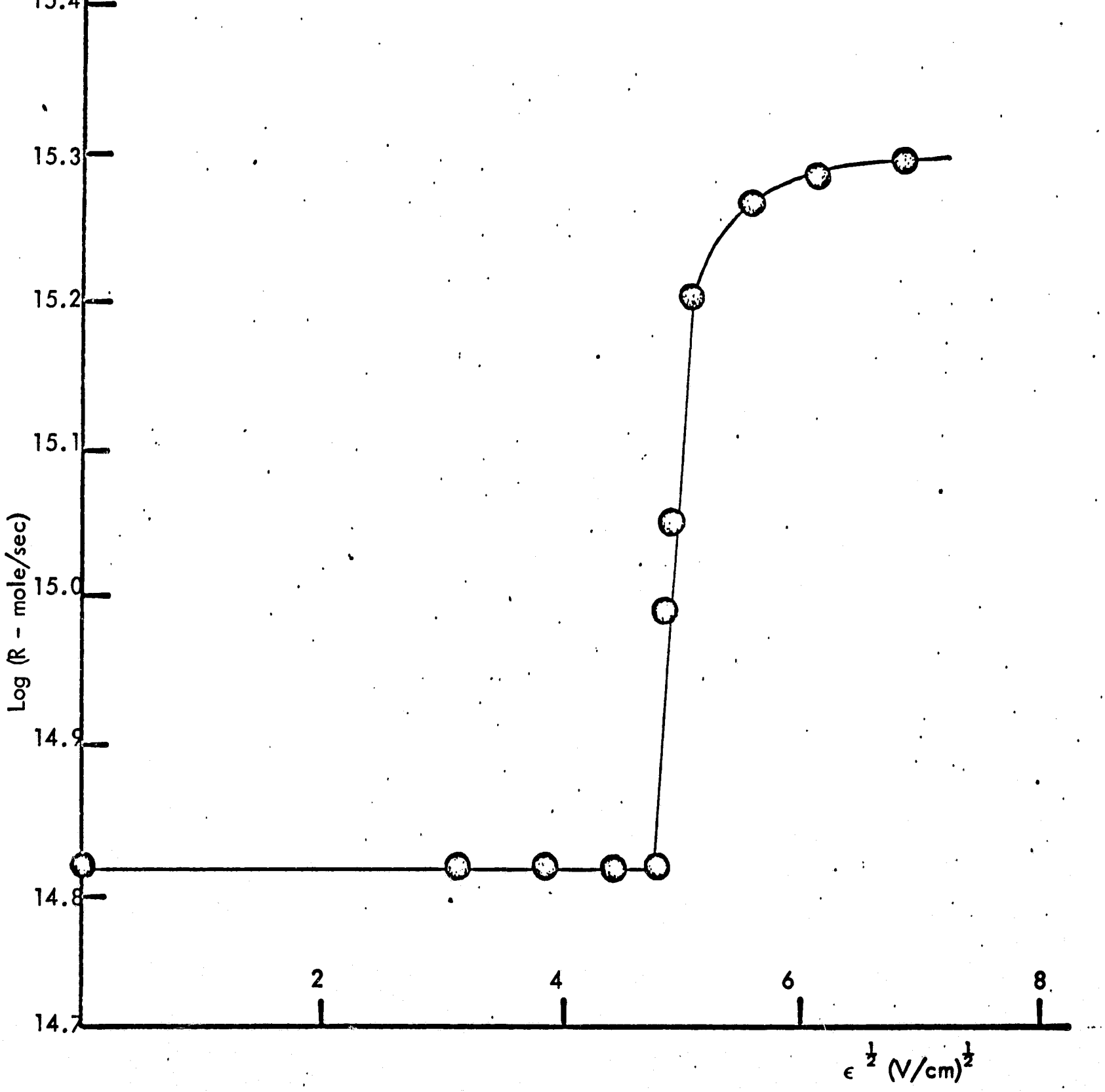

15.4
15.3
15.2
15.1
15.0
14.9
14.8
14.7
Log (R - mole/sec)
2
4
6
8
$\epsilon^{\frac{1}{2}}$ (V/cm)$^{\frac{1}{2}}$

Figure 1-11

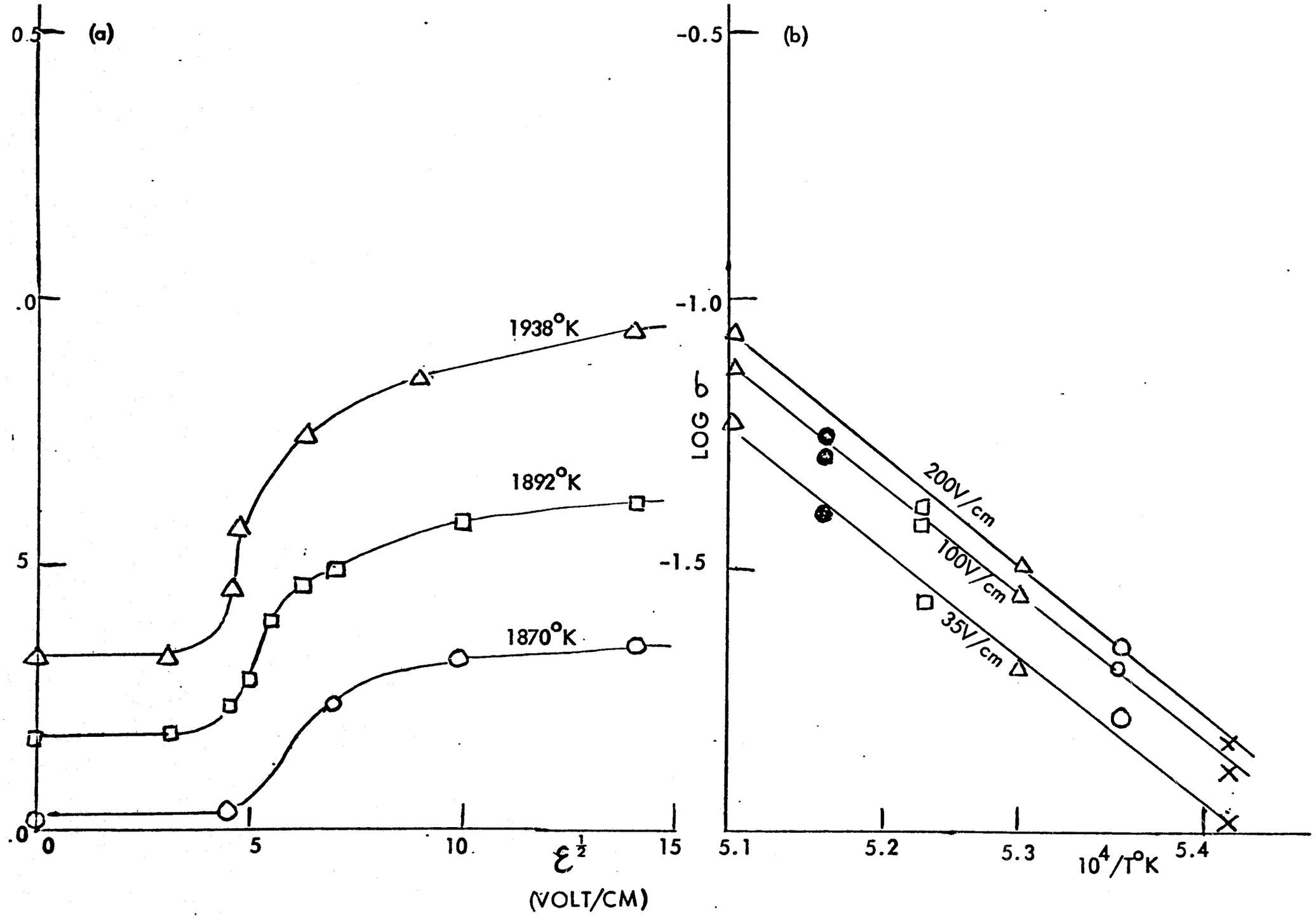

(a)
0.5
.0
5
0
1938°K
1892°K
1870°K
0
5
10
15
$\mathcal{E}^{\frac{1}{2}}$
(VOLT/CM)
(b)
-0.5
-1.0
-1.5
LOG b
200V/cm
100V/cm
35V/cm
5.1
5.2
5.3
5.4
$10^4/T°K$

Figure 1-12

2. MAGNETRON STUDY

The apparatus used for this part of the work was described in the second annual report[1]. It has been found necessary to alter some of the conditions of operation of the magnetron as no negative ions could be detected using those which were described, using a large number of monomers. Low voltages were required to obtain low values of the ratio I_A^*/I_A in vacuum, where I_A is the anode current with the solenoid off and I_A^* that with it on. The results reported in the first section would indicate that voltages greater than ~20V will be required before negative ions will be produced. On the other hand, the value of the ratio I_A^*/I_A increases with increasing voltage. Figure 2-1 shows typical results for the variation of I_A^* and I_G^* (the grid current) with solenoid current I; in these experiments, an equal voltage V_G was applied to the grids 1 and 2 and plates P, and a voltage V_A was applied to the anode, such that $V_A = (V_G + 30)$ volts, both voltages being positive with respect to the filament. For grid voltages of 10, 25 and 50V, the values of I_A^*/I_A are about 0.02, 0.03 and 0.06, respectively, for the maximum solenoid current of 4.6A. The total emission current ($I_A^* + I_G^*$) decreased slightly at higher solenoid currents, but at no stage was a "cut-off" attained. The relatively high values of I_A^*/I_A obtained indicate that an appreciable proportion of the electrons emitted from the filament in vacuum are able to penetrate to the anode with the solenoid on. It is therefore assumed that in the presence of monomer and with the same solenoid current, a similar proportion of electrons which are emitted from the filament reach the anode. This assumption makes it possible to make a correction to I_A^* which removes the contribution due to electrons. Similarly, with the solenoid off, a proportion of the electrons emitted in vacuum are collected by the grid, and using this fraction, a small correction to I_A^* may also be made to allow for the negative ions collected by the grid. Hence I_N, the negative ion current, and I_e, the electron current, may be derived from a measurement of I_A^* and I_G^* under any experimental conditions. A value of V_G of 30V was used in the experiments to be reported.

Resistance measurements were made using a Wheatstone Bridge circuit, slightly different ones being used for hot and cold resistances.

Three monomers, tetramethy Isilane, butadiene, and neopentane, have been studied. The first was chosen because of its relevance to the mass spectrometer study, the second because it was examined in earlier studies[1] and because it has been used in other studies of polymer film production[6], and the last because of its similarity to tetramethy Isilane. Since neopentane contains only carbon and hydrogen, carbiding of the tungsten filament can be examined by resistance techniques; it also enables a comparison to be made between carbon and silicon containing compounds.

Figure 2-2 shows typical primary data for experiments with TMS with a tungsten filament maintained at 1980°K at a variety of TMS pressures. By making the corrections discussed above, Figure 2-3 results. This shows that a linear increase of I_N occurs with increasing pressure, while the electron current simultaneously decreases, rapidly initially at low pressures and then more slowly and almost linearly with increasing pressure at higher pressures. This result fits in well with the theory outlined in the first section.

The voltage V_G is well above the critical voltage V_C, and so the rate determining step is probably the formation of the intermediate adsorbed species, which will depend directly on the TMS pressure, as shown in Figure 2-3. As the coverage of adsorbed intermediates increases, electron emission will decrease from the vacuum value, as is observed, due to a gradual increase in the work function of the surface with increasing coverage. Both I_N and I_e increase with increasing filament temperature. Figure 2-4 shows plots of log I_N and log I_e versus I/T for data obtained at a pressure of 2.0×10^{-3} mm of TMS. Activation energies for ion and electron desorption calculated from these two lines are 5.9 and 3.8 eV, respectively. The value of 5.9 eV or 135 kcal/mole is not far from the value of ~110 kcal/mole obtained in the first section for the rate of disappearance of tetramethy Isilane, and this result helps to lend weight to the assumption that the latter measurement is equivalent to measuring the negative ion current.

Analogous results to those obtained for tetramethy Isilane have been obtained with neopentane and butadiene. Figure 2-5 shows the dependence of I_N and I_e on the pressure of neopentane at a filament temperature of 1950°K. The

behavior is very similar to that observed with tetramethy Isilane. Figure 2-6 shows log I_N and log I_e versus I/T plots for two pressures. Both pairs of lines are parallel, indicating that the activation energy for ion and electron production is essentially constant, at least over the straight line portion of the plots of Figure 2-5. The activation energies of ion and electron production are 4.8 and 3.9 eV, respectively. Figures 2-7 and 2-8 show the equivalent results for butadiene. The relationship between I_N and pressure is non-linear and may reflect a different type of reaction occurring in the formation of the adsorbed species or a different rate determining step in the formation of the negative ions. From Figure 2-8, the activation energies for the formation of negative ions and electrons are calculated to be 4.5 eV and 3.8 eV, respectively. In no case was it possible to examine the vacuum emission after an experiment, as the emission changed rapidly together with a high rate of desorption from the anode. It should be noted that the activation energy for desorption of electrons with the three monomers was close to 3.8 eV. This will be discussed below.

Figure 2-9 shows results for the carbiding of the tungsten filament during reaction with neopentane, obtained from resistance measurements. Figure 2-9 (a) depicts the change of cold resistance of the filament (obtained by cooling the filament at various stages) plotted against the time of reaction. Curve A shows the change in resistance for reaction with a field and curve B that for reaction without a field. Figure 2-9 (b) shows corresponding hot resistance changes (measured continuously during reaction) and 2.9 (c) shows the change in emission in the presence of monomer with time during reaction with a field.

Consider first the reaction with a field. The change in cold resistance is much more rapid than without a field. If it is assumed that the maximum cold resistance corresponds to the formation of only W_2C, the extent of carbiding is calculated to be about 40%, using resistance data for W_2C given by Andrews[7]. The cold resistance drops off slowly after the maximum is reached; since the resistivity of WC is lower than that of W_2C, it is suggested that this corresponds to the formation of WC. This is borne out by the fact that the hot resistance continues to increase. The difference of behavior indicates a different temperature coefficient of resistance

and therefore a different filament composition in the later stages of carbiding. Similarly, the emission behavior supports the assumption, as the activation energy for electron production obtained for electron desorption in the presence of monomer and which we assume is approximately equivalent to the vacuum work function is ~3.8 eV, which is close to that for the reported value for WC[8]. It would thus appear that after the first ten minutes of carbiding, the surface of the filament is essentially that of WC, although the bulk composition is still a mixture of W, W_2C and WC. It is interesting to note that the surface obtained with tetramethy Isilane, neopentane and butadiene has essentially the same activation energy for electron desorption. It would thus appear that the decomposition of tetramethy Isilane with a field gives only carbiding; i.e., all the silicon of the TMS is desorbed in the negative ions and other species, such as adsorbed CH_3 groups, give rise to carbiding as well as desorption of H_2 and CH_4, etc.

For reaction without a field, the situation is different. The cold resistance at no stage approaches that for carbiding with a field and yet the hot resistance exceeds that with a field after a time. It must therefore be postulated that the reaction is throughout forming W_2C, which would agree with results of previous workers for other hydrocarbons[7] and also agrees with the assumption regarding the initial stages of the reaction with a field. The latter point is borne out by an experiment which was carried out in which the field was switched on after reaction had been carried out for some time without a field. The emission was high, as expected for a W_2C surface, but fell off rapidly as after the peak in Figure 2-9 (c). Figure 2-10 shows more detailed results of an experiment of the type shown in Figure 2-9, line B. Figure 2-10 (a) illustrates the variation of hot resistance obtained during the carbiding of tungsten by neopentane without a field at 2100°K. After each point was taken, the cell was evacuated and data was obtained, over a slightly lower range of temperatures, for Richardson plots. Figure 2-10 (b) shows the vacuum emission at 1700°K and Figure 2-10 (c) shows the corresponding vacuum work function corresponding to the data depicted in Figure 2-10 (a). The work function of the surface drops from about 5.4 eV to a value of about 2 eV after about 80 minutes carbiding. Due to a compensation between the pre-exponential factor in

the Richardson equation and the work function, the emission current does not vary by nearly as much as might be expected; this compensation is illustrated in Figure 2-11.

Figure 2-12 shows the resistance data for butadiene. The hot resistance and emission data are similar to those of neopentane, but it was found that if, at a point B during the rapid change in resistance A to D, the filament was cooled to room temperature, the subsequent change in resistance followed BC; i.e., parallel to DE but of lower magnitude. It would appear that this is caused by a change in the nature of the surface during the cycle to room temperature. This change is probably due to the formation of WC being favoured over the formation of W_2C at some intermediate temperature, the surface remaining essentially that of WC on increasing the temperature back to reaction temperature. This probably occurs with butadiene (C_4H_6) and not with neopentane (C_5H_{12}) because of the relatively higher proportion of carbon as opposed to hydrogen in the former compound, and this will favour the formation of WC rather than W_2C.

2

Future work will involve an investigation of the formation of negative ions from various monomers on the surface of a metal which does not carbide. Initially, rhenium will be used, with neopentane as a monomer. The investigation will include a magnetron study, the determination of the kinetics and mechanism of the disappearance of the monomer using the mass-spectrometric flow system, and an examination of the nature of the negative ions produced. The work will then be extended to an examination of the reaction of the negative ions with metal surfaces and an investigation of the processes occurring during electron bombardment of the completed polymer.

LEGENDS FOR FIGURES - PART 2

Figure 2-1 — The variation of anode current (I_A*) and grid current (I_G*) with increasing solenoid current I, for the magnetron in vacuo.

Figure 2-2 — Typical primary data for the variation of the measured magnetron currents with increasing pressure of tetramethy Isilane. I_A and I_G are the anode and grid currents, respectively, without a magnetic field; I_A* and I_G* are the equivalent currents with the magnetic field. Filament temperature = 1980°K.

Figure 2-3 — Corrected electron current, I_e, and corrected ion current, I_N, as a function of pressure of tetramethy Isilane.

Figure 2-4 — Arrhenius plots (log I versus I/T) for the variation of I_N and I_e with temperature for tetramethy Isilane.

Figure 2-5 — The variation of I_N and I_e with pressure for neopentane. Filament temperature = 1950°K.

Figure 2-6 — Arrhenius plots for neopentane.

Figure 2-7 — The variation of I_N and I_e with pressure for butadiene. Filament temperature = 1820°K.

Figure 2-8 — Arrhenius plots for butadiene.

Figure 2-9 (a) — The change of cold resistance of the filament as a function of time for the carbiding with neopentane at 1950°K. Line A is for reaction with a field and line B is for reaction without.

(b) — The change of not resistance for the same experiments.

Figure 2-9 (c) The total emission (I_N and I_e) during the reaction with a field, corresponding to line A in (a) and (b).

Figure 2-10 (a) The variation of hot resistance during the carbiding of tungsten with neopentane without a field at 2100°K.

(b) Vacuum emission data at 1700°K obtained after each point in (a).

(c) The corresponding work functions calculated from Richardson plots.

Figure 2-11 Plot of the work function shown in Figure 2-10 (c) versus the log of the pre-exponential factor of the Richardson equation.

Figure 2-12 (a) The change of hot resistance with time of reaction of butadiene with a field, at a filament temperature of 2050°K. Line B resulted from an experiment in which the filament was cooled to room temperature and reheated at point B.

(b) The variation of total emission with time corresponding to line ABDE.

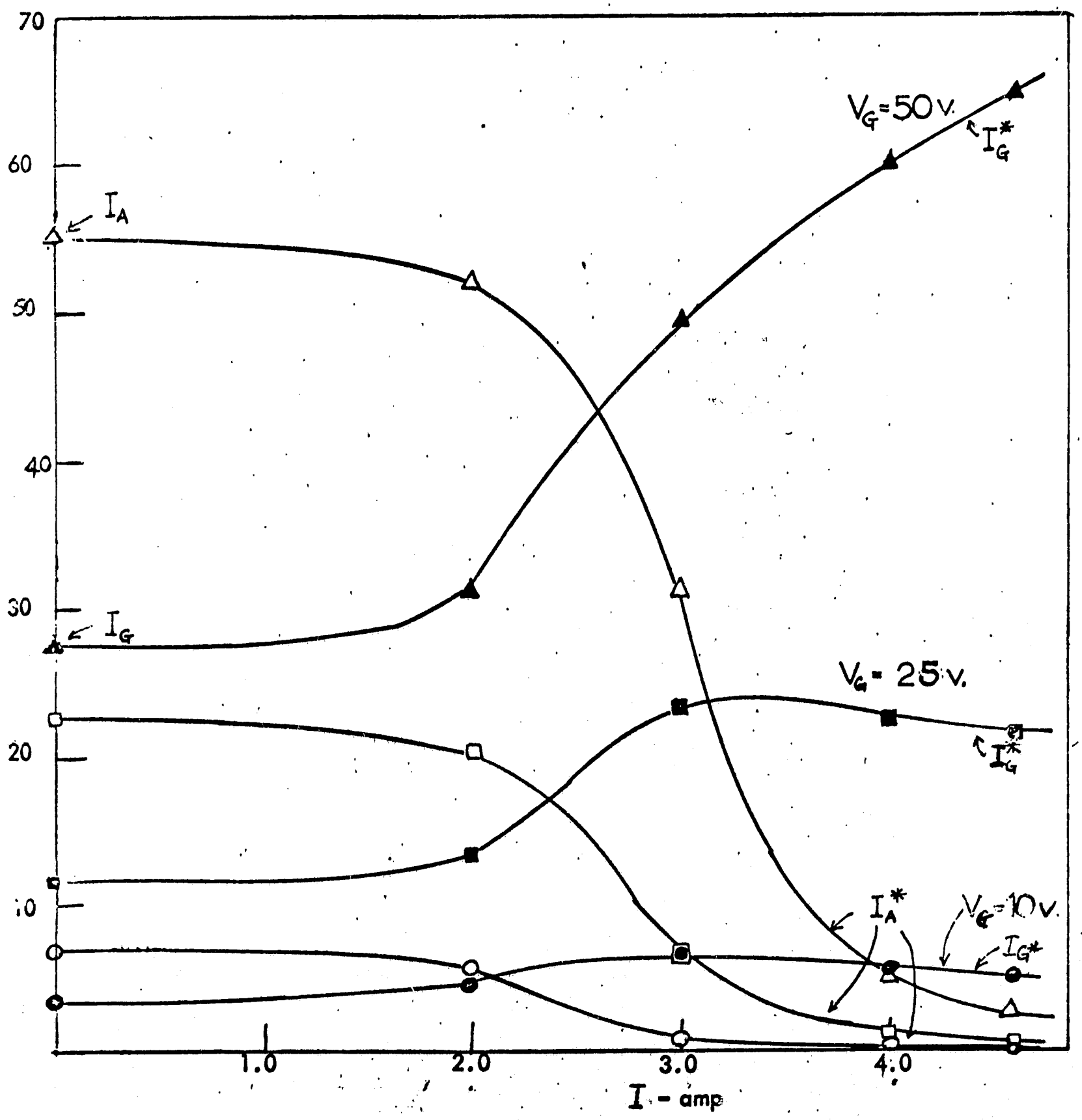

70
60
50
40
30
20
10
I - mA
I_A
I_G
V_G=50 v.
I_G^*
V_G= 25 v.
I_G^*
I_A^*
V_G=10 v.
I_G^*
1.0
2.0
3.0
4.0
I - amp

Figure 2-1

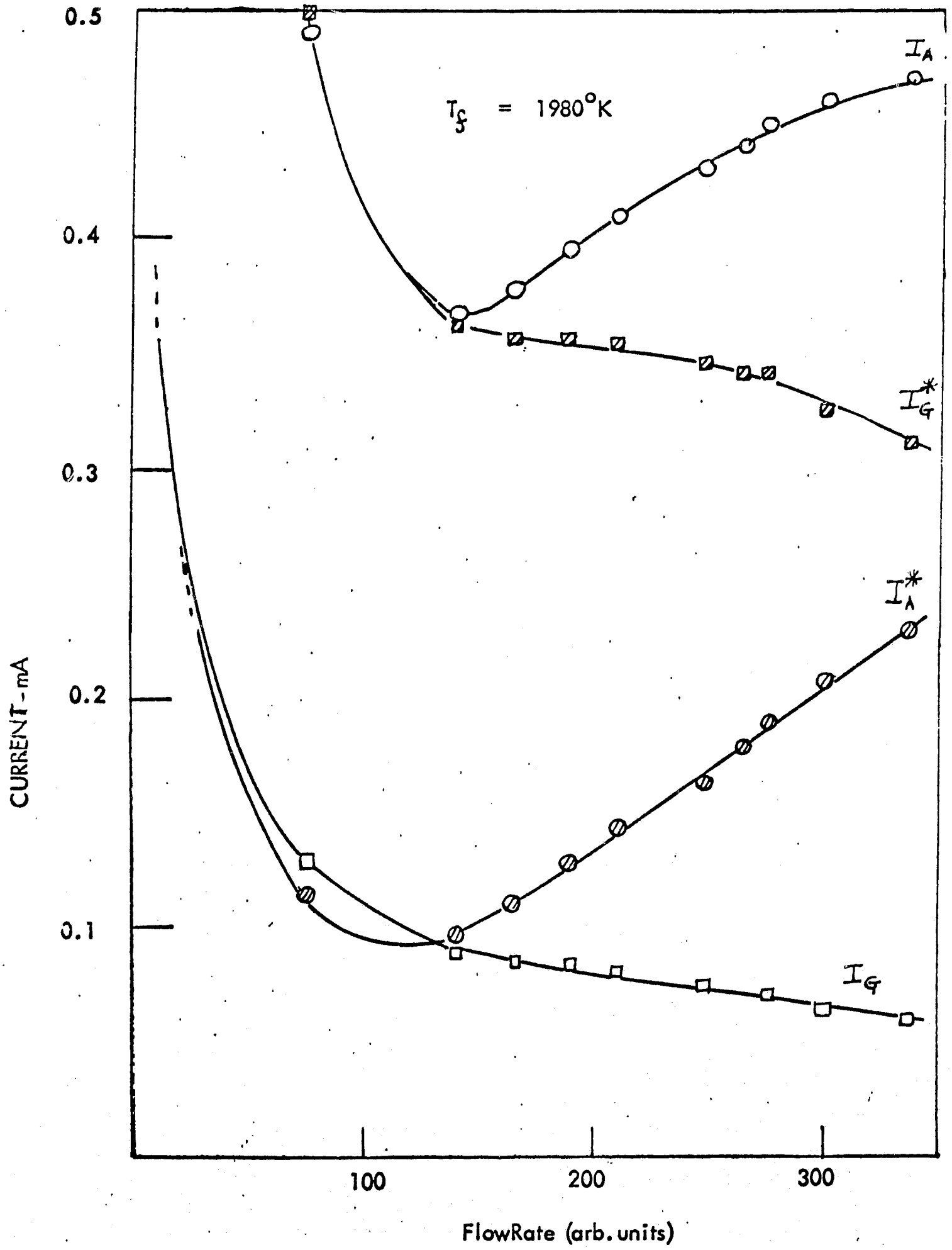

0.5
0.4
0.3
0.2
0.1
CURRENT-mA
T_f = 1980°K
I_A
I_G^*
I_A^*
I_G
100
200
300
FlowRate (arb. units)

Figure 2-2

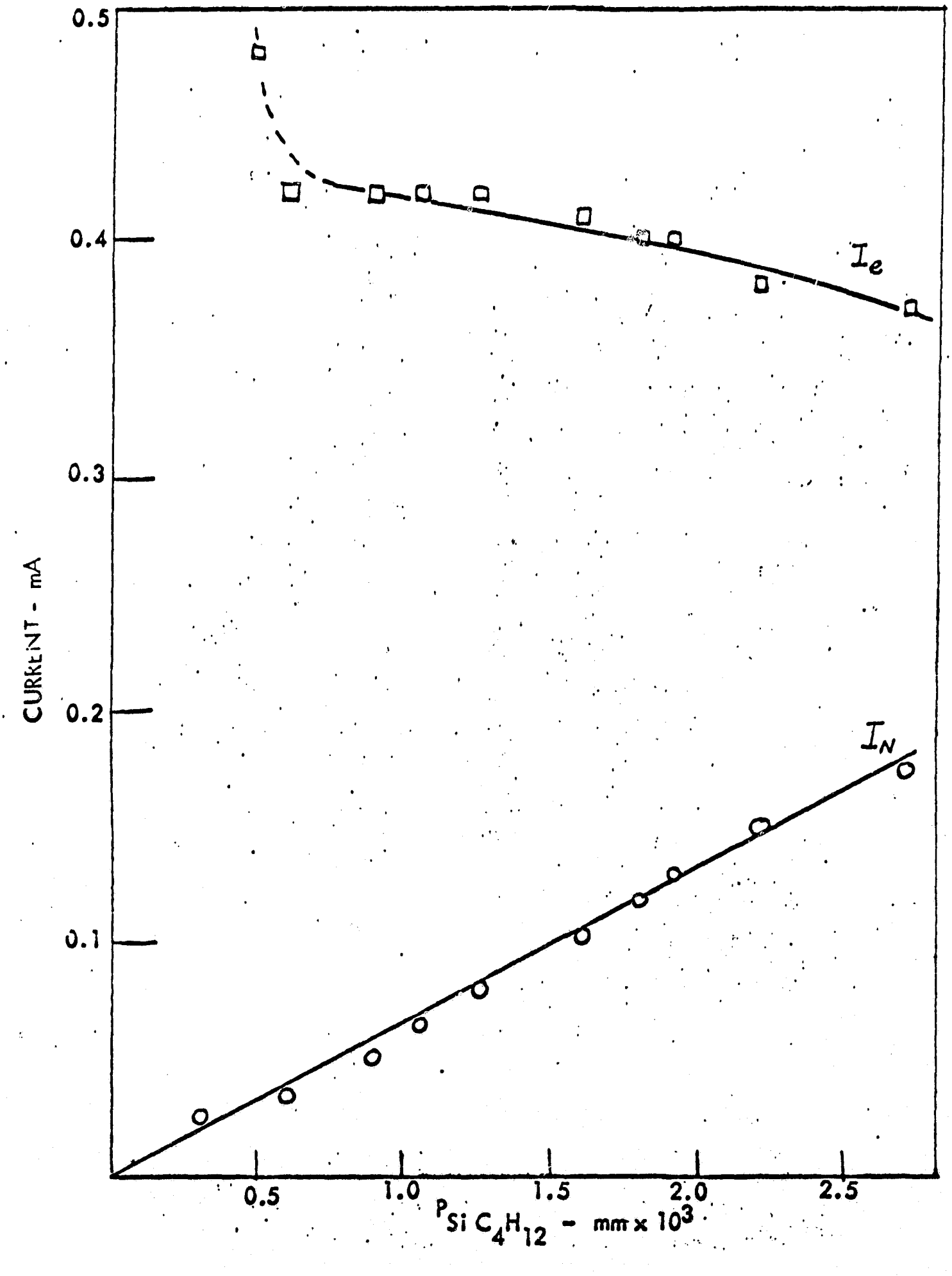


Figure 2-3

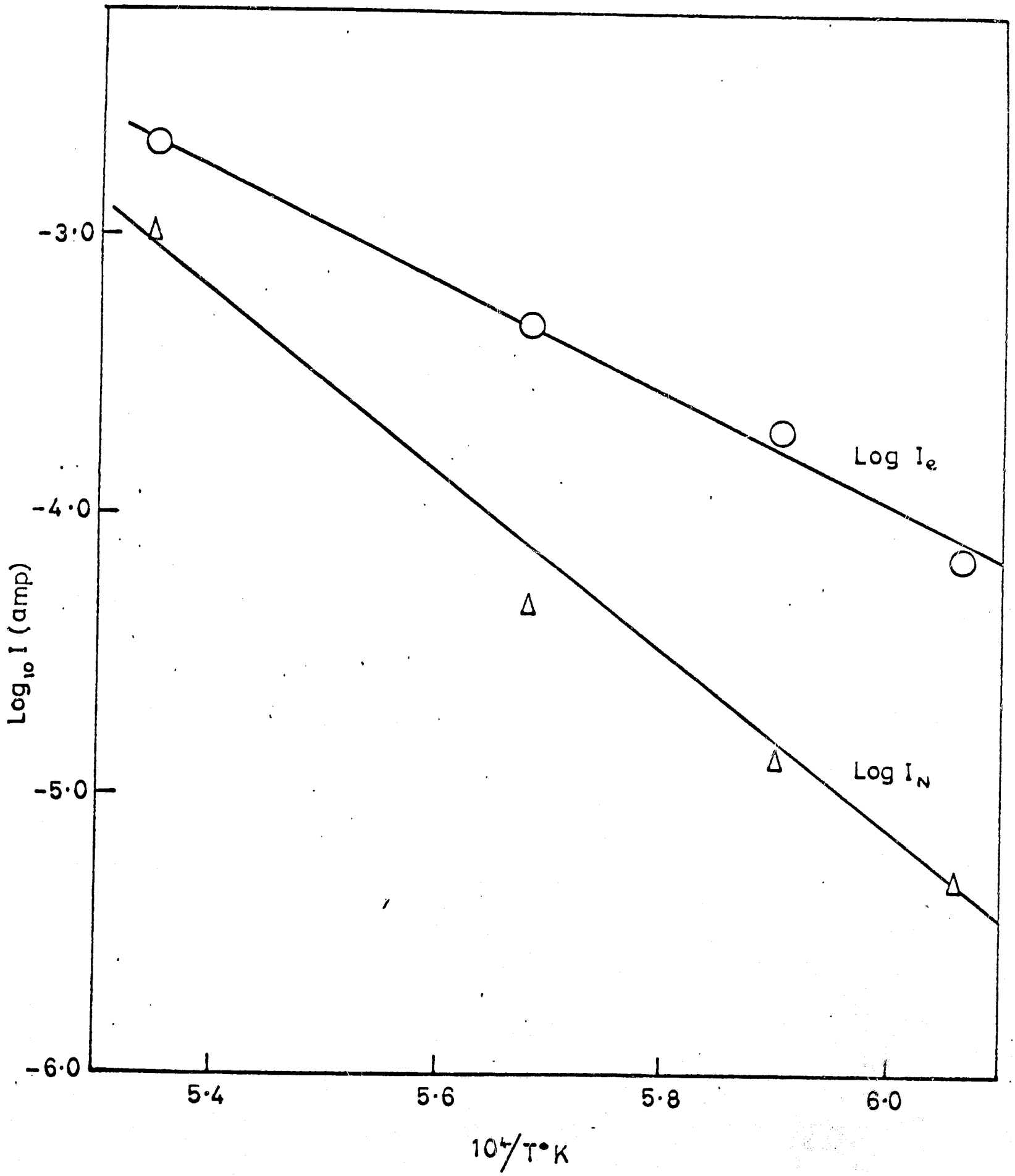


Figure 2-4

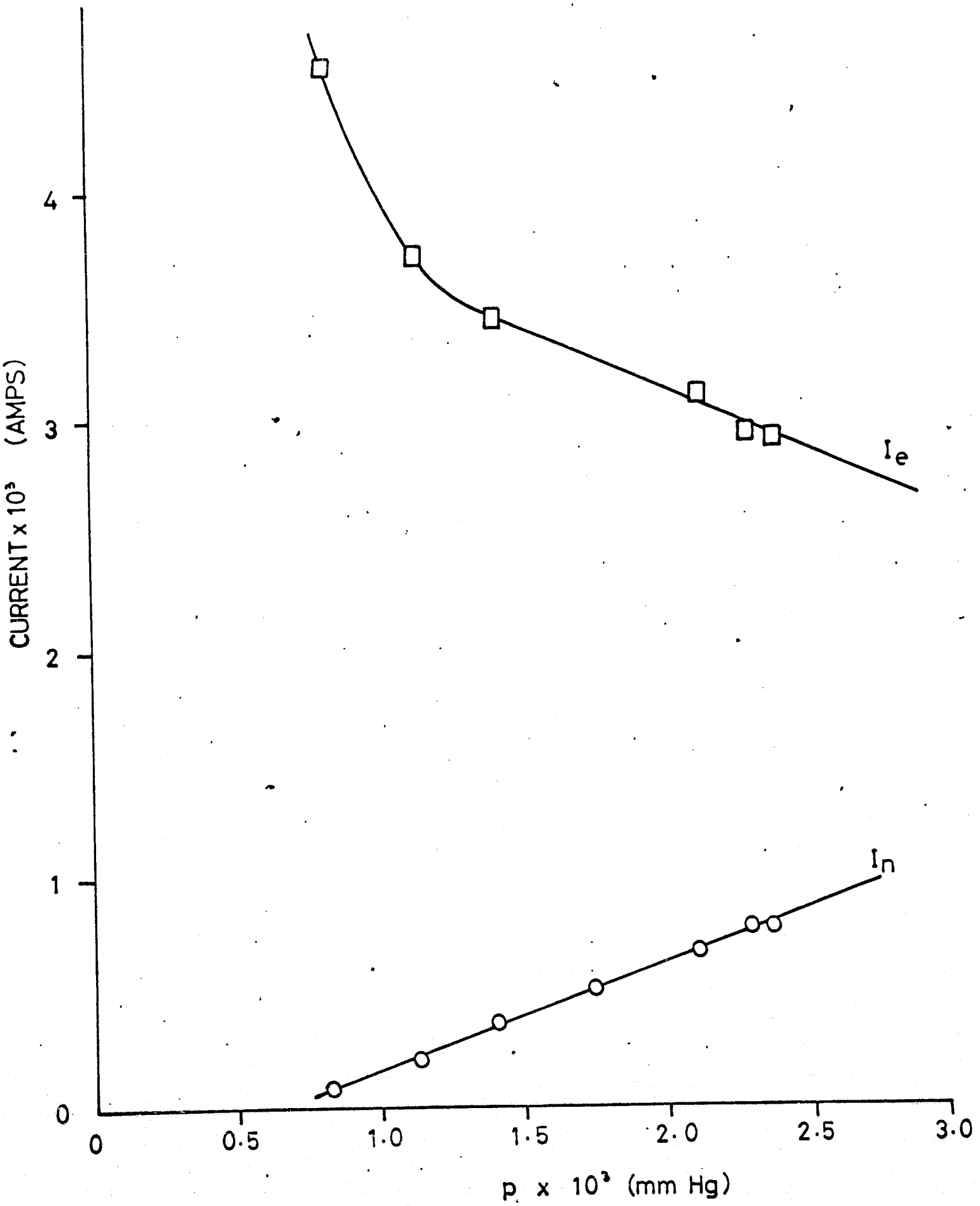

NEOPENTANE
CURRENT x 10³ (AMPS)
4
3
2
1
0
0
0.5
1.0
1.5
2.0
2.5
3.0
p x 10³ (mm Hg)
Ie
In

Figure 2-5

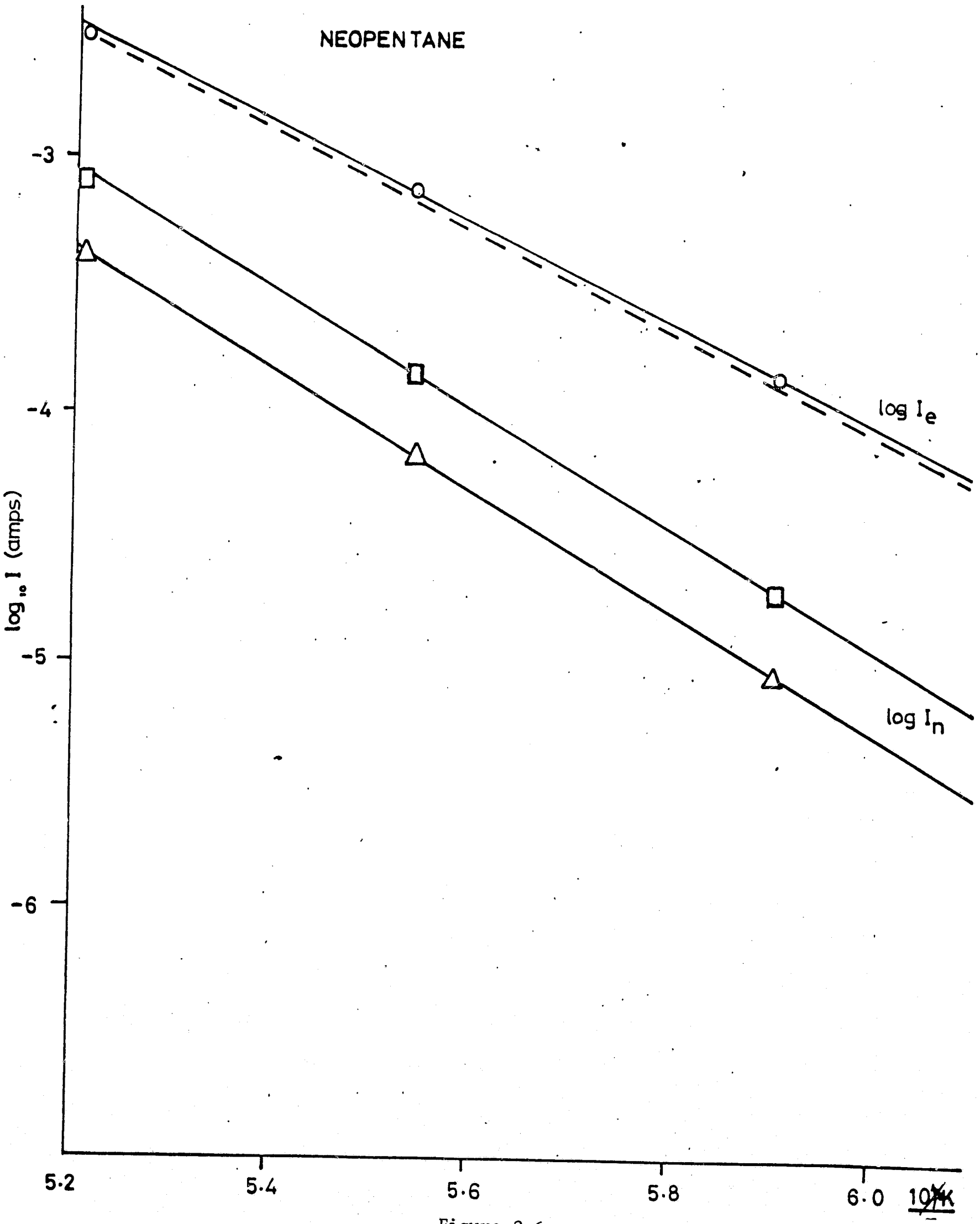


Figure 2-6

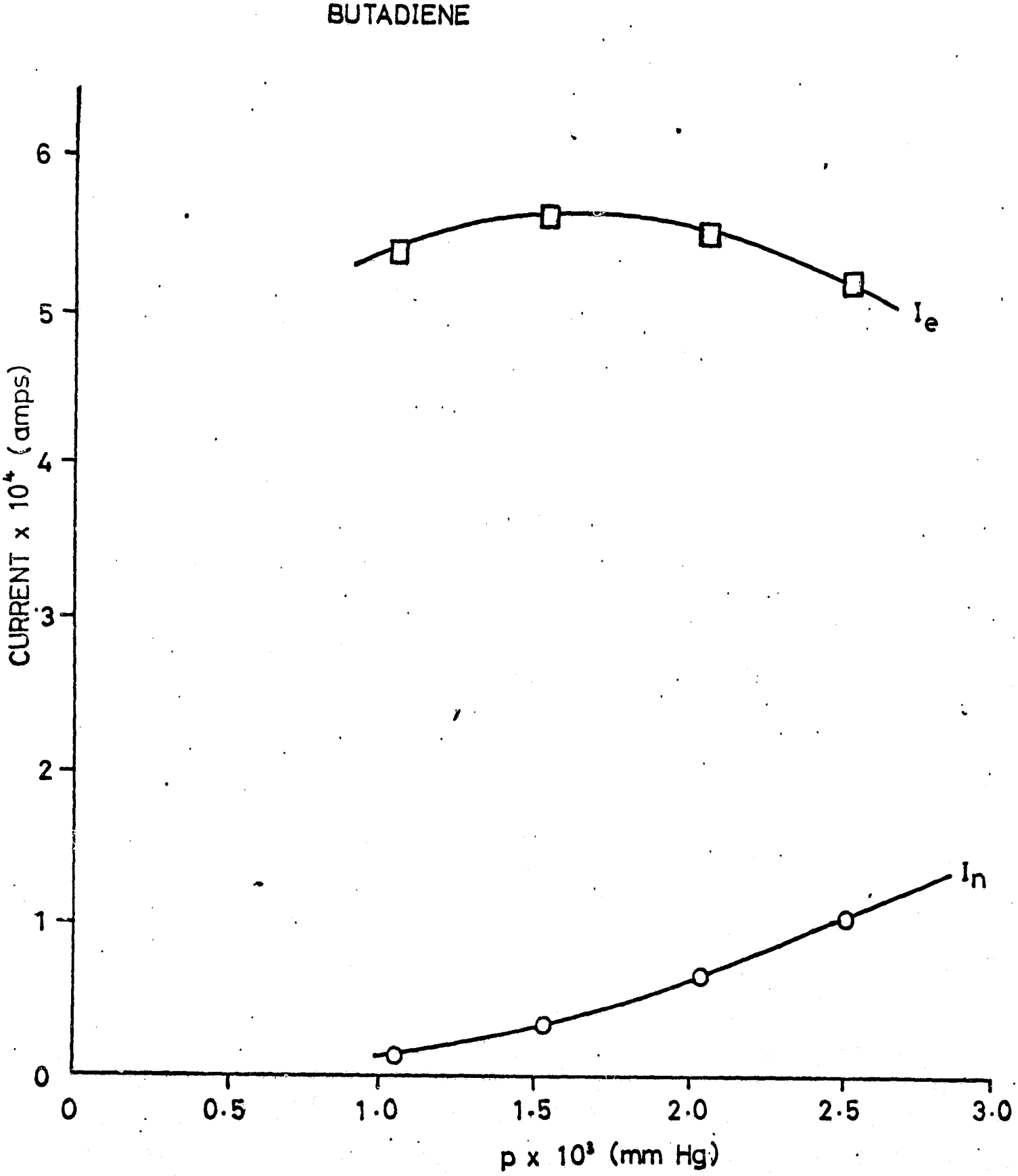

BUTADIENE
CURRENT x 10⁴ (amps)
6
5
4
3
2
1
0
0
0.5
1.0
1.5
2.0
2.5
3.0
p x 10³ (mm Hg)
I_e
I_n

Figure 2-7

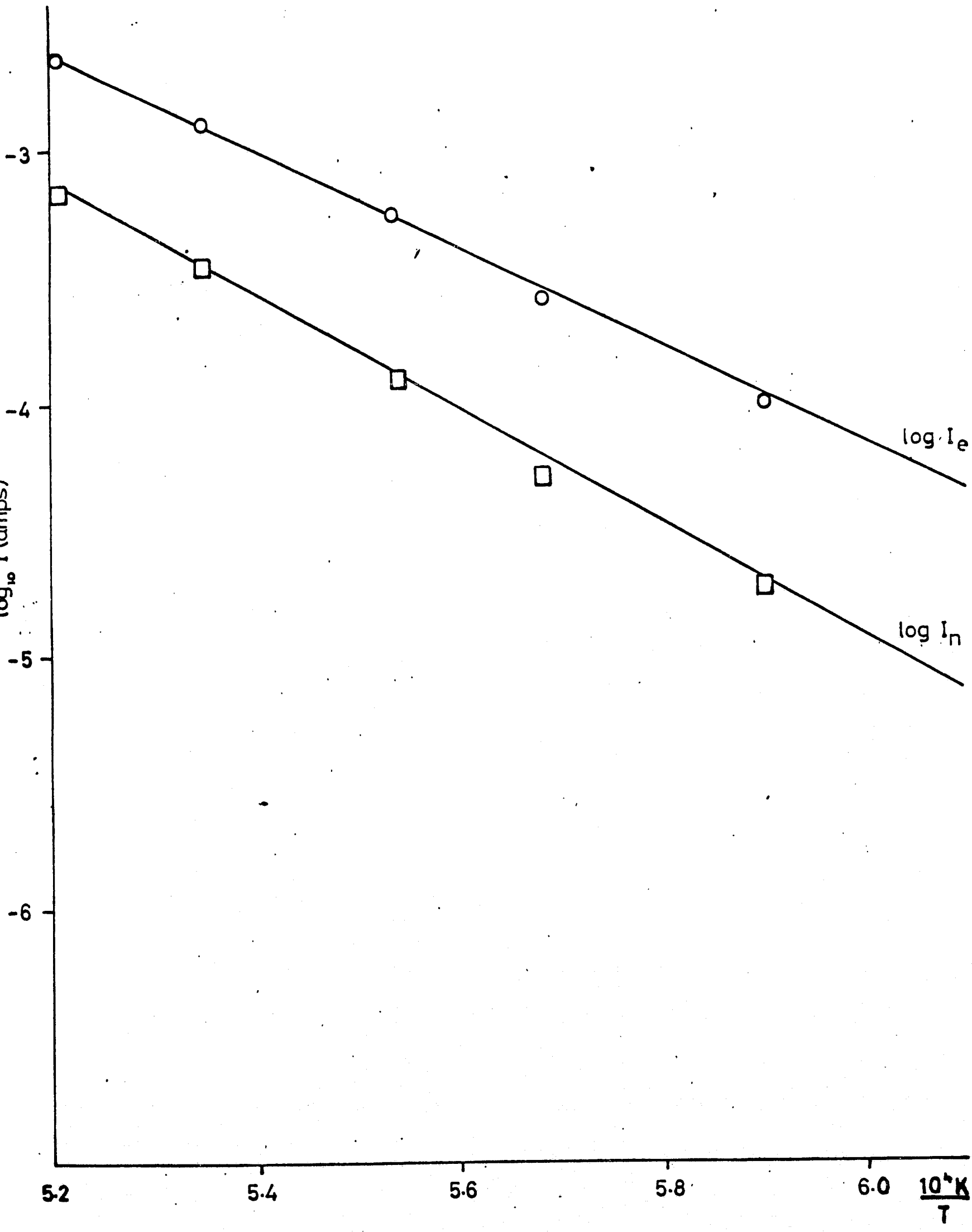


Figure 2-8

NEOPENTANE

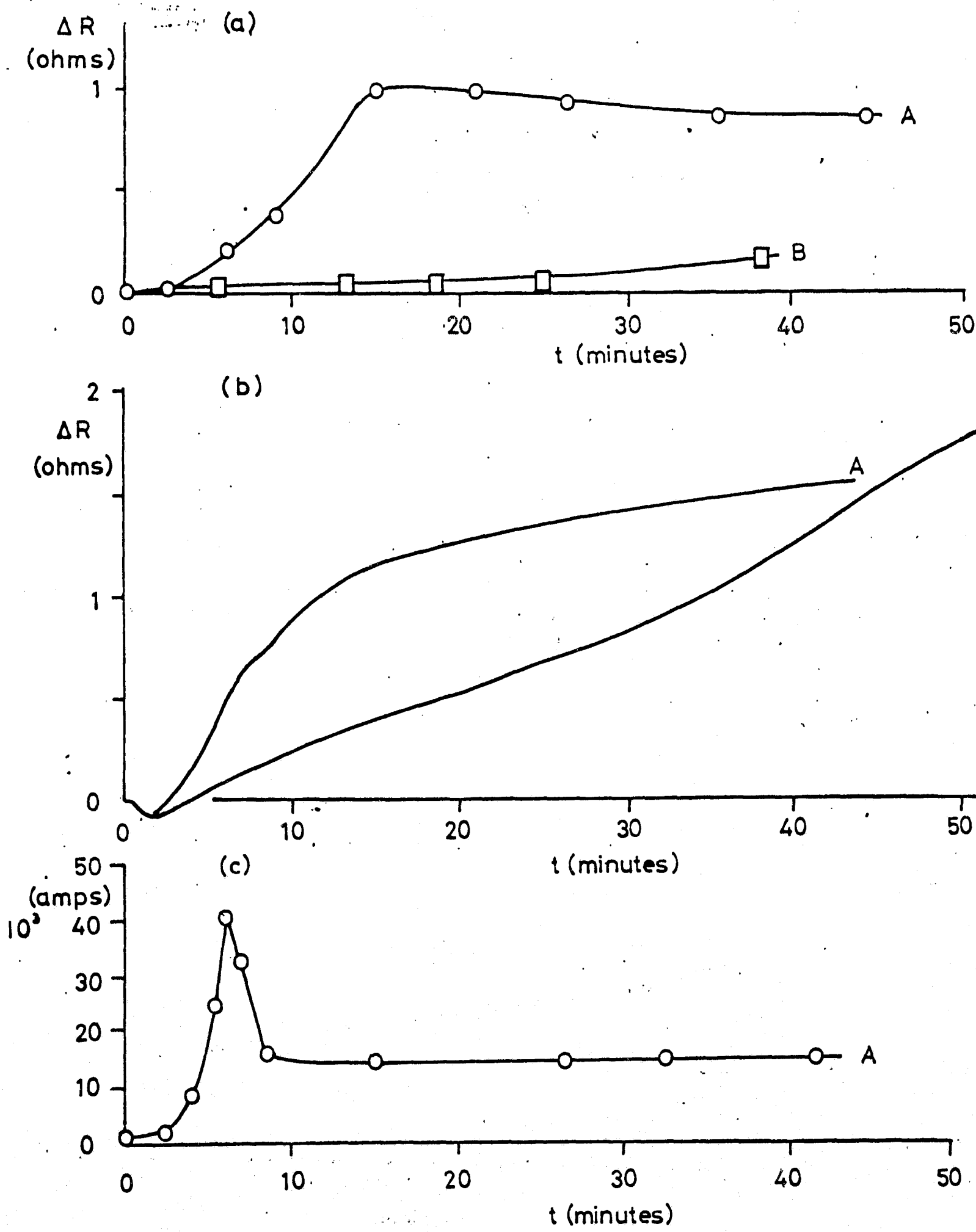


Figure 2-9

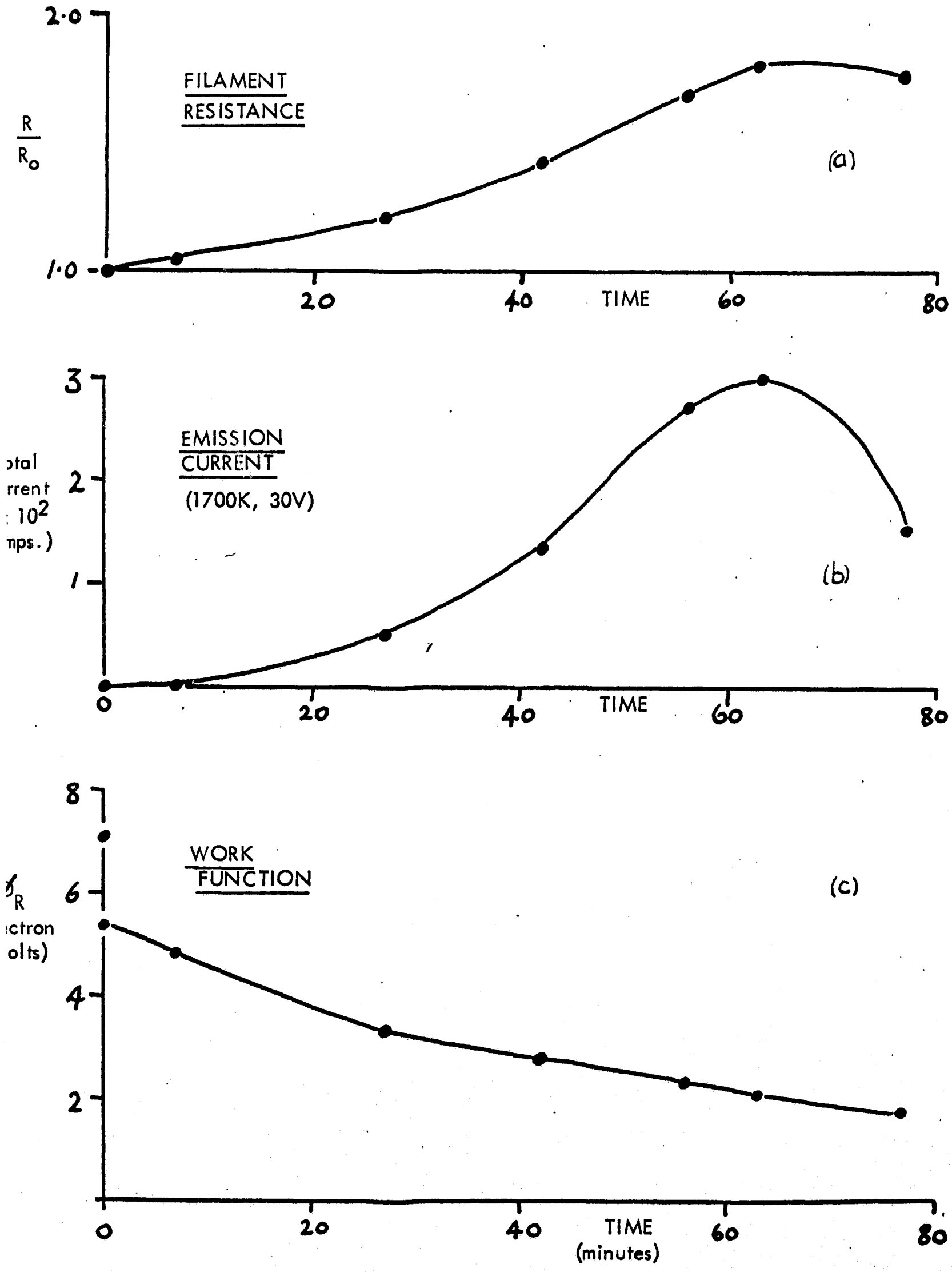

2·0
1·0
R
R_o
FILAMENT
RESISTANCE
(a)
20
40
TIME
60
80
3
2
1
0
EMISSION
CURRENT
(1700K, 30V)
(b)
20
40
TIME
60
80
8
6
4
2
WORK
FUNCTION
(c)
0
20
40
TIME
(minutes)
60
80

Figure 2-10

RESULTS FOR NEOPENTANE CARBIDING;

CHANGE OF PRE-EXPONENTIAL FACTOR WITH ϕ_R

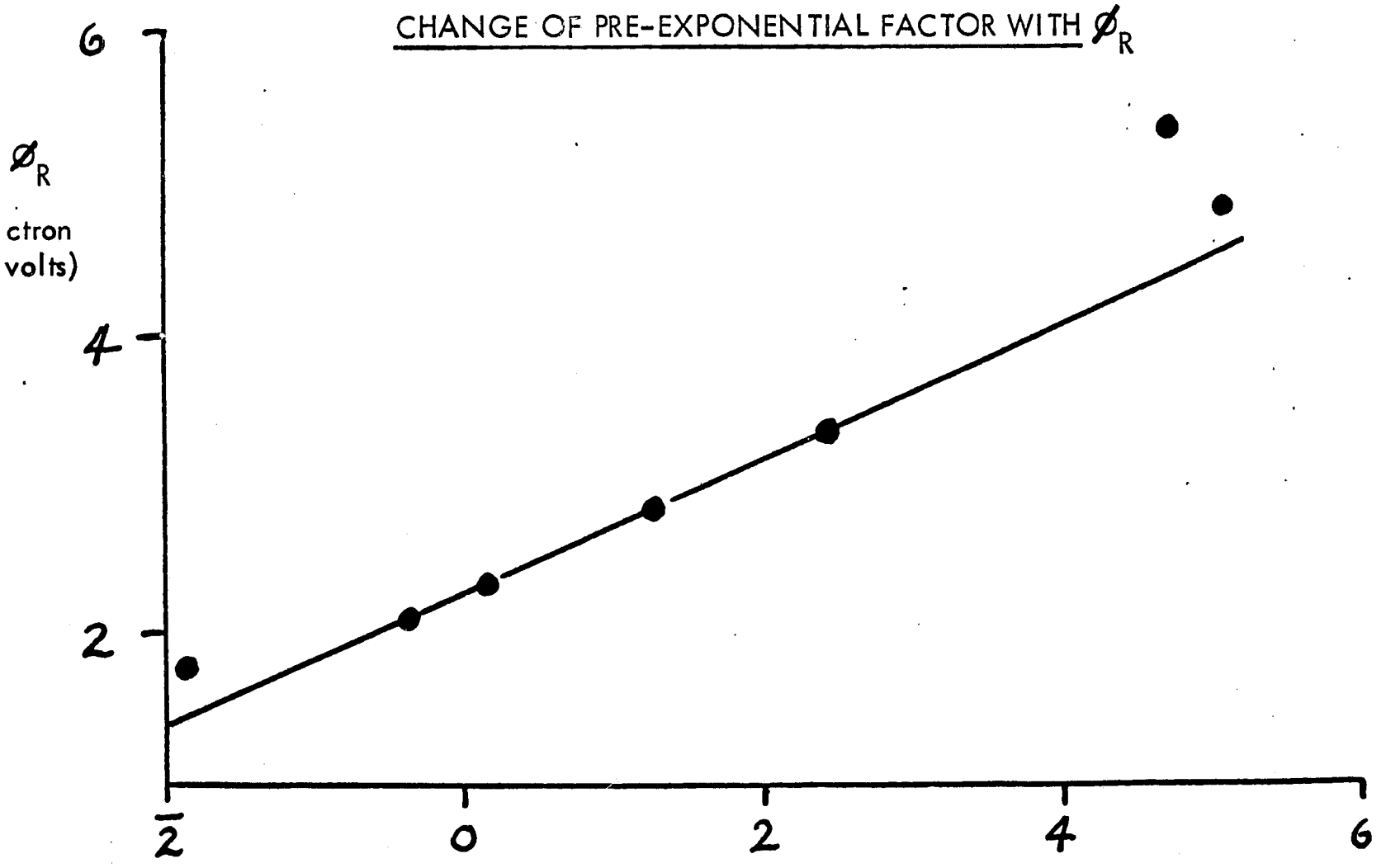
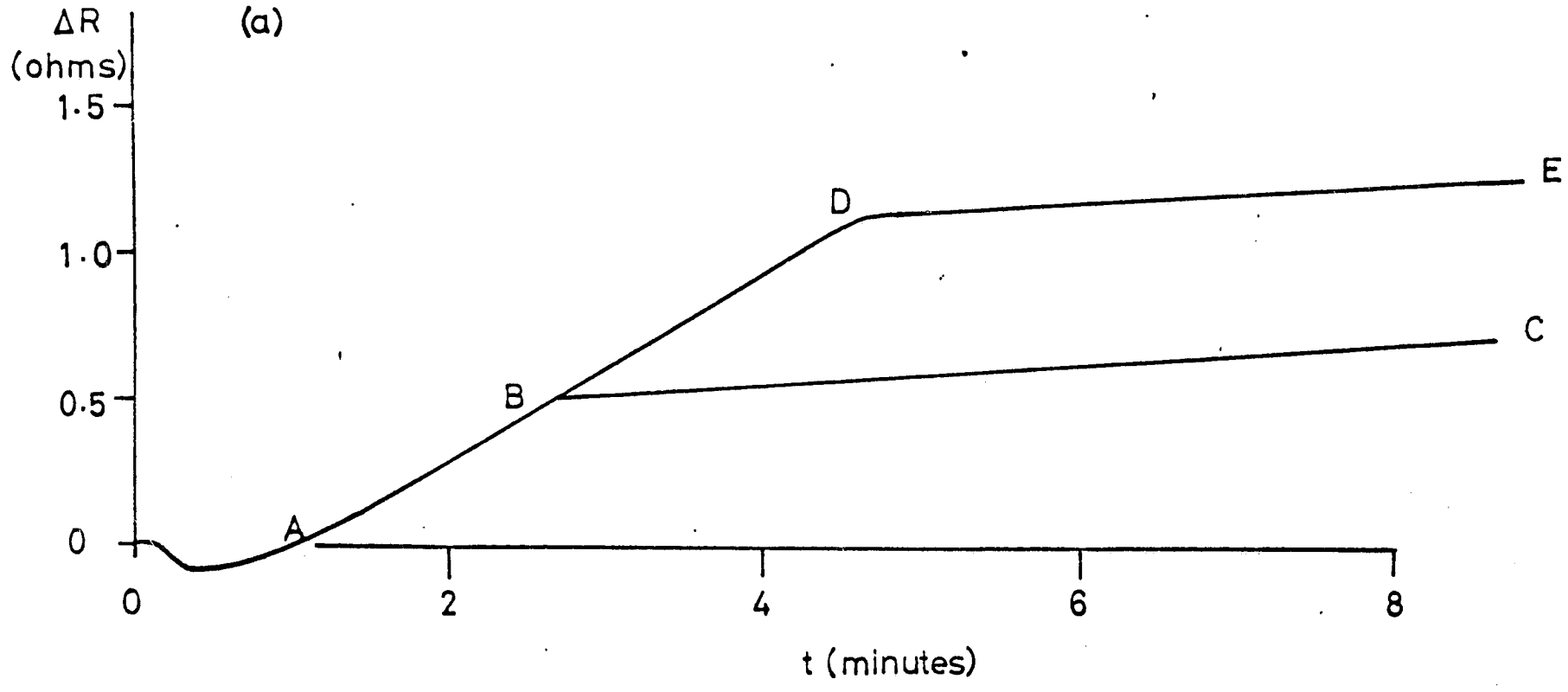


Figure 2-11

BUTADIENE



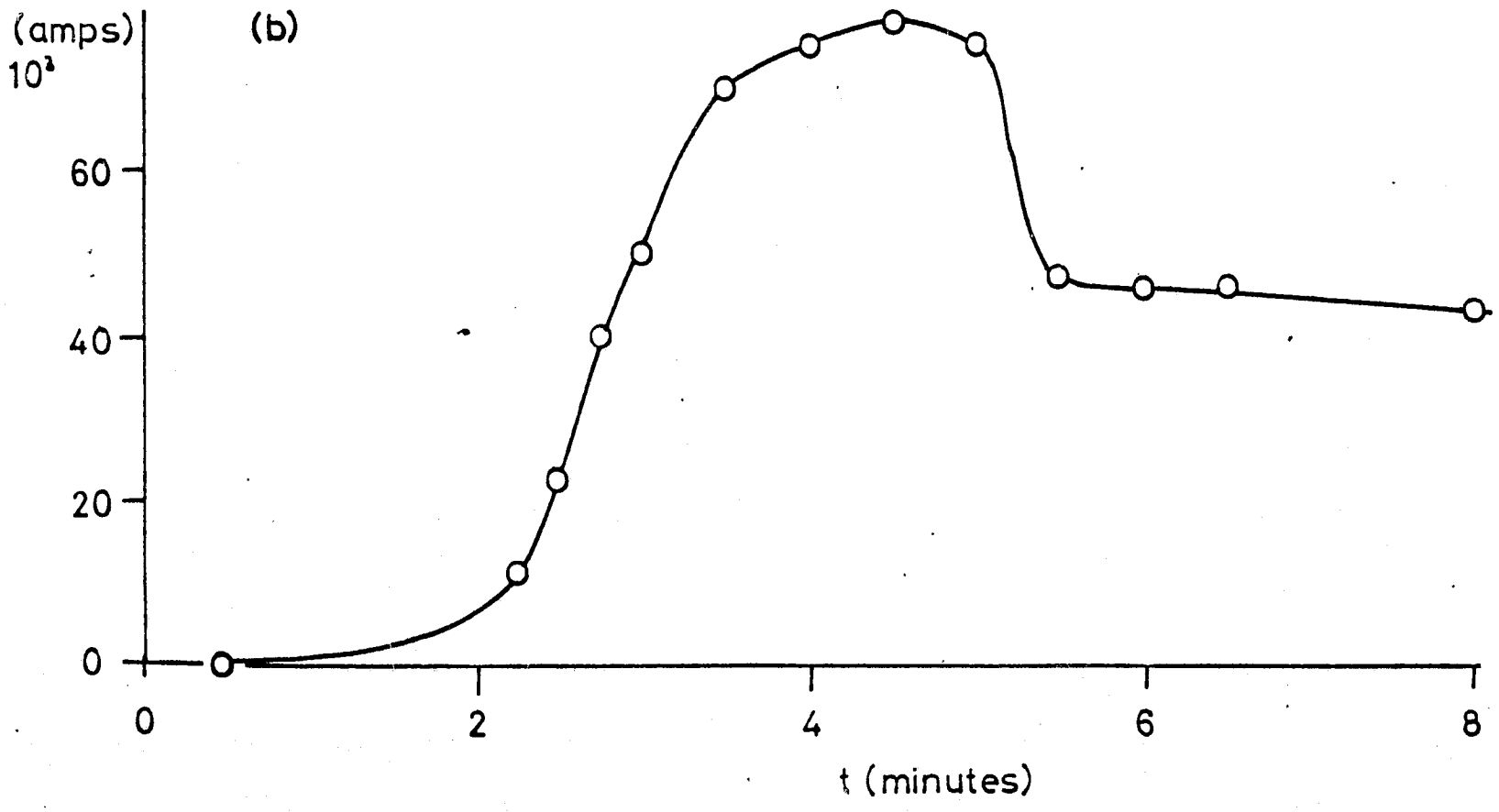


Figure 2-12

3. CONTACT ANGLE STUDY

For a drop of liquid on the surface of a rigid solid, the forces acting at the point of contact have been treated[9] in terms of a mechanical equilibrium between γ_{LV}, γ_{SV}, and γ_{SL}, where these terms represent the average free energies/unit area of the liquid/vapor, solid/vapor, and solid/liquid interfaces, respectively (see Figure 3-1). It can be seen from Figure 3-1 that

$$\gamma_{SV} = \gamma_{SL} + \gamma_{LV} \cos \theta \qquad (3\text{-}1)$$

This equation is known as the Young-Dupre equation.

It has been shown experimentally (see Zisman[9]) that for many liquids on a variety of solids, the angle of contact θ (see Figure 3-1) which each liquid makes with the solid surface decreases as γ_{LV}, the surface tension of the liquid, increases. For a homologous series of liquids on one solid, plots of cos θ versus γ_{LV} have been found to give straight lines obeying an equation of the form:

$$\cos \theta = a - b\gamma_{LV} \qquad (3\text{-}2)$$

where a and b are constants. It is found that data for all liquids if plotted in this manner give points which fall within two parallel lines as shown in Figure 3-2.

This led to the definition of a term which Zisman calls the Critical Surface Tension, γ_c, of the solid, below which liquids will spread; γ_c is the surface tension of the liquid which gives a contact angle of 0°. Zisman has shown[9] that the lower limit of the spread of γ_c shown in Figure 3-2 is characteristic of the solid.

Bernett and Zisman[10] determined the value of γ_c for polyethylene and tetrafluoroethylene using aqueous solutions of surface active agents and simple alcohols, and conclused that the values of γ_c obtained were in good agreement with those obtained from pure organic liquids.

Equation (3-1) is empirical and has as yet received no theoretical justification; nor is there any theoretical reasoning behind γ_c, but it has proven to be a useful quantity in comparing the surface properties of a series of solids. Zisman has concluded that perfluorocarbon polymers have the lowest values of γ_c recorded. Figure 3-3, taken from a paper by Shafrin and Zisman[11], illustrates the variation of the wettability with the constitution of the solid surface. Three types of surface are shown; bulk polymers, single crystals, and monolayers of organic acids adsorbed on a solid surface; in the latter, the carboxyl groups are adsorbed in contact with the solid and Figure 3-3 illustrates the effect of substituents in the alkyl grouping.

In the present study, it was hoped to use the method of contact angles to examine the variation of the constitution of the surface of thin films formed by the so-called electron bombardment process, both for a variety of monomers and for a variety of preparation conditions. It was decided initially to study polymers formed from perfluoro-butene-2; it was hoped that this would form a polymer with a surface with similar properties to those of polytetrafluoroethylene. This monomer has been investigated previously[1] in a study of the chemical properties of thin films, and was found to be the most inert film examined.

In the preliminary experiments carried out, both a series of pure liquids and a series of dilute solutions of alcohols in water were used. Contrary to the results of Bernett and Zisman[10] quoted above, coincidence was not obtained between the cos θ vs γ_{LV} plots for pure liquids and solutions. It must therefore be concluded that adsorption of alcohol molecules is occurring on the surface of the thin film. An analysis of the adsorption has been made for films prepared under a variety of preparation conditions, and the results are compared with those obtained on two bulk polymers, polystyrene and polymethylmethacryllate. The technique is shown to provide valuable information regarding the nature of the surface of the thin films. Below, γ_c obtained for solutions will be termed γ_c' for clarity.

The samples used in the contact angle study are formed in the reaction vessel shown as an exploded diagram in Figure 3-4. A general view of the apparatus is shown in plate 1 and a close-up of the reaction vessel is shown in plate 2. Monomer is introduced through a capillary at a known rate to strike an optical glass plate on which a tungsten film has been evaporated. Electrons (and negative ions) are simultaneously accelerated toward the plate or anode from the electron gun shown. The filament was held at earth potential and the volatage of the accelerating grid G, was varied between +35 and +500V. The focussing grid was maintained at +10V, and the potential of the anode was varied between +50 and +3000V. Contact to the tungsten film was made by platinum strips attached to the glass. Except in a few cases, the films were colorless and did not show interference colors. Contact angle measurements are made at atmospheric pressure in a dust free enclosure. Angles are measured using a telescope fitted with a goniometer, and angles are reproducible to within $\pm$ 1/2°. Alcohol solutions are prepared immediately before use, the value of the surface tension of each solution being taken from tables[12].

The results of a preliminary experiment in which the contact angle of drops of methanol solution were measured on polymers prepared on tungsten from perfluorobutene-2 are shown in Figure 3-5. A value of γ_c' of ~23 dynes/cm was obtained, and a very similar value was found for polymers prepared under a variety of different conditions. However, when using a series of pure liquids, a value of ~42 dynes/cm (see below) was obtained. Thus, the value of γ_c' of ~23 dynes/cm obtained for the methanol solutions must be due to adsorption of CH_3OH on the surface giving an adsorbed monolayer with CH_3 groups pointing outwards and hence a much less energetic surface. Such a value of γ_c is characteristic of a surface composed largely of CH_3 groups, e.g., paraffin wax[9]. No similar adsorption on low energy solids (γ_c <100 dynes/cm) has been recognized, although adsorption from solution on high energy solids is a well known phenomenon[13]. In order to test the hypothesis that adsorption was occurring and to develop a satisfactory interpretation, contact angle measurements have been made on thin films of polyperfluorobutene and also on bulk polystyrene and polymethylmethacryllate (PMMA), using butanol-water solutions, butanol was used in preference to methanol as more reproducible results were obtained.

For a drop of water on the surface of a solid, the Young-Dupre equation (equation 3) is

$$\gamma_{SV(W)} = \gamma_{SL(W)} + \gamma_{LV(W)} \cos \theta_W \qquad (3\text{-}3)$$

and for a solution of concentration C,

$$\gamma_{SV(C)} = \gamma_{SL(C)} + \gamma_{LV(C)} \cos \theta_C \qquad (3\text{-}4)$$

For dilution solutions, it can be shown experimentally that $\gamma_{SV(W)} = \gamma_{SV(C)}$ and so equation (3-5) follows:

$$F = \gamma_{SL(W)} - \gamma_{SL(C)} = \gamma_{LV(C)} \cos \theta_C - \gamma_{LV(W)} \cos \theta_W \qquad (3\text{-}5)$$

where F, the surface pressure, is related to the surface excess of alcohol, Γ_2, at the solution-solid interface by a modified form of the Gibbs Adsorption Equation

$$F = \Gamma_2 RT \ln a_2 + C \qquad (3\text{-}6)$$

Here, a_2 is the activity of the alcohol in solution and C is a constant. Hence Γ_2 is obtained from the gradient of a plot of F vs log a_2, and hence an isotherm depicting the surface excess of alcohol at various concentrations can be constructed. This approach was first used by Fowkes and Harkins[14].

Figures 3-6 to 3-8 show the results for bulk polystyrene, bulk PMMA, and thin films of polyperfluorobutene-2. In each figure, (a) represents plots of cos θ vs γ_{LV} for a variety of pure liquids. In each case, all the points lie within a narrow band, and the values of γ_c obtained for the two bulk polymers agrees well with values in the literature. Graph (b) in each case represents the results obtained for dilute aqueous butanol solutions; the values of γ_c' obtained are much lower than for the pure liquids, and in each case γ_c' ~25 dynes/cm, which is the same value obtained for a series of pure liquids on a bees-wax surface[9]. It must therefore be concluded that butanol is adsorbed by each surface, giving rise to a surface which

is characteristic of CH_3 groups outermost. The values of γ_c obtained are summarized in Table 1.

Table 1

Surface	Critical Surface Tension	
	Pure Liquids γ_c	Butanol Solutions γ_c'
Polystyrene	33 - 34	26.9
PMMA	37.5 - 41.0	23.2
Polyperfluorobutene-2	41 - 44	26.0

In contrast to the results for pure liquids (graph a), the cos θ vs γ_{LV} plots (graph b) do not remain linear beyond a point C in each case. It will be shown below that the behavior between the point for pure water and the point C is characteristic of the sites on the polymer surface.

For each polymer, graph (c) is a plot of F vs log a_2. From these data, graph (d) is constructed in each case as described above. The lettering on (b), (c) and (d) shows corresponding points in each case. Consider first Figure 3-6 (d), i.e., a plot of the surface excess of butanol on the surface of polystyrene. Initially, up to point A, there is a rapid adsorption of butanol on the surface; the surface excess then falls back to zero at point B. This is thought to correspond to the filling up of surface sites by adsorbed butanol molecules, which leaves these sites similar in character to that of the clean surface. Subsequently, further adsorption occurs up to point C, when the whole surface is characteristic of adsorbed butanol molecules: point C corresponds to the start of the linear section of Figure 3-6b, which implies a constant surface composition. Hence, we conclude that the first peak A, when it exists (cp Figure 3-7d), is indicative of the number of special sites, e.g., unsaturation at the polymer surface, and the peak at C is characteristic of the normal surface. Thus, the polymer formed from perfluorobutene-2 has a smaller number of special adsorption sites, and once these are filled, water at first preferentially adsorbs between them (Figure 3-8c, point B) and subsequently the whole surface adsorbs butanol.

Figure 3-9 shows the effect on the cos θ vs γ_{LV} plots for pure liquids on polyperfluorobutene-2 films of varying the preparative conditions used. Figure 3-9a shows that increasing the time of preparation of the polymer increases the surface energy while Figure 3-9b shows that a decrease of anode potential also increases the surface energy. Similarly, decrease in the grid potential also gives a higher energy surface (Figure 3-9c). Changes in the gradient of the cos θ vs γ_{LV} plots are also indicated.

Figure 3-10 shows plots of cos θ vs γ_{LV} for solutions of butanol on polyperfluorobutene-2 formed with an accelerating grid potential, V_G, of +35V, and a variety of anode potentials, V_A. For V_A <1000V, the value of cos θ for pure water, cos θ_W, is found to increase with increasing V_A, and γ_c' also decreases. For V_A >2000V, the trend is reversed. The curvature of the plots in the region OAB as defined in Figure 3-6b remains approximately the same, indicating a similar concentration of active sites on the surface. Figure 3-11, on the other hand, shows that when V_A is kept constant at 500V and V_G is increased, cos θ_W decreases and γ_c' increases for $V_G \leq 300V$. For V_G = 500V, cos θ_W has decreased again but γ_c' has decreased once more. The curvature of the region OAB decreases with increasing V_G, indicating a decrease in the number of active sites. When the filament temperature was increased from 2300°K to 2500°K with V_G = 35V and V_A = 500V, the value of cos θ_W decreased and γ_c' increased, which is a similar trend to those observed with increasing value of V_G, i.e., increasing field at the filament. Table 2 summarizes the results of Figures 3-10 and 3-11.

Almost all the increases in cos θ_W seem to parallel decreases in γ_{LV}'. As water is one of the pure liquids which will fall within the parallel straight lines of Figure 3-2, a decrease in cos θ will reflect a decrease in the value of γ_c which would be obtained with a pure liquid, i.e., a decrease in the surface energy of the solid. If we suppose that the strongest adsorption of alcohol will occur on the surface with the highest surface energy, then the most ordered layer of adsorbed molecules and hence the lowest value of γ_c' will result.

Table 2.

Filament Temperature	Acc^{n} Grid Voltage	Anode Voltage	γ_c'(dynes/cm)	Cos θ_W
2300°K	35V	300V	26.0	0.435
2300°K	35V	500V	25.25	0.515
2300°K	35V	1000V	24.75	0.580
2300°K	35V	2000V	28.5	0.500
2300°K	35V	(3000)V	-	0.480
2300°K	100V	500V	25.75	0.487
2300°K	300V	500V	27.7	0.340
2300°K	500V	500V	24.5	0.275
2500°K	35V	500V	28.2	0.420

An increase in V_G will cause an increase in the emission current collected by the anode; similarly, when the temperature of the filament is increased, the emission current will be increased. As a result, as long as the time of polymerization is constant, as in the present case, the thickness of the polymer will increase. In both cases, cos θ_W was found to decrease and γ_c' increased. This will therefore correspond to a decrease in γ_c; i.e., when a thicker polymer is formed, the surface energy decreases. From the change in curvature of the plots, it was also concluded that the number of active sites decreased and this is also associated with a thicker polymer. These sites must be caused by strain in the surface induced in the polymer by irregularities in the tungsten surface, and the number will decrease with distance from the metal. A check of these conclusions will be to examine the effect of increasing time of preparation; these experiments are at present being carried out.

When V_G is kept constant at 35V (i.e., the emission current is constant), and V_A is increased, the surface energy of the resultant polymer rises and the number of active sites remains constant. Thus, it would appear that more cross-linking or unsaturation (see part 1) occurs with increasing voltage and thus gives rise to a higher value of γ_c (cp Figure 3-3). This occurs either because of the increased energy of the negative ions which form the polymer or by bombardment of the completed polymer by more energetic electrons. In the cases where V_A = 2000 or 3000°V, the field at the filament due to the anode voltage exceeds that due to the grid voltage, and so increasing V_A has the same effect as increasing V_G discussed above.

It is unfortunately not possible to compare the results of Figure 3-3 with these conclusions, as the preparative conditions for the films were not the same in both cases, the flux of molecules being much higher for the experiments shown in Figure 3-3. Experiments on the wetting of similar polymers to those shown in Figures 3-10 and 3-11 are now being carried out. It is intended also to carry out similar experiments with other monomers and with other metal substrates.

LEGENDS FOR FIGURES - PART 3

Figure 3-1 — The forces acting on a drop of liquid at rest on a flat surface:

γ_{LV} = surface tension of the liquid-vapor interface;
γ_{SV} = surface tension of the solid/vapor interface;
γ_{SL} = surface tension of the solid/liquid interface;
θ = angle of contact.

Figure 3-2 — Schematic representation of Cos θ vs γ_{LV} data for a series of pure liquids on a solid surface, showing limits of spread. (After Zisman[9]).
Critical Surface Tension = γ_c.

Figure 3-3 — Diagram showing the variation of γ_c with surface constitution. (After Shafrin and Zisman[10]).

Figure 3-4 — Exploded view of reaction vessel.

Figure 3-5 — Plot of Cos θ vs γ_{LV} for a series of methanol solutions on the surface of perfluorobutene-2.

Figure 3-6 — Results for polystyrene

(a) Plot of cos θ vs γ_{LV} for a series of pure liquids.
(b) Plot of cos θ vs γ_{LV} for aqueous solutions of butanol.
(c) Plot of the surface pressure, F, versus log a_2, where a_2 is the activity of the butanol in the solutions.
(d) Plot of the surface excess of butanol (no. of molecules/100Å^2) against mole fraction of butanol in solution.

Figure 3-7 — Corresponding plots for polymethylmethacryllate.

Figure 3-8 Corresponding plots for a thin film of polyperfluorobutene-2 formed on an evaporated tungsten film.

Figure 3-9 The effect of the preparative conditions on the wetting characteristics of polyperfluorobutene-2 films formed under a variety of conditions for the series of pure liquids.

(a) The effect of time of preparation.
(b) The effect of varying the anode potential (V_A).
(c) The effect of varying the accelerating grid potential (V_G).

Figure 3-10 The effect of increasing V_A on the wetting characteristics obtained with butanol solutions. V_G = 35V; filament temperature = 2300°K; time of preparation = 30 minutes.

Figure 3-11 Effect of increasing the grid voltage on the wetting characteristics obtained with butanol solutions. V_A = 500V; filament temperature = 2300°K; time of preparation = 30 minutes.

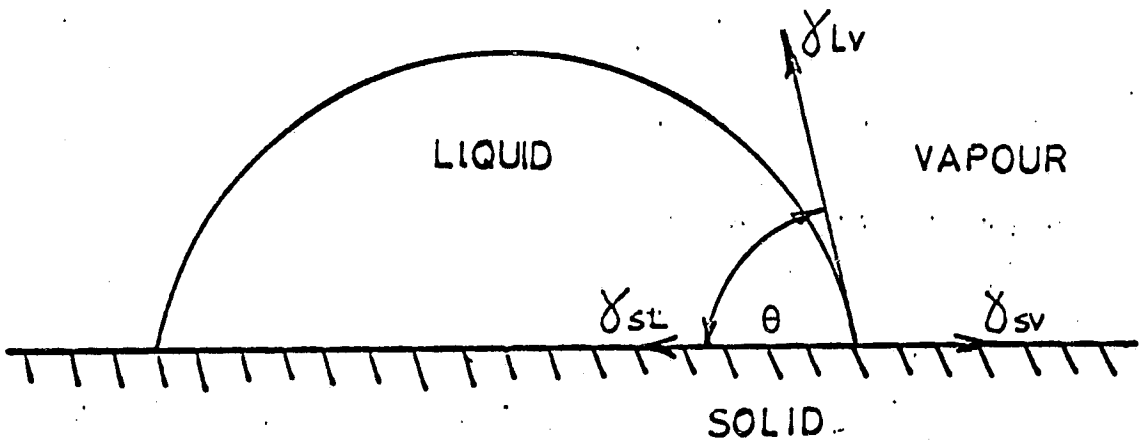


Figure 3-1

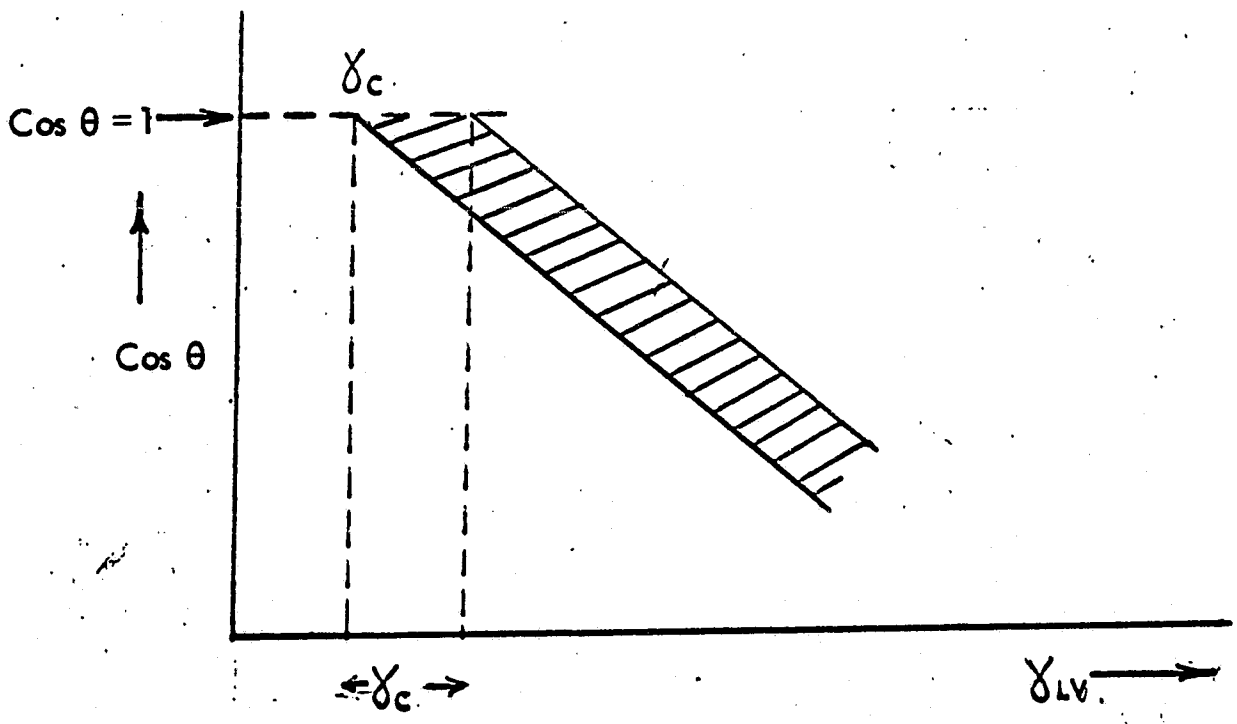
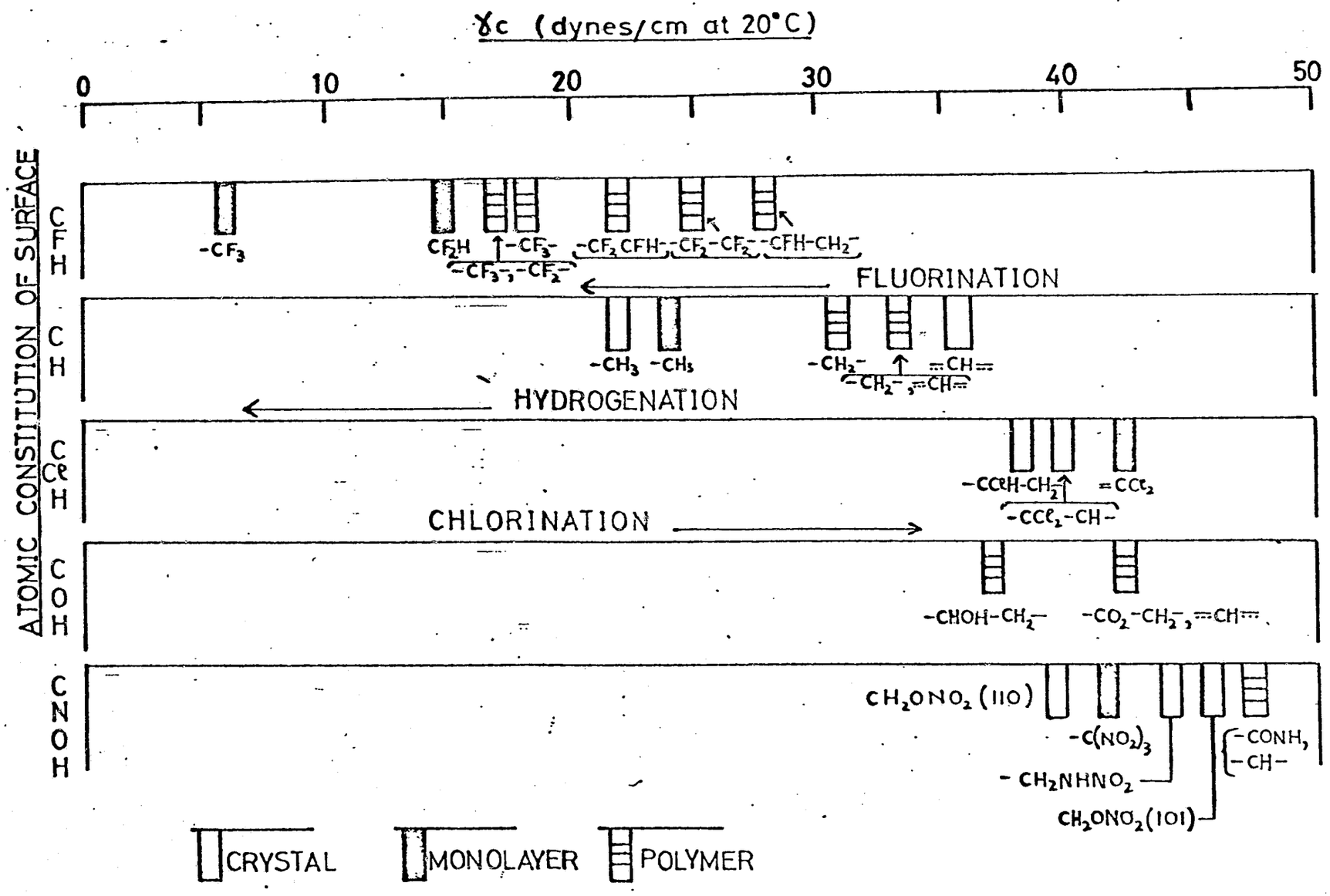


Figure 3-2.



WETTABILITY SPECTRUM FOR LOW ENERGY SURFACES

Figure 3-3

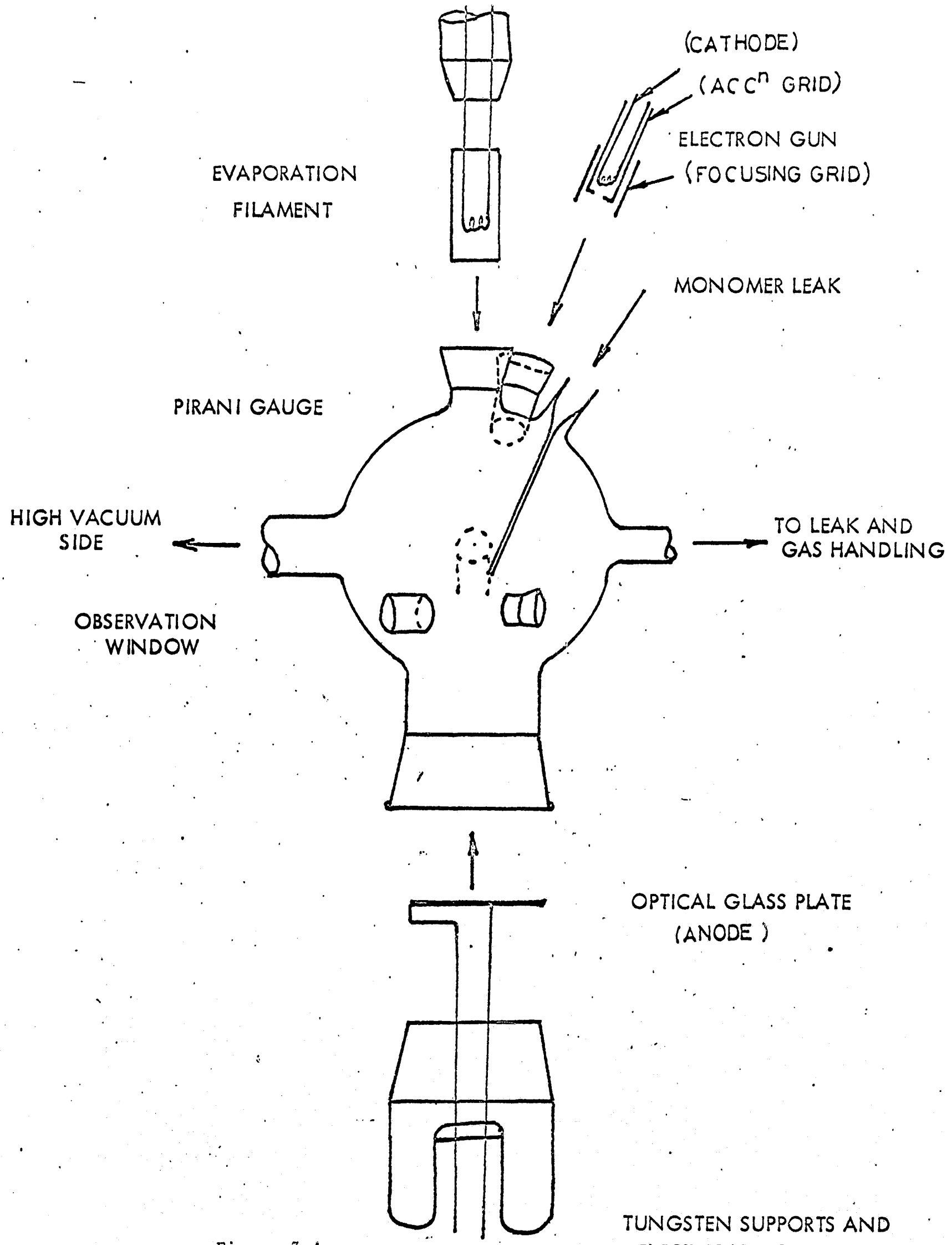

(CATHODE)
(ACC^{n} GRID)
ELECTRON GUN
(FOCUSING GRID)
EVAPORATION
FILAMENT
MONOMER LEAK
PIRANI GAUGE
HIGH VACUUM
SIDE
TO LEAK AND
GAS HANDLING
OBSERVATION
WINDOW
OPTICAL GLASS PLATE
(ANODE)
TUNGSTEN SUPPORTS AND
ELECTRICAL CONTACTS

Figure 3-4

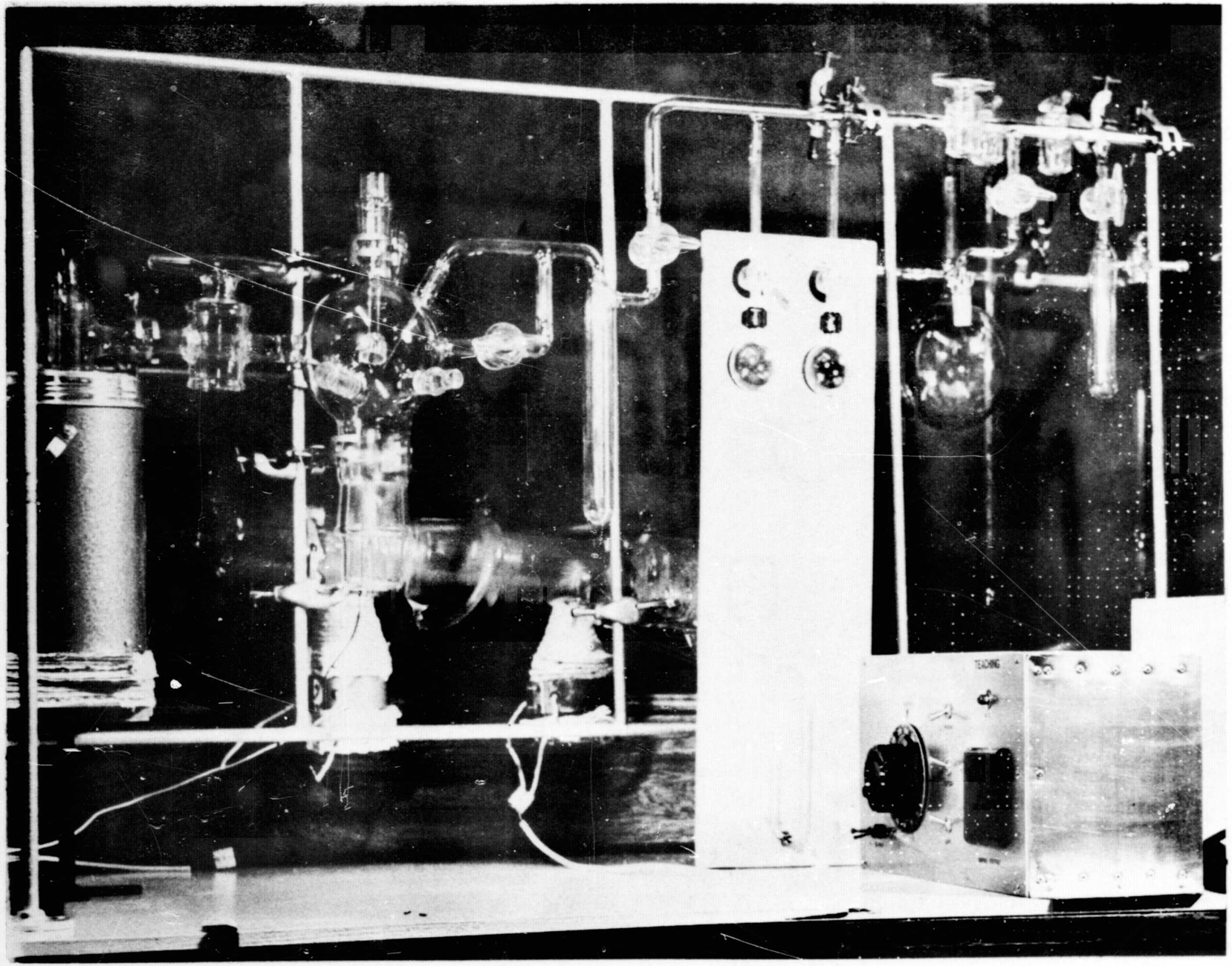


Figure 3-4 PLATE 1

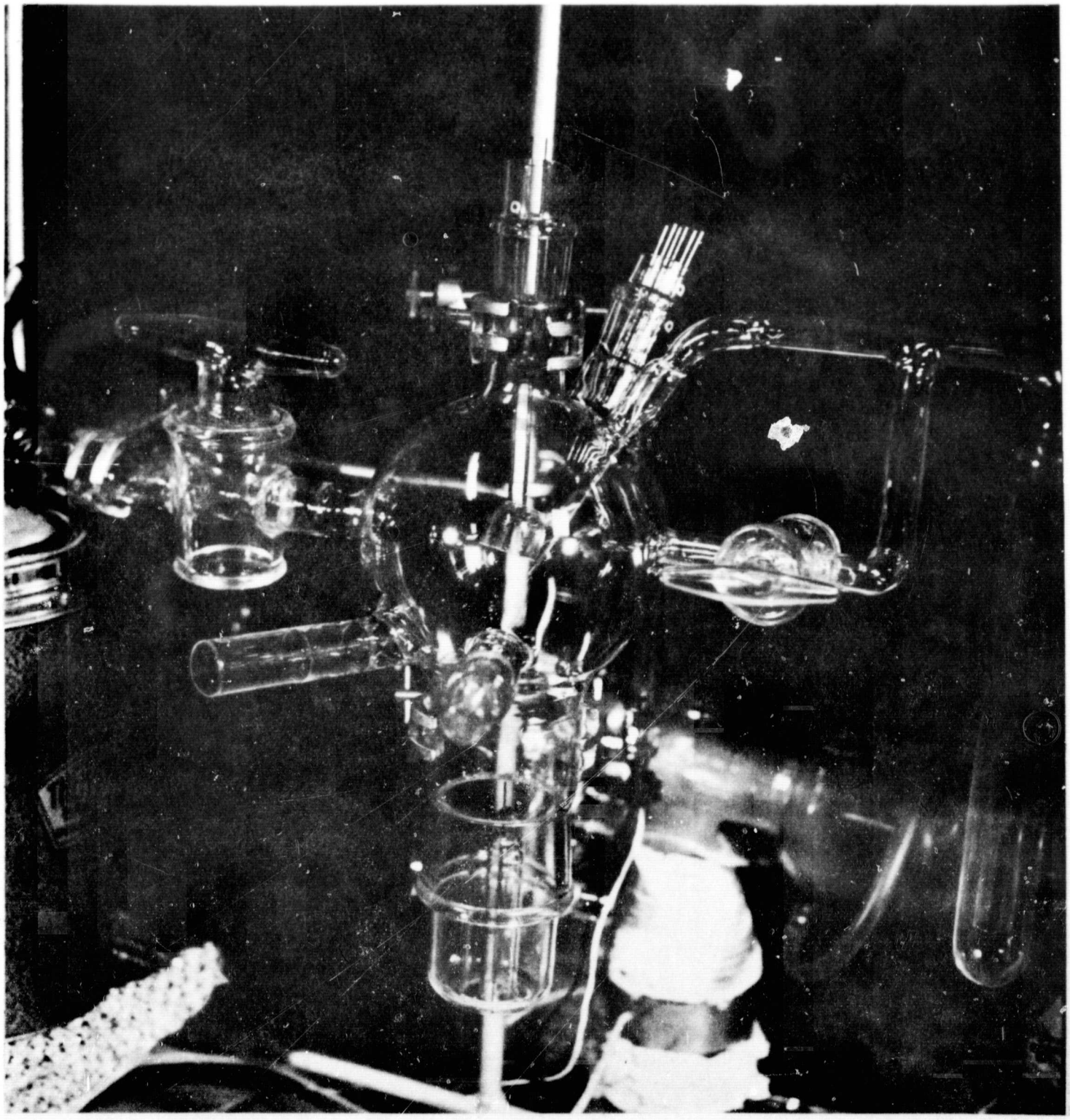


PLATE 2

Figure 3-4

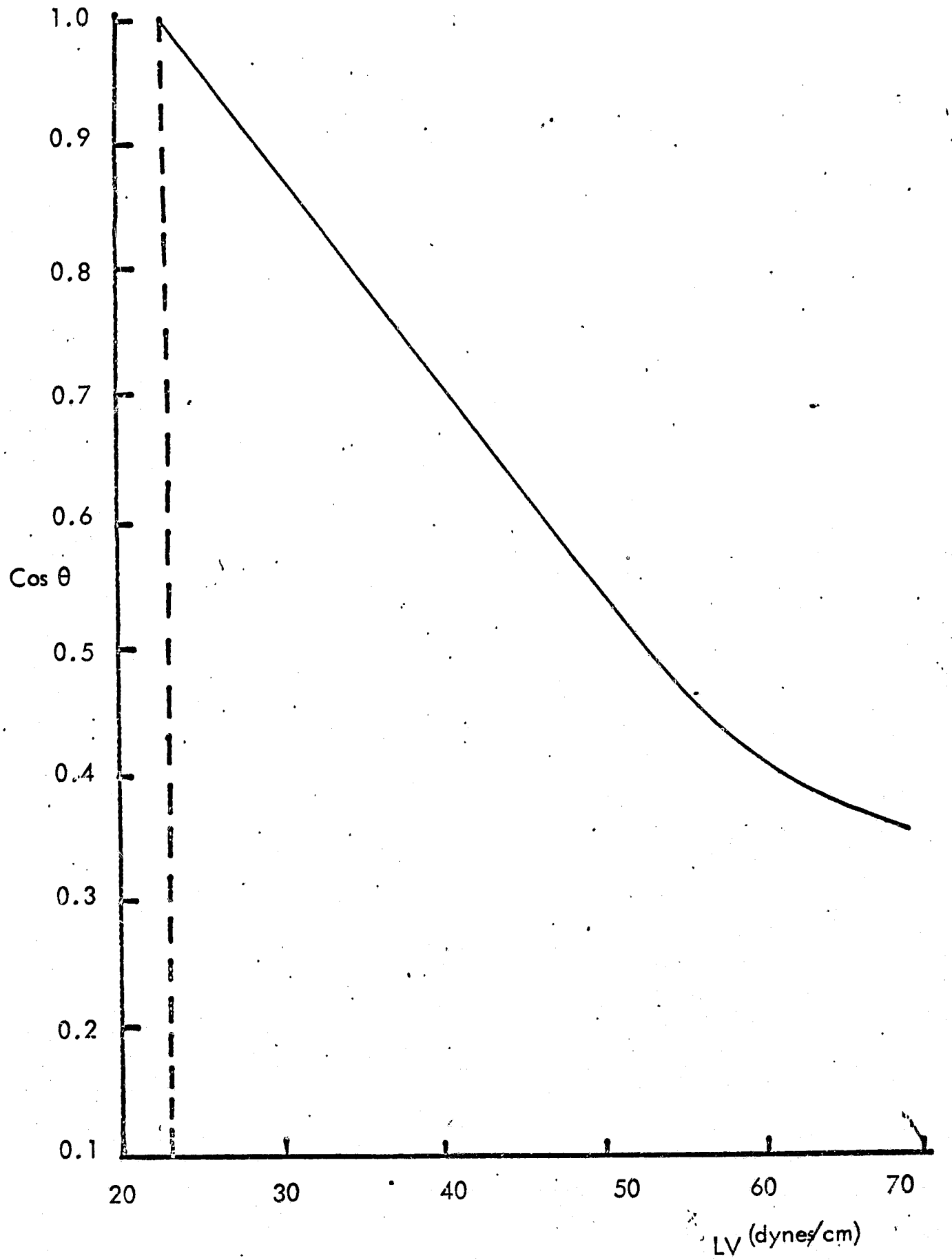


Figure 3-5

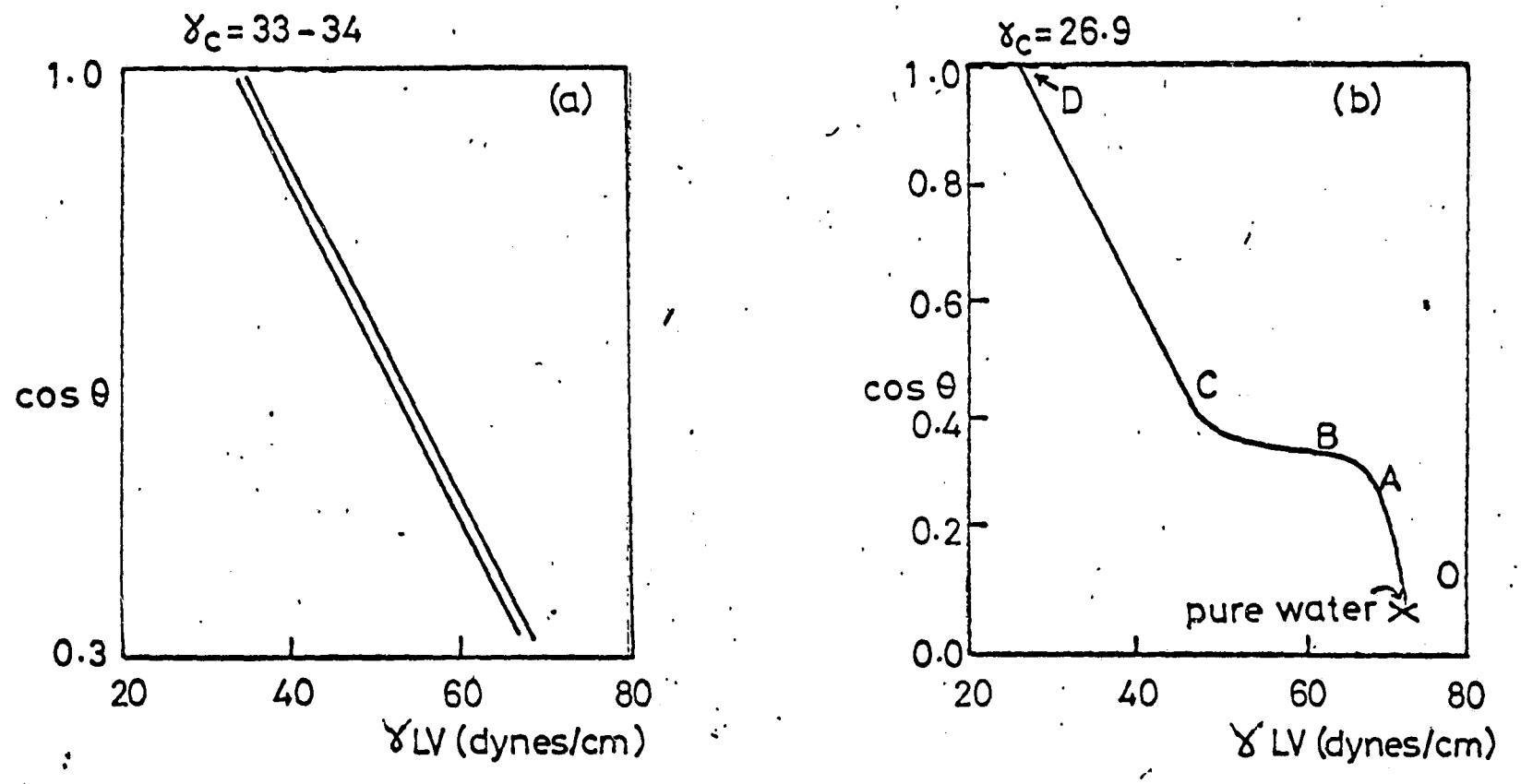
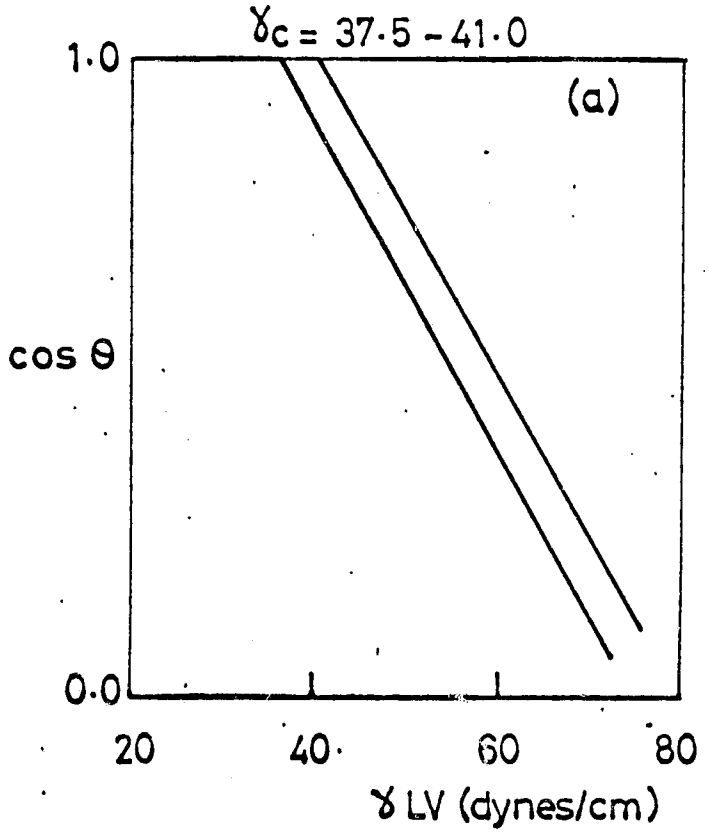
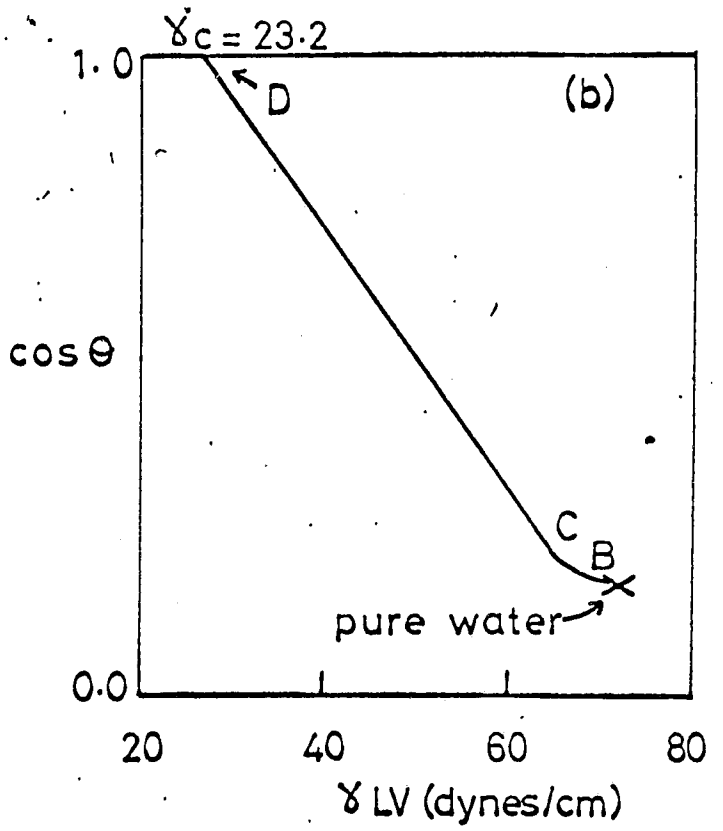
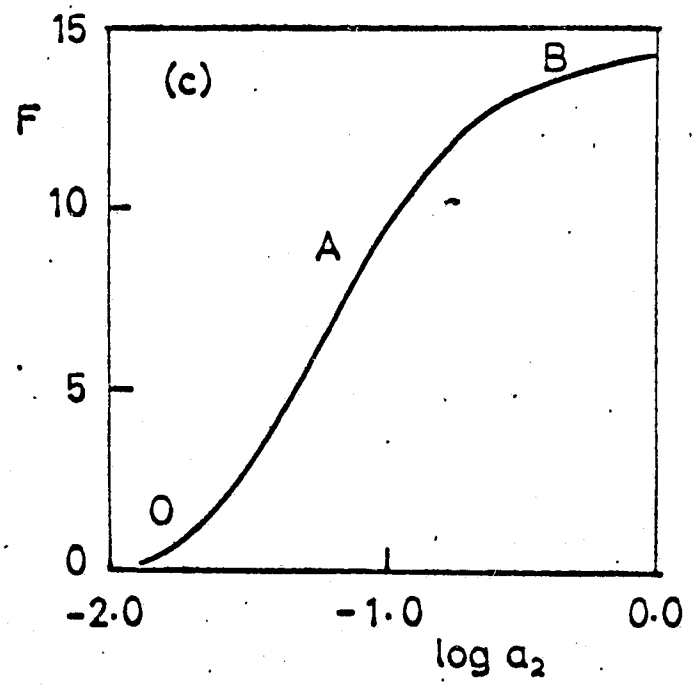

POLYSTYRENE
$\gamma_c = 33-34$
(a)
1.0
0.3
cos θ
20
40
60
80
γ_{LV} (dynes/cm)
$\gamma_c = 26.9$
(b)
D
C
B
A
O
pure water
1.0
0.8
0.6
0.4
0.2
0.0
cos θ
20
40
60
80
γ_{LV} (dynes/cm)
(c)
C
D
A
B
O
25
20
15
10
5
F
-3.0
-2.0
-1.0
0.0
log a_2
(d)
A
C
B
D
6
4
2
0
Na-molecules/Å x 10^{-2}
0
5
10
15
Mole fraction of butanol (x10^2)

Figure 3-6

POLYMETHYLMETHACRYLATE







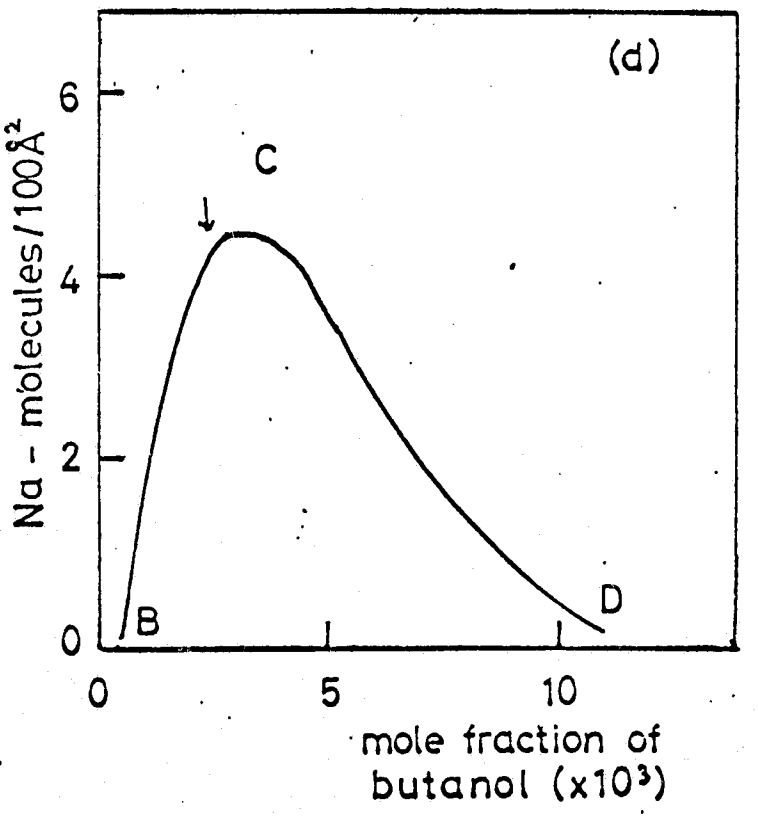
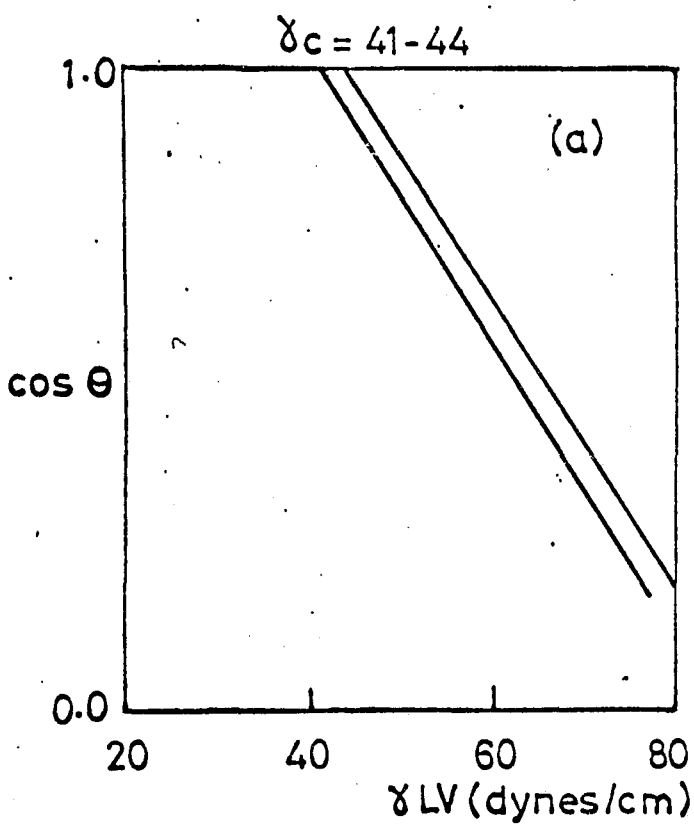
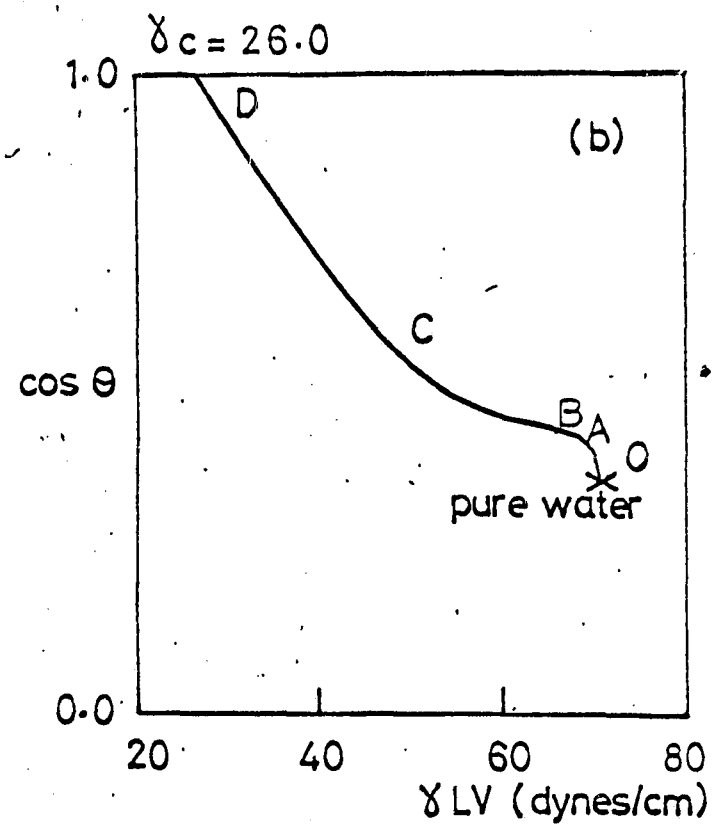
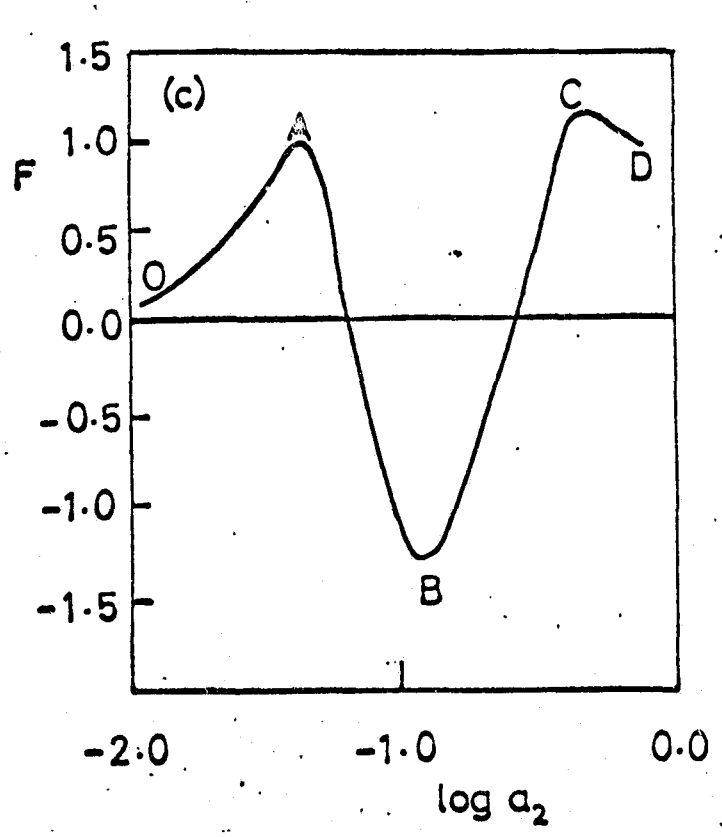


Figure 3-7

POLYPERFLUOROBUTENE-2







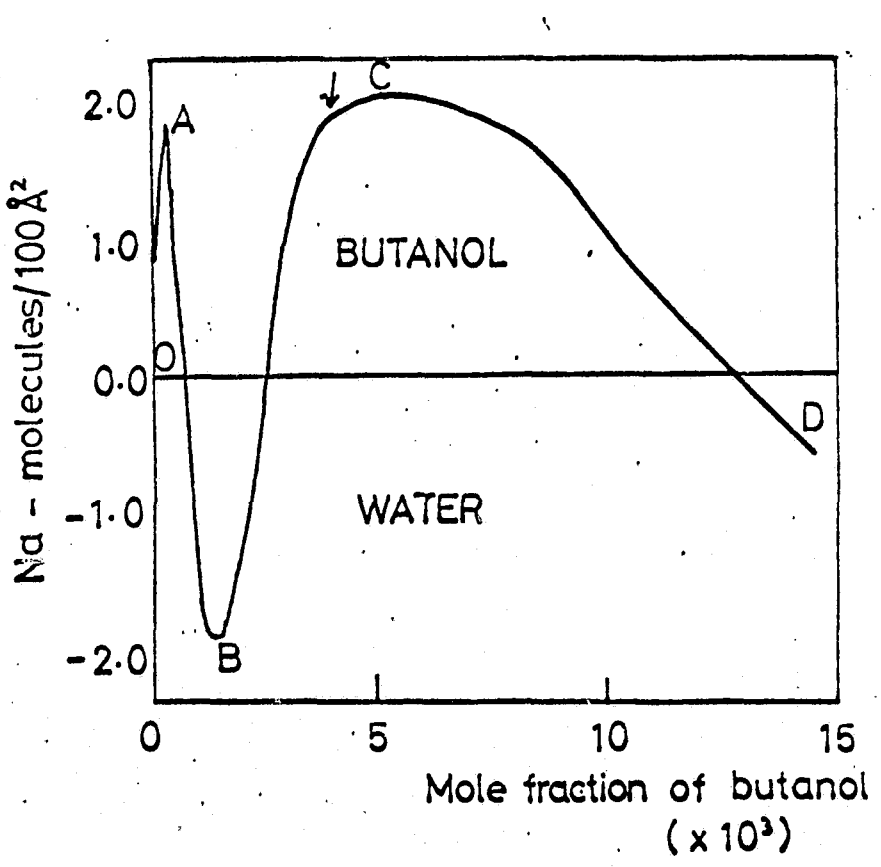
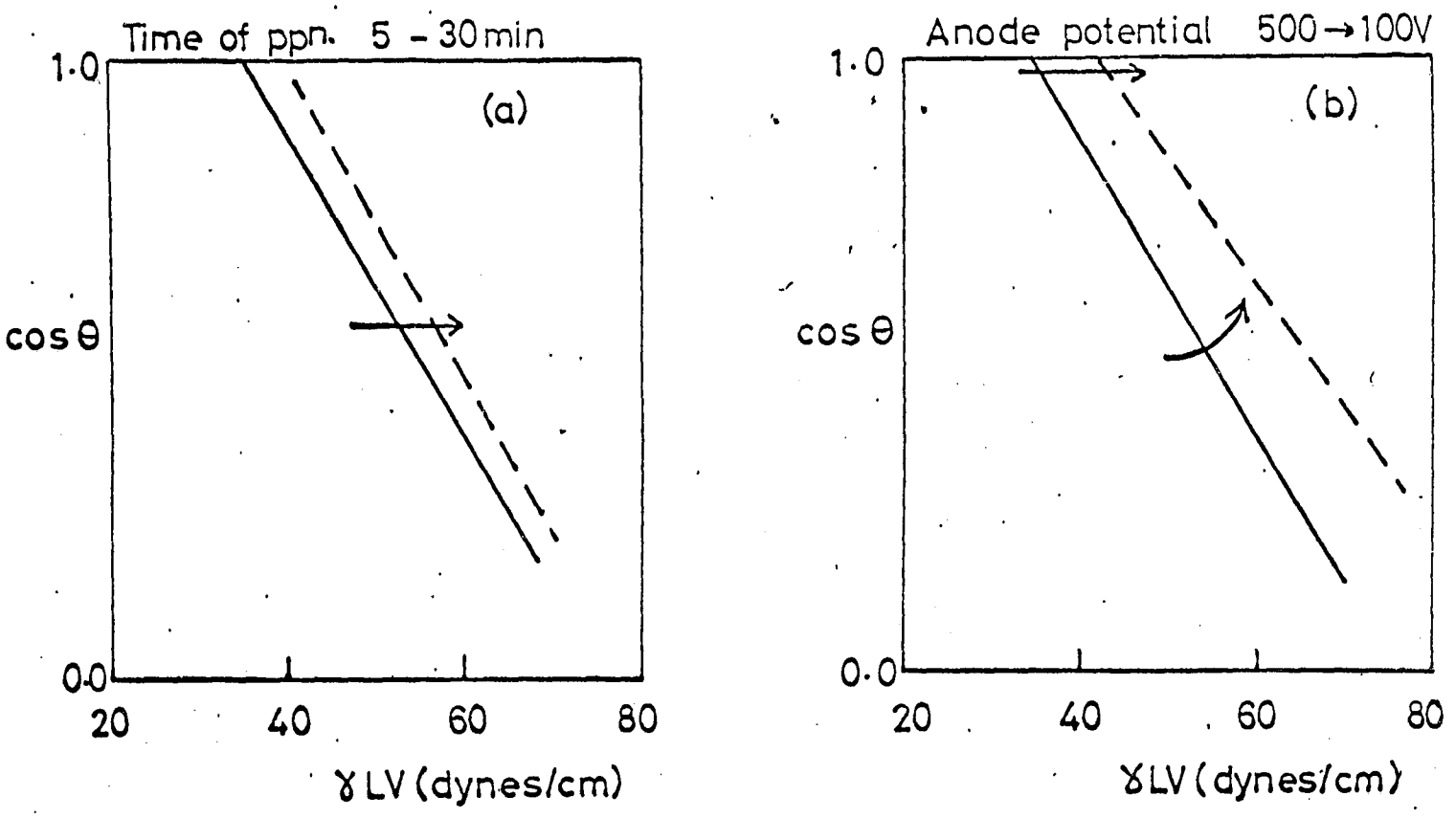


Figure 3-8


Time of ppn. 5 - 30 min
(a)
1.0
0.0
cos θ
20
40
60
80
γ LV (dynes/cm)
Anode potential 500 → 100V
(b)
1.0
0.0
cos θ
20
40
60
80
γ LV (dynes/cm)

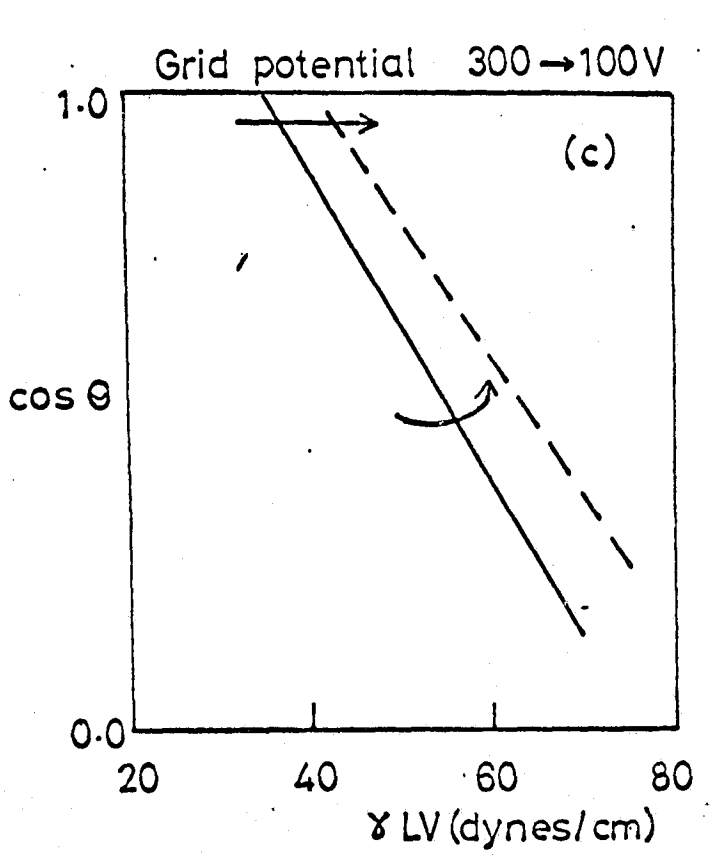

Grid potential 300 → 100V
(c)
1.0
0.0
cos θ
20
40
60
80
γ LV (dynes/cm)

Figure 3-9

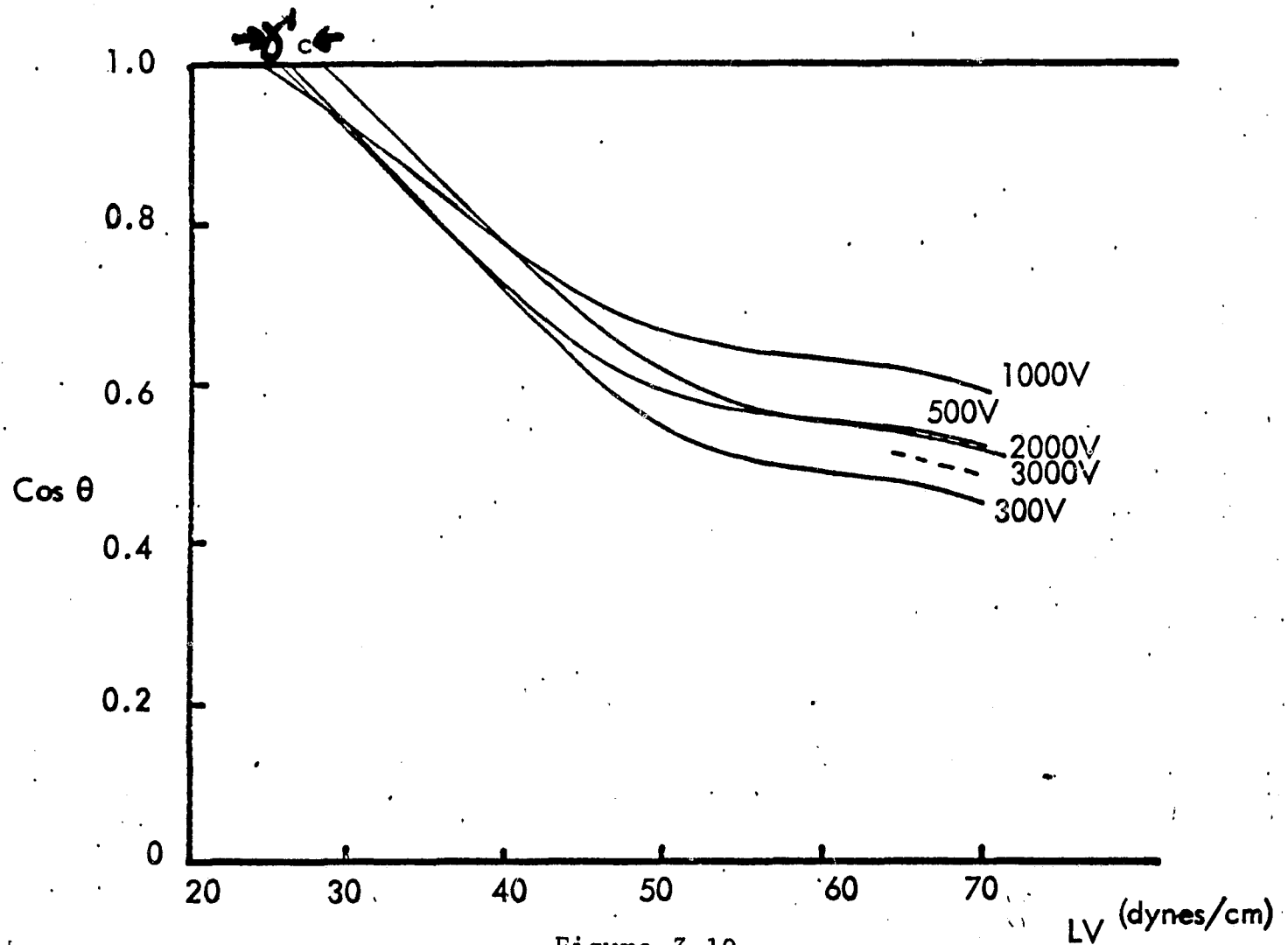


Figure 3-10

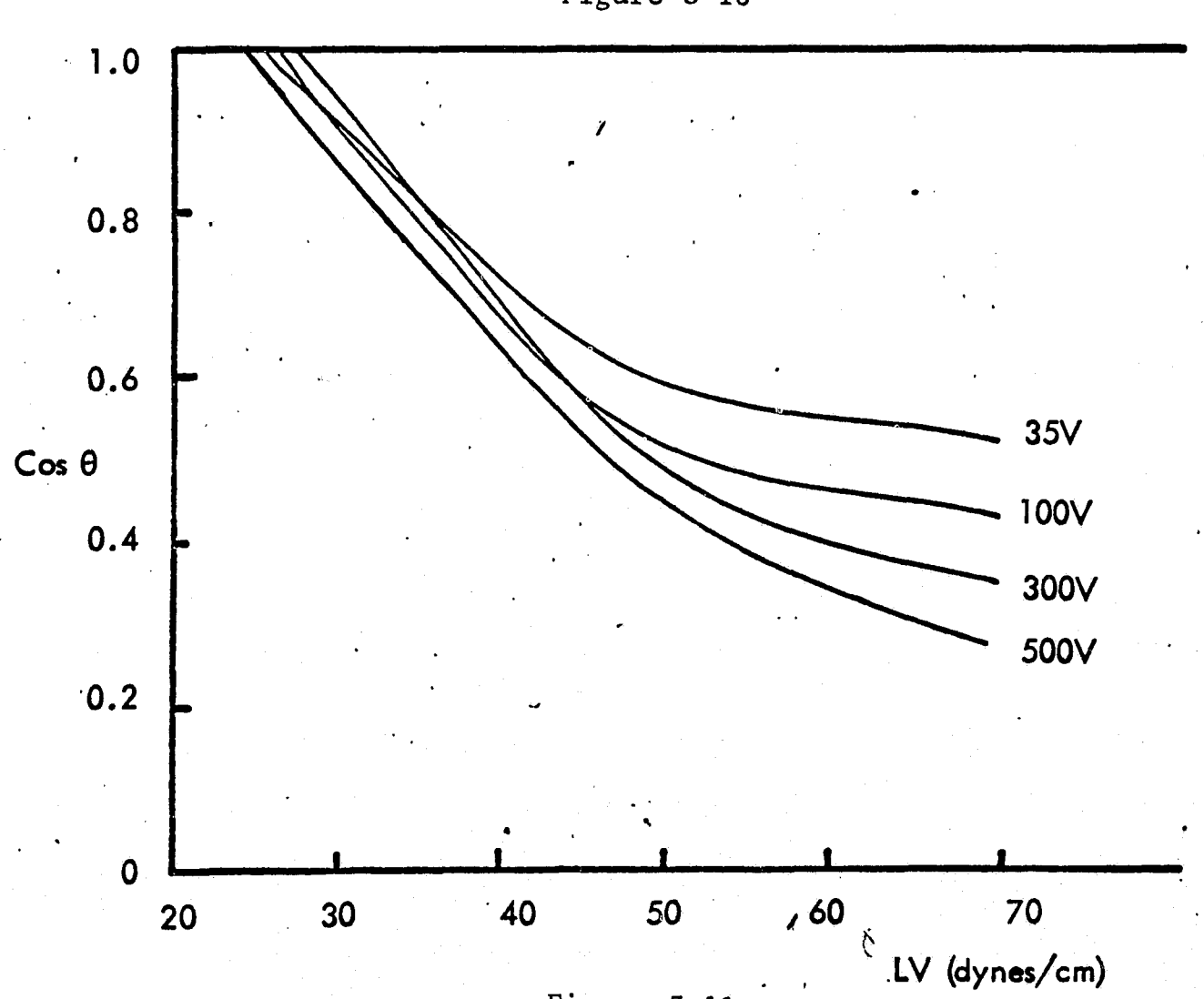


Figure 3-11

REFERENCES

1. M. W. Roberts, J. R. H. Ross, and J. H. Wood, "The Formation of Surface Films by Electron Bombardment", Final report, University of Bradford, October 1967 - September 1968.

2. T. W. Hickmott, J. Appl. Phys., 31, 128, (1960).

3. M. Boudart, D. F. Ollis, and G. W. Harris, Trans. Faraday Soc., 65, 510, (1969).

4. M. Kaminsky, "Atomic and Ionic Impact Phenomena at Metal Surfaces", Springer-Verlag, Berlin, 1965.

5. L. N. Dobretsov, "Electron and Ion Emission", 1952. NASA Technical Translation, 1963.

6. I. Haller and P. White, J. Phys. Chem., 67, 1784, (1963).

7. M. R. Andrews, J. Phys. Chem., 27, 270 (1923).

8. E. S. Ritner and R. Levi, J. Appl. Phys., 33, 2336 (1962).

9. W. A. Zisman, Advances in Chemistry Series, 43, 1 (1964) (Amer. Chem. Soc.)

10. M. K. Bernett and W. A. Zisman, J. Chem. Phys., 63, 1241 (1959).

11. E. G. Shafrin and W. A. Zisman, J. Phys. Chem., 64, 519 (1960).

12. International Critical Tables.

13. For example, J. J. Kipling, "Adsorption from Solutions of Non-Electrolytes", Academic Press, 1965.

14. F. M. Fowkes and W. D. Harkins, J. Amer. Chem. Soc., 62, 3377 (1940).

N70-39404

APPENDIX B

PHYSICAL AND CHEMICAL PROPERTIES OF THIN POLYMER FILMS

Final report of work carried out during the period

October 1968 - 31 January 1970

at

Dartmouth College
Hanover, New Hampshire

by

Robert W. Christy
Laurence E. Babcock

1.0 SUMMARY

The purpose of this work is to elucidate the electronic structure of thin polymer films which are formed on a substrate by electron bombardment in the presence of molecules of an organic or silicone vapor. These films have useful dielectric, mechanica, and chemical properties. Under suitable conditions of formation they are extremely resistant to mechanical abrasion and chemical attack, and they are therefore promising as a protective coating for other materials, as in the present application to valve technology. Other potential applications are in the area of microelectronics, since the films can form extremely thin insulating layers for capacitors, isolation of thin-film circuits, etch resists, or passivation of surfaces. For some of these applications an important feature is the possibility of selective deposition of the film by scanning or masking the electron beam. When this is not necessary, it may be noted that very similar films are formed by bombardment with ultraviolet photons rather than electrons. In any case, the properties of the films vary widely with the conditions of formation and treatment. Since these properties are determined by the molecular and electronic structure of the films, it is essential to gain an understanding of the underlaying mechanisms. Studies of the chemical kinetics of film formation are relevant, as well as studies of electrical and optical effects in the finished films. The latter aspects are the focus of the present work.

The films are formed by the free-radical polymerization of the molecules adsorbed on the surface, under the action of the bombarding electrons. The molecules are cross-linked by the electron beam to form a solid polymer film. The molecules used in the present study were DC 704 (Dow-Corning), a tetramethyltetraphenyltrisiloxane. In the limit of large electron/molecule ratios during the formation of the film, the resulting structure could be similar to silicone monoxide with the incorporation of some organic radicals, assuming that a large fraction of the original organic radicals would be detached by the electron bombardment. We have therefore approached the analysis of our films from the standpoint of band theory of inorganic semiconductors rather than that of organic molecular crystals. The fact that the structure is amorphous instead of crystalline is expected merely to smear out the energy band edges and to lower the electron mobility.

Experimentally we have made measurements of the photocurrent through thin polymer films sandwiched between two evaporated metal electrodes (one of which is semitransparent). The photocurrent was measured in the range of photon energies from 3 to 5 eV, with a light intensity on the order of 100 $\mu W/cm^2$ and an applied bias voltage up to 3V. The polymer thickness was about 140Å. Under these conditions, the photocurrent was normally smaller than the darkcurrent. Pulsed light was used for the photocurrent measurements, in order to subtract the darkcurrent and to avoid polarization effects. Our measured darkcurrents were in agreement with those measured by H. T. Mann in the thickness range from 500 to 2500Å. The logarithm of the current was approximately proportional to the square-root of the electric field, as observed previously.

The purpose of this experiment was to measure photocurrent as a function of photon energy and bias voltage applied to various metal-polymer-metal sandwiches. By making one of the metal films semitransparent, both metal electrodes and the polymer could be illuminated. Photoemission of electrons into the polymer from the metal electrodes as well as optical generation of charge carriers in the polymer is accomplished by this technique. The number of charge carriers produced in the polymer is dependent upon the absorption coefficient of the polymer at the incident wavelength. At wavelengths for which the polymer is transparent the photocurrent is produced by the photoelectrons from the electrodes. A study of these currents as a function of photon energy and bias would give the variation of conduction band height as a function of distance through the polymer. At wavelengths for which the polymer absorbs light, the photocurrent will include a component due to carriers produced in the bulk of the polymer. This latter component was found to be the dominant one in our experiments. It furnishes information on energy levels in the polymer and the width of the band gap. We concluded that the photocurrent is due to the optical generation of charge carriers by the excitation of electron-hole pairs across an energy band gap of about 2 eV in the polymer. Since the photocurrent is a volume effect rather than an electrode effect, it is likely that the darkcurrent is a volume effect also. The darkcurrent can be explained in terms of the Poole-Frenkel effect - field assisted thermal ionization of charge carriers from localized states (traps).

In the present phase of the work, we have studied the effect of varying the electron/molecule ratio which obtains during the formation of the polymer film. The following parameters were held constant: a) flux density of DC 704 molecules at the substrate, b) substrate temperature, c) thickness of final film. The bombarding electron current was varied between about 0.1 and 1 mA/cm^2, so that the electron/molecule ratio varied by an order of magnitude. The photocurrent in the resulting films shows a moderate increase with increase of the bombarding current during the film formation. The increase occurs mainly because the threshold photon energy is decreased, corresponding to a decrease in energy gap from about 3 eV. By contrast, the darkcurrent increases by several orders of magnitude with the increase of bombarding current.

The difference between the effects on the photocurrent and darkcurrent is not surprising, since they have been attributed to completely different mechanisms - intrinsic creation of electron-hole pairs in the case of the photocurrent and ionization of traps in the case of the darkcurrent. The electron/molecule ratio during bombardment is expected to affect two aspects of the polymer film structure: 1) the number of crosslinks between adjacent molecules of the original trimer, and 2) the number of free radicals which do not form crosslinks. We propose that the crosslinks increase the electron mobility in the polymer by increasing the number of conduction paths, and that the free radicals function as electron (or hole) traps. Since the number of possible crosslinks per molecule is not very large, the mobility will increase slowly with bombarding current except at very low currents, whereas the free-radical density could be more strongly dependent upon bombardment. Thus the photocurrent, which depends only on the mobility, will be weakly dependent on bombarding current, but the darkcurrent, which depends on number of traps as well as mobility, would be more strongly dependent. The effect of aging the films in air (several orders of magnitude decrease in darkcurrent) confirms these associations. Since the free radicals are highly reactive, their number will be vastly reduced by exposure to oxygen, whereas the number of stable crosslinks will be relatively unaffected. The temperature dependence of the photocurrent is very slight, and appears to be mainly due to a slight decrease of energy gap at higher

temperatures. The mobility thus appears to be nearly independent of temperature. The dark current is more strongly temperature dependent, showing an activation energy of about 0.6 eV above room temperature.

Dartmouth has shown that photocurrent measurements on thin polymer films can be interpreted theoretically, and thus serve as a useful tool for investigating their structure, in addition to such other complementary approaches as darkcurrent, infrared absorption, electron spin resonance, and mass spectrometry which have been used in the past. Variation of the bombarding electron/molecule ratio gives a wide range of structures, which could extend between an organic molecular material at one extreme and silicon monoxide at the other. The asymmetry which can occur in the current-voltage characteristic of the photocurrent suggests that in a single films it should be possible to vary the energy band structure as a function of distance through the film in a controlled way, merely by varying the electron/molecule ratio. Such structures might offer the possibility of very interesting protective-coating or electronic applications.

For the future, it would be most interesting to extend this kind of investigation to other starting materials. It is known that solid films can be formed by polymerizing a variety of silicone and organic molecules. Using a linear methyl siloxane could show clearly the effect of the type of organic radical which forms the crosslinks, and cyclic siloxanes could show the effect of the polymer backbone configuration. Similarly, linear and cyclic hydrocarbons could show the influence of the backbone consitution. One would expect that a wide variety of material properties could be obtained by suitably choosing the starting materials from among these possibilities. In addition, it would be useful to study further the effects of aging the films in air, and to determine the effects of radiation damage.

2.0 SAMPLE FABRICATION

2.1 DESCRIPTION OF A SAMPLE

The samples are polymerized DC 704 diffusion pump oil sandwiched between aluminum electrodes as in Figure 1. A sample is composed of three layers. The electrode is an L shaped aluminum strip which is evaporated first onto the glass substrate. The polymer itself is deposited next and covers most of the glass substrate including the electrode. The counter-electrodes are four aluminum strips at right angles to the electrode. They are evaporated over the polymer. Thus at the cross-overs of the electrode and counter-electrode strips, in layers over the glass, are electrode, polymer, and counter-electrode. This system provides four samples on one substrate. The indium dots shown in Figure 1 provide points to fasten electrical leads to the sample.

The polymers discussed in this paper are all 140 Å $\pm$ 14 Å thick. No attempt was made to control electrode thickness except that the electrodes were made sufficiently thick to be opaque, about 1000 Å thick. The thickness of the counter-electrodes was set at about 100 Å. Thus the counter-electrodes are semi-transparent with about 25 percent transmission.[1] Each sample is assumed to be a rectangle, the area of which (the product of the electrode and counter-electrode widths) is about 0.031 cm^2.

2.2 DESCRIPTION OF SAMPLE FABRICATION APPARATUS

Most of the components of the apparatus used to fabricate the samples are components of the sample fabrication apparatus used by R. H. Colburn.[2] A Deposit Thickness Monitor (Sloan Instrument Co. Model DTM3) was installed to control the thickness of the counter-electrodes. The shutter was modified so that it can control the electron beam impinging upon the substrate during sample fabrication. The masks used on the electrode and the counter-electrodes were modified to shape the evaporated aluminum strips. The diaphragm limiting the substrate area bombarded by electrons was removed, and the mounting of both the electron gun and the oil source was modified so that they may be moved mechanically from outside the vacuum apparatus during sample fabrication.

The detector head of the Deposit Thickness Monitor is indicated by the point of intersection of the horizontal and vertical line segments labeled 1 in Figure 2. The detector head is mounted at approximately the same distance from the Al source as the substrate. Aluminum is evaporated onto the detector head of the Deposit Thickness Monitor and onto the substrate simultaneously. Therefore, the thickness of the counter-electrodes may be controlled by the thickness of the aluminum evaporated onto the monitor.

The shutter was altered by the addition of extra flaps so that the shutter could be used to interrupt the electron beam and interrupt the evaporated aluminum going to the Deposit Thickness Monitor detector head. Mechanical linkages were added so that the shutter could be opened and closed mechanically from outside the vacuum apparatus.

The new electrode mask is the backwards L shaped slit indicated by line segments labeled 2 in Figure 3. The large hole underneath the gear wheel in Figure 3 allows electrons to impinge on the substrate during sample bombardment. The counter-electrode mask is indicated by the line segments labeled 3 in the same figure. The electrode mask differs from Colburn's, which formed a shallow circular arc, in that it adds a tab extending to edge of the substrate. Colburn completed his electrode by smearing an indium strip to the edge of the glass. Due to the irregularity of this strip, the total electrode area was not constant from substrate to substrate, and therefore the bombarding current density could not be calculated precisely. In Colburn's apparatus the irregularity of the indium strip did not matter because he had a diaphragm between the sample and the electron gun which kept electrons from striking the indium strip. Because the diaphragm had an undesirable lens effect which focused electrons onto the center of the substrate, it was removed exposing the irregular indium smear to electrons. Therefore the evaporated tab was substituted for the indium smear so that the total electrode area would be constant from substrate to substrate.

The counter-electrode mask makes possible the simultaneous evaporation of all four counter-electrodes so that the counter-electrode thickness is the same for all counter-electrodes on the same substrate. These four counter-electrodes intersect at the center of the sector shaped shutter shown in

Figure 4. If equal counter-electrode thicknesses are not desired, the counter-electrodes can be uncovered one by one in four successive aluminum evaporations to give a sequence of counter-electrode thicknesses.

The electron gun and the oil source are the same ones used by Colburn. They are indicated by the line segments labeled 4 in Figure 2. Both the gun and the oil source were mounted on an arm which could be moved from outside the vacuum apparatus. They are mounted so that both the oil and electron beams are directed at the substrate. During the polymerization process the two sources were swept back and forth at a rate of about 2 sweeps per minute to provide a more uniform average flux of both oil and electrons over the substrate. A uniform sample could also be made without sweeping by offsetting the electron gun to the left.

The electron and oil sources were operated in the same way that Colburn operated them except that the cathode of the electron gun was only -300 V instead of -400 V and the oil source was biased sufficiently negative to repel stray secondary electrons, thus preventing the formation of a polymer scum on the surface of the oil. The scum affects the oil flux impinging on the substrate.[3]

The total primary electron flux incident upon the electrode during sample polymerization was meausred using the circuit shown in Figure 6. The samples were fabricated with + 90V applied to the electrode. This bias would collect most of the secondary electrons, and therefore our total electron flux hitting the electrode is higher than the primary electron flux measured by this circuit. Mann[4] has measured the ratio of total electron flux to primary electron flux to be about 1.8.

2.3 PROCEDURE TO CONSTRUCT A SAMPLE

The samples are constructed on a 1.5 cm by 5 cm glass substrate cut from a microscope slide. The substrates are cleaned in an ultrasonic cleaner, first using a soap solution to remove grease from the substrate and then using deionized water to rinse away the soap. After drying in forced hot air, indium dots are soldered onto the substrate where the electrode and

counterelectrodes will overlay them. The substrate is then mounted in a substrate holder and a lead to allow biasing the electrode is attached to the substrate, using the indium dot which will be overlayed by the electrode. The whole is placed in the vacuum coater which is then evacuated to 5 to 8×10^{-7} torr pressure. The vacuum coater is liquid-nitrogen trapped to prevent backstreaming of diffusion pump oil.

The filament of the electron gun is now heated to operating temperature. The gun is heated before the aluminum electrode is evaporated so that contaminants driven from the gun by heating will not cover the electrode after it is deposited. These contaminants would give an insulating layer which was a composite instead of the desired uniform polymer layer.

After operating temperature of the electron gun has been reached the electrode strip is vacuum coated onto the glass. The substrate is positioned by means of index marks over the electrode mask. High current is passed through a tungsten wire bearing pure aluminum, thereby melting and evaporating the aluminum. The shutter is opened allowing aluminum to pass through the electrode mask to the substrate. When sufficient aluminum has been deposited onto the glass to make an opaque electrode the shutter is closed interrupting the evaporation and the current is turned off.

The deposition of the polymer is next. The sample is positioned over the electron gun and associated mask using the index marks. The + 90V electrode bias is applied. Opening the shutter initiates the sample bombardment. The duration of sample bombardment is timed using a stop watch and the total bombarding current is monitored with the ammeter in series with the sample bias supply. The total bombarding current varies slightly with time during the bombardment of a single substrate. It is, therefore, held constant by making minor adjustments of the electron gun heating current. In addition, the gun is mechanically swept back and forth to produce a more uniform time average of the bombarding current density over the entire substrate. After the required time has elapsed the sample bombardment is terminated by reclosing the shutter.

Lastly, the counterelectrodes are vacuum coated onto the polymer. The +90 V electrode bias is removed and the substrate is positioned over the counter-electrode mask using the index marks. Pure aluminum is melted as before. Because temperature affects the reading of the Deposit Thickness Monitor, this monitor must now be zeroed. The zero setting was chosen at 400 Hz, to avoid a considerable dead region at the low frequency settings of the Deposit Thickness Monitor. The shutter is now opened and held open until the reading of the Deposit Thickness Monitor has increased 120 Hz. The shutter is then closed, completing the sample construction.

3.0 RATE OF FORMATION

3.1 THEORY

The rate of polymer film formation as a function of electron flux has been calculated by Christy.[5] His result is that the rate of formation R is related to the flux of electrons per unit area f, the mean time of stay of an oil molecule on the surface τ, the cross section for the cross-linking process σ, the flux of oil molecules per unit area F, and the volume of an oil molecule v, by the equation

$$R = vF/(1 + 1/\sigma\tau\ f) \qquad (3\text{-}1)$$

This result holds when the unpolymerized oil molecules do not completely cover surface. Rewriting Equation (3-1) as

$$f/R = (1/vF)f + 1/\sigma\tau\ v\ F \qquad (3\text{-}2)$$

we see that data plotted as f/R vs. f should lie on a straight line with slope 1/vF and vertical intercept at f = 0 of $1/\sigma\tau$ v F.

The thickness of the samples is obtained from capacitance measurements at 1 kHz using the equation for a plane parallel plate capacitor, $d = \varepsilon A/C$. The quantity A is the area of the same and C is the measured capacitance. The value of the dielectric constant $\underline{\varepsilon}$, 2.5×10^{-13} F/cm, was measured by Mann[3] using thicker samples. The thickness calculated from the capacitance yields a result slightly in excess of the real thickness due to penetration of the electric fields into the metal electrodes.[6,7] Assuming a spherical fermi surface for Al and a Fermi energy of 11.7 eV at T = 0 the free electron density is about 1.8×10^{23}/cc. The calculated contribution of skin effects to the total sample thickness based on these assumptions is about 3Å.

The rate of formation of the polymer film as a function of bombarding current density is shown in Figure 7 in comparison with the earlier results of Christy.[5] In both cases the lines drawn through the points are theoretical curves with the parameters in Equation (3-1) chosen to give the best fit.

Figure 8 shows how the parameters in Equation (3-1) can be obtained by plotting the data of Figure 7 according to Equation (3-2). The slope of the straight line is 6.2 sec/Å amd its vertical intercept at f = 0 is 0.065 $Å^{-3}$. Christy's values for the same quantities were 3.0 sec/Å and 0.080 $Å^{-3}$.

3.2 DISCUSSION

The data presented in Figures 7 and 8 confirm Christy's previous theory. It remains to explain the differences in the magnitudes of the various parameters.

The fact that the rate of formation of polymer saturated at a value (vF = 0.16Å/sec) about one half of Christy's value (0.33 Å/sec) suggests that the oil flux F was less in our system. Christy's vacuum system was not trapped and backstreaming pump oil was present.

Figure 7 shows that R, the rate of formation of polymer, saturated at a smaller value of measured electron bram current density J than did Christy's. The difference is probably due to the fact that our substrates were positively biased during polymerization whereas Christy's were not. This positive bias would collect the secondary electrons; therefore the actual total electron flux at the substrate was greater than that calculated from the measured net electron beam current. The measured beam current (with bias) gives only the number of primary electrons.

The value for $\sigma\tau$ which would be obtained from the intercept in Figure 8 is two and one-half times Christy's value, whereas it should be the same. This difference is also explained by the collected secondary electrons. Let the real polymerization current (including secondaries) f be related to the measured (primary) current f' by $f = \alpha f'$ where α is a constant. Equation (3-2) should be correct when the real value (primaries plus secondaries) is used for the electron flux. From Equation (3-2) we have

$$f/R = (1/vF)\ f + 1/\sigma\tau\ v\ F$$

where F is the oil flux in the same fabrication apparatus used for this work. The data in Figure 8, however, are plotted with the measured (primary) current f'. Since $f = \alpha f'$, we have from Equation (3-2):

$$f'/R = (1/v\ F)f' + 1/\alpha\sigma\tau\ v\ F \qquad (3\text{-}3)$$

thus our measured slope is still given by 1/vF, but the intercept contains the new factor α. Assuming that Christy's values for $\sigma\tau$ and v are the same as our values for the same quantities, we may evaluate α from the ratio of our vertical intercept using Equation (3-3) to the vertical intercept found by Christy using Equation (3-2):

$$F_c/\alpha F = 0.81$$

where F_c is the oil flux in the sample fabrication apparatus used by Christy, and 0.81 is the value of this ratio calculated from the two measured intercepts. We know the value of the ratio F_c/F from the two measured slopes to be 2.1 and thus we find α to have the value 2.5. The secondary ratio δ, defined as the number of secondary electrons per primary electron, is $\delta = (f - f')/f' = \alpha - 1 = 1.5$. This value is in satisfactory agreement with Mann's directly measured value of 1.8 for conditions similar to ours. Thus the difference in the intercepts reflects the difference in the methods of measuring the electron flux, and thus explain the saturation at lower current in a quantitative way.

4.0 DARKCURRENT

4.1 THEORY

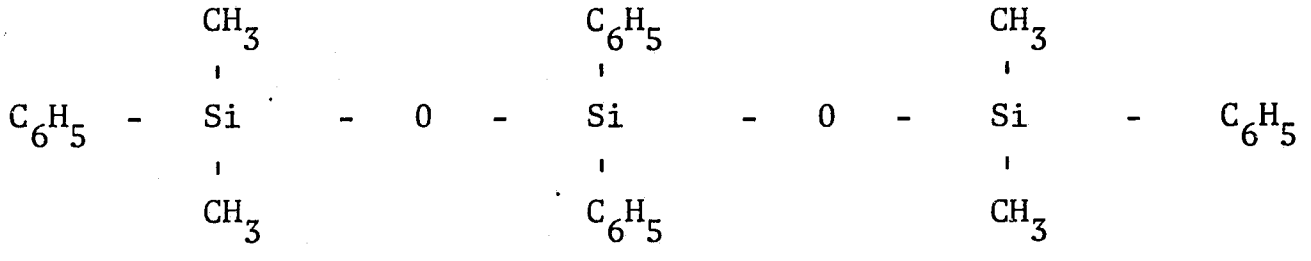
The high-field darkcurrent of the polymer films will be seen to result from a bulk controlled process known as the Poole-Frenkel effect or the internal Schottky effect[8]:

$$J = Ne\mu E \exp\left[\left(-\phi + e^{3/2}\sqrt{E}/\sqrt{\varepsilon}\right)/kT\right] \qquad (4\text{-}1)$$

In Equation (4-1), N is the carrier density whose interpretation depends upon the model chosen for the polymer, e the electronic charge, μ the carrier mobility, E the applied field, ϕ the energy difference between the bottom of the conduction band and the Fermi level, ε the dielectric constant and k and T are Boltzmann's constant and the temperature, respectively.

By analogy with the results of Mead's work with Ta_2O_5 insulating films[9], (which exhibited the Poole-Frenkel effect at high fields) at low fields we expect the darkcurrent to be dominated by the "hopping"[10] form of ohmic condution. "Hopping" is the phonon assisted tunneling of a charge carrier from an occupied trap to an unoccupied trap, and results in linear I vs. V behavior.

Each unpolymerized oil molecule is a trisiloxane of the form[3,11]



or with another permutation of the phenyl and methyl radicals. During the sample formation process, the polymerizing electrons create free radicals like Si - CH_2 or Si - C_6H_4. These will either remain free radicals or, if there is another free radical nearby, the two will cross-link thereby tying two molecules together. The crosslinking can be an

ethylene bond Si - CH_2 - CH_2 - Si or a methylene bond Si - CH_2 - Si.[12] Also a silicon bond Si-Si (or phenyl-phenyl, phenyl-methyl, or phenyl) is possible. The crosslinks are assumed to influence the mobility. This will be discussed in Section 5.1. The uncrosslinked free radicals are known to be highly reactive. It will be seen below that the darkcurrent is strongly dependent on bombarding flux and upon the amount of exposure to air. This strong dependence suggests that the uncrosslinked free radicals are the Poole-Frenkel defects.

4.2 APPARATUS

During the measurement of both the darkcurrent and the photocurrent the sample was kept at pressures below 5×10^{-4} torr in the vacuum cryostat shown in Figure 9. The sample was mounted on a coldfinger which projects from the bottom of the liquid nitrogen reservoir. A quartz window in the side of the vacuum jacket allowed the sample to be illuminated for photocurrent measurements. Electrical connection was by means of a nine pin electrical feedthrough, leads from which were indium soldered to the glass substrate using the indium dots associated with the electrode and counter-electrodes. In addition, a thermocouple was indium soldered to the substrate in order to monitor the temperature.

The circuit for the measurement of darkcurrent is shown in Figure 10. This circuit was chosen because the sample bias is large and easily measured, while the darkcurrent is small. Leakage currents that are detected by the ammeter are minimized by this circuit because all leakage currents through the voltmeter, between the chasis ground and real ground of the ammeter, and all leakage currents in the X-Y plotter bypass the ammeter.

The variable voltage source was a linear voltage ramp generator with rise time of about 1V/min constructed from an operational amplifier. The voltmeter was a Keithley model 600 electrometer, the ammeter was a Hewlett Packard model 425A, and the X-Y plotter was a Hewlett-Packard model 7035B.

4.3 RESULTS

Figure 11 shows the dependence of log J/E on $\sqrt{E}$ for sample No. 38B. At fields above about 10^6V/cm, the logarithm of the conductivity σ(=J/E) varies linearly with the square root of the applied field. This is the dependence predicted by the Poole-Frenkel effect, Equation (4-1).

One sample formed at our lowest bombarding flux (30μA/cm^2) showed a linear I vs. V behavior at field strengths less than .8 x 10^6V/cm. This linear behavior at low field strengths was also observed by Christy[11] in a sample which had not been exposed to air formed at 50 μA/cm^2.

The temperature dependence of the films for temperatures above room temperature are shown in Figures 12 and 13. Figure 12 shows the dependence of the darkcurrent at 10^6V/cm for sample No. 49A upon temperature. The activation energy of 0.38 eV calculated from these data enables one to calculate ϕ of Equation (4-1) to be 0.65eV, and N of the same equation to be about 10^{13}/cc, assuming μ = 0.1 cm/Vsec. We have assumed μ = 0.1 cm/Vsec because we believe this is the smallest reasonable value for μ. The exact interpretation of N depends upon the model chosen for the polymer. Figure 13 shows that above room temperature the slopes of the ln σ vs. $\sqrt{E}$ curves are approximately independent of temperature. Mann[3] has previously shown these slopes to be independent of temperature down to nitrogen temperatures.

The darkcurrent in the high field region as a function of electron flux during film formation was also studied. The oil flux was held constant. The results of this study are shown in Figures 14 and 15. Figure 14 shows the darkcurrent density at a fixed field of 10^6V/cm as a function of the electron flux. The straight line shown corresponds approximately to a 7th power dependence of darkcurrent (at fixed field) upon electron flux. Figure 15 shows the dielectric constant $\varepsilon_{p.f.}$ calculated from the slope β of the ln σ vs. $\sqrt{E}$ curves as a function of electron flux for the samples studied. These data show that the dielectric constant increases with increasing electron flux.

Figure 16 shows the change in the darkcurrent at fixed field (measured in the fabrication apparatus) as one sample was exposed to air. The darkcurrent changes by nearly five orders of magnitude in the first 60 seconds. Christy's[11] earlier work had shown that the darkcurrent changed by only one order of magnitude after 24 hours' exposure to air. Probably Christy's darkcurrent changed slower because his thicker silver counterelectrodes kept air from reaching the polymer. Because the change in darkcurrent observed by Christy was so small we originally assumed that the five to seven minute period during which the sample was being transferred to the vacuum cryostat from the fabrication apparatus would not change the sample properties very much. It is now clear that although this assumption was false, we were able to get consistent results among different air-exposed samples because the darkcurrent was changling slowly by the time the samples were transferred to the vacuum cryostat. The slope β of the $\ln \sigma$ vs. $\sqrt{E}$ curves did not change with exposure to air, however, This result allows comparison of this work to that of Mann and Christy, even though they measured the darkcurrent properties without previous exposure to air.

4.4 DISCUSSION

On the basis of the data presented, the Poole-Frenkel effect would properly explain the high field region of the darkcurrent. Frenkel's theory in his original formulation, however, applies only to an insulator with partially ionized uncompensated donors.[13,14] But it will be seen that an improbably small density of condution band states is inferred unless there is some compensation. Therefore, the final choice of the Poole-Frenkel effect as opposed to Schottky emission from the electrodes is based upon the argument presented by Colburn[15], namely, that the photocurrent appears to be a bulk process and therefore the darkcurrent must be also. Henceforth, the darkcurrent will be assumed to be explained by the Poole-Frenkel effect, even though the temperature-independence of the slope β of the $\ln \sigma$ vs. $\sqrt{E}$ curves shows that the Poole-Frenkel theory outlined earlier is not the complete explanation of the sample behavior.

Previous ESR measurements[3] indicate that the free radical density is about 10^{18}/cc for a sample which has been exposed to air. This density implies

that there is one free radical for each cube of polymer 100 Å on a side. The maximum in the potential energy of the field associated with the free radical occurs at about 40 Å, using $R_{max} = \sqrt{e/\varepsilon E}$ from the Poole-Frenkel theory. Therefore, assuming the Poole-Frenkel defect to be a free radical, the dielectric constant of the polymer calculated from the slope β is a local dielectric constant with contributions only from the molecules and crosslinks. The other free radicals do not contribute because the coulomb field of one does not overlap another free radical very much. However, the dielectric constant calculated from the capacitance must be greater because the external field polarizes both the molecules with crosslinks and the free radicals. This may explain why Mann's capacity dielectric constant ε_c is 2.8 while we calculate his Poole-Frenkel dielectric constant $\varepsilon_{p.f.}$ to be about 1.7. Furthermore, on the basis of this model, one would not expect $\varepsilon_{p.f.}$ to change with exposure to air, which presumably destroys mostly uncrosslinked free radicals, while ε_c would change with exposure to air because of the destruction of the free radicals. Both expectations have been substantiated experimentally.

The density N of Equation (4-1) has been calculated from the activation energy to be about $10^{13}/cm^{-3}$. If there are only donors in the polymer, we find the density of donors N_d to be about $10^{8}/cm^{-3}$,[16] assuming the density of states at the bottom of the conduction band N_c to be only 10^{18}. This result is improbably small; therefore it is likely that the polymer has compensating acceptor levels. If we assume, for instance, that $N_d \sim N_a$, where N_a is the density of acceptors, then[14]

$$N = N_c \ (N_d - N_a/N_a) \text{ if } N_d > N_a \tag{4-2}$$

If we let $N_d \simeq 10^{18}$, then we have from (4-2)

$$N_a \simeq 10^{18} \ N_c/(10^{13} + N_c) \tag{4-3}$$

But $N_c >> 13$, so Equation (4-3) reduces to $N_2 = 10^{18}$. Therefore, by using this model or ones similar to it, we see that the small value of N does not rule out the Poole-Frenkel mechanism as an explanation of darkcurrent.

5.0 PHOTOCURRENT

5.1 THEORY

Colburn's[15] photocurrent results led him to propose that the photocurrent was due to carriers optically excited across the bandgap in the sample bulk. Due to the magnitude of the absorption coefficient, 10^4 cm^{-1}, Colburn suggested that possibly the transitions were direct transitions into conduction band states which were linear combinations of crystalline wave functions, in analogy with the proposed explanation by Tauc[17] of the photocurrent in amorphous germanium. These transitions do not conserve k vector, implying an energy dependence of the photocurrent typical of indirect transitions. It is not yet known whether the above theory is the proper explanation of the observed photocurrent in polymer films made from DC704. However, Colburn's evidence that the photocurrent is a bulk process seems conclusive. Therefore, it is assumed that the absorption edge, measured by means of the photocurrent cutoff, is a measure of the band gap width.

In the model of the film structure presented in the darkcurrent theory, the free radicals created by impinging electrons may unite, thereby crosslinking two nearby molecules. If we consider these crosslinks to be current paths, then an increase in the number of crosslinks results in an increase in the number of current paths. If the photocurrent is due to intrinsic charge carriers, as argued above, this increase in the number of current paths increases the mobility of these intrinsic charge carriers. Therefore we expect the photocurrent to increase with the bombarding flux, but weakly because once two molecules are crosslinked, further crosslinking should have only a moderate effect on the mobility. A molecule must be crosslinked at least once in order to have become part of the solid film at all.

The photocurrent will be seen below to be given by:

$$I = K\, h^2 (\nu - \nu_o)^2\, L_\nu\, (V - V_o)\sqrt{|V - V_o|} \qquad (5\text{-}1)$$

where $h\nu$ is the photon energy in eV, $h\nu_o$ the band gap width also in eV, $L\nu$ the intensity of the incident light at the frequency ν and V the applied

bias. The intercept V_o of Equation (5-1) probably reflects the fact that the polymer nearest the electrode was formed first and subsequent bombarding electrons impinge on it. (See Section 5.4). The linear dependence of photocurrent upon incident light intensity L was established by Colburn, as was the energy dependence. The results of a more detailed study of the bias dependence previously measured by Colburn is presented in this report. The dependence of K and $h\nu_o$ upon the polymerizing electron flux was studied in some detail.

5.2 APPARATUS

Photocurrent measurements were made with the sample in the same vacuum cryostat described in Section 4.2. The circuit used is shown in Figure 17. This circuit produced X-Y plots of photocurrent vs. wavelength. Photocurrents as small as 10^{-12} A, at 3.5 Hz, are dropped across the load resistor to create a photovoltage. This photovoltage is amplified by the two Tektronix type 122 preamps. A P.A.R. model C.W. 1 box car integrator synchronously demodulates the signal and averages the noise. The resultant voltage is plotted vs. wavelength on the X-Y plotter. The direction of current flow is known because for sufficiently large biases the current flow is in the same sense as the current through a resistor. The polarity of the voltage reading on the boxcar is set to be in the same sense. A current was taken to be positive when the direction of flow of positive charge in the sample was towards the electrode. A ten-turn potentiometer attached to the wavelength scanning knob of the momochromator provides a voltage proportional to wavelength for the plotter x-input.

In order to read the photocurrent accurately, the current limiting element must be the sample itself. In some cases, with higher biases and greater photon energies, it was necessary to use a smaller load resistor to get accurate results. A smaller load resistor could be switched in to achieve this end.

The light intensity was calibrated at various wavelengths using a Texas Instruments L.S. 400 phototransistor. These devices are intended for reading punch-cards. The end of the soft glass jacket was removed and the

phototransistor placed in a sealed quartz tube to obtain a cheap photosensitive device whose response at 2500 Å is about 1/5 of its response at 6000 Å. This photosensitive device was calibrated after the above alterations using an EG & G Radiometer as a secondary standard.

Substituting the phototransistor apparatus for the vacuum cryostat, a plot of phototransistor response vs. wavelength was made at the end of each set of photocurrent measurements. It is necessary to correct for a slight nonlinearity in the photoresponse vs. intensity of the phototransistor and for the phototransistor spectral response in order to calculate the light intensity. The light intensity calibration is the weak point in our system, due to irregular changes in the Hg Lamp intensity with time and possible aging of the phototransistor.

The sample bias is measured with a Keithley model 600 electrometer which is removed after measurement in order to keep its noise out of the system.

5.3 RESULTS

Figures 18 and 19 show typical photocurrent results. Figure 18 shows the dependence of photocurrent upon applied positive bias at a fixed wavelength, Figure 19 the dependence upon photon energy at several fixed biases. Both sets of data are accurately described by the slight lines drawn. In Figure 18 the most interesting information is the slope, which indicates a 3/2 power law dependence of photocurrent upon bias. This result is independent of wavelength and bombarding current. In Figure 19 the threshold energy is measured to be 2.2 eV, independent of bias. The dependence of this threshold energy $h\nu_o$ upon electron flux during polymerization (J_p) is shown in Figure 20.

Figure 21 shows the dependence of the constant K in Equation (5-1) upon sample polymerizing current. Probably errors in the calibration of the light intensities caused the large scatter of data points in Figure 21. The temperature dependence of the photocurrent is shown in Figure 22. As can be seen the photocurrent changed little, probably within the light intensity calibration error.

5.4 DISCUSSION

The samples showed a displacement of the origin in the photocurrent with respect to bias that was not shown in the results [V_o of Equation (5-1)]. This asymmetry yielded a photocurrent at zero bias voltage that was in the direction from the electrode to the counterelectrode (a "negative" current with our sign convention). The asymmetry suggests that the bandgap near the electrode is narrower than near the counterelectrode. Figure 20 shows that increased polymerizing electron flux narrows the bandgap. The asymmetry in photocurrent is therefore consistent with the data of Figure 20, since the polymer near the electrode has been bombarded more than polymer near the counterelectrode. We have no detailed explanation why increased bombarding flux decreases the bandgap, however.

The independence of the photocurrent from temperature supports the hypothesis that the photocurrent is optical excitation of intrinsic carriers, because the bandgap width should be nearly independent of temperature. The fact that the photocurrent is linearly dependent upon the square of the photon energy is also consistent with this hypothesis, as this square dependence is characteristic of indirect transitions across the bandgap. Colburn has previously shown that the bulk optical absorption cutoff energy and the photocurrent cutoff energy are equal.[2] Therefore, it seems safe to conclude that the photocurrent is due to the optical excitation of intrinsic carriers in the sample bulk. Whether the excitation is direct as Colburn suggested or indirect is still unanswered.

The bias dependence of the photocurrent is not understood. A 3/2 power dependence occurs for a space charge limited thermionic vacuum diode. The polymer might be similar to a vacuum diode if the mobility in the polymer were large enough so that carriers injected at one electrode were swept into the other electrode with few collisions. If this were the case, however, then the photocurrent would not be a bulk process. Thus the 3/2 power dependence of the photocurrent must be due to some other mechanism.

REFERENCES

1. L. Holland, Vac. Deposition of Thin Films, (Chapman and Hall Ltd., London, 1966).

2. R. H. Colburn, Advanced Valve Technology, Final Report Contract NAS 7-436, Report No. 06641-6023-R000, January 1969.

3. H. T. Mann, J.A.P., 35, 2173 (1964).

4. H. T. Mann, Electrochemical Tech., 1, 287 (1963).

5. R. W. Christy, J.A.P., 31, 1680 (1960).

6. C. A. Mead, Phys. Rev. Letters, 6, 545 (1961).

7. H. Y. Ku and F. G. Ullman, J.A.P., 35, 265 (1964).

8. J. Frenkel, Phys. Rev., 54, 647.

9. C. A. Mead, Phys. Rev., 128, 2088 (1962).

10. A. Miller and E. Abrahams, Phys. Rev., 120, 745 (1960).

11. R. W. Christy, J.A.P., 35, 2179 (1964).

12. L. Holland and L. Laurenson, Vacuum, 14, 325 (1964).

13. P. Mark and T. Hartman, J.A.P., 39, 2163 (1968).

14. J. G. Simmons, Phys. Rev., 155, 657 (1967).

15. R. H. Colburn and R. W. Christy, J.A. P., 40, 3958 (1969).

16. C. Kittel, Int. to Solid State Physics, 3rd Edition, J. Wiley and Sons, Inc., New York, 1967, pg. 313.

17. J. Tauc, Science, 19, 1943.

FIGURE CAPTIONS

Figure 1. Typical sample.

Figure 2. Side view of vacuum evaporation apparatus.
1: Deposit thickness monitor detector head
4: Electron gun and oil source

Figure 3. Top view of vacuum evaporation apparatus with substrate holder removed to show the various masks.
2: electrode mask
3: counterelectrode mask

Figure 4. Bottom view of substrate holder.

Figure 5. Top view of substrate holder.

Figure 6. Sample fabrication circuit.

Figure 7. Rate of formation as a function of bombarding current density. The oil flux is held constant.

Figure 8. The ratio of electron flux to rate of formation as a function of electron flux.

Figure 9. Side view of vacuum cryostat.

Figure 10. The circuit used to measure darkcurrent.

Figure 11. The conductivity as a function of the square root of the field strength for sample 38B which was formed with our greatest bombarding current density, $1mA/cm^2$. The counterelectrode was positive.

Figure 12. The temperature dependence of the darkcurrent. The slope of the straight line shown was used to calculate the activation energy.

Figure 13. The conductivity as a function of the square root of electric field strength with temperature as a parameter. Sample 49A was formed with a bombarding current density of $.33mA/cm^2$.

Figure 14. The darkcurrent density at fixed field as a function of bombarding current density.

Figure 15. The dielectric constant calculated from the slopes of the conductivity vs. square root field curves as a function of bombarding current density. The □ is for one of Mann's samples on which he calculated the dielectric constant from the capacitance to be 2.8.

Figure 16. The change in the darkcurrent upon exposure to air. The value of J at T = 0 was 8×10^{-3} A/cm^2.

Figure 17. The circuit used to measure photocurrent.

Figure 18. The photocurrent as a function of bias with wavelength of incident light as a parameter.

Figure 19. The square root of the photocurrent as a function of the energy of the incident radiation with bias as a parameter.

Figure 20. The photocurrent cutoff energy, which we have equated to the band gap, as a function of bombarding current.

Figure 21. The constant K of Equation (5-1) as a function of bombarding current density. The units of K are $Acm^2/(eV)^2V^{3/2}$ watts.

Figure 22. The square root of the photocurrent as a function of the energy of the incident radiation with bias and temperature as parameters.

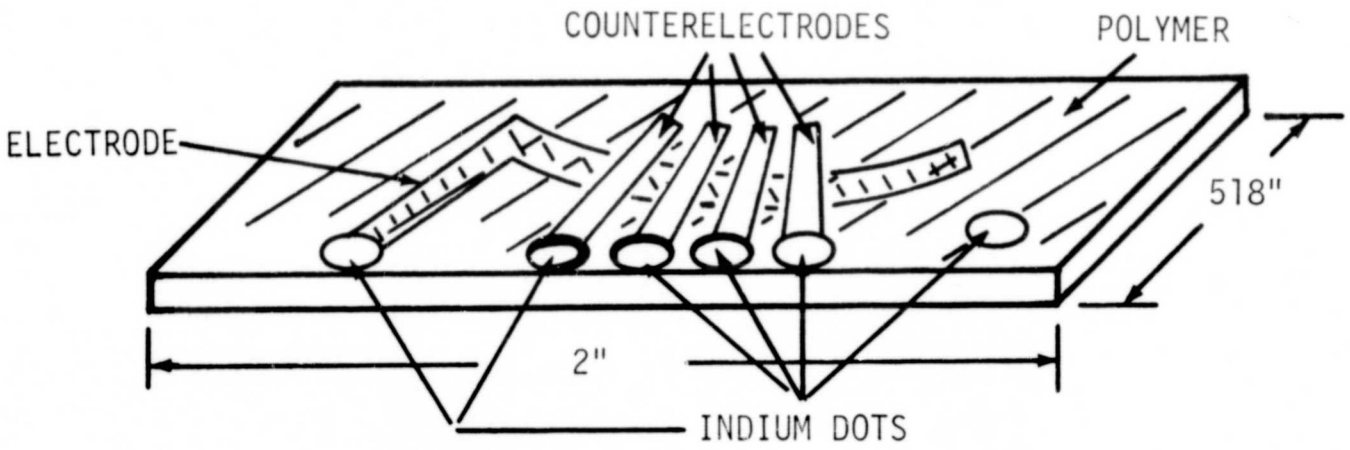


Figure 1

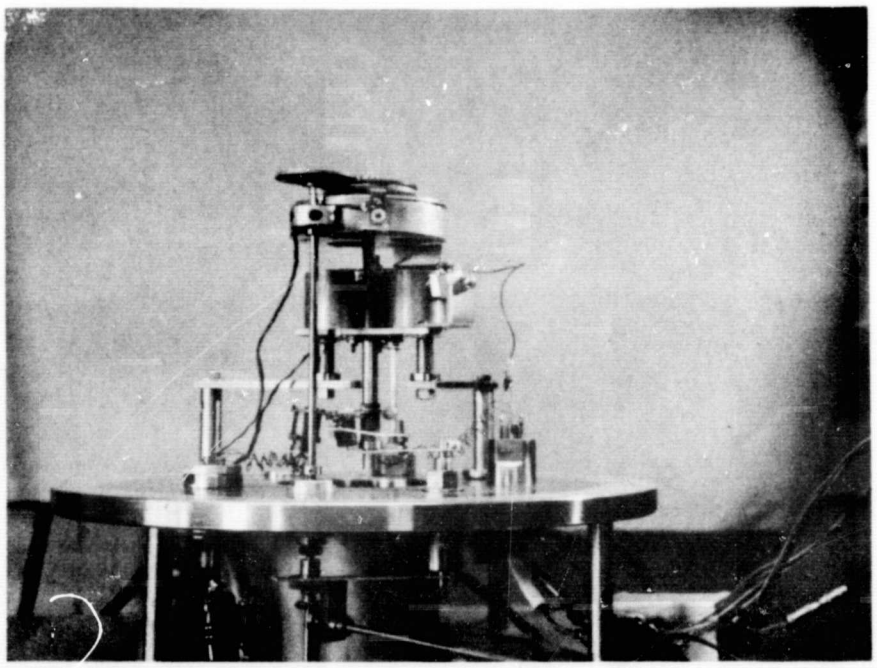


Figure 2

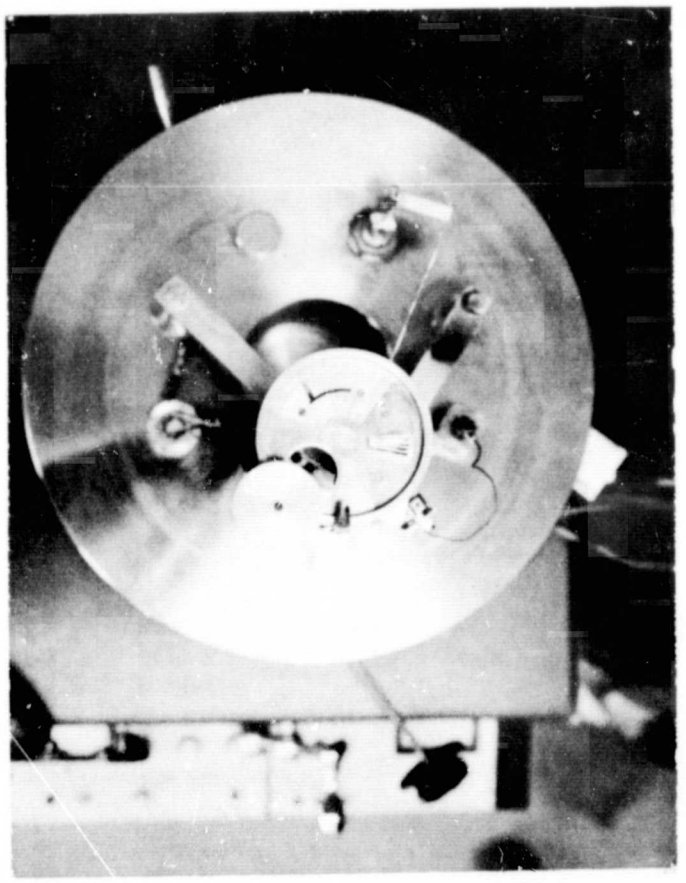


Figure 3



Figure 4



Figure 5

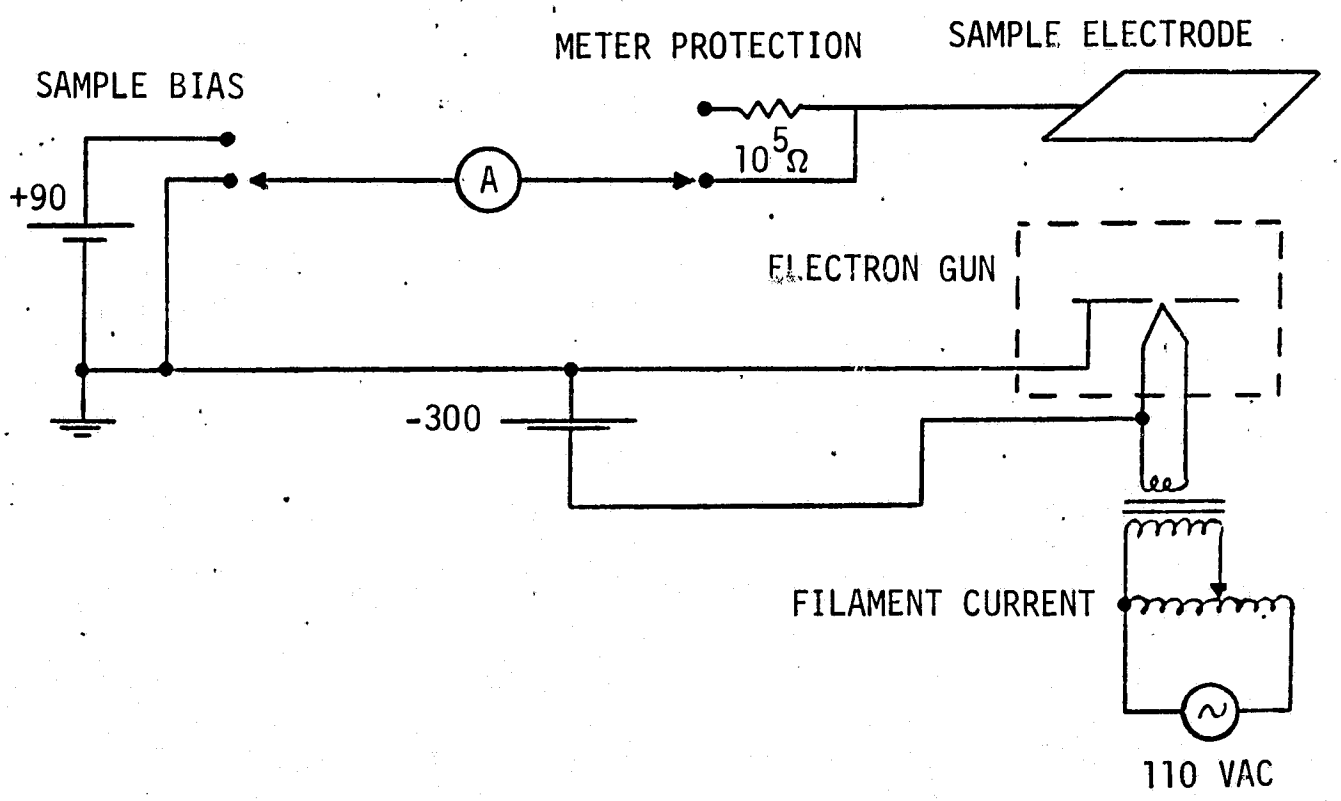


Figure 6

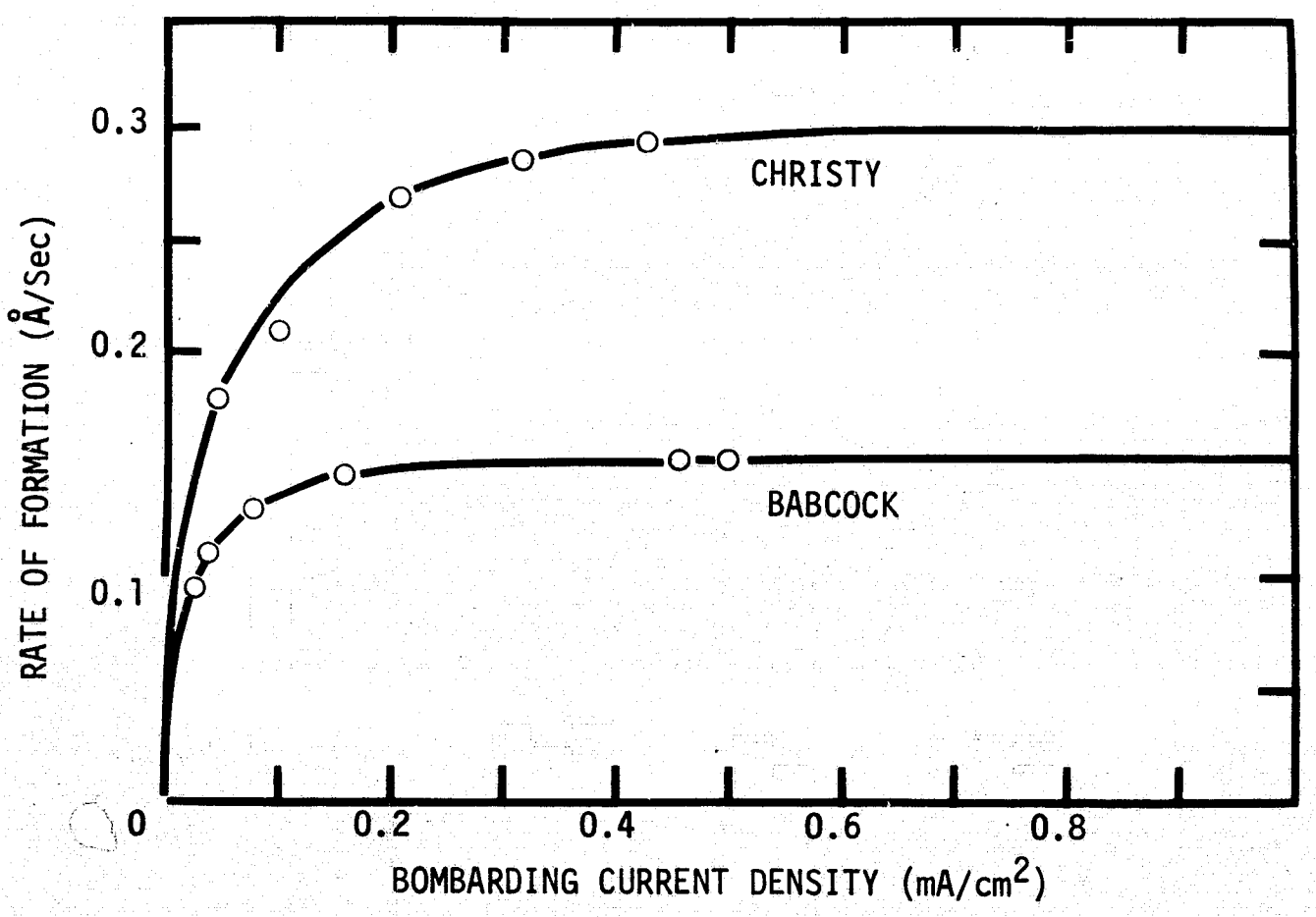


Figure 7

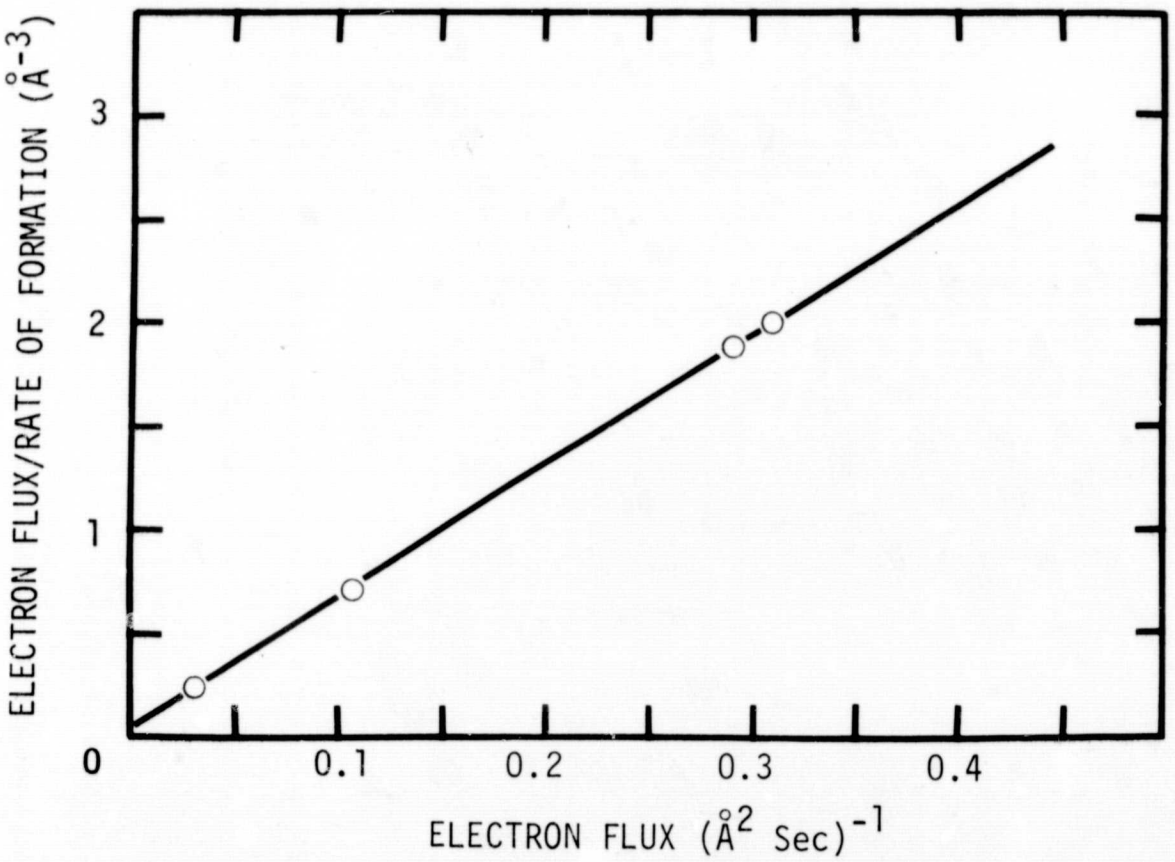


Figure 8

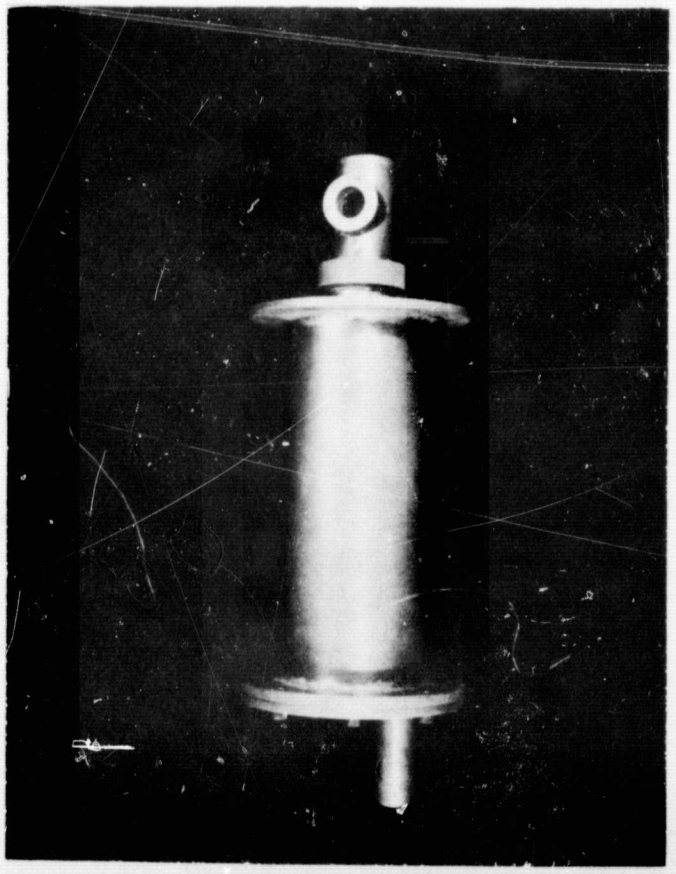


Figure 9

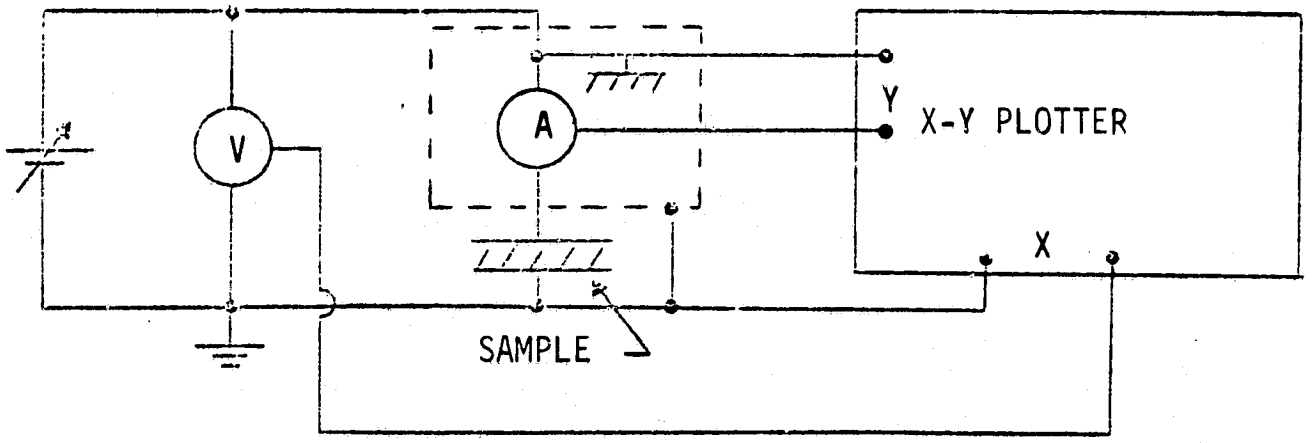


Figure 10

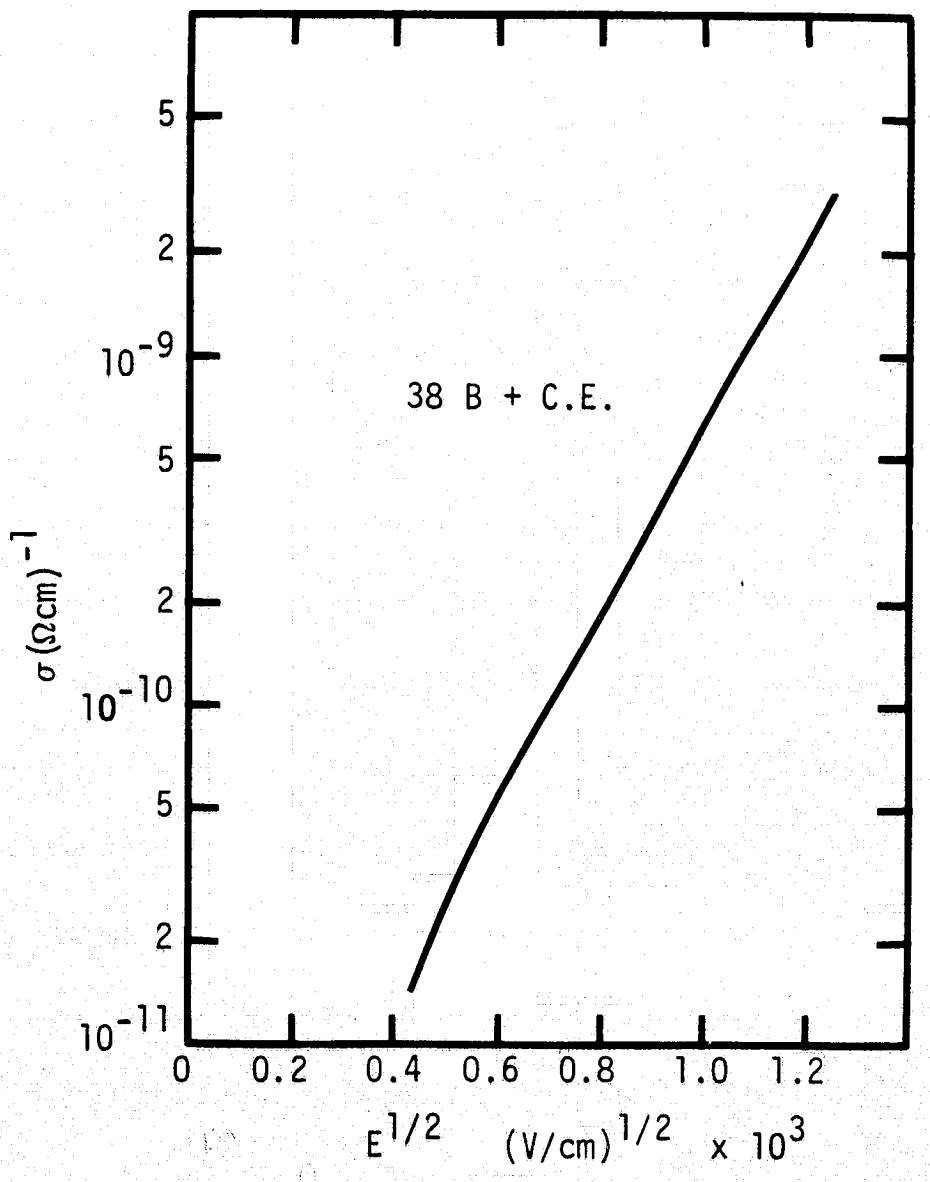


Figure 11

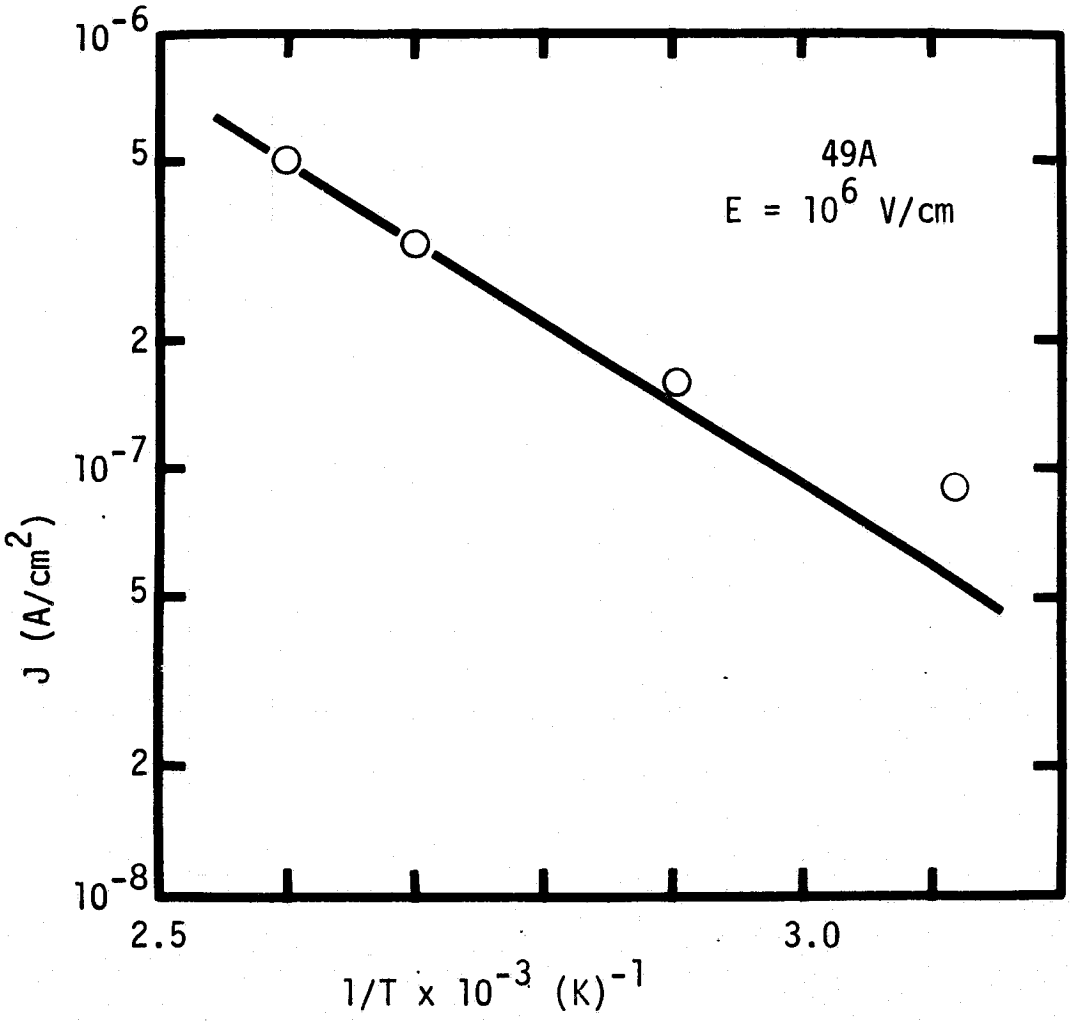


Figure 12

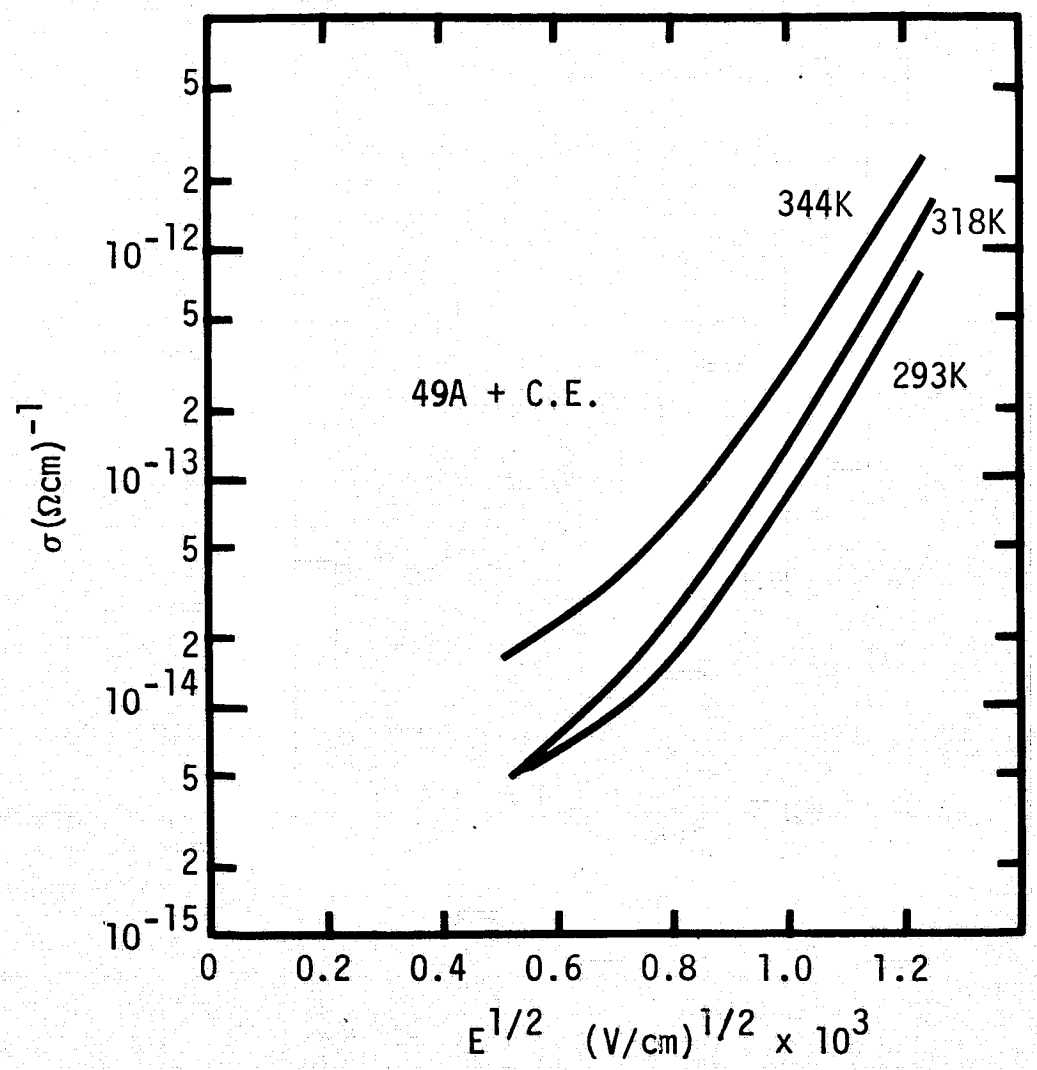


Figure 13

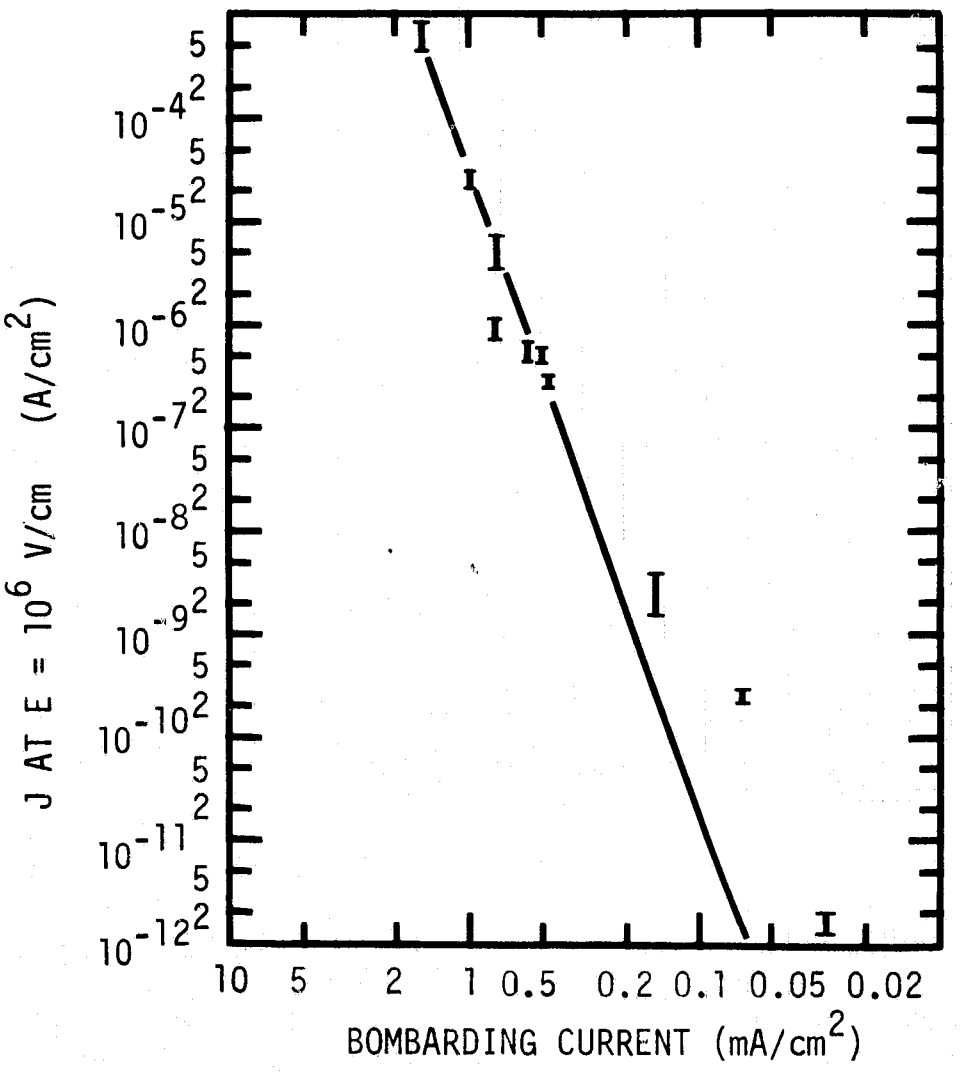


Figure 14

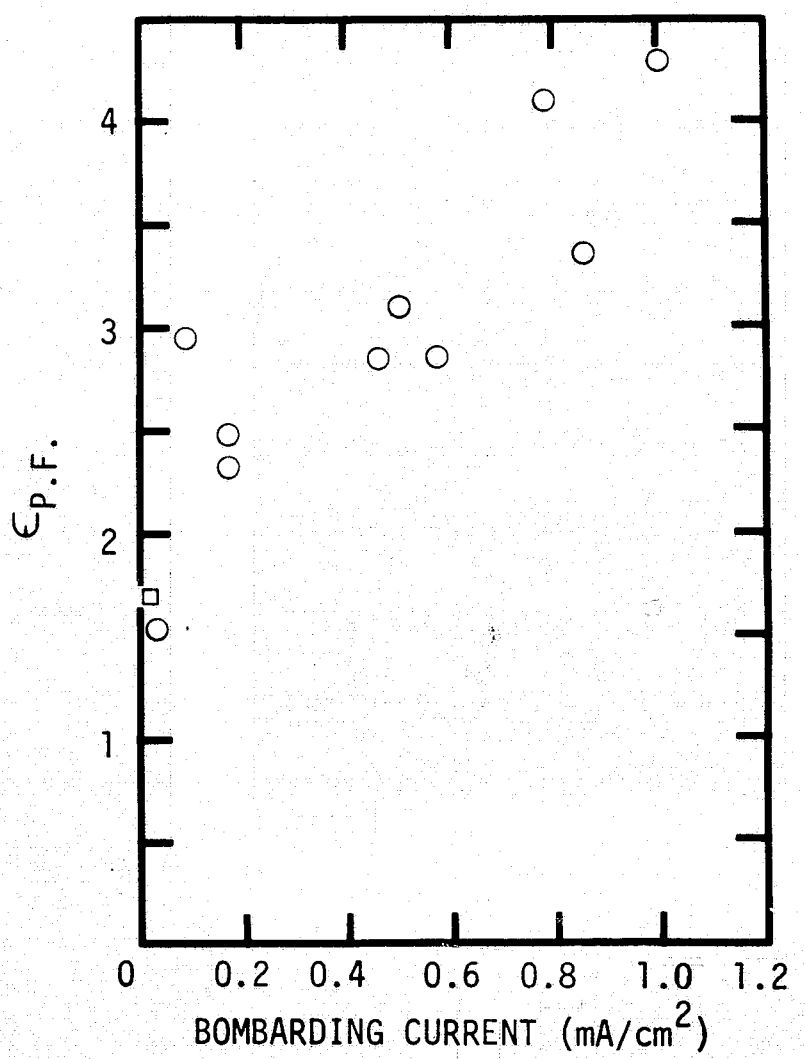


Figure 15

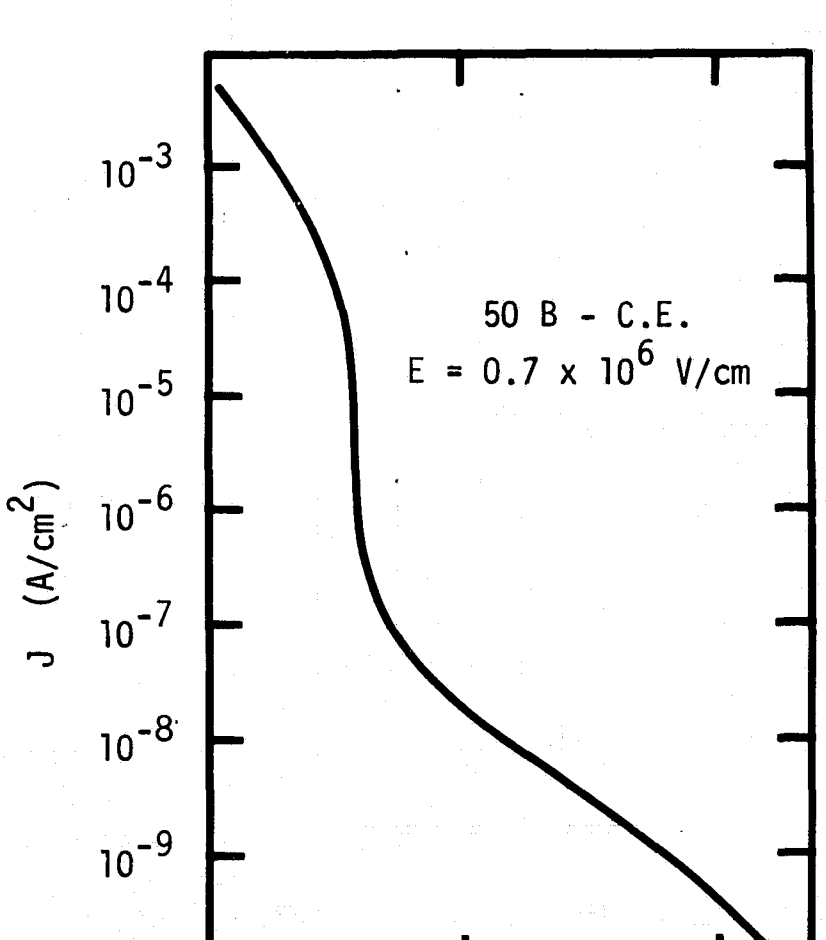


Figure 16

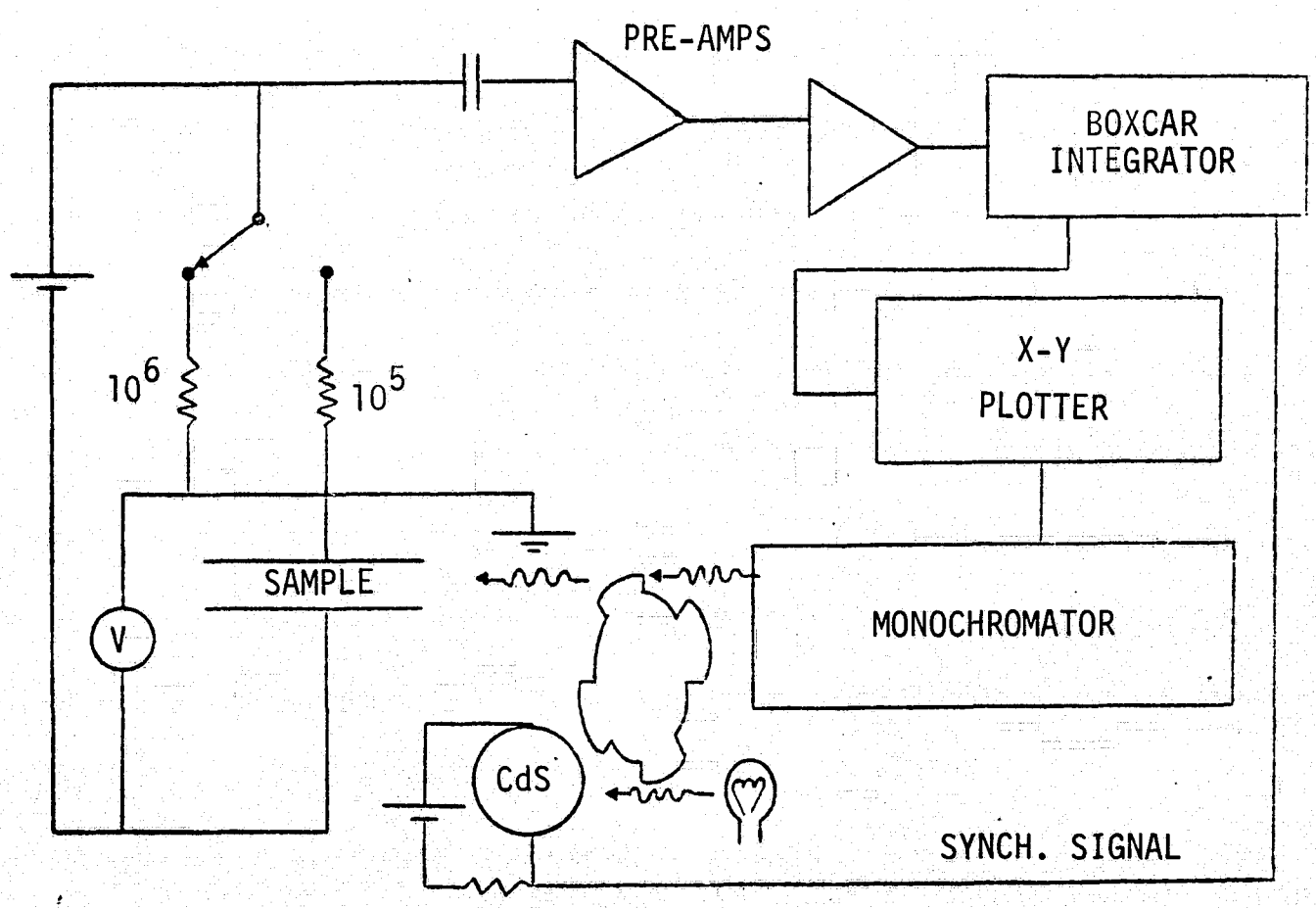


Figure 17

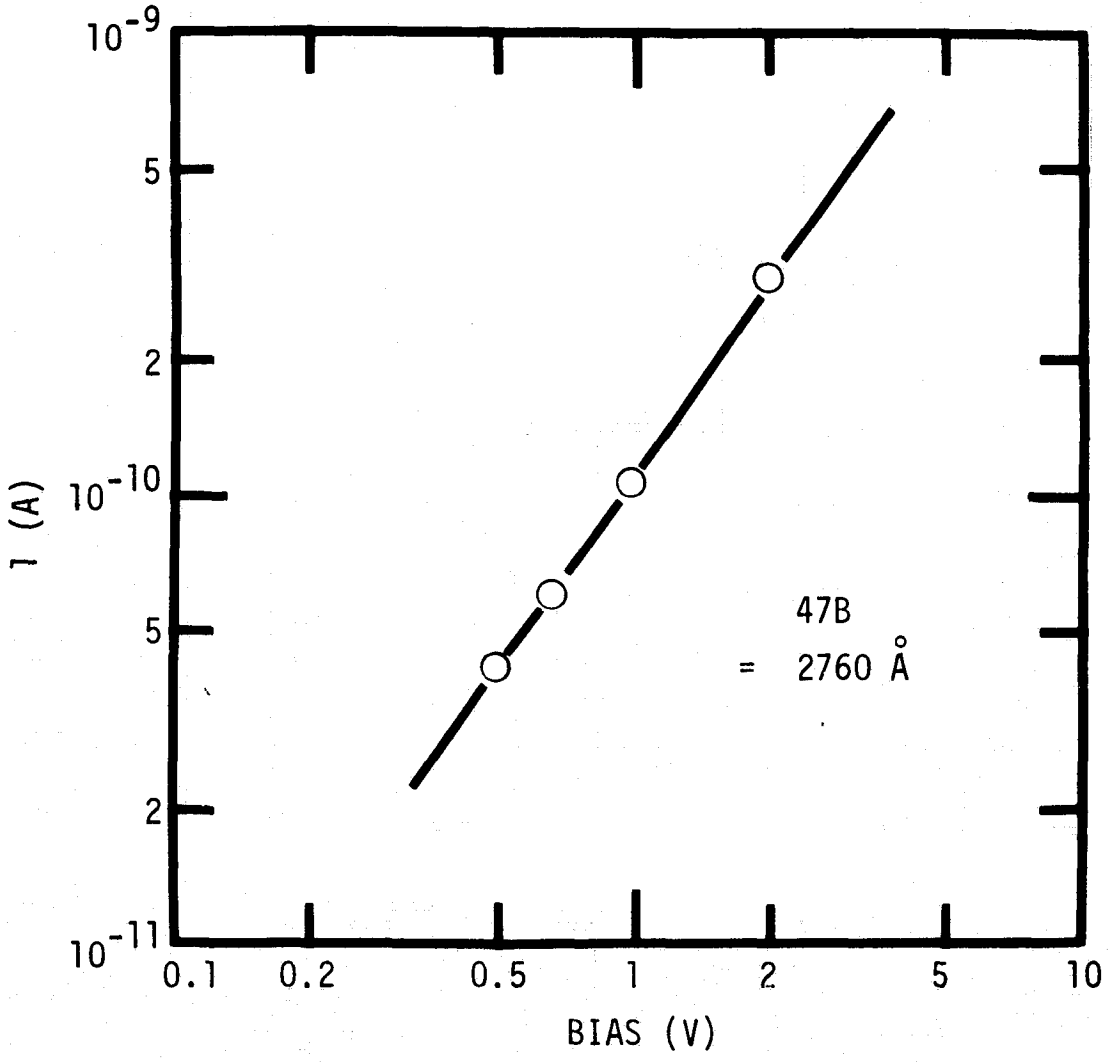


Figure 18

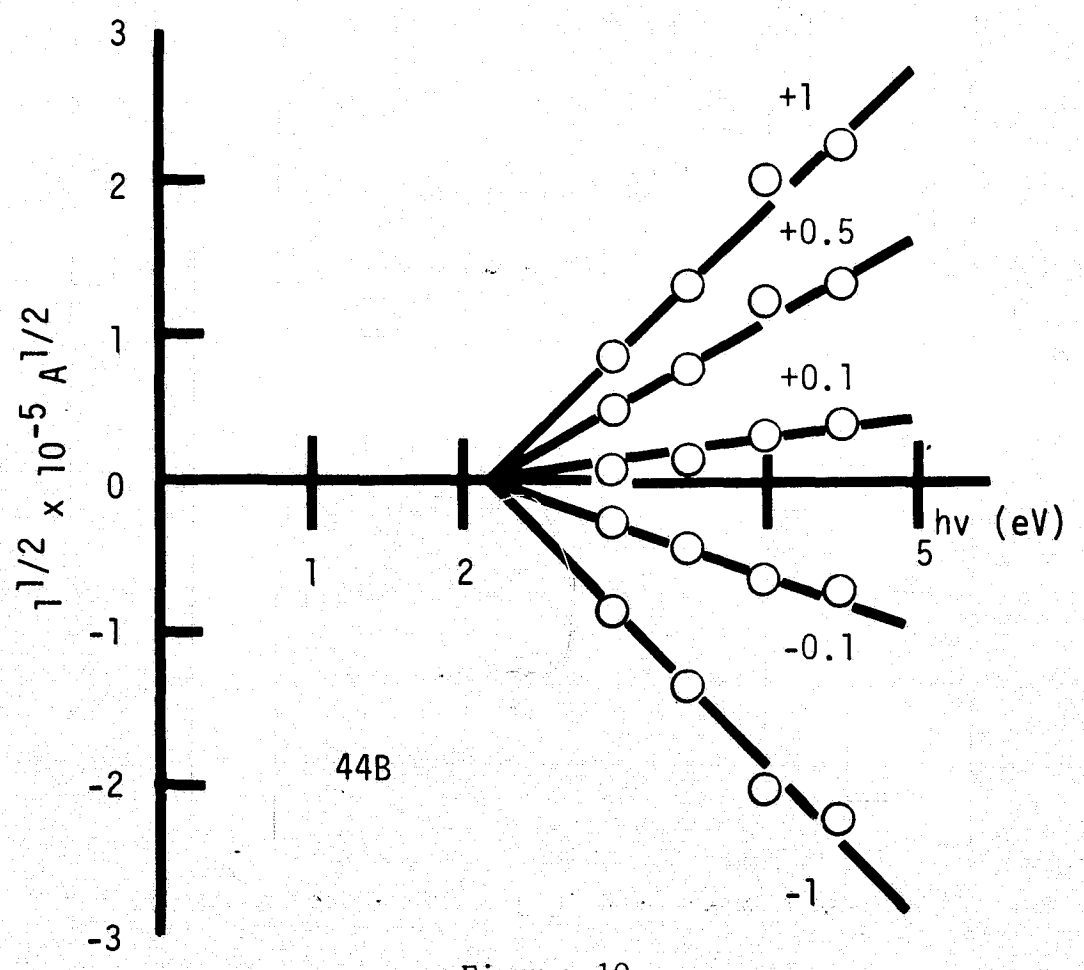


Figure 19

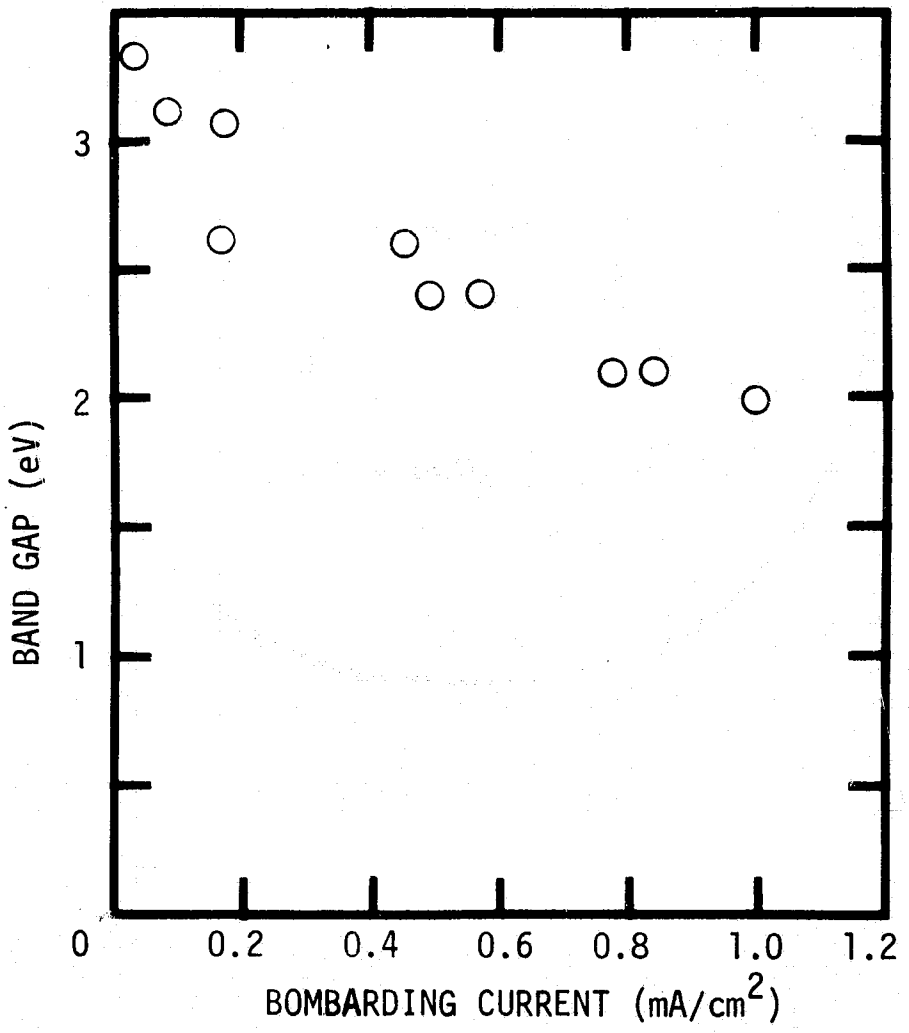


Figure 20

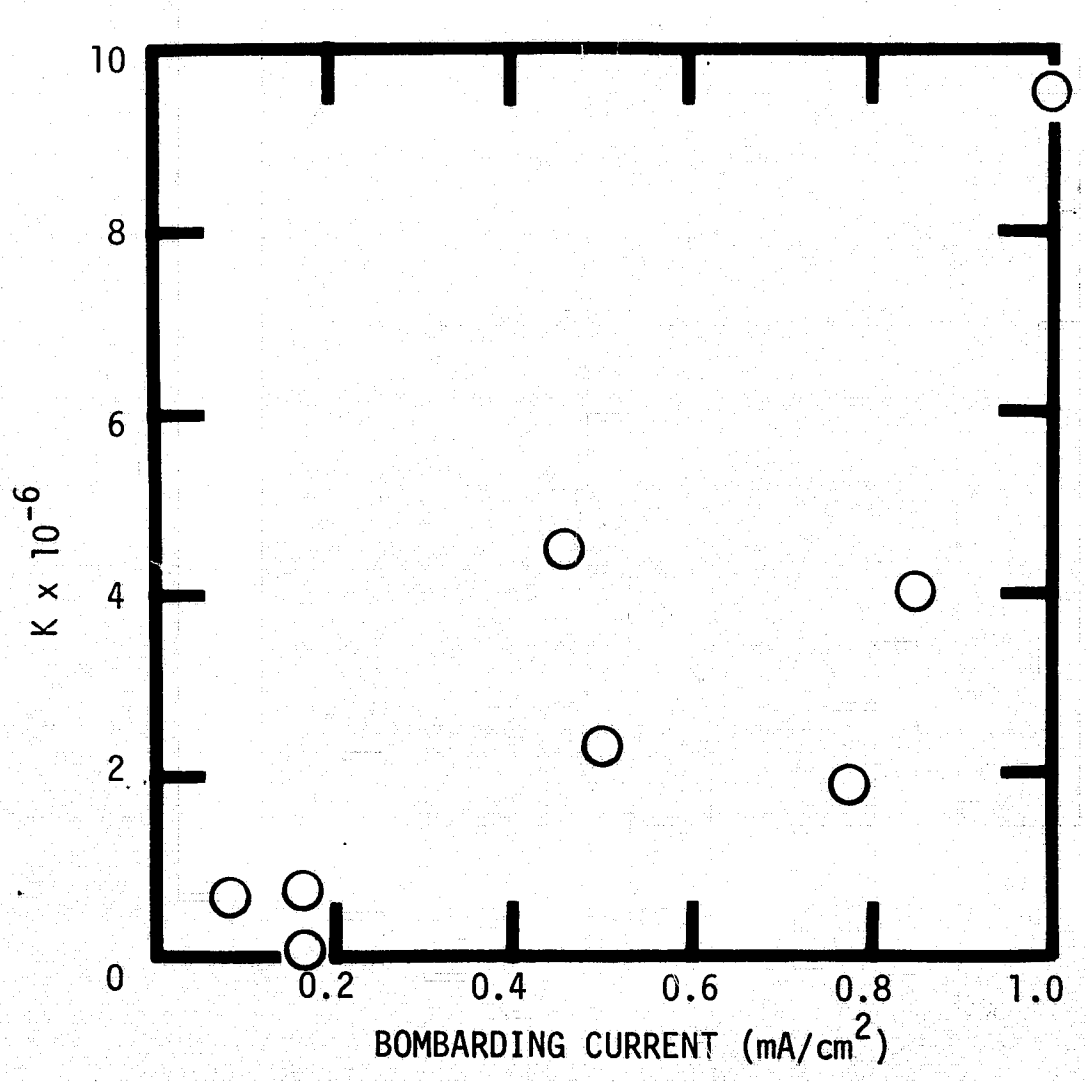


Figure 21

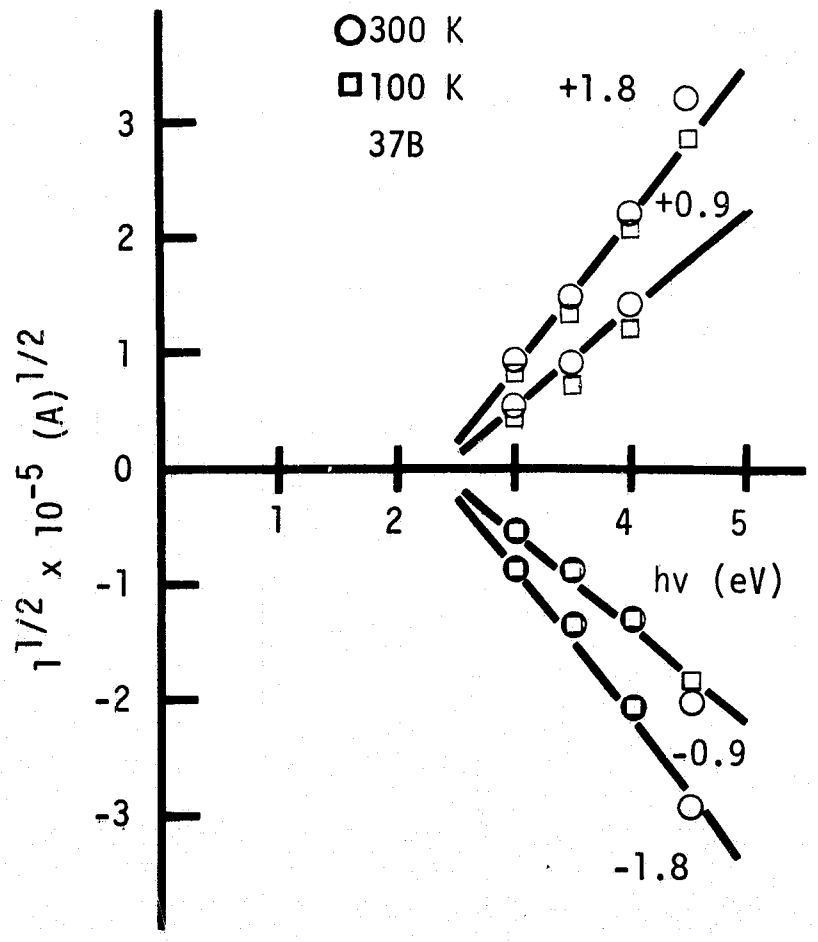


Figure 22

5.0 NEW TECHNOLOGY

New technology evolved under Contract NAS 7-717 is reported in the following.

5.1 ENERGIZED SEALS

The energized seal concept is based upon compressing the seal material in a contained volume. The concept is especially important using seal materials that are plastics, such as Teflon. Elastomers are also suitable for the application, however, in sealing reactive propellants, plastics are preferred. The advantages of this seal are zero leakage and contamination insensitivity. A detailed description of the seal is given in Sections 2.2, 2.3 and 2.4 of this report.

5.2 PROTECTED SEAL VALVE DESIGN

The protected seal valve design utilizes a polymer seal in series with a metal-to-metal seat. The polymer seal is protected from the dynamic flow of reactive propellants such as fluorine and oxygen difluoride. The metal seat provides positive flow control area while the polymer seal provides leakage control. The design is described in Section 2.3.

5.3 THERMOHERMETIC ISOLATION VALVE CONCEPT

This valve concept is based on the use of a thermally heated material which, upon expansion, actuates the poppet which is used to pierce a hermetically sealed diaphragm. The valve is used to replace the squib actuated isolation valves where high response is not required. The advantages of the valve are zero leakage, lower cost and higher reliability. The design is described in Section 2.6.1.

5.4 FLUIDIC FLOW REGULATOR

The fluidic flow regulator uses a cavitating venturi sump which provides an absolute pressure reference for the fluidic controller. The sump also provides a dump for the liquid to the main propellant stream without affecting flow conditions in the main line. This concept is presented in Sections 3.2, 3.3 and 3.4.

5.5 METAL/METAL INTERFERENCE SEALS

Metal spherical balls forced into a cylindrical tube at a predetermined interference to provide metal-to-metal sealing is the basis of this disclosure. Although higher actuation forces over the common valve designs are necessary, the advantages of low leakage with metal-to-metal seats for application to highly reactive rocket propellants may warrant its used. This concept is described in Section 4.2.

5.6* THERMALLY STRESSED POLYMER SEALS

The seal in this disclosure is confined and upon application of heat is stressed to provide good leakage control. A closed loop servo is used to minimize the heat requirements, leakage being sensed and fed to the controller of the heater supply.

5.7* FERROMAGNETIC FLUID LOGIC DEVICE (TRW Docket No. 5240)

The device uses a ferromagnetic fluid which is controlled by a permanent magnet and electromagnetic field to perform digital logic and electrical to fluid transducer functions. The device uses no moving mechanical parts.

5.8* FLUIDIC SET POINT CONTROLLER (TRW Docket No. 4995)

This concept uses fluidic circuits to detect a gage pointer for use in controlling motions and processes. High and low limit control can be performed by the use of an additional pointer sensor. The device should be simple and inexpensive and can be used by unskilled personnel. It is inherently explosion proof and can be used in any kind of environment. Applications are seen in the chemical and food processing industries.

5.9* AUTOMOTIVE AIR INDUCTION SYSTEM (TRW Docket No. 5017)

The use of a fluidic diverter valve without moving parts provides more complete combustion within the internal combustion engine. The diverter valve either diverts flow through a bypass loop where it is mixed and heated or directed straight through to the cylinders. This concept provides more thorough mixing of the fuel and air resulting in higher combustion efficiency.

---

*The innovation is not described in the final report, however, a disclosure has been documented by TRW.